UNIVERSIDADE DA BEIRA INTERIOR
Engenharia

FCT
Fundação para a Ciência e a Tecnologia
MINISTÉRIO DA CIÊNCIA, TECNOLOGIA E ENSINO SUPERIOR

Modelling of Transcritical Jets by the use of a Real Fluid Equation of State

Eduardo Luís Santos Farias Antunes

Tese para obtenção do Grau de Doutor em
Engenharia Aeronáutica
(3º ciclo de estudos)

Orientador: Prof. Doutor André Silva
Orientador: Prof. Doutor Jorge Barata

Covilhã, Março de 2018

Dedicatória

À minha mulher Julita e à minha filha Liliana.

Na esperança de que os esforços e sacrifícios de hoje se traduzam na realização dos nossos sonhos e desejos.

Agradecimentos

Quero agradecer ao meu orientador, Professor Doutor André Resende Rodrigues Silva, pela orientação, apoio científico e teórico, mas também pelo enorme encorajamento e elevado otimismo que me transmitiu ao longo de todo o trabalho e principalmente nos momentos mais difíceis.

Quero agradecer ao meu orientador, Professor Doutor Jorge Manuel Martins Barata, por me dar a oportunidade de trabalhar integrado no grupo de investigação e por todo o apoio científico e teórico prestado durante a realização do trabalho.

Resumo

O presente trabalho tem como o objectivo o estudo e modelação de jactos de azoto criogénico numa gama de condições transcriticas e supercriticas. A injecção de combustível em condições de alta pressão e temperatura apresenta-se como o principal objecto de aplicação da presente investigação. Este tipo de injecção é típica não só em motores foguetes mas também em modernos motores diesel assim como em turbinas de gás, em ambos os casos pressões e temperaturas de combustão têm aumentado com o objectivo de aumentar eficiência e performance reduzindo ao mesmo tempo e emissão de poluentes.

Uma aproximação numérica de densidade variável, originalmente desenvolvida para a modelação de jactos gasosos, turbulentos e incompressíveis foi utilizada para a modelação deste tipo de escoamentos. Os resultados demonstraram o potencial desta aproximação. No entanto, a mesma não previa os efeitos resultantes da transmissão de calor nos fluidos nem o comportamento de gases reais. Para colmatar estas deficiências foi incluída a equação da energia assim como equações de estado de gás real. Para a determinação das propriedades dos fluidos foram empregues e testadas diferentes metodologias.

Os resultados obtidos mostram uma boa concordância no seu geral com os dados experimentais divergindo apenas no comprimento do cone potencial. Uma conclusão importante dos resultados é a da importância que a turbulência tem neste tipo de escoamento quando comparada com as propriedades moleculares.

Palavras-chave

Ponto crítico; Jatos criogénicos; Injeção de combustível; Motores foguete; Escoamentos supercríticos; Termodinâmica de gases reais.

Resumo alargado

A prevenção das alterações climáticas assim como a salvaguarda dos recursos naturais do nosso planeta são hoje dois dos maiores desafios que a humanidade enfrenta. O uso excessivo dos combustíveis fosseis está de forma evidente na base destes problemas, por esse motivo é urgente a sua redução. A humanidade também se encontra numa corrida pelo conhecimento do universo, entre as varias tecnologias necessárias para obter uma melhor compreensão do que nos rodeia estão as tecnologias que nos permitem realizar viagens espaciais, bem como desenvolver a capacidade de construir motores foguete cada vez mais fiáveis e com melhor desempenho.

Uma tendência que tem sido adotada de forma generalizada por parte de projetistas e construtores para o aumento da eficiência e desempenho de motores de combustão interna, de que são exemplo os motores diesel, as turbinas de gás, os motores foguetes e outros, é o aumento das pressões e temperaturas de operação. Estas trazem no entanto complexidades adicionais. Ao aumentar a pressão e temperatura de operação, não raras vezes, atingem-se os valores críticos termodinâmicos destas variáveis. As consequências não são de todo inócuas, em volta do ponto crítico e acima deste existem vigorosas variações do comportamento dos fluídos. No ponto crítico, por um lado, propriedades como a difusividade mássica, a tensão superficial e o calor latente desaparecem, por outro lado, o calor especifico a pressão constante, a compressibilidade isentrópica e a condutividade térmica aproximam-se a infinito. É também sabido que em condições supercríticas, definidas pelo facto da pressão e temperatura estarem ambas a valores acima dos críticos, dá-se uma variação do comportamento da estrutura dos jatos, esta passa de um típico jato liquido injetado num gás para algo que mais se assemelha a um jato gasoso injetado num ambiente gasoso. No entanto os maiores desafios aparecem na modelação de jatos em condições próximas do ponto crítico já que nestas condições o conhecimento é ainda hoje limitado.

No presente trabalho pretendeu-se modelar a injeção de azoto criogénico numa camara repleta de azoto gasoso a condições supercríticas. O azoto é injetado a duas temperaturas diferentes que correspondem no caso da temperatura mais baixa a condições transcríticas, quando a pressão é supercrítica mas a temperatura subcrítica, e no caso de temperatura mais elevada corresponde a condições supercríticas de injeção. Várias estratégias diferentes foram empregues, todas elas baseadas nas médias de Favre das equações de Navier-Stokes e utilizando um modelo de turbulência $k - \varepsilon$. Inicialmente foi empregue uma estratégia originalmente desenvolvida para jatos gasosos de densidade variável, esta abordagem faz uso da lei de Amagat, por via da fração de mistura, para obter a densidade e que usa um valor constante para viscosidade molecular. Outras estratégias, que empregam duas diferentes equações de estado de gás real, Soave-Redlich-Kwong e Peng-Robinson, foram também empregues. Nestas metodologias foi necessário integrar a equação da energia, originalmente não presente na formulação, por forma a obter o campo de temperaturas. Foram também testados diferentes métodos para a determinação de propriedades como a viscosidade molecular, condutividade térmica e calor especifico.

Os resultados obtidos mostram boa concordância com os resultados experimentais e também com simulações Large Eddy Simulation (LES) de outros autores principalmente para a razão de abertura do jato e para a distribuição radial da densidade a diferentes distâncias axiais. Já para a distribuição axial da densidade na linha central houve algumas discrepâncias nomeadamente na determinação do comprimento do cone potencial. A partir da comparação dos resultados

entre as varias metodologias pôde ser concluído que a variação da metodologia de calculo das propriedades moleculares tem uma fraca influência sobre os resultados, isto sugere que são as características turbulentas do escoamento que de facto mais influenciam o mesmo.
Como futuro trabalho sugere-se o estudo da influência do numero de Prandtl turbulento e a sua eventual variabilidade ao longo do escoamento.

Abstract

The prevention of further climate as well as the exhaustion of natural resources in our planet are two of the biggest challenges faced by humankind. To achieve this objectives, emissions and fossil fuel consumption must be reduced. At the same time humankind puts great effort in the understanding of our universe, space flights are an important mean to achieve such knowledge and for those better performance and reliability of rocket engines are required.
Increasing the operating pressure and temperature of power systems such as diesel engines, gas turbines, rocket engines, and others, is a known way of increasing efficiency and performance. Over the past years, this increase has become an important trend in the design of new power units.
In order to study the high pressure and high temperature operating condition of the variety of internal combustion engines, a cryogenic nitrogen jet injected into supercritical chamber conditions was simulated numerically. The Favre averaged Navier-Stokes equations were employed together with a $k - \varepsilon$ turbulence model. To determine the density value different approaches were employed, one making use of Amagat's law based on mixture fraction, and another employing the Soave-Redlich-Kwong or the Peng-Robinson real fluid equations of state, and also integrating the favre averaged energy equation. To determine the fluid properties also different approaches were tested.
The obtained results have shown an acceptable agreement with experiments, mainly in terms of the jet spreading rate as well as for radial density distribution. For the axial density distribution was found a more difficult agreement for the length of the potential core. Results also suggest the a strong influence of the turbulent characteristics over the flow of study.

Keywords

Critical Point, Cryogenic Jets, Fuel Injection, Rocket Engines, Supercritical Flows, Real Fluid Thermodynamics.

Contents

List of Figures

List of Tables

Nomenclature

a	real fluid equation of state constant
b	real fluid equation of state constant
B	transfer number
β_v	evaporation rate
c_p	specific heat at constant pressure [$J.kg^{-1}.K^{-1}$]
c_v	specific heat at constant volume [$J.kg^{-1}.K^{-1}$]
C_μ,$C_{\varepsilon 1}$,$C_{\varepsilon 2}$	coefficients of the turbulence model
d	droplet diameter [m]
d_0	initial droplet diameter [m]
D	injector diameter [m]; normalized droplet diameter
$\delta_{i,j}$	Kronecker delta
δ_τ	viscous lengthscale
$\delta'_{vis,0}$	visual thickness of shear layer
e	internal energy [J]
e_t	total energy [J]
ε	dissipation rate of turbulent energy
f	misture fraction; body force
F	mean mixture fraction
G	buoyancy term
γ	ratio of specific heat
h	enthalpy [J]
i	axial direction index
j	radial direction index
λ	thermal conductivity [$W.m^{-1}.K^{-1}$]
k	turulent kinetic energy; index
K	von Karman constant
M_n	molar mass [$kg.mol^{-1}$]
μ	molecular viscosity [$Pa.s$]
μ_t	turbulent viscosity [$Pa.s$]
n	amount of substance [mol]
ϕ	generalized variable
ω	chamber-to-injection fluid density ratio (ρ_∞/ρ_0); acentric factor
P	pressure [Pa]
P_c	critical pressure [Pa]
P_∞	chamber ambient pressure [Pa]
P_k	production of turbulent kinetic energy
P_r	reduced pressure (P_∞/P_c)
Pr	Prandtl number
Pr_t	turbulent Prandtl number
ρ	density [$kg.m^{-3}$]
ρ_0	injected fluid density [$kg.m^{-3}$]
$\rho_{gs}\infty$	injection chamber's fluid density [$kg.m^{-3}$]
ρ_c	critical density [$kg.m^{-3}$]

q	heat transfer
Q	heat
r	radial coordinate [m]
R	gas constant [$J.mol^{-1}.K^{-1}$]
R/D	radial distance normalized by injector diameter
R_{diam}	injector radius [m]
Re	Reynolds number
Re_t	friction Reynolds number
S_ϕ	source term
$\sigma_k, \sigma_k\varepsilon$	coefficients of the turbulence model
t	time [s]
T	temperature [K]
T_c	critical temperature [T]
T_r	reduced temperature (T/T_c)
T^*	pseudo-boiling temperature [K]
τ	viscous stress
τ_w	shear stress at the wall
u	axial velocity [$m.s^{-1}$]
u_τ	friction velocity
u^+	dimensionless velocity
U	mean axial velocity [$m.s^{-1}$]
U_{in}	injection axial velocity [$m.s^{-1}$]
v	radial velocity [$m.s^{-1}$]
$\vee_t$	turbulent kinematic viscosity
V	mean radial velocity [$m.s^{-1}$]; volume[m^3]
V_m	molar volume [$m^3.mol^{-1}$]
$\vec{V}$	velocity vector [$m.s^{-1}$]
X	axial coordinate [m]
x/D	axial distance normalized by injector diameter
y^+	distance from the wall measures in viscous lengths
Z	compressibility factor

Acronyms List

AFRL	Air Force Research Laboratory
CFD	Computational Fluid Dynamics
CNRS	French National Center for Scientific Research
DLR	German Aerospace Center
DNS	Direct Numerical Simulation
EoS	Equation of State
FANS	Favre Averaged Navier Stokes
LES	Large Eddy Simulation
LOX	Liquid Oxygen
NIST	National Institute of Standards and Technology
OpenFOAM	Open source Field And Manipulation
PDF	Probability Density Function
PIV	Particle Image Velocimetry
PLIF	Planar Laser-Induced Flourescence
PR	Peng-Robinson
RANS	Reynolds Averaged Navier-Stokes
SIMPLE	Semi-Implicit Method for Pressure Linked Equations
STP	Standard Conditions for Temperature and Pressure
SRK	Soave-Redlich-Kwong

Chapter 1

Theroretical Review

1.1 Introduction

Humankind is currently in a moment of history were it is strongly dependent on fossil fuels to sustain and further advance the technological development, while other alternatives sources of energy have not yet been found as an effective replacement despite intensive research. However, these fossil fuels are not unlimited, so a more efficient use of them must be found meanwhile. Also, we live in a planet that relies in a very fragile balance of its ecosystem. Pollution originated by the burning of fossil fuels is proved to be able to destabilize this fragile balance with possible disastrous consequences. Thus, a less harmful way of burning these fuels must be found, or at least a way of while fulfilling our energetic demands, burning those fuels in smaller amount.

One way of fulfilling the objectives above is by the development and adoption of more efficient combustion power systems. When relying on combustion to produce energy, there are some very important aspects concerning to it, one of those is the fuel injection. Fuel injection is the biggest responsible for a good mixing of the fuel with the oxidizer, which is crucial for an efficient combustion. This way, the study of fuel injection is since the start of the development of a power production system a very interesting case of study.

Increasing the operating temperatures and pressure of power systems like diesel engines, gas turbines and rocket engines is also a known way of enhancing the fuel efficiency of such engines. However the increase of temperature and pressure does not come without costs. Initially the main engineering difficulties appeared in the form of the resistance of materials both to stress and temperature. Big effort was made by the industry in the way of finding better materials to use in such engines. Today the main problems observed, with the increase of operating pressure and temperature, are mostly thermodynamic problems.

When operating pressure and temperature increase, the fuels and oxidisers used by propulsion systems may experience the exceeding of their critical values. The issue is that under conditions of pressure and temperature that exceed or are around the critical values, fluids have shown to have quite distinct behaviour from the usually observed while at conditions far from these. The critical point, where both pressure and temperature are at their critical value, is considered itself as a singularity. In this particular condition fluid properties like effective mass diffusivity, surface tension and latent heat were observed to vanish. On the other hand, the heat capacity at constant pressure, c_p, the isentropic compressibility, k_s and the thermal conductivity, λ, all become infinite [1]. The non-existence of latent heat causes that to vaporize the liquid no heat needs to be added, and thus, there isn't vaporization heat. This conclusion is also defended by Yang [2]. The fluid at critical condition presents this way a behaviour resembling that of a boiling liquid. However if the behaviour at the critical point is somewhat quite well described, there are an infinity of conditions around this particular point in which the fluid shows strong behaviour variations, that are not yet totally described.

A proper analysis and study of the conditions must be performed. In order to do so, four regions or regimes around the critical point will be described.

When both temperature and pressure are subcritical the region is called “saturated” (or subcritical) regime [3], in this region two phase flow is possible depending on the temperature and pressure, and when injecting liquid fuels atomization can be observed. Increasing the pressure to supercritical values while maintaining subcritical temperature the system falls into a different region called “transcritical” regime, under these conditions is observed a compressed liquid that remains at this state until supercritical values of temperature are achieved, this regime is currently the one for which researchers hold less knowledge about, and the one that represents more challenges in recent researches. When the temperature of the fluid is supercritical it becomes impossible to obtain a liquid state any longer, independently of the pressure’s value. In fact an extreme increase of the pressure value will ultimately lead to the deposition of the fluid into solid state without passing through the liquid state. Two different regions can be identified with supercritical temperature. At subcritical pressures the region is called “superheated” regime, under these conditions the fluid has an ideal-gas behaviour When both pressure and temperatures have supercritical values the region is called the “supercritical” regime at which the fluid has a gas-like behaviour with the particularity of conserving a liquid-like density thus being called a dense gas [3] or generally as “fluid” as described in Bellan’s work [1]. These four regimes are schematized in Figure 1.1.

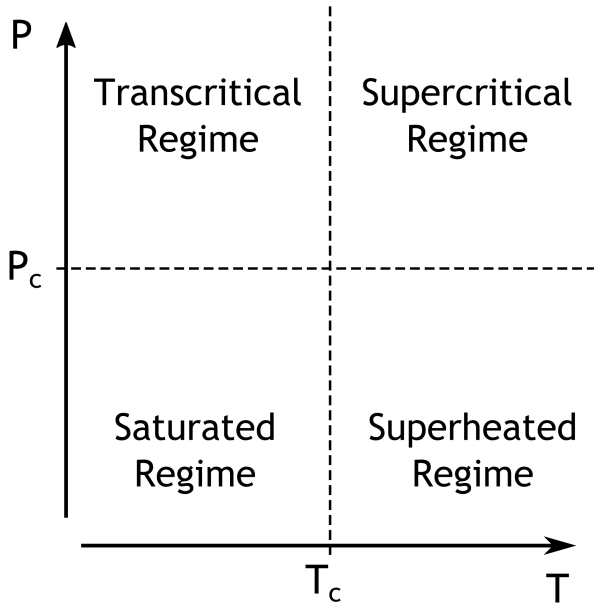

Figure 1.1: The four regimes around the critical point.

For single component flows the existence of supercritical values of pressure and temperature, which defines the regime in which the fluid is, just depends on the fluid physical properties. However, when dealing with more than just one substance, the variation of the mixture fraction can strongly influence critical values of the fluid as described by Lacaze and Oefelein[3].
It’s quite common the use of fuel for refrigeration proposes in rocket engines before injecting them into the thrust chamber [4]. In this case fuel enters the thrust chamber at already supercritical temperatures enabling only the superheated and supercritical regimes inside the thrust chamber. And because also the pressure inside the thrust chamber is usually subcritical lonely during the starting moments of engine operation, most of the operation of liquid rocket

engines is made in the supercritical regime. This can be corroborated by the examples of the liquid-H2/liquid-O2 space shuttle main engine, with the combustion chamber operating at pressures of 22.3 MPa and the Vulcain engine (of Ariane 5 rocket) that with the same propellants can reach up to a recorded value of 28.1 MPa [5]. Both this pressure values are well above of the Hydrogen and Oxygen critical values of P_c = 1.313 MPa and P_c = 5.043 MPa, respectively. The critical temperatures of Oxygen (T_c = 154.6 K) and of Hydrogen (T_c = 33.2 K)[6] are also evidently overcome in rocket engines.

In the purely supercritical regime, the fluid has as described a behaviour of a dense gas and can be treated as a variable density gaseous jet as was tested is previous works[7], [8]. The biggest uncertainty in the study of rocket engines comes when the fuels are injected below the critical temperature. This happens in the cases when fuels are not use to refrigerate the engine or when are used fuels that are in the liquid state at room temperature (also in the examples above only the hydrogen is used to cool the thrust chamber, the oxygen is not warmed before injection and this way is injected with temperature bellow critical, so at transcritical regime). In these cases the area immediately after the injector becomes very important because it's the area where the injected fuels may still retain subcritical temperatures, and this way, obeying to the transcritical regime where the liquid state exist in the form of a compressed liquid.

Another question is raised by Negro and Bianchi [9] which is the possibility in fuel refrigerated engines and high pressure injection systems of flash evaporation due to the superheating of fuels. Flash evaporation may appear inside the injection nozzle due to a sudden decrease of the pressure during the injection process and can cause strong variations in the injection process.

Diesel engines are currently following the trend of progressively increasing operating pressures manly due to higher compression ratios and the generalized use of supercharging, a trend mainly motivated by the understanding that increased ambient density relative to the density of the injected fuel results in better mixing and increased rates of combustion. This however leads to operating pressures that commonly exceed the critical pressure of the injected fuel by a factor of two or more [10]. Because so far there isn't an usual practice of heating the diesel fuel before the injection, injection temperatures in diesel engines are clearly subcritical. This makes the diesel injection operation to be between the saturated and transcritical regimes in the beginning of injection. The fuel will then probably enter into the superheated and supercritical regimes as temperatures increase due to combustion. This way, it is possible the existence of fours regimes in diesel engines, a fact that raises great challenges in this kind of injection, especially because in diesel engines may exist the transition from a transcritical regime to a supercritical regime which are by far the less well known conditions up to the present date.

A similar trend observed in diesel engines is also observed in new generation gas turbine engines. Gas turbine engines operate at higher and more continuous temperatures than diesel engines while at lower injection and combustion chamber pressures. However, the continuous trend of turbine manufactures to increase the operating pressures (and also temperatures) to enhance efficiency may in the future lead to appearance of transcritical and supercritical regimes in turbines combustion chamber, which will probably make the current, mainly two phase flow, turbine injection models obsolete for these studies.

Focusing on a more recent trend which is the gasoline direct injection systems, it is possible to observe lower operating pressures when compared to diesel engines while higher combustion chamber temperatures. However, as in diesel engines, the recent generalized use of higher compression ratios and supercharging, mainly due to the new engine downsizing trend in the

automotive industry, may be responsible for the achievement of supercritical values of pressure and temperature in a near future. This can be responsible to make the transition of the classification of the gasoline direct injection from a saturated regime to maybe transcritical or even supercritical regime.
It becomes understandable that critical and around-critical conditions described above appear in everyday real operating conditions of current engines, and following the current trend, it will appear even with greater magnitude in the future. Kim [11] stated in is paper that it has been widely recognized that the comprehensive numerical model could be the ultimate tool for the design analysis of liquid rocket combustion systems. Therefore means to better understand these conditions in order to be able to simulate and model them are of great importance not only for liquid rocket combustion systems, but to all new generation engines design, in the way of reducing development and research costs (by limiting the amount of experimental tests needed), as well as in improving efficiency and reducing fuel and maintenance costs.

1.2 Droplets Studies

Several authors have been studying not only around-critical point properties of fluids but also the injection process in those conditions. One of first steps in any problem is to study the individual parts of it. This way one of the earliest approaches to the present problem was to study the physical properties of the fluids at trans-and-supercritical conditions. In order to perform such study single droplet evaporations at high pressures are usually observed.
The study of single drops has the advantage of allowing the elimination of non-thermodynamic effects from the study such as for example aerodynamic effects resultant of the injection procedure. This way becomes easier to distinguish which effects are direct result from the pressure and temperature conditions imposed and how the proximity to the critical point influences them.
One of the most commonly studied cases for supercritical condition is the one of evaporation and emission of single liquid droplets. This kind of studies has the objective of determine the processes that a liquid droplet encounter when mixing with the ambient gas and also to determine the mixing rate. Knowing the evaporation/emission rate of a liquid droplet is a very important information because this allows to determinate the droplet lifetime, the travelled distance for example in a combustion chamber, the time of the combustion and also the ignition delay, and all of this information is of the most relevance in the project of combustion chambers for engines and their respective injection systems.
Givler S.D. and Abraham J. [10] elaborated a revision about several previous studies conducted in the subjects of vaporization and droplets combustion under supercritical conditions. In their paper they describe the various conclusions achieved. One of the reached conclusions is that, despite its enormous importance for the modelling of combustion in sprays, until the paper's date (1996) there was not any published study about the interaction effects of multiple droplets in supercritical regime combustion. The same is not valid for the study of single droplets. A comparison is made in this work between the subcritical and the supercritical case. One of the conclusions achieved is that the droplet mixture process goes through two different stages. One initial transient stage in which the fluid droplet undergoes a temperature increase resulting from the fact of being in a higher temperature environment. The second stage of the process is one where the droplet temperature is constant and uniform, having reached

the thermal equilibrium. At this stage the droplet is in quasi-steady regime at a temperature slightly below the boiling point and all the heat transferred to the droplet will be associated with the evaporation of more fluid quantity from the droplet.

These two stages described before are always seen in the subcritical case. It was also verified that in the subcritical case, especially under low pressure conditions, the transient stage has a significantly small duration when compared with the quasi-steady stage. At these conditions, by neglecting the transient stage, the droplet evaporation rate obeys to the square diameter evaporation law, often simply referred as "D^2 Law", and is correctly described by the next expression:

$$d(t)^2 = d_0^2 - \beta_v t \quad \textbf{(1.1)}$$

Where d_0 is the initial droplet diameter, t is the time and β_v is the evaporation rate constant which may be shown to be:

$$\beta_v t = \frac{8\rho_{gs} D_{gs}}{\rho_l} \ln(1+B) \quad \textbf{(1.2)}$$

With: ρ = density;

D = normalized droplet diameter ($d(t)/d_0$);

B = transfer number.

During these quasi-steady conditions the droplet is referred as being in a "wet-bulb state". The subcritical evaporation at low temperature is correctly described by the previous expression, as mentioned before. However, when ambient conditions approach critical values of pressure and temperature is observed that the transient stage suffers an increase in duration. In addition it is also observed that the evaporation begins to occur in this stage and not only in the quasi-steady stage. In opposite to what happens in the quasi-steady stage, in the transient stage the droplet temperature is neither constant nor uniform and the D^2 Law can't be applied. Therefore, this law doesn't describe the first stage of the evaporation process and can only be used to describe the second stage. This leads to values increasingly deviating from the experimental values when ambient conditions approach the critical conditions. As a consequence, many works described by Givler and Abraham [10] focused on the study of evaporation/emission to the transcritical and supercritical cases. In this kind of studies, it becomes important to distinguish between those performed in normal gravity conditions and others performed in micro-gravity conditions. The gravity is an important factor for the evaporation/emission studies because it is responsible for the buoyancy and convective effects. These effects have great influence in droplets evaporation/emission rate leading to its rise, and it becomes more difficult to conclude which physical phenomena are effectively responsible to an evaporation/emission rate variation and the way how it happens. Thus, it's interesting to conduct studies in microgravity conditions where the buoyancy and convective effects are minimized and it is easier to observe the direct changes in evaporation/emission rate caused by ambient pressure and temperature variations

[10], [12].

With microgravity conditions Bellan [1] refers that higher pressures leads to a duration increase of the heating transient stage, which leads to a deviation from the D^2 linear model. In order to explain this deviation, several studies cited by Bellan [12] were performed with the objective of determining the droplet lifetime. These studies concluded that the temperature rise leads always to a decrease in the droplet lifetime. This is a logic and easy to understand conclusion, but the dependence of the droplet lifetime with pressure variations is not so easily understandable. It was found that the dependence relatively to the pressure varies with the temperature. So, for a temperature above about 1.2 times the critical temperature ($T_r \sim 1.2$) the pressure rise leads to a monotonous decrease of the droplet lifetime. As for temperatures below about 0.8 times the critical pressure ($T_r \sim 0.8$) the droplet lifetime increases with the pressure increase. Some authors also suggest that there might be a temperature at which the droplets lifetime is independent of pressure (see Bellan [1]). However, it should be pointed out that the studies done in microgravity conditions must be carefully analysed since, even with gravity values as low as 10^{-2} in parabolic flights and 10^{-3} for experiences performed in drop towers, the buoyancy and convective effects are still present. Givler and Abraham [10] refer in their work that the experimental observations under conditions of microgravity are inconclusive, but their work was performed 5 years earlier that the one made by Bellan [1].

Harstad and Bellan published in 1998 two papers where are described their numerical studies of droplets behaviour in transcritical and supercritical environments, both in an isolated drop configuration [6] and in a cluster of drops configuration [13].

The first model [6] was developed for the behaviour of an isolated fluid drop of a single compound immersed into another compound in finite, quiescent surroundings at supercritical conditions. In this study was modelled an isolated drop of liquid oxygen immersed into gaseous hydrogen environment. The used model is based on the fluctuation theory of Keizer that accounts for non-equilibrium processes and naturally leads to the most general fluid equations by relating the partial molar fluxes and the heat flux to the thermodynamic quantities. According to the author non-equilibrium processes must be considered since there is no physical justification for equilibrium. This model accounts for Soret and Dufour effects. The Soret effect is named to the mass flux that separate heavier molecules from lighter molecules is created by the existence of a temperature gradient, on the other hand, the appearance of a heat flux created by the existence of a concentration gradient is called Dufour effect. These effects depend on thermal diffusion which is generally very small but can be sometimes significant when the participating species are of widely differing molecular weights. The grid is time dependent.

In this numerical simulation the drop of Oxygen has an initial temperature of 100K and an initial radius of 0.050 mm, the radius of sphere influence is 1mm. Other drop radius were tested from 0.025 mm until 0.300 mm. The hydrogen environment has temperatures between 500 K and 1000K and were tested pressures between 10 and 80 MPa. The hydrogen is consequently at fully supercritical conditions while the Oxygen start the simulation at transcritical conditions, and as it warms up over the critical temperature passes to supercritical conditions as well. In order to obtain conclusions and perform comparisons with experimental studies thermal conductivity, temperature, mass fraction, density, Lewis number and specific heat are calculated by the model across the domain of study. One of the first statement of the author about supercritical conditions is that while in the subcritical situation where the interface is well defined by a surface there is a sharp change in density, in the supercritical situation there is an arbitrariness in defining an interface that should be followed in time. This way one is free to choose an interface that wants to follow. The results obtained in this work corroborate the previous

statement since the number of phases were monitored at each time step and at all locations, and for the conditions of the study, only one phase could be found at all times and locations. Relatively to the quasi-steady gas behaviour described before in other studies these authors refer that this assumption is only strictly valid at low pressures where the liquid density is three orders of magnitude larger than that of gas, excluding this way this assumption in transcritical and supercritical conditions.

Comparing the droplet lifetime obtained by other authors for both subcritical and supercritical condition with data obtained in this work [6] it was concluded that, when at subcritical pressures, an increase of pressure results in a decrease of droplet's lifetime. However, the opposite happens when supercritical conditions are set, an increase of pressure leads to a decrease of droplet lifetime. These results were obtained by observation of the density over time for different ambient pressures. It is also concluded that increasing pressure causes the existence of larger gradients of temperature and density. The practical consequence of these findings is that increasing turbulence is necessary to mix the reactants at larger pressures. This is however somewhat an opposite conclusion to the understanding exposed in the paper of Givler and Abraham [10] that increased ambient density (and by consequence pressure) relative to the density of the injected fuel results in better mixing. Another interesting conclusion is that the gradients of the mass fraction and density do not coincide, in fact there is a much faster decrease of density than of mass fraction, this indicate that the fast decreasing of density is not caused by the mixing of the liquid Oxygen with the Hydrogen but in fact by an expansion of oxygen that happens as it get warmer. This is even more evidenced when it is noted that the relaxation of temperature and density profiles occurs much faster than that of mass fraction. Concerning to the drop size, the main result of increasing the drop size is the delay of drop heating, production of a more uniform LOx distribution at this time, and maintaining the strong density gradient for longer times.The diffusion of LOx is observed to be enhanced at larger temperatures but the difference decreases with increasing pressure. Finally the authors describe the supercritical behaviour as a slow diffusion process. It is also stated in this work that appropriate equations of state with consistent mixing rules and transport properties valid over transcritical/supercritical conditions are required in the study of the conditions present in rocket combustion chambers.

The second model [13] was developed for the behaviour of cluster of drops and includes the interaction induced by drop proximity. This is a relevant study since during atomization process the breakup of jets generate clusters of drops that have a collective behaviour This model is based upon the isolated drop model [6], using the same equations developed for the previous model, but here with boundary conditions calculated using a global cluster model. The calculations for each drop in its sphere of influence is made using the same exact procedure used in the study of isolated drops [6], for the interstitial region the density is calculated by the equation of state while for the temperature and mass fraction the differential equations are solved using a second order predictor-corrector method. The typical situation studied was a general-volume-shape cluster with a radius of 20 mm, containing 5.92×10^6 LOx drops with an initial radius of 0.5 mm and initially at a temperature of 100 K, immersed into a Hydrogen environment with a temperature of 1000 K and a pressure of 20 MPa. In order to obtain results of the effect by the variation of the several conditions of the study, the initial variables were changed along the simulation, and results like temperature, mass fraction, density and sphere of influence radius are shown and compared. The authors conclude that changing the initial cluster radius has no effects to the simulation, the same however doesn't happens with the variation of the size of drops inside the cluster. The effect of having larger drops in the cluster is the change in the

characteristic time of the diffusion process that dominates at supercritical conditions. In this particular case of increasing droplet radius, its heating is made at a slower rate and this way steeper density gradients are maintain for longer periods. The effects of pressure variation were also tested for a range of pressures between 10 and 80 MPa. A very important conclusion from this study was achieved, unlike in the isolated drop situation where gradients were greater with increasing pressure, with clusters of drops the opposite is observed. The effect of drop interaction causes the gradients smear by increasing the cluster volume with increased pressure. Thus, contrary to the case of an isolated drop where increasing pressure over supercritical conditions reduces the mixing of different compounds, the presence of cluster of drops in burning sprays tends to render the dependent variables more uniform with increasing pressure. In this respect, clusters of drops are a desirable aspect because they aid the interdiffusion of the reactive components. Authors also concluded that the cluster behaviour is not sensitive to the value of the Nussel number. One important effect of cluster effect according to authors is the accumulation of a non-negligible amount of LOx with decreasing drop interdistance. The effect of drop proximity decreases with increasing pressure, in that the behaviour of the fluid droplets in a very dense gas becomes increasingly similar to a pure diffusion process.

Finally, one of the most important conclusions of two works of Harstad and Bellan exposed above is that a strong variation in behaviour exists between an isolated drop and a cluster of drop, so even if some important conclusions can be achieved by the study of isolated drops, not every aspects of it can be generalize to the expected behaviour of a cluster of drops or even less to behaviour of jets.

Zhang et al. [14] conducted a computational investigation using a numerical model that included the high pressure transient effects, temperature and pressure dependent variable thermo-physical properties in the gas and the liquid phases and the solubility of inert species in the liquid phase, for a moving n-heptane droplet evaporation in a zero-gravity nitrogen environment. The unsteady equations of mass, species, momentum and energy conservation in axisymmetric spherical coordinates are solved using the finite-volume and SIMPLEC methods. The axisymmetric numerical model has been thoroughly validated against the extensive microgravity experimental data of Nomura et al. [15], in a work also referenced by Bellan [1] and Givler and Abraham [10].

In this work [15] was noted that in high pressure environments (transcritical and supercritical regimes) the droplet is at a transient phase during all its lifetime, never reaching the quasi-steady phase of constant and uniform temperature. It was also verified that the increase of pressure is responsible for a decrease of droplet penetration distance and a rise in evaporation/emission rate.

As previously referred, studies of droplets evaporation/emission at normal gravity conditions have reported a problem of convection and buoyancy phenomena interference over the analysis of the direct effects of pressure and temperature on the evaporation/emission rate. However, smaller technical difficulties in the execution of these studies lead to more consistent results between different experiences. Investigations reviewed by Bellan [1] indicate that for low pressure environments the emission rate obeys to the D^2 Law. However, as the pressure increases, it becomes more difficult to fit the obtained experimental results in the D^2 Law. It is known that the convection effects increase with the pressure and it becomes difficult to understand if the observed variation in emission rate comparatively to the D^2 Law is due to the thermodynamic mechanisms, to the fluids mechanic (through convective effects) or to the combination of both.

Givler and Abraham [10] also refer that Tsue et al.[16] had conducted one of the most re-

markable experimental investigations about droplets supercritical vaporization, by achieving in all ambient conditions quasi-steady droplets vaporization. In agreement with previous studies, they concluded that the vaporization rate increases with ambient pressure. It is however concluded that the vaporization rate achieves a maximum and then decreases with further increases in ambient pressure. The experimental studies conducted with normal gravity by Givler and Abraham [10] agree that a higher ambient pressure corresponds to a vaporization rate increase. The final conclusions of the previous authors indicate that for subcritical and supercritical conditions with normalized pressure and temperature below two, both transient and quasi-steady phases exist, indicating that for some supercritical conditions the quasi-steady model may be acceptable. However, for supercritical conditions where normalized pressure and temperature are above two all the emission process is made at the transient phase and in this situation the quasi-steady model is not applicable. Finally, it is concluded that for supercritical pressures and temperatures the droplet lifetime decreases when the temperature increases.

A numerical investigation of n-heptane droplet evaporation in nitrogen under transient and supercritical conditions, performed by Zhu and Aggarwal [17] reached similar conclusions. It was used a Lagrangian-Eulerian numerical method and were measured the density, latent heat, molar fraction, gas compressibility factor and the droplet lifetime. They concluded that droplet heat up time increases and becomes a more significant part of the droplet lifetime when the ambient pressure rises. As the droplet surface reaches a critical mixing point the latent heat of vaporization decreases and drops to zero. They also concluded that the droplet lifetime behaviour it's not linear, and at low and moderate ambient temperature the droplet lifetime increases with pressure. However, at higher pressures, for temperatures of 500 and 700K, the droplet lifetime decreases with pressure. At higher temperatures the droplet lifetime also decreases with increasing pressure. Finally Zhu and Aggarwal [17] concluded that when the droplet surface approaches the critical mixing state, the difference between the gas and liquid phases disappears.

Meng and Yang [18] attempted to develop a unified treatment of fluid flow over the entire range of thermodynamic states. To do so a model for droplet evaporation was created. In order to cope with transcritical and supercritical conditions a modified Soave-Redlich-Kwong equation of state was employed. Good agreement with experimental data was found for the droplet lifetime. Despite showing a complex thermodynamic approach, the investigation offers interesting clues for the calculation of fluid properties, in particular the specific heat.

Fieberg et al. [19] conducted an experimental and numerical work about fuel droplet evaporation under high pressure and temperature. They studied temperatures between 300K and 500K and pressures between 0.1MPa and 3.7MPa. For the experimental work the Phase Doppler Anemometry (PDA) technique was used and for numerical work the FLUENT 6.0 CFD software. They measured the evaporation time, the surface temperature, the droplet diameter and the drag coefficient. It was also taken into account the effects of interaction between droplets in droplet chains. The conclusions reached in this work are that during the evaporation, the boundary layers increase because of the rapid diameter reduction and the exchange process between droplet surface and the adjacent gas phase slows down. Droplet deceleration in a droplet chain is much smaller compared to a single droplet, indicating that when injecting a group of droplets the penetration length should be much bigger than when injecting only one droplet. However, the burning rate of a single droplet is higher because of the existence of more available oxygen. For the experimental conditions, numerical results show that evaporation calculations in engine applications using quasi-steady modelling of the gas phase are valid even for supercritical conditions and produce acceptable errors compared to a fully transient

calculation agreeing this way with the conclusions achieved by Givler and Abraham [10] that for some supercritical conditions the quasi-steady model is still valid. Since the evaporation takes place in a spray plume, the surrounding gas is cooled below the critical temperature and only a small number of droplets evaporate under supercritical conditions. The effect on the whole spray is thus further reduced.

1.3 Jet Studies

The study of single droplets and clusters of droplets in transcritical and supercritical conditions provides a big amount of information about how the thermodynamic properties of the fluid change under these conditions. However, in the process of fuel injection not only thermodynamic properties are involved. In these cases, are also of extreme importance the influences caused by aerodynamics phenomena which also interact with the different thermodynamic properties. The example given by the works of Harstad and Bellan [6, 13] shows that at the same thermodynamic conditions a single drop can reveal an opposite behaviour from a cluster of drop, demonstrating this way that aerodynamic interactions between drops strongly influence the general behaviour of a fluid. This way trying to understand conditions around the critical point by the simple study single drops and thermodynamic properties is proved to be extremely reductionist.
This last conclusion conducts to the necessity of study of sprays and jets under the conditions around the critical point.

1.3.1 Experimental

The first approach to obtain information about the behaviour of jets and sprays under conditions around the critical point are the experimental studies. Experimental studies are of great importance because are the ones that allow the visualizations of the several phenomena that appear in the flow of interest. In order to visualize the flow in an experimental installation several techniques are possible. The simplest method available is by direct visualization aided by some mean of lighting and then captured by photography. While this is the most obvious solution it offers many limitations and only qualitative information is possible to be obtain. In order to obtain some more useful but yet, mostly qualitative data, another technique is used with the name of shadowgraphy, this is a simple method in which the flow is illuminated with a backlight and the shadow captured by means of photography. It has been shown to be an effective diagnostic tool to investigate single and coaxial jet injections. Due to the huge density gradients of the cryogenic supercritical fluids relative to the background gas, it is possible by this method to determine geometrical properties such as spreading angle and potential core length regardless of whether the jet is subcritical or supercritical. Using a short time-exposure light source, more detailed information on features reflecting the interaction of the jet with its environment can be obtained. For instance, geometric properties of the jet surface area and characteristic length scales of the density variations in the mixing layer of the supercritical jet can be revealed [20]. In single components and single phase shadowgraphy can give a very good clue about the density values since as seen in Figure 1.2 the light rays are deflected by the molecules of fluid, this way causing dark shadows in the image after passing the fluid. Thus darker shadows represent bigger defection of light which means more concentration of molecules and this way higher density. Bigger difficulties with shadowgraphy appears when

trying to study multicomponent and two phase flows.

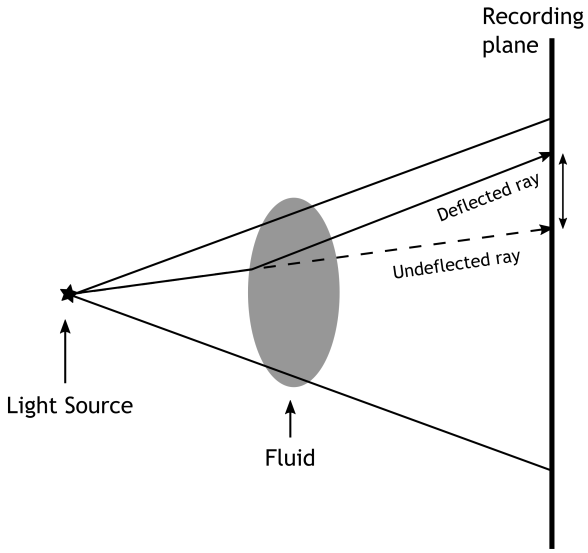

Figure 1.2: Setup for Shadowgraph without optical components.

A more complex technique of visualization is Spontaneous Raman Scattering. When a medium is irradiated with a light beam, some fraction of the beam is scattered in all directions. If the medium contains particles of molecular dimension, a weak scattered radiation with the same wavelength is observed, called Rayleigh scattering. Raman, in 1928, discovered that the wavelength of a very small fraction of the scattered radiation by certain molecules shifted by an amount dependent upon the chemical structure of the molecules responsible for the scattering. The Raman spectra are obtained by irradiating a sample with a powerful visible monochromatic source, usually a laser beam. The scattered radiation is a very small percentage of the source, as a result, detection and measurement is generally difficult with some exceptions. The scattered light is of three types, Stokes, anti-Stokes, and Rayleigh. The Rayleigh component has exactly the same frequency as the monochromatic light beam and is much more intense than the other two components. The wavelengths of the peak lines of the other two components are however independent of the wavelength of the excitation source, but specific to the scattering molecule. This way, in multicomponent flows, Raman scattering allows the detection of each individual component. This property of the Raman diagnostics is an important advantage when compared to the visualization techniques such as shadowgraphy when analysing mixing processes during a two-component coaxial injection. Another very important and useful characteristic of the Raman scattering is that the Raman signal strength at ambient conditions is proportional to the molecular number density [20]. Raman scattering is this way shown to be a very complete and useful visualization tool that allows the user to obtain the chemical composition and it's density in any part of the flow, adding much more information when compared with other visualization techniques.

Other flow visualization techniques are possible for use, like the case of Planar Laser-Induced Fluorescence (PLIF) which, when combined with Particle Image Velocimetry (PIV) allows simultaneously the measurement of a fluid velocity field and species concentration. Information about the flow can also be obtained by the use of probes, but this solution has always the

inconvenient of disturbing the original flow.

Newman and Brzustowski were the first to observe how an injected fluid behaves near the critical point in their paper of 1971 [21]. They experimentally tested the injection of liquid CO2 into a test chamber with different mixtures ratios of gaseous CO_2/N_2 ranging from 0% to approximately 80% of CO2 in composition. The chamber temperature was ranging from 295.15 K to 333.15 K (critical temperature of CO_2 is 304.15K) and pressure from 6.31 MPa to 9.06 MPa corresponding to reduced pressures between 0.856 and 1.228. The liquid CO_2 was injected with velocities between 2.0 and 4.0 m/s through an injector with a diameter of 0.66 mm and at a temperature of 295.15 K. Photography, shadowgraphy, and filming were used in order to obtain results of mean axial velocity and jet spreading angle. It was observed that for both subcritical and supercritical conditions the increase of gas density causes a finer spray, this way, an increase of the chamber pressure causes a reduction in size of droplets. These, in the limit, become so small that the liquid phase evaporates within the field of view. An important conclusion obtained in this earlier work was the reduction of the surface tension that authors described to be linked to the increase of temperature, however they also state that the influence of temperature in surface tension is smaller when the pressure is lower. The reduction of the surface tension is suggested to be the major contribution to the increase atomization efficiency. The authors describe the difference in evaporation between a system at subcritical pressures and another at supercritical. They state that at subcritical pressure the liquid cannot gasify directly suffering this way a boiling process in which all the droplet first approach saturation temperature and then start evaporating. A different process is described to happen at supercritical pressure, in this case the liquid as it reaches critical temperature directly gasifies. It is questioned whether one can still refer to the supercritical flowfield as a spray, as the extremely small droplets caused by a very low surface tension result in a flow situation similar to that of a continuum rather that a heterogeneous liquid-gas mixture. However, the authors continue to admit the existence of atomization near critical pressures. Some quantitative conclusions were also obtained, it was seen that the rate of decay of the nondimensional mean axial velocity decreases with the increase of the density ration (ρ_l/ρ_g). The jet spreading angle decreases with the increase of density ratio and finally all the jet parameters seemed to be independent of the initial jet velocity.

In order to study the influence of the critical and supercritical conditions in the fuel injection is also important to collect information about the behaviour of a jet in subcritical conditions in order to establish a control for comparison. In 1988 Papamoschou and Roshko [22] conducted an experimental study concerning turbulent shear layers in supersonic flow, a study that later would became one very important references for authors studying fuel injection. The main focus of this study was shear-layers and growth rates in supersonic gases, however subsonic conditions were also analysed in order to compare them with compressible flow. In this experiment was used a two-stream, blow-down supersonic, intermittent wind tunnel. Tests had durations between 1.5 and 2.0 seconds. The visualization was made by means of photography with back illumination and was used a pitot probe in order to measure pressure, with the Mach number being calculated by the Rayleigh Pitot formula. Were used in the experiment N_2, Ar and He gases in order to modify density ratio (ω) between 0.24 and 4.4, also the Mach number was varied between 0.2 and 3.4. Most of the conclusions achieved in the study concern supersonic conditions and comparisons with the subsonic case, thus, with less relevance for the study of critical and supercritical injection. But also several results are presented for the general case of jet flows. Results of visualization and pressure profiles allow the identification of spreading rates in the shear-layers. Pitot-thickness data is used to calculate the turbulent

growth rate in incompressible shear-layers. Later the authors derived correlations between the growth rate and the flow parameters. It was deduced an equation for the visual thickness of the shear layer that shows to be in fairly good agreement with the experimentally observed visual rates of subsonic shear layers:

$$\delta'_{vis,0} = 0.17 \frac{\left[1 - \frac{U_2}{U_1}\right]\left[1 - \left(\frac{\rho_2}{\rho_1}\right)^{1/2}\right]}{1 + \frac{U_2}{U_1}\left(\frac{\rho_2}{\rho_1}\right)^{1/2}} \quad (1.3)$$

With: $\delta'_{vis,0}$ = visual thicness of the shear layer;
U_1 = velocity of the first fluid;
U_1 = velocity of the second fluid;
ρ_1 = density of the first fluid;
ρ_2 = density of the second fluid;

The presented equation is useful for the determination of the growth rate in subsonic and subcritical jet conditions and this way, can act as a mean of comparison. Other conclusions about subsonic jets were obtain from this study, like for example the fact the jet is dominated by instabilities that later culminate in organized large structures. This large structures arising from the subsonic flow are also observed in the supersonic flow. Conclusions over the behaviour of jet at subsonic speeds and methods of determining shear layers and growth rates would became of great importance in the future for authors studying jets under transcritical conditions. In 1998 Mayer et al. released a paper [23] in which experiments from three different prestigious research institutions, DLR, CNRS and AFRL are described and the results evaluated. The introduction of this paper provides a very good insight over supercritical conditions and why they must be treated in different way when compared with the typical subcritical case. Authors state that at supercritical conditions there is a disappearance of the surface tension as well as vanishing of enthalpy of vaporization, other singularities of properties are observed near the critical point. Another important information is that critical point of the fluid can vary dynamically depending on the mixing, this was also confirmed later in the result of the observations performed in the experiment. The importance of this conclusion is that during real engine operation the mixture may suffer steep changes during injection, these variations will cause the appearance of different regimes of fluid which can cause instabilities that can compromise the combustions and even structural integrity of the engine. Is also important to refer that in this paper, transcritical conditions are merely described as conditions in which propellants can pass from subcritical to a supercritical state, or vice versa. This designation doesn't correspond to the one that given before in Figure 1.1, however here the authors also state that this designation is given for reasons of brevity. In these experiments cryogenic fluids were injected into various gases under both cold-flow and hot-fire conditions. In the hot-fire experiments two coaxial jets of liquid oxygen and gaseous hydrogen are injected in a windowed combustion chamber. Different combustion chamber pressures between 1 and 10 MPa were tested. The liquid oxygen was injected with a temperature of 100 K while the hydrogen at temperatures ranging from 150 K to 300 K. In this experiment there are two different regimes, prior to ignition and after ignition. At subcritical pressure (1.5 MPa) the jet surface has a very smooth appearance and were visible oxidizer ligaments and droplets, these however are not

visible in the regime after ignition, when the temperatures are already supercritical. These differences can be better explain by the regimes presented in Figure 1.1, initial there is a fluid at saturated regime that when combustions starts passes to a superheated regime. When increasing pressure to supercritical values (6 MPa) little evidence of droplets existence could be found, instead stringy of thread-like structures appeared that did not detach from the main jet but rapidly dissolve and fade away. It's also important to refer the observation that the jet breakup length decreases with chamber pressure increase indicating this way a possible better mixture rate. Hot-fire visualizations are however difficult to make at supercritical pressure since with increasing pressure there is also a strong increase of the flame brightness that causes a distortion of the optical field. Cold flows studies are this way required, and for those, liquid nitrogen is coaxially injected with gaseous helium into a gaseous helium environment at chamber pressures between 1.0 and 6.0 MPa. Detachments of droplets can be observed at 1.0 MPa but not at 6.0 MPa, at which mixing looks more like the one between a dense and a light fluid in a turbulent layer. Figure 1.3 shows the injection of a single jet of liquid nitrogen into a gaseous nitrogen environment. It is visible that initially with subcritical pressure the jet surface is smooth, with large disturbances but without apparent detachment of fluid from the jet. As pressure increases to 3.0 MPa, which is near critical pressure, the strong reduction of surface tension makes the jet instabilities able to disturb the interface and cause the detachment of droplets from the jet. Clearly at 4.0 MPa there is no more signs of the existence or a interface or droplets and the jet has more similarities to a dense gas than to a liquid. Other visualizations allow the conclusion that as said before the mixture of gases is responsible for important changes in the critical values of the fluid, causing in the flow several changes along injection between subcritical and supercritical. In the particular experiment of liquid nitrogen being injected into a gaseous mixture between Helium and Nitrogen the authors state that the surface tension apparently ceases to be important in the jet disintegration process somewhere at reduced pressure between 1.6 and 2.1. An important conclusion taken from this work and that must be taken in consideration for modelling is that under conditions close to critical the jet behaviour and breakup process is extremely sensitive to small perturbations in pressure, temperature, local mixture concentrations and initial jet conditions. This means that a very small change in one of those can result in severe changes of jet behaviour which makes the proper and exact knowledge about these condition very important when designing engines operating in these conditions.

Oschwald and Schik [24] conducted in 1999 an experiment in which liquid cryogenic nitrogen was injected into a nitrogen environment at supercritical conditions. The objective was to achieve a better understanding of the physics and flow dynamics of the processes of injection and atomization of cryogenic liquid fuels in high pressure rocket engines. Liquid nitrogen was injected at temperatures ranging from 100 K to 140 K and at velocities of 5 and 20 meters per second. The injection chamber was filled with gaseous nitrogen at a temperature of 298 K and pressures of 4 and 6 MPa corresponding to reduced pressures of 1.17 and 1.76 respectively. The injector had a diameter of 1.9 mm. Spontaneous Raman Scattering was used to obtain values of density and the temperature was derived from the value of density by a ρ/T diagram. Using Full Width of Half Maximum of density and temperature were obtained the jet spreading angles. Normalized density and temperature profiles together with the jet spreading angle were used to perform comparisons between jets at different chamber and injection conditions. It was found that under supercritical pressures the specific heat suffers a peak when close to critical temperature, this peak tends to an infinite value when both pressure and temperature are approach the critical value. This is one of the factors that evidences the strong sensibility of

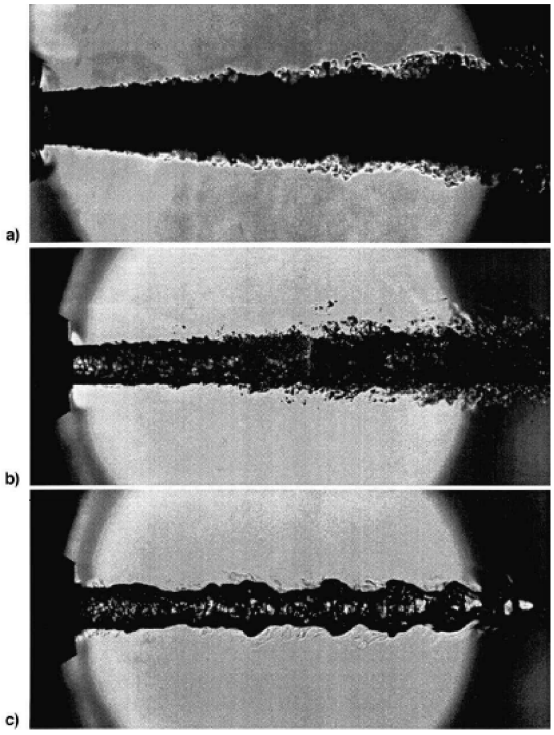

Figure 1.3: LN_2 injection into GN_2 at a) 4.0, b) 3.0, and c) 2.0 MPa [23].

the flow when close to critical conditions. Comparing the effects of temperature in the jet at 4 and 6 MPa authors were able to understand that the jet is much more sensible to temperature changes at lower pressures, while at higher pressures the injection temperature has a weaker effect on the jet behaviour, as it gets generally more stable. At a chamber pressure of 4 MPa, it was observed different spreading angles according to the distance to the injector, when less than 16 diameters it had a value of $5.2°$ increasing to $8.4°$ for distances bigger than 16 injector diameters. The same change in jet spreading angle is not observed for a chamber pressure of 6 MPa. At higher injection temperatures, there's a faster decrease in jet density while in lower temperatures the increase of pressure leads to faster temperature increase. Finally, authors stated that heat transfer from the reservoir gas to the supercritical fluid results primarily in fluid expansion and not in temperature increase. thus, the supercritical flow behaves similar to a liquid at its boiling point. Because in this conditions the role of surface tension in the jet disintegration and mixing process varies locally equilibrium thermodynamics may not be adequate to describe the phenomena.

Chehroudi et al. [5] performed shadowgraphy and Raman scattering experiments with the objective of evaluating the shear layers and growth rate of nitrogen jets between subcritical and supercritical conditions. According to the visualization of shear layer using the technique of shadowgraphy it was observed the transition from a liquid-like to gas-like injection. Increasing the chamber pressure causes the disappearance of ligaments and droplets being substituted by finger like structures. Further increase causes a reduction in length in thickness of dense core and a change to a gas like-jet. These changes are attributed to reduction of the surface tension and enthalpy of vaporization. According to the growth rate the increase of pressure leads to the increase of spreading rate. Comparison between shadowgraphy visualizations and Raman measurements allow to observe an agreement of the growth rate between the shadowgraphs and twice of the Full Width of Half Maximum (FWHM) of density obtained in Raman.

With the objective of better characterize jets spreading angle and centreline densities Oschwald and Micci [25] performed an experimental study in which a cryogenic nitrogen jet is injected into a gaseous nitrogen filled chamber at ambient temperature. Different injection temperatures were tested between 100 K and 140 K exploring the injection bellow supercritical temperature and above. There were also tested two different chamber pressures 4 MPa and 6 MPa, both above the critical pressure of nitrogen and densities ratios ranging from 0.064 until 0.299. The injector had a diameter of 1.9 mm with a L/D of 11.6. Results of the centreline variation of normalized density and temperature, full width of half maximum of the density and temperature profiles, and spreading angle were obtain by the use of Spontaneous Raman Scattering. The authors of the paper start by reinforcing some of the conclusions already achieved previously by different authors such as the vanishing of the surface tension when the fluid approaches the critical point having as result the disappearance when in trans- and supercritical conditions of the well-defined jet surface existent in the subcritical region. The jet becomes similar to a gas jet at pressures above the critical but still retaining the density of a liquid. Like in previous investigations in this study was also perceived the strong influence that mixing conditions can have in the effective critical point, this can strongly change the behaviour of the cryogenic jet since around critical point the fluid shows to be extremely sensitive to small perturbations of temperature and pressure. The authors identify in their work the existence of a singularity at the critical point, this singularity is characterize by the specific heat becoming almost infinite and the thermal diffusivity almost annulling itself. These two characteristics are responsible for the observed initial behaviour of the jet, heat transfer to nitrogen at conditions close to the critical point doesn't increase its temperature but only expands the fluid, a behaviour similar to that of a liquid at its boiling point. This explains the difference observed in the results between an injection of fluid bellow critical temperature and above, in the first case it is visible a strong decrease of density while the temperature keeps almost constant in the initial period, while in the second there is a decrease of both density and temperature at the earliest stages of the jet. However, the biggest objective of the study was to determine spreading rate and develop means of calculating and predicting it. Spreading rates of the jet were derived by the full width of half maximum of the density and temperature. For the density it was noticed a change in the slope at an axial distance of 15 injector diameters, this way the analysis was made separately for the two different regions, with the region after 15 injector diameters showing better agreement with the slope obtained for the temperature. The authors then compare the results obtained for axial distances over 15 diameters with previous studies in order to obtain conclusions and trying to establish relations between the fluid conditions and the obtained spreading rate. It was firstly concluded that inertia is by far the most dominant force in the tested supercritical conditions, it is observable a fast decrease of the spreading angle as the density rate decreases, proving a more difficult mixing when chamber environment has lower density. The authors state however that the spreading angle shown to be significantly different from the density and temperature profiles, a behaviour not observed in variable density gas jets, and even at pressures as high as 1.8 times the critical pressure the spreading angle and the density centreline variation show that the free jet of supercritical fluid cannot be described as a variable density jet of ideal gases. Finally and concerning the potential core, the authors defined its length as the distance at which the two opposite surfaces of the shear layer meet when a gas jet exist the nozzle and a shear layer develops.

Mayer and colleagues [26] performed an experiment in 2003 with the objective of studying the injection of a cold nitrogen jet into a warm nitrogen environment. A numerical study was also performed but will be described latter. The experimental part of the study consisted in

the injection of cold nitrogen initially at a temperature between 126.2 and 140.5 Kelvin into a chamber of gaseous nitrogen at a temperature of 298 K and pressure ranging from 3.95 to 5.98 MPa. The cold nitrogen was injected through single injector with a diameter of 2.2 mm at velocities between 1.8 and 5.4 m/s. Shadowgraphy and Raman scattering were used to obtain, respectively, visualizations of the injection flow, and values of the density along the jet flow. There were also used thermocouples at the injector exit in order to obtain the injection temperatures, for these a separated measurement campaign was performed since the use of thermocouples strongly disturbed the jet. It is important to refer that Raman measurements at conditions close to critical are very difficult to perform due to optical breakdown, also at subcritical conditions the sharp density gradients cause big refraction. As a consequence of this they restrict their measurements to supercritical conditions, however this restriction didn't eliminate all the problems and different densities were obtain between the Raman values and the expected densities calculated by the measured temperatures given by the thermocouples. There were distinguished three different zones of the jet, the first one is the potential core that contains mostly injected fluid and is characterized by a flat region in the density profile. The authors calculated a length of the potential core of approximately 10 injector diameters in their study. Then appears a development or transition region, authors characterize this region as the one of turbulent mixing for a jet and attribute to it great influence for the jet development. Finally appears the region where the jet becomes self similar, a behaviour that the authors describe as the one where a function of only one variable can express the flow field profiles as no longer varying in the axial direction. Concerning the start of the self similar region there is some disagreement with some authors defending that it starts around 20 injector diameters while others defend that it commences more closely to 40 diameters, in the present paper the authors concluded that for a axial distance of 25 injector diameters the jet seems to not have reached yet self similarity. Experimental result shown that around critical point small variation in temperature correspond to extreme density gradients, this way temperature must not be neglected in possible numerical approaches. For these reason the authors stated that real gas effects must be taken into consideration when determining flow properties demanding this way real gas models and relationships. Analysing the variation of the centreline density profile for the different conditions it is possible to easily recognize the existence of a flat line in the profile. This corresponds to the potential core for injection temperatures below the critical temperature, however, the same is not so noticeable for injection temperatures above the critical temperature. Also in this experiment was referred the existence of a maximum in the specific heat value when at critical conditions, this may represent the explanation for the non visualization or a very short potential core at higher temperatures, since in this case there is no maximum in the specific heat that may be the cause for an initial density's lack of variation for the lower temperature cases. According to variation of the velocity, was observed that for the lower temperature cases, the increase of the injection velocity seems to have the effect of creating a bigger and more pronounced potential core. Pressure appears to have the opposite influence over the potential core, since the increase of pressure appears to reduce the length and the ability to distinguish the potential core. The jet divergence angle is one of the most relevant parameters for jet flows, unfortunately the edge of the shear layer is difficult to determine using Raman images, for these reason the full width of the half maximum of density (FWHMD) is used. However, for the coldest cases (with warming of the jet in transcritical conditions), the angles based on FWHMD are very small or even negative near the injector. The conclusion is that close to the injector the position of the half maximum of density is smaller and does not correspond to the growth rate of the shear layer.

Joining the experimental work of two independent laboratories, DLR and AFRL, Oschwald et al. in 2006 [20] published a paper describing and analysing both laboratories results. Several different injection configurations were study by both institutions. At some instances, the developed studies were similar, allowing conclusions to be drawn regarding the degree to which the results at each laboratory corroborate each other. In other instances, studies at one laboratory extended beyond what was done in the other, allowing a breadth of scope which would not been possible at either laboratory. As previous authors did, also in this paper the authors start by evidencing the differences in behaviour observed when a fluid achieves critical and supercritical conditions. General conclusions obtained by previous authors are confirmed. Including the gas-like behaviour of fluids under supercritical conditions, the specific heat maximum observed at a temperature designated as pseudo-boiling temperature, T^*, a maximum that becomes infinite when pressure and temperature are critical in a phenomenon that is characterized as a singularity, at the same time, thermal diffusivity exhibits its minimum. Also, the high density's sensibility to temperature when close to critical pressure and the importance of the critical pressure and temperature values for mixture of fluid are confirmed. The experimental studies are divided in two categories, single-jet investigations and coaxial jet investigations.

In single-jet investigations liquid nitrogen is injected into a gaseous nitrogen environment under sub-to-supercritical pressures. The chamber temperature varies from 298 to 300 Kelvin while the injection temperatures are between 97 and 133 K. The chamber pressures are ranging from 1 to 9 MPa. Different injector diameters were tested between 0.254 and 2.2 mm and the Reynolds number oscillated from 42830 to 75281. In order to obtain results, Shadowgraphy and Spontaneous Raman Scattering were employed. The analysis of the shadowgraph images (Figure 1.4) performed both in DLR and AFRL for three distinct pressures show the strong variation of the jet behaviour with the increase of pressure. At subcritical pressure ($P_r = 0.91$) the jet has a classical spray appearance with the formation of drops and very fine ligaments. At pressure above critical ($P_r = 1.22$) drops are no longer observed and at the interface of the jet are observed "finger-like" entities. Rather than breaking up into droplets, the interface dissolves at different distances from the dense core. Finally at strongly supercritical pressure ($P_r = 2.71$) there is a decrease of the dense core length and thickness as the pressure increases, and the jet starts behaving as a turbulent gaseous jet injected into a gaseous environment without any droplet production or other classical liquid atomization evidence. The results obtained here are very similar to the ones obtained before by Mayer et al. [26] in Figure 1.3 for the near critical and supercritical pressures. A difference was found for the subcritical conditions, this can nevertheless be explained by the fact that in the Mayer's experiments pressure was very far from critical values ($P_r = 0.59$) while in here the subcritical case quite close to critical pressure ($P_r = 0.91$). This fact also allows the conclusion that in Mayer's case at 2.0 MPa the surface tension is yet strong enough to maintain the integrity of the jet, while at 3.1 MPa the surface tension is still strong enough to allow formation of droplets but not to maintain integrity of jet. The utilization of nitrogen in the experiments were justified by the authors by the fact that in previous experiments nitrogen had shown similar behaviour to the oxygen while not presenting risks of combustion.A fractal analysis was also performed since it is intimately connected with the concepts of self-similarity. The fractal dimension was measured and compared between experiments and results from other researchers. When at supercritical pressures the fractal dimension approaches a value similar to gaseous turbulent jets and mixing layers, complementing this way the imaging data. Also the transition from liquid-like fractal dimension to gas-like fractal dimension occurs at about the same pressure as the transition in visual appearance and growth rate. The length of the potential core is currently a point

of disagreement between the two laboratories needing this way further research, however the results of both laboratories fall inside the interval proposed by Chehroudi et al. [27] in 1985. A relevant difference in the jet behaviour is found between cases there the nitrogen is injected bellow and above the critical temperature. When injected at a temperature bellow the critical the jet will pass through a period of warming up in which T^* will be achieved, at this temperature, as said before, the specific heat suffers a strong increase achieving a maximum. This cause in the injected nitrogen a behaviour similar to a liquid at its boiling point. Heat transferred to the nitrogen does not increase temperature but merely expands the fluid, this causes different behaviour both of temperature and density fields and also in the potential core. When injected at a temperature of 120 K a potential core with a length of approximately 10 injector diameters is observed, however at an injection temperature of 133 K very little or no potential core is observed, a conclusion already obtained in the work of Mayer et al. [26]. It's also noted the maximum of the specific heat becomes less pronounced as pressure increases over the critical value. Measurements of the growth rate of a jet are of great importance for the characterization of a jet, in this experiments measurements were taken after an axial distance of around 21 injector diameters. Comparing Raman intensity measurements (that are proportional to the density) to shadowgraphy was concluded that the best agreements were obtain for twice the Full Width of Half Maximum (FWHM) of the Raman intensity. The authors pointed out in this paper the reduction of surface tension and heat of vaporization to zero as the reasons behind the gas-like behaviour in supercritical conditions. It is also raised the hypothesis of existence of 2 characteristic times, one of formation and separation of bulges of fluid and a second characteristic time connected to gasification. It's suggested that gas-behaviour appears when the gasification time becomes shorter than the formation/separation characteristic time. Transition between liquid-like and gas-like behaviour would be governed by finding the time at which these time scales are approximately equal.

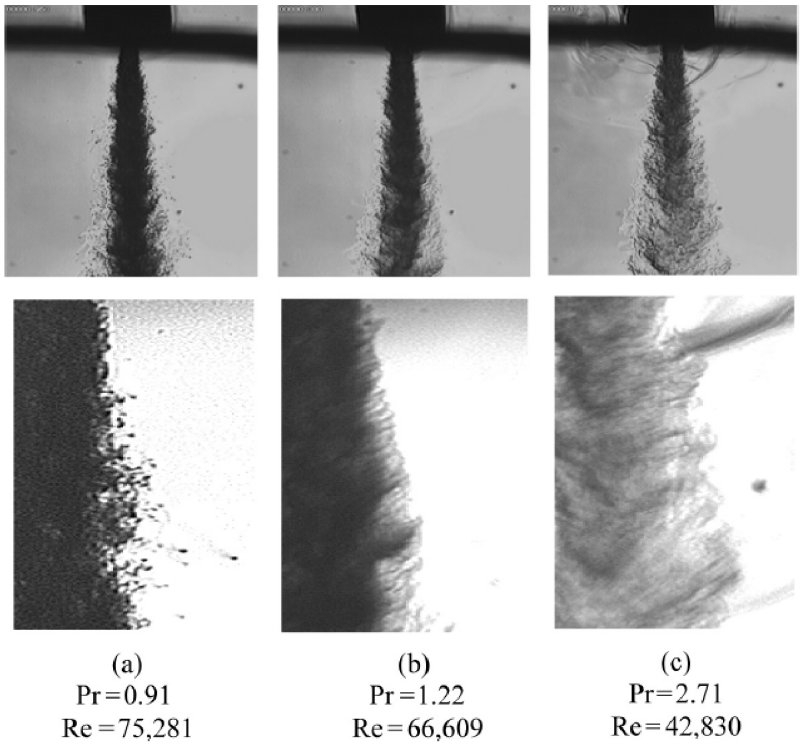

Figure 1.4: LN_2 injected into GN_2 at three reduced pressures ranging from subcritical to supercritical. The bottom row contains magnified images of the top row [20]

In the coaxial jet investigations different configurations were experimented, most of them non-reactive but also some reactive, hot-fire, experiments. The visualization of a coaxial jet of liquid nitrogen and Helium injected into chamber pressures between 1 and 6 MPa was performed. Density measurements of a coaxial liquid nitrogen and gaseous hydrogen jet are made for chamber pressure of 4 MPa. And also liquid nitrogen jet with gaseous coaxial nitrogen jet is studied. Similar conclusions and visualizations to the ones already obtained for single jets are obtained for the coaxial experiments. For the injection of liquid nitrogen (at 97 K) and helium (at 280 K) at 1 MPa the nitrogen clearly seems to be a liquid jet with detachment of droplets while at 6 MPa no more droplets are visible and both nitrogen and helium appear to have gaseous behaviour. The authors state that the influence of the surface tension forces as compared to the shear forces appears to be negligible for this case. For the reactive study liquid oxygen is injected together with gaseous hydrogen at chamber pressures ranging from 1.5 to 10 MPa, equivalent to the reduce pressures relative to oxygen between $P_r = 0.30$ and $P_r = 1.98$. When at 1.5 MPa a spray is formed having flow patterns similar to those visualized in cold flow studies, Ligaments detach from LOX jet surface giving origin to droplets. Increasing the chamber pressure to 10 MPa causes droplets to no longer be visible, and stringy or thread-like structures are seen attached to the oxygen jet and typically develop, grow, and dissolve rapidly without separation from the main jet. It is also concluded that a much faster jet disintegration happens for the subcritical case.

Jackson et al. [28] performed injection experiments in order to validate their numerical simulations. Firstly, it was performed an injection of supercritical ethylene into a chamber filled with gaseous nitrogen at subcritical and transcritical pressures. The chamber conditions are however always subcritical for the ethylene. Data for this experiments were obtained through shadowgraphy, direct-lighting imaging, and also by the placement of K-type thermocouple probes for temperature measurement. There were also performed visualizations using a transparent injector in order to observe the flow behaviour inside the injector at different injection parameters. In the experiment, the chamber pressure was between 0.14 and 3.4 MPa which relatively to ethylene correspond to reduced pressures from 0.0278 to 0.674. Two injector nozzle diameters were used with 1.0 and 0.5 millimetres, the injection pressure was ranging from 5.42 to 6.25 MPa and the injection temperature was between 280.6 and 358 K.

The general conclusion after the single jet, coaxial jets and reactive injection studies is that the behaviour of jet changes from a conventional spray at subcritical pressures to a gas-like behaviour at supercritical pressure. These conclusion is valid for the three cases showing that in most of cases single jet non reactive studies can be generalize (with some care) to the more complex case of coaxial reactive injection.

In 2008 Martinez et al. [29] using an windowed, direct injection, two-stroke diesel test engine performed an experimental work. His work had the objective of generating a correlation that would accurately predict liquid penetration length at conditions typical of modern Heavy Duty common rail diesel engines with direct fuel injection. For this propose diesel fuel was injected into an inert environment of nitrogen at a pressure of 130 kPa, thus a subcritical pressure condition. The injection pressure varies from 30 to 130 MPa and the injector diameter from 0.115 to 0.200 mm. The chamber temperature was 343.15 K. The liquid penetration length was measured by optical means using the technique of Ombroscopy. A correlation to predict liquid penetration length was found that better predicts experimental data, achieving very accurate results. It was observed that the liquid penetration is strongly influenced by the nozzle diameter, increasing together with it. The injection pressure and density of the working fluid have comparable and inverted effects on the liquid penetration length. An increase of

the injection pressure increases the liquid penetration, but also provokes premature droplet break-up within the jet. On the other hand an increase of the nitrogen density decreases the liquid penetration length. An interesting result is the observed insensitivity of the liquid penetration to the discharge coefficient.

Segal and Polikhov, in 2008, conducted an investigation [30] with the objective of determining the influence that the surrounding gas pressure and temperature have on jet breakup. An experimental set-up was tested, where liquid FK-5-1-12 was chosen to be injected into gaseous nitrogen environment at pressures ranging from 0.372 MPa to 4.09 MPa, corresponding to reduce pressures between 0.2 and 2.2, and temperatures ranging from 300K to 564K, a reduced value between 0.68 and 1.28. The liquid FK-5-1-12 was injected through an orifice with a diameter of 0.84mm with velocities between 7 and 25 m/s. The Reynolds number ranged from 11 000 to 42 000. In order to generate insight over the injection process Planar Laser Induced Fluorescence (PLIF) was used, allowing to obtain a section through the jet of the density field and density-gradient field. All the information produced in this experiment can be taken from these two fields. The authors also produced a chart where the several test cases are classified according to the three possible regimes (subcritical, transitional or supercritical) to which they fit. Subcritical is defined as the regime where the fluid is dominated by surface tension and there is little appearance of droplets due to strong surface tensions. On the other hand, in supercritical regime surface tension no longer plays a role in determining fluid behaviour, shear forces exceed capillary forces and they dominate. At this regime appears the gas like behaviour, and the mixing processes similar to a gas/gas mixing. Diffusion is very important in supercritical regime and density gradient decrease significantly, at this regime mixing process is enhanced. In this paper transitional or transcritical regime is defined as the thermodynamic condition at which both subcritical and supercritical fluid characteristics appear. In this regime there is the appearance of ligaments from which parcels of liquid detached due to the decrease of surface tension. An important conclusion stated by the authors is that around critical conditions the jet behaviour is generally influenced by local conditions making this way possible to coexist subcritical and supercritical behaviour Also the mixing conditions of the fluid will interfere in the pressure and temperature critical values of the mixture. A linear stability analysis was also performed with the results showing good correlation with experimental data.

Schmitt et al. [31] studied in 2012 the injection and mixing of two coaxial jets under supercritical conditions. The objective of this work was to recreate the conditions observed in liquid rockets engines were typically the inner jet, oxygen, is injected in a transcritical (at a pressure higher than the critical value but at a temperature lower than the critical) or liquid-like state and it is surrounded by a higher velocity hydrogen stream injected in a gaseous state at a supercritical temperature. For this liquid nitrogen is injected at temperatures between 117K and 128K through an injector with a diameter of 0.51 mm and with densities ranging from 220 to 590 $kg.m^{-3}$. Coaxially is injected gaseous nitrogen at temperatures ranging from 152K and 192K from an injector with an inner diameter of 1.59 mm and outer diameter of 2.42 mm and fluid density between 68.3 and 101 $kg.m^{-3}$. The chamber temperature is 213K with a pressure of 3.56 MPa ($P_r = 1.04$), having this way the chamber nitrogen a density of 59.6$kg.m^{-3}$. This work had both experimental and numerical components. In the experimental study was observed the behaviour of the coaxial injection by the use of Shadowgraphy. Visualizations for different momentum flux ratios allowed the conclusion of the high nonlinearity of the thermodynamics of supercritical and transcritical flows and also to obtain experimental data useful for later comparison of numerical results. By the observation of the shadowgraph images for different momentum flux ratios it is possible to observe that an increase of it causes a decrease of the

jet potential core length. This is associated with the formation of vortical structures that cause an enhancement of mixing between inner and outer streams. It was also conclude that acoustic modulation has the ability of changing jet behaviour by influencing in greater degree the outer jet. One important conclusion is that the observed nonlinear behaviour may demand for the use of real gas equations of state such as the Peng-Robison equation of state used in the numerical part of this study.

1.3.2 Numerical

While some aspects of conclusions, obtained along the several performed experimental works, may be in disagreement between the different authors, there are common results that were obtained over time. Conclusions which allow us to make a summary of the characteristic of jets around the critical point. The reduction of surface tension and its final disappearance was one of the first observations achieved by the several researchers, initially was thought that this phenomenon was only a consequence of the temperature increase but the influence of pressure is also now recognize. Several authors characterize as having gas-like behaviour a jet when at supercritical conditions, and in fact it was possible to treat it as a dense gaseous jet. However, is close to the critical point, in transition between subcritical and supercritical conditions, that more doubts were raised. It was observed the strong instability that jet parameters suffer when close to critical point that translates in nonlinear behaviour making the critical point a singularity. In this singularity specific heat becomes infinite and thermal diffusion disappears. An important conclusion obtain by several authors is the fact that mixture properties strongly influence the values of critical pressure and temperature, in a combustion system this is of extreme importance since along combustion composition of gases in combustion chamber suffer strong variations and this must be taken in consideration since they will affect the behaviour of gases in a nonlinear fashion. An important fact raised by several authors is that under real engine operations pressure and temperature values are far from being constant. These values vary along the initial warming up of engine, vary also according to exterior environment pressure and temperatures being different in different parts of combustion chamber. The conclusion that around critical conditions fluids show strong sensibility not only to pressure and temperature values, but also to mixing conditions, makes the task of modelling flows at these conditions extremely demanding. As said above the behaviour of fluids under transcritical conditions is strongly nonlinear, because of this a number of researchers concluded that an ideal gas equation of state cannot be well suited for modeling these flows and instead a proper real-gas equation of state must be applied.

The extreme temperatures and high pressures involved in the study of transcritical and supercritical fluids turns it into a very expensive and technical demanding experimental activity. In some cases the study of transcritical and supercritical injection in real operation engines can even be prohibitively expensive (for example in rocket research) for other research groups that not largely nationally financed institutions. This way modelling and simulation of these flows are an important tool in order to add some more information to the experimental data, treat and help a better understanding of experimental data and finally by the modelling of the conditions in real operation engines help in the task to enhance and optimize its performance.

The simulation or modelling are mainly performed by the use of numerical methods in order to solve the governing equations for the fluid flow. The basis of almost all approaches are the Navier-Stokes equations that define any single phase fluid flow. The Navier-Stokes equation are however strongly non-linear and analytical solutions can only be obtained for very simple

problems. This way, iterative numerical methods, where the considered domain is split into a finite number volumes (nodes) and the conservation equation solved for each one of it, were employed with the objective of solving more complex flows. The more direct approach in solving the Navier-Stokes equations is by the use of direct numerical simulation (DNS). Even if being a latecomer in terms of possibility to be applied to actual flows of interest, when compared with other modelling approaches, conceptually it is the simplest approach. This method consists in solving the Navier-Stokes equations, resolving all the scales of motions, with initial and boundary conditions appropriate to the flow. Each simulation produces a single realization of the flow. DNS is unrivalled in accuracy and level of description provided, it has however some limitations. Because in this methods all length scales must be solved, in order to give accurate solutions a very refined grid must be used, this result in a very large amount of nodes for which all variables must be calculated. The obvious consequence is that large computational efforts are required which in practice reduces the range of solvable problems from low-to-moderate Reynolds number since computational cost in DNS increases as $Re^{\frac{9}{4}}$ [32].

Nearly all of the computational effort in DNS is expended on the smallest, dissipative motions named Kolmogorov scales. However, as Kolmogorov argued, all the information about the geometry of the large eddies - determined by the mean flow field and boundary conditions - is lost as the energy passes down the energy cascade to the small scales. This way it is possible to deduce that the Kolmogorov scales, in a fluid flow, do not depend of the geometry of the flow. In fact, they only depend on the energy transfer rate from larger scales and the kinematic viscosity, which are parameters independent of the flow geometry and this way universal. This knowledge lead to the application of another possible approach to the simulation of fluid flows, the technique called Large Eddy Simulation (LES). In this technique the large scales to the flow which are dependent of the flow geometry and represent a smaller computational cost are simulated exactly like in DNS. However, the smaller scales that don't depend on flow geometry and which simulation requires a higher computational effort are modelled In order to do so, LES equations are solved for a "filtered" velocity field which is representative of the larger-scale turbulent motions. The equations solved include a model for the influence of the smaller-scale motions which are not directly represented [32]. The filtering operation appears this way as the most critical phase of this method. When compared with DNS, LES presents less accuracy and lower level of description, with the advantage of avoiding the vast computational cost of explicitly representing the small-scale motion.

The computational cost in LES can be controlled by the user in the process of filtering. A coarse filtering will reduce computational cost having as expense a reduction of accuracy. However, for engineering purposes, where complex flows with large Reynolds numbers are studied and quick results are expected, Large Eddy Simulation still requires nowadays large computational resources. A less computationally demanding approach is however available, the Reynolds Averaged Navier-Stokes models or RANS models. Even being referenced here at last this approach was one of the first to be employed, one of the more accessible for those with less computational resources and the most widely used approach. These models employ the Reynolds-averaged Navier-Stokes equations which are time-averaged equations of motions for fluid flow. In order to do so, the quantities in the equations of Navier-Stokes are separated into an average and a fluctuating part by a mathematical technique called Reynolds decomposition. When applying the Reynolds decomposition to Navier-Stokes, appears one non-linear unknown term named Reynolds stress. This term has a difficult physical interpretation and is closely connected with velocity fluctuation and the phenomenon of turbulence. Since in this method are only represented terms for the mean flow, the Reynolds stresses must be related with the average flow in

order to obtain closure of Reynolds equations (having as many equations as unknown variables). Unfortunately, there is no rigorous process to do this and the closure of Reynolds equations represents the turbulence problem. There are several different paths of finding closure for Reynolds-averaged equations, each different process consists itself in a different model, and according to the type of flow a different model is more suitable to properly represent the flow. The Reynolds stresses can be obtained by a turbulent-viscosity model in which is included the $k-\varepsilon$ model which belong to the class of two-equation models, in which transport equations are solved for two turbulence quantities. The $k-\varepsilon$ model is the most widely used complete turbulence model, and it is incorporated in most of commercial CFD codes. Reynolds stresses can also be directly modelled in approaches called Reynolds-stress models (RSM) in which the transport equations are solved for the individual Reynolds stresses and for the dissipation ε (or another quantity).

A variation of the Reynolds Averaged Navier-Stokes method where, instead of a simple time-averaging of equations, is employed a mass-weighted time averaging of the Navier-Stokes equation can also be used. Instead of Reynolds decomposition this method uses the Favre [33] decomposition of equations which eliminated the complex terms that appear due to density fluctuations in compressible and variable density flows. Computational approaches that use this method of averaging of equations are called Favre Averaged Navier-Stokes.

There are possible other approaches to the simulation or modelling of flows, one example is the approach based on probability density function (PDF) or combination of approaches, however are the ones described above that were more commonly used for the simulation and modelling of fluids closed to the thermodynamic critical point.

Sanders et al. published in 1997 a paper [34] describing a numerical investigation of variable density effects in axisymmetric turbulent jets, even if not being a study of thermodynamically conditions close to critical, the geometry of the studied jet and the variable density makes this study conceptually very close to transcritical and supercritical studies. To accommodate the mixture between gases with different densities, the mixture fraction (F) is introduced and obeys to a convection-diffusion equation. The mean density can be obtained from the mean mixture fraction using the equation of state that is in this model approximately a linear function of the instantaneous mixture fraction. In order to perform the study two different models were used, a standard first-order $k-\varepsilon$ model and a second-order Reynolds stress model (RSM). Compared with experimental results RSM performs somewhat better than $k-\varepsilon$ model, although the differences between both models are small and no conclusive disagreement with experimental data is observed. Without buoyancy, the first and second-order models show no significant effects of the density ratio ($0.25 < \omega < 20$) on the far field characteristic parameters such as spreading rates, decay rates, turbulence intensity and “unmixedness”. Regarding buoyancy and the effects of turbulence production due to buoyancy, there are large differences between the two models as $k-\varepsilon$ model cannot simulate buoyancy turbulence production since it lacks the turbulence production terms. Finally, it is also concluded that both models cannot correctly predict the velocity spreading rate trend however the scalar spreading rate trend is in agreement with measurements.

Barata et al. [7] used a computational $k-\varepsilon$ model, similar to the one used by Sanders et al. [34], originally developed for incompressible but variable density flows, for the study of jets under supercritical conditions. In this study was modeled the injection of a cryogenic nitrogen jet at a temperature between 100K and 110K through an injector with a diameter of 0.254 mm into environment filled with gaseous nitrogen at a temperature of 300K. The environment had reduced pressures ranging from 0.91 to 2.71. In the results were obtained the velocity

and scalar fields of mixture fraction and density, were also obtained velocity and density axial variation as long as it decays. The Full Width of the Half Maximum of the density and velocity allowed the calculation of the tangent of jet spreading angle that was then compared with previous experimental results from different authors. The results of the jet spreading angle position this study in a good agreement with previous experimental works such as those obtained by Chehroudi et al. [35] and theories. This shown that according to the authors even the computational code not having been written for that situation it performed surprisingly well with the jets having quantitatively the same growth rates as incompressible variable density turbulent jets, but at supercritical pressures. This results evidenced the gas-like behaviour of a liquid at supercritical conditions already suggested in experimental studies. The computer programs revealed also great capabilities to study cryogenic jets injected initially at subcritical temperature into an environment at supercritical temperature over a range of subcritical and supercritical pressures. Other conclusions such as the decrease of length and thickness of the dense core as the chamber pressure increases and the velocity decay along the centreline increase with pressure are results suitable to be compared with other studies. Is important also to state that some disagreement with experimental work is observed as the density ration decreases and the jet approaches spray behaviour.

Complementing the knowledge acquired by the experimental work Mayer et al. [26] also performed the modelling of the flows of interest. The conditions modelled were the same already presented in the experimental work before. In order to do the modelling are employed the Favre Averaged Navier-Stokes (FANS) equations for incompressible flow. Since the test conditions are in supercritical conditions real gas properties of nitrogen are necessary and are employed in the CFD-ACE commercial software. The FANS equations introduce the Reynolds stresses that are estimated by a $k - \varepsilon$ turbulence-viscosity model. It was used a 2D axisymmetric grid with just over 100,000 cells. The models went through between 20,000 and 30,000 iterations in order to ensure convergence. The mass flow balance provided the final proof of convergence. The numerical results compares fairly well with experimental data from the tested conditions. However, some disagreement is obtained mostly for the value of potential core. In several cases the numerical results predict a potential core that is in fact smaller or not visible in the experimental data. An important conclusion sustained by the authors is the importance of use of real gas effects in modelling supercritical flows.

Zong et al. [36] performed a bi-dimensional large eddy simulation with the objective of studying the cryogenic nitrogen injection into a nitrogen gaseous environment. The governing equations were based on the Favre-filtered conservation equations of mass, momentum and energy. Thermodynamic properties were determined by a modified Soave-Redlinck-Kwong (SRK) equation of state, while transport properties were estimated by the use of a 32-term Benedict-Webb-Rubin equation of state. The flow configuration consisted on a liquid nitrogen injection through a 0.254 mm injector at a temperature of 120K and velocity of 15 m/s into a gaseous nitrogen chamber at 300 K and with supercritical pressures ranging from 4.3 to 9.3 MPa. The authors in this numerical work paid special attention to the appearance of nonlinear fluid properties when conditions are close to critical such as the specific heat peak reported by previous experimental investigations. The importance of the use of a proper real gas equation of state due to the nonlinear behaviour of fluid is evidenced along this numerical work mostly because the jet dynamics are largely dictated by the local thermodynamic state of the fluid. Density, temperature, and vorticity fields show the turbulent nature of the jet interface, demonstrating an increase of vortices formation and size with increase of pressure. The strong density stratification, which inhibits the formation of instability waves, observed at lower pressure (close

to critical pressure) dissipates with increase of pressure. As in other investigation, the authors also divide the jet evolution in three different phases, potential core, transition region and self-similar region as shown in Figure 1.5.

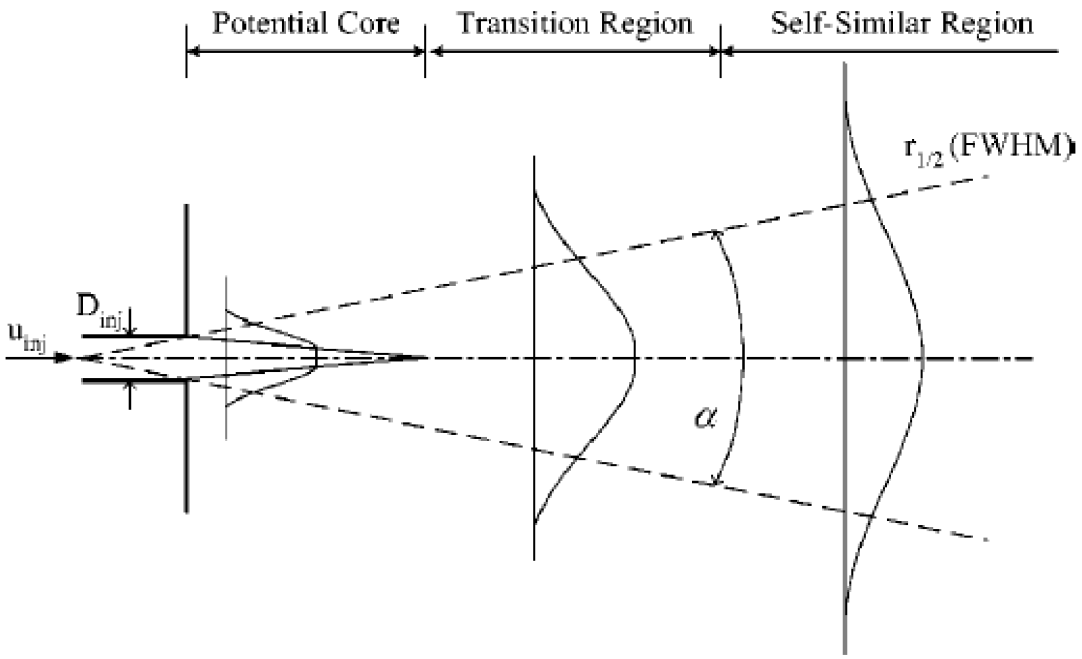

Figure 1.5: Schematic of fluid jet evolution [36]

Oschwald et al. [20] also performed a modeling work in order to obtain further information over their experimental work about single-jet injection at high pressure. In an initial effort of modelling the jet growth rate the authors proposed an formula based on equations of previous authors but including the characteristic times, discussed earlier, together with density ratio. A numerical simulation was performed using the same procedure used by Mayer et al. [26] with the commercial CFD-ACE software package. There were simulated chamber pressures between 3.9 MPa and 5.0 MPa, injection temperatures ranging from 123K to 133K and injection velocities between 2.0 and 5.4 m/s. The numerical calculations have shown to have good agreement with the experimental work, however also predicting bigger potential cores then in experiments or its existence when in the experimental work they are not visible. In general there were found very similar conclusions to the ones already achieved in Mayer's work [26]. Interesting to note that while temperature is slightly above the pseudo-boiling line, the model over predicts the potential core. The same doesn't happens when it is below this line, in this case the predicted potential core is exactly the one observed in experiments.

Zong and Yang [37] published in 2006 a paper where a Large Eddy Simulation of 3 different flow configurations is described. Full conservation laws as well as real fluid thermodynamics were included in the simulation, in order to do so a modified Soave-Redlich-Kwong (SRK) real fluid equation of state along with a 32-term Benedict-Webb-Rubin equation of state were employed. The first flow configuration studied was the one of a cryogenic nitrogen injection into a gaseous supercritical nitrogen environment. The injection fluid was injected with a temperature of 120K and a velocity of 15 m/s through an injector of 0.254 mm of diameter into an environment with a supercritical pressure ranging from 6.9 to 9.3 Mpa and at 300K. The pressure ratios for this simulation were between 0.128 and 0.164 with Reynolds numbers ranging from 42300 to 44700. The use of a real equation of state allows a better representation by the simulation of the

changes already observed in experimental works, this way the disappearance of the interface at supercritical conditions is correctly captured in this work. The analysis of the compressibility-factor shows that the fluid behaves almost ideally for a pressure of 6.9 Mpa. The increase of the chamber pressure results in a reduction of the potential core and an upstream moving of the observed vortices. There are identified three distinct flow regimes, potential core, transition and self-similar region, these three different regions had already been previously identified by Mayer [26]. Finally comparing the simulated jet growth rate with the experimental data from Chehroudi [35] a very good agreement was found with only a maximum deviation of 5%. The second flow configuration studied was the one of a simplex swirl injector. The interest of this kind of injector comes from the fact that it improves intra-element mixing efficiency as compared with shear coaxial injector, it is used for example in the RD-0110 liquid rocket engine. In this bi-dimensional simulation, liquid oxygen (LOX) is injected through the swirl injector at a temperature of 120K ($T_r = 0.776$) into a gaseous oxygen ambient at a pressure of 10.1 MPa ($P_r = 1.98$) and a temperature of 300K. The model shows a single phase flow, not distinguishing the injected fluid from the gas core in the injector, this is attributed to the fact that the chamber pressure is well above the critical pressure of oxygen. The obtained results of mean density, velocity, and temperature fields as well as streamlines, allows to improve injector geometry in order to increase performance. Finally, was studied a shear coaxial injection flow. In this configuration liquid oxygen at a temperature of 150K and velocity of 10 m/s is injected together with an exterior coaxial jet of methane at temperature between 150K and 220K and velocities ranging from 30 and 60 m/s into a methane gaseous environment at 300K and with a pressure of 10.1 MPa. The bi-dimensional large eddy simulation generates the mass fraction, vorticity field, density field, and velocity field. The obtained result shows the existence of several vortices in the mixing layer between the liquid oxygen and methane. The increase of methane injection velocity generates much stronger vortices that accelerate the growth of the mixing layer and enhance mixing between the oxygen and methane. It's also observable that the mixing between the two species streams results mainly from the dynamic of large eddies. This conclusion puts in evidence the necessity of a model that correctly predicts turbulence in order to correctly model the real mixing between species. The results also show a strong density stratification from which effects become more relevant at higher injection temperatures of methane and that the flow dynamics are dictated largely by local thermodynamics state through its influence on the fluid thermophysical properties.

The three flow configurations in the above numerical work shown the big importance that local thermodynamic properties and turbulence have in the mixing and general behaviour of the flow, so in order to correctly model supercritical flows real fluid equation of state and correct turbulence treatment shows to be required.

Jackson et al. performed in 2006 [28] a numerical simulation in which a jet of supercritical ethylene is injected into a chamber with gaseous environment. The numerical approach used was the Favre Averaged compressible Navier-Stokes equations with the turbulence modelled by a hybrid $k-\varepsilon/k-\omega$ two-equation model. For single phase was used the Peng-Robinson equation of state. In order to accommodate two-phase simulation and transition the computational approach employs two different models, a homogeneous equilibrium model that uses a different equilibrium equation of state when the fluid density is within the saturation limits, this model entirely circumvents the possibility of unstable phase transition, and a nucleation/growth model that calculates the parameters connected with droplet formation, this model requires the solution of two additional transport equations, one for the total droplet number density and one for the vapor-phase mass fraction. Numerical results of Mach number line contours, ethylene mole

fraction, temperature, pressure, volume fraction, droplet diameter distribution, and mass flow rate were compared with the experimental results. The conclusion obtained show in most of cases a good agreement between the numerical and experimental results. However, authors state that the nucleation/growth model appears to be restricted to higher injectant temperatures.

Aouissi et al. [38] performed the modelling of variable density heated jets and also non-premixed diffusion flames. Favre-averaged Navier-Stokes governing equations a standard $k-\varepsilon$ turbulence model were employed. Turbulent jet flows with strong temperature and density gradients, like the ones modelled, always presented difficulties in the calculation of heat flux, remaining, at the time of investigation, as one of the unresolved problems of fluid dynamics. Thus the concept of turbulent heat diffusivity was introduced. Turbulent heat diffusivity can be defined through the turbulent viscosity (also called eddy viscosity) and the turbulent Prandtl number, which, in its turn, is a non-dimensional term defined as the ratio between the eddy viscosity (μt) and the scalar diffusivity [39]. However, the use of a constant turbulent Prandtl number is not considered by the authors as a useful concept in the context of heated turbulent jets and diffusion flames. The objective of this investigation was to assess the performance of a turbulence model with a variable turbulent Prandtl number for the prediction of thermal and scalar fields. In order to do so, two extra conservation equations for temperature variance and its dissipation rate were introduced for the calculation of a variable turbulent Prandtl number. No real fluid equation of state is referred to have been used, with the density having been calculated through a $\beta - PDF$ and mixture fraction. Authors claimed to achieve good agreement with experimental data.

Schmitt et al. [40] performed a numerical work with the objective of building and testing a real gas LES solver that can compute large configurations with intricate geometries. This was achieved by using the AVBP solver together with the real-gas Peng-Robinson equation of state in order to take in account the strong non-idealities. It was simulated single round nitrogen jet injected into a gaseous nitrogen closed reservoir. The nitrogen was injected with temperature ranging from 126.9K to 137.0K and velocity between 4.9 and 5.4 m/s. The reservoir in this simulation was at a pressure of 3.97 MPa and a temperature of 298K. The simulated density ratios (ω) were between 0.104 and 0.270. The mesh used contains 950 000 points with a refinement close to the injector. Results show the formation of ligament structures emerging from the central core, this observation is in agreement with data of previous experiments. The centreline density value along the jet axis is at very close agreement with experimental data mainly in the case with lower injection temperature. The tangent of the spreading angle of density is obtained with the Full Width of Half Maximum of Density and is also in good agreement with experiments for case with lower injection temperature while for higher temperature the simulated spreading angle is lower than what observed experimentally. Schmitt et al. also performed a simulation of a reacting coaxial liquid oxygen/hydrogen injection. The simulations were performed at a chamber pressure of 6 MPa. It was observed the combustion to happen around the oxygen jet however the authors state that to capture the correct behaviour of the flame a better grid resolution is required. There were found strong discrepancies between the temperatures obtained experimentally and the LES results, this shows that the developed model was not yet able to correctly simulate a reacting flow in opposite to the observed good ability to treat non-reacting flows.

Kim et al. [11] performed a numerical modelling cryogenic nitrogen jets at near-critical and supercritical pressures. In order to do so the Reynolds averaged Navier-Stokes equation were solved using a finite-volume improved PISO algorithm and closure is obtained by means of a

$k-\varepsilon$ turbulence model. There were tested two different real-fluid equations of state, the Soave Redlich Kwong (SRK) and the Peng-Robinson (PR) equation of state. Four different test cases were investigated with a nitrogen cryogenic jet at temperatures ranging from 126.9 and 137K and velocities between 4.9 and 5.71 m/s being injected through a 2.2 mm injector into a gaseous nitrogen environment at 298K and a pressure between 4.0 and 5.98 MPa. The authors initially show the ability of both SRK and PR equations of state to correctly predict the peak of the specific heat close to critical point. Both equations of state are in good agreement with the NIST data, the same doesn't happen with an ideal equation of state. The modelling of the 4 test cases is made always comparing the two real-fluid equations of state, the experimental data [41] and also the ideal equation of state. The two real-fluid equations of state show in general good agreement with experimental data, with the PR equation of state showing in most of the cases better performance than SRK, the exception happens for relatively higher injection temperatures when the SRK performs better than PR. The ideal equation of state is never able to correctly predict the experimental data with exception to velocity values for which all equations of state present good agreement, yet the real-fluid equations of state are still able to perform better. The authors point out a conclusion that can in part explain some of the supercritical behaviour, it is pointed that the supercritical state can lead to unique behaviour similar to those of a liquid at its boiling point, meaning that heat transfer to the nitrogen does not increase the temperature but merely its specific volume. It's suggested that part of the energy resulting from the expansion can be transferred to the kinetic energy and this way to the velocity, explaining this way a smaller decay of normalized velocity when compared with the normalized density. Numerical results also suggest that discrepancies with experimental data for the four real-fluid mixing jets could be attributed to neglect of heat transfer between the injected nitrogen and the injector as well as shortcomings in the physical models representing turbulence and real-fluid effects.

Zhou et al. [42] performed a Large Eddy Simulation in order to study a diesel engine fuel injection. In this numerical study diesel oil was injected into a constant volume vessel filled with an inert composition of N_2, CO_2 and H_2O. The diesel was injected during a short time of 0.35 ms (making of this a highly transient flow) through an injector of 0.108 mm diameter. The injection pressure was of 110 MPa and the injection temperature of 373K. The chamber which simulates the combustion chamber of the Caterpillar 3400 diesel engine, was set at a temperature of 601 K. In order to perform the simulations a modified version of KIVA-3V by the implementation of a LES model was used with the name of KIVA-LES. The simulations obtained by LES were compared with simulations obtained by a $k-\varepsilon$ RANS model and experimental data. Comparisons between LES and RANS models shown that the LES results are in much better agreement with experimental data than those obtained by the $k-\varepsilon$ model. In LES, the accuracy of prediction increases with the decrease of distance between nodes in the grid. Unlike RANS that has an optimum volume mesh, in LES refinements of grid give always more accuracy. The authors conclude that LES approach should be used as a more advanced tool for predicting detailed characteristics of engine turbulence flow and mixing processes since RANS approaches have difficulty in dealing with strong transient flow fields due to their nature.

Negro and Bianchi [9] conducted a 1D numerical experiment where the flash evaporations of liquid jets inside and outside the injector is studied. The authors suggest the possibility of flash evaporation at conditions close and above critical, and performed this study in order to provide boundary conditions for 3D CFD spray simulations. In order to do so a 1D homogeneous two-phase framework was developed using FORTRAN and named 4-flash. A Homogeneous Relaxation Model is used and incorporates a Volume Translated Peng-Robinson equation of state

that is able to describe the thermodynamic fluid state in subcritical, critical and supercritical conditions. This model was used to simulate the injection of dionized water through an injector of 0.7 mm from a pressurized liquid vessel at 0.7 MPa into an ambient at pressures between 0.1 and 0.5 MPa. There were obtained results of the intact jet length and internal flashing. It was also performed the detection of choking conditions in the injector. The results were in good agreement with experimental data. The main importance of this work comes from the fact that in direct injection engines, high pressure pump systems can increase the fuel temperature at the injection to conditions close or above supercritical, which can originate superheated conditions in which flashing evaporation becomes possible to happen.

Shinjo and Umemura [43] conducted in 2011 an investigation simulating a liquid-gas intermittent injection, similar to what happens in diesel engines, with the objective of characterizing liquid surface instabilities and investigation of the surface instabilities that can lead to atomization. It was used a numerical method based on the level-set interface capturing. To assure volume conservation was used a method called Multi-interface Advection and Reconstruction Solver (MARS), the surface tension was given by the Continuum surface force (CSF) and the advective terms are solved by the Cubic Interpolated Pseudo-particle (CIP) method. In this simulation were obtained visualizations of the jet structure and velocity profiles. The results provided some insight over the jet instabilities formation and how these can lead to jet break-up.

As part of an effort to develop a validated and reliable numerical tool for the simulation of a whole rocket combustion chamber Jarczyk and Pfitzner [44] implemented real gas thermodynamics into the open source CFD code named OpenFOAM. The final goal of the work is to analysed the injection in multiple coaxial injectors, because this is, as authors' state, a strongly three-dimensional and unsteady flow, Large Eddy Simulation is seen by the authors as the most promising method. The OpenFOAM's solver used for the investigations was the PISO algorithm with the incorporation of a Peng-Robinson (PR) equation of state. For a first validation of the thermodynamic model the calculations performed with the PR equation of state were compared with NIST data, the results shown that the PR EOS is able to correctly predict the NIST data over both transcritical and supercritical conditions. The validation of the solver was performed with an initial 1D investigation were the solver proved to perform well enough for this generic test case. For the validation of the solver to transcritical and supercritical jet flows a configuration with two different test conditions was chosen. This configuration involved the injection of a cryogenic liquid nitrogen jet with temperatures ranging from 126.9 to 137K and velocities between 4.9 and 5.4 m/s through an injector of 2.2mm diameter into a chamber with gaseous nitrogen at a temperature of 298K and a pressure of 3.97 MPa ($P_r = 1.16$). The numerical simulations provided the axial density distribution, the instantaneous density iso-surface, and the density gradient. The axial density distribution was compared against the experimental data of Mayer et al. [26]. Quite good agreement was found for the case with higher injection temperature (fully supercritical condition). However, the agreement was worse in the case with lower injection temperature injection where the injection fluid has to perform a transition between transcritical conditions to supercritical conditions.

Lacaze and Oefelein [3] performed in 2012 a Large Eddy Simulation with the objective of studying the flame structure of hydrogen-oxygen diffusion flames at supercritical conditions. For this study was used a configuration in which two opposite injectors produce a H_2 and a O_2 jet in each other directions and the configuration having an outlet positioned at 90 degrees from the jets axial plane. The chamber pressure is between 5 and 9 MPa while the hydrogen is injected at a temperature ranging between 295 and 500K and the oxygen between 120 and 500K. A real-fluid Peng-Robinson equation of state was employed in the model as it was found to be more suitable

for conditions when the temperature is greater than the critical temperature. A flamelet model was developed in order to account for combustion phenomena. The authors described in this paper the four different regimes already presented before in Figure 1 and defined the compressibility factor as an indicator of how far a fluid is from ideal-gas properties. They also state that close to critical conditions small changes in pressure and temperature as well as mixture can lead to combustion instabilities that influence the performance of a burner and can even lead to its damage and destruction. Comparing with references authors found slightly thinner flames but correct values of temperature leading also to accurate density gradients. They also found that pressure has limited impact on flame structure in mixture fraction space at supercritical pressures and defend that under fully supercritical conditions a single-fluid approach is relevant to simulate the existing flows.

High-order schemes were used by Terashima and Koshi [45], [46] for the simulation cryogenic fluid mixing under supercritical pressures. To govern the fluid there were used the conservation equations of mass, momentum, and mass fraction of species, also a pressure evolution equation is used instead of enforcing the total energy equation. A real fluid equation of state of the type Soave-Redlich-Kwong was employed in order to evaluate the thermodynamic flow properties under supercritical pressure, temperature is obtained through it using an iterative method. The pressure evolution equation is used for satisfying the pressure equilibrium and the consistent numerical diffusion terms for the velocity equilibrium at the fluid interfaces, authors state that a fully conservative form of the governing equations leads to spurious oscillations and the pressure evolution equation is a way of counteracting them. There were performed two different simulations. A one-dimensional nitrogen and nitrogen/hydrogen interface advection problem with the objective of simulating the capabilities of the present method at a supercritical pressure of 5.0 MPa. And a two-dimensional cryogenic jet mixing where both nitrogen and hydrogen liquid cryogenic jets are injected into a gaseous nitrogen environment. The chamber pressure has the value of 5 MPa which corresponds to a reduced pressure of 2.62 for nitrogen and 1.13 for hydrogen. Results of density, pressure, temperature, speed of sound and mass fraction scalar field were obtained. Since, according to the authors, no existing measured data for a planer jet under supercritical pressures were found, only a qualitative demonstration of the multidimensional capability and robustness of the method was possible. Authors conclude that the major source of error is originated from the equation of state and that the construction of methods that satisfy velocity and pressure equilibrium is the key for the application of high-order schemes in such thermodynamic conditions.

Park [39] conducted a numerical investigation with the objective of evaluating the performance of RANS turbulence models and LES in the simulation of cryogenic nitrogen injection into a gaseous supercritical nitrogen environment. Four different RANS turbulence models were used as well as two different Large Eddy Simulations. All models were implemented in a PISO algorithm which was slightly modified in order to handle the large density ratios for supercritical fluid flows. It was also evaluated the importance of the equation of state in numerical performance by testing three different equation of state: the ideal equation of state; the Soave-Redlich-Kwong; and the Peng-Robinson EoS. The different models and equations of state were used to simulate two test cases in which the chamber pressures were ranging from 4.0 to 5.98 MPa, corresponding to reduced pressures of 1.17 and 1.76, and the injection temperatures from 126.9 to 128.7K. The injection velocity was between 4.90 and 5.47 m/s while the injection chamber was at an initial temperature of 298K defined by an isothermal wall. The obtained numerical results allow the visualization of the axial and radial density variation, instantaneous mixture fraction and c_p field, axial variation of velocity and turbulent kinetic energy and also

the jet spreading rates. One of the main conclusions of these results was that the choice of a suitable equation of state is more decisive for the numerical performance than the selection of a turbulence model. It was concluded that ideal EoS is insensible to the changes of c_p between gas and liquid. PR and SRK EoS on the other hand can predict the pseudo-boiling behaviour and this way probably account for the changes in physical state observed in supercritical and transcritical injection. The use of a real-fluid EoS allows the visualization of small vortices that appear from the ring vortex in experiment and are not visible with ideal EoS. For the result of spreading rate there are different results for different turbulence models, the LES results are in good agreement with experimental data while by comparison the RANS results are a little higher.

Schuler et al. [47] performed a numerical work intending to simulate the thermal field of submerged supercritical water jets. Their numerical approach was built inside the commercial CFD code ANSYS FLUENT®via user defined functions. The Favre-averaged conservation of momentum, mass and energy were solved and a realizable $k-\varepsilon$ turbulence model was used for closure. The authors state that in fully turbulent flow field the molecular conductivity is negligible when compared with the heat transfer due to turbulent fluctuations. Thus for the diffusion term of the specific energy equation it was used an effective conductivity that consists in the sum of the molecular conductivity with the turbulent conductivity. Due to the strong variation of water's physical properties when at near-critical pressures, the authors identified the need for a method to cope with such changes. Different approaches based on a variable turbulent Prandtl number were chosen by the authors to deal with the strong properties changes when close to the critical point. Thus there were performed with different methods for determination of the turbulent Prandtl number. Initially it was used a model with constant turbulent Prandtl, the simulations reached, according with the authors, acceptable agreement with the experimental data [48], also provided by the same authors. However, they admit the existence of a slight over prediction of jet cooling. Variable turbulent Prandtl models were then implemented, authors point that while in the far-field, self-similar area of the jet turbulent Prandtl reaches values between 0.7 and 0.8, in the near-field of jet turbulent Prandtl is more close to values ranging from 0.4 to 0.5. Three different variable turbulent Prandtl models were implemented and compared with each other. A model uniquely function of the temperature. Another model, physically more meaningful, which establishes a dependency on the molecular Prandtl number instead of with temperature. And finally a scalar-variance model [40] for which it was needed to solve two additional transport equations for the energy variance and its dissipation rate. Comparison between the experimental data and the four different simulations demonstrate that the scalar-variance model matches the experimental data much better than any other approach used in the investigation. Is also important to refer that in this investigation no real fluid equations of state were used to calculate the water properties. These were obtained from the NIST data base for each respective pressure and temperature. Authors also conclude that in these flows turbulent conductivity controls heat transfer and that CFD simulations at near-critical conditions involve the fluid's transition from sub- to supercritical and are therefore far more troublesome due to the strongly varying properties around the pseudo-critical point.

Together with experimental investigation, the work of Schmitt et al. [31] included also a numerical part. A Large Eddy Simulation with real gas thermodynamics given by a Peng-Robinson EoS were implemented in the AVBP flow solver. Laminar viscosity and heat conductivity coefficients are determined with the Chung et al. [49] method. The flow configuration simulation by this numerical approach was the same already described in the experimental part of this paper. Comparisons between shadowgraph visualization and instantaneous density distribution

obtained from simulations show similar flow patterns. Radial profiles of density obtained in simulations are also in very good agreement with the experimental data. The numerical model is this way in great degree validated by experimental data. The authors have the future objective of continuing LES development and validation for transcritical and supercritical flow calculations both in average field as in fluctuations.
Using their "home-made" code called "SiTCom-B" (Simulation of Turbulent Combustion with Billions of points) Petit et al. [50] decided to simulate transcritical and supercritical cryogenic nitrogen jets. The code performed a Large Eddy Simulation of the cases 3 and 4 of Mayer et al. [26] already described before. There were used two different real fluid, cubic, equations of state, a Peng-Robinson and a Soave-Redlich-Kwong equations of state, which replace a classic ideal gas law and link the pressure, temperature and density. Due to the large variations of transport or thermodynamics properties observed around the critical point or the pseudo-boiling line, those properties are determined by the high-pressure relations proposed by Chung et al. [49] which the authors state to be more accurate than classic techniques. Both equations of state were compared against NIST data for the fluid properties like density, heat capacity at constant pressure, compressibility, cinematic viscosity or thermal diffusivity and have shown good agreement. However, for temperatures below 130K start appearing some discrepancies for both equations with the SKR EoS matching betters the NIST data. For the flow simulation, authors provide density profiles and the Full Width of Half Maximum of density (FWHM) as results. Like in previous works the FWHM of Density is used to calculate spreading rates of jets. Comparison of simulations with experimental data show for case 3 good agreement for the centreline density profile and a slight under-prediction of the FWHM of Density and by consequence the jet spreading rate. For case 4 the obtained potential core length is in agreement with experiments but further downstream there's an under-prediction of the density. Once again spreading rates for case 4 are not possible to be compared with experimental due to the inexistence of data from Mayer [26]. There was also performed in this investigation a simulation of a co-axial LOX/Methane injection which found fairly good agreement with experimental data. Finally authors also find the lack of experimental data the limitation for more advanced comparisons.

The analysis of a number of numerical works performed until this date allowed to obtain a series of important conclusions. From the several numerical approaches available only two are extensively used in the study of supercritical and transcritical jets, are the Reynolds Averaged Navier-Stokes with prevalence in using the $k-\varepsilon$ turbulence model and the Large Eddy Simulation. Direct Numerical Simulation could also produce good and very precise results but its extremely high computational expense makes it not suitable for the studied flows. Between LES and RANS authors that compared the two approaches obtained generally more accurate results with LES.
Several authors conclude that in supercritical and transcritical flow the jet behaviour is very sensitive not only to thermodynamic conditions but also to the mixture properties. The thermodynamics of fluids are this way dictated by pressure, temperature, and also mixture in the case of more than one specie involved in the injection. Jet dynamics are largely dictated by the local thermodynamics, however when close to the critical point small changes in pressure, temperature or mixture can strongly, and in a non-linear way, change the thermodynamic properties and this way the behaviour of the jet. Real fluid thermodynamics must be included in the numerical approach if one wants to treat the jet behaviour correctly when close to the critical thermodynamic point. Two types of real fluid equations of state, the Peng-Robinson [51] and the Soave-Redlinck-Kowng [52], were generally implemented and tested in the several numeri-

cal studies above. They show very good results when compared with an ideal fluid equation of state.

Numerical approaches in fact shown that the implementation of a real fluid equation of state is more relevant to obtaining good numerical results than the choice of the turbulence model for the closure to Navier-Stokes [39]. The real fluid EoS must obviously take in consideration pressure and temperature but also, in the case of multi species flows, the mixture properties, since the local value of mixture largely influence the jet dynamics.

Some authors have indeed developed work with the objective of identifying the equation of state that better fits their conditions of study or even, more ambitiously, find a generalized equation of state. It's the case of Kim et al., in their works [53], [54] they developed a numerical method for the calculation of thermodynamic and transport properties when conditions are near critical of supercritical. In the first investigation [53] there were tested the Soave-Redlich-Kwong and Peng-Robinson equations of state in their ability to provide the correct thermodynamic properties such as density, isobaric heat capacity, entropy, and sound speed for the mixture Kerosene/LOx used in rocket combustion. Then the recently developed three-parameters, generalized cubic equation of state, named RK-PR EoS [55], was also integrated in their developed numerical methods and compared with the two other equations of state. This equation uses the two parameters also present in SRK and PR EoS, and a third parameter that is adjusted based on the characteristics of pure fluid or mixture. In the second investigation [54] a similar research was performed for dimethyl ether. In this case transport properties such as viscosity and thermal conductivity are reproduced by the help of the model of Chung et al. [49]. The interest in the dimethyl ether fuel in this case comes from the fact that it can substitute diesel fuel without major modification in engines. Results of both investigations proved this recent equation of state to be more accurate than both SRK and PR equations of state.

Kim et al. [11] had already performed numerical study where the PR and SRK equation of state had been tested and compared against NIST data. They concluded that PR EoS performed better at supercritical pressures with lower temperature injection while the SRK EoS gave better agreement for the relatively high temperature range at near critical pressures.

The comparison provided by Park et al. [39] between the PR and SRK equation of state shown that when tested against NIST data the SRK equation provided quite better accuracy for density and molecular viscosity in the lower temperature range. When at higher temperatures both equation perform well.

Petit et al. [50] also performed in their work a comparison between the Peng-Robinson and the Soave-Redlich-Kwong equations of state. They conclude that both equations are able to find good agreement with NIST data but with the results showing a slightly better performance of the SRK equation.

1.4 Objectives

The present research has as objective the development and test of a different model for the calculation of rounds jets at conditions of pressure and temperature around the critical point. The model that will be presented is based on the variable density approach used in the works of Barata et al. [7] and Antunes et al. [8] but with the inclusion of the real fluid thermodynamics identified by several authors as essential for the calculation of near-critical and supercritical flows. The algorithm used for the inclusion of real fluid thermodynamics into the existing numerical approach was different from the method followed by the majority of the reviewed

authors and leads to a major change of the calculation procedure existent in the original variable density approach.
Several authors have used Large Eddy Simulations with the inclusion of real fluid equations of state for the simulation transcritical and supercritical flows. The conservation equation of energy was calculated in works performed by Zong et al. [36], [37], Jarczyk and Pfitzner [44], Schmitt et al. [31], and Petit et al. [50]. In these works, temperature can be obtained through energy equation and then density is obtained through equation of state. However, this methodology is not explained in an explicit way by all the authors cited above leaving in some cases doubts about the real method. For instance Park et al. [39] uses both LES and RANS approaches but doesn't solve the energy equation for the presented simulation, temperature is calculated through mixture fraction and density through SRK and PR equations of state. Barata et al. [7] used a variable density approach in which the density was calculated through a linear relation of mixture fraction. In its Favre Averaged Navier Stokes modelling Mayer et al. [26] solves the energy equation in order to obtain heat transfer but the real fluid properties are obtained through the CFD-ACE software package and no reference to a real fluid equation of state is done. The works of Aouissi [38] and Schuler [47] for example use the FANS method, solving also the favre averaged energy equation and obtaining this way the thermal field. However in both studies no equation of state is referred and density is obtained through a beta probability distribution function together with mixture fraction for the Aouissi study [38] or by the NIST data in the case of Schuler [47].
One can conclude that no specific method is generally accepted for the simulation of transcritical and supercritical flows. However, some trends are observed, like for instance the use of a real fluid equation of state, which can't be ignored. In the present work was decided to start from the variable density approach already used by Barata et al. [7] and make the necessary modifications for the incorporation of real fluid thermodynamics. Real fluid equations of state were analysed, tested and selected for incorporation in the existing code. Since originally the initial variable density approach didn't provide the calculation of temperature field, it was decided to calculate it through the incorporation of a Favre Averaged Energy equation. Problems however arisen due to the strong non linearity of fluid properties at condition around the critical point.
In order to validate the developed approach, the experimental work performed by Mayer et al. [26] has been modelled for its cases 3 and 4. The choice of these cases was made due to the acceptance by several authors [40, 44, 50] as reference cases of study since case 3 is at transcritical conditions while case 4 is at supercritical conditions. The obtained results will also be compared against the Large Eddy Simulations of other authors [40, 44, 50].

1.5 Structure of the document

In chapter 1 the motivations for the present research were presented. It was as well made a description of the state of art for the scientific field. And finally, the objectives for the present work were presented.
Chapter 2 will focus on the description of the mathematical approach used for the calculation of the flow parameters. The Navier-Stokes equation for fluid motion will be presented as well as their mean forms and the methodology for the treatment of turbulence.
The real fluid thermodynamics, essential for the treatment of fluid around and above the thermodynamic critical point, will be discussed in chapter 3. This chapter will describe how fluid

density, viscosity, thermal conductivity, and specific heat at constant pressure are obtained from equations which intend to provide the closest approximation possible with reality.
Chapter 4 will describe the numerical approach which allow to obtain the solution for the set of equations described in chapters 2 and 3. In this chapter will be also presented the flow configuration as well as the cases of study.
In Chapter 5 the results obtained from the model described in previous chapters are presented. Are obtained results from different methodologies of calculation of the fluid properties. These results are validated not only against experimental data but also against numerical data from different authors.
Finally in Chapter 6, the main conclusions achieved in the present investigation are presented, and future work is suggested.

Chapter 2

Mathematical Approach

2.1 Introduction

In the present chapter the mathematical formulation which allowed the calculation of the flow variables will be described. As was referred in the previous chapter, the field of computational fluid dynamics incorporates several different approaches which were already briefly described. In the present work was used a variation of the Reynolds Averaged Navier-Stokes approach in which the Reynolds Averaging procedure is substituted by a Favre Averaging. All the referred approaches have as basis the Navier-Stokes equations for fluid dynamics. This chapter will start with a description of those equations. However, due to computational constraints these equations are not possible to be solved directly, thus the Reynolds and Favre averaging procedures will be presented. For this methodology, turbulence must have a dedicated treatment, thus a turbulence model is required. Under the present mathematical approach a "$k-\varepsilon$" turbulence model was employed and described in this chapter. After this, there will be presented the conservative equations specified for the axisymmetric flow which also include the equations for other fluid properties. Finally, the wall treatment employed in the present approach will be described.

2.2 Governing Equations for Fluid Dynamics

The equations of motion for a homogeneous fluid are called the Navier-Stokes equations. This set of equations derives directly from the application of the law of conservation of mass, Newton's second law, and first law of thermodynamics to fluid motion.

The conservation of mass contributes to the system with one equation, the same as the first law of thermodynamics also called conservation of energy. Newton's second law, conservation of linear momentum, is a vector equation and, therefore, provides three scalar equations for a three dimensional problem. Is important to refer that for incompressible flows, when density ρ is constant, the equation for conservation of energy can be omitted from the system of equations, not being solved. It isn't however the case in the present work.

The system of equations contains nine unknowns which include ρ (density), u, v, w (components of the velocity vector), e_t (total energy) or h (enthalpy), p (thermodynamic pressure), T (temperature), μ (dynamic viscosity), and k (thermal conductivity). The system of equations is closed by introducing thermodynamic relations, in the form of an equation of state for instance, and auxiliary relations for the coefficient of viscosity and thermal conductivity [56]. In the case of a two dimensional problem, like the one in study, one equation and one unknown is eliminated, the velocity component w and its corresponding equation.

2.2.1 Conservation of Mass

The differential form of the conservation of mass is known as the continuity equation, and in a vector form it is expressed as:

$$\frac{\partial \rho}{\partial t} + \nabla.(\rho \vec{V}) = 0 \quad \textbf{(2.1)}$$

The same equation can be written in the tensor form assuming the following representation:

$$\frac{\partial \rho}{\partial t} + \frac{\partial}{\partial x_i}(\rho u_i) = 0 \quad \textbf{(2.2)}$$

In the present investigation the flow was treated as being in a steady state. For steady state problems $\frac{\partial}{\partial t} \equiv 0$, and, therefore the equation can be simplified into:

$$\frac{\partial}{\partial x_i}(\rho u_i) = 0 \quad \textbf{(2.3)}$$

2.2.2 Conservation of Linear Momentum

By the application of Newton's second law to a differential element in an inertial system, the equation for conservation of linear momentum is obtained, which is here expressed in the general vector form:

$$\frac{\partial}{\partial t}(\rho \vec{V}) + \nabla(\rho \vec{V}\vec{V}) = \rho \vec{f} - \nabla p + \nabla.\tau \quad \textbf{(2.4)}$$

Writing the same equation in the tensor notation:

$$\frac{\partial}{\partial t}(\rho u_i) + \frac{\partial}{\partial x_j}(\rho u_i u_j) = \rho f_i - \frac{\partial p}{\partial x_j} + \frac{\partial}{\partial x_j}\tau_{ij} \quad \textbf{(2.5)}$$

Viscous stresses are related to the rates of strain by a constitutive law. For most fluids, this relation is linear and they are named Newtonian fluid. For a Newtonian fluid with Stokes hypothesis the equation takes the form:

$$\frac{\partial}{\partial t}(\rho u_i) + \frac{\partial}{\partial x_j}(\rho u_i u_j) = \rho f_i - \frac{\partial p}{\partial x_j} + \frac{\partial}{\partial x_j}\Big[\mu\Big(\frac{\partial u_i}{\partial x_j} + \frac{\partial u_j}{\partial x_i}\Big)\Big] - \frac{\partial}{\partial x_j}\Big[\frac{2}{3}\mu\Big(\frac{\partial u_k}{\partial x_k}\Big)\Big] \quad \textbf{(2.6)}$$

For a steady state flow we have $\frac{\partial}{\partial t} \equiv 0$, in the present work body forces such as gravity will be neglected so $\rho f_i = 0$, our equation simplifies to:

$$\frac{\partial}{\partial x_j}(\rho u_i u_j) = -\frac{\partial p}{\partial x_j} + \frac{\partial}{\partial x_j}\Big[\mu\Big(\frac{\partial u_i}{\partial x_j} + \frac{\partial u_j}{\partial x_i}\Big)\Big] - \frac{\partial}{\partial x_j}\Big[\frac{2}{3}\mu\Big(\frac{\partial u_k}{\partial x_k}\Big)\Big] \quad (2.7)$$

2.2.3 Conservation of Energy

The energy equation derived from the first law of thermodynamics may be written in various forms. One of such formulations known as the total energy equation is:

$$\frac{\partial}{\partial t}\Big[\rho\overbrace{(e + \frac{1}{2}V^2)}^{e_t}\Big] + \nabla\Big[\rho\overbrace{(e + \frac{1}{2}V^2)}^{e_t}\Big] = \frac{\partial Q}{\partial t} - \nabla.\vec{q} + \rho(\vec{V}.\vec{f}) - \nabla(p\vec{V}) + \nabla(\tau\vec{V}) \quad (2.8)$$

Taking the assumption of the inexistence of heat generation $\frac{\partial Q}{\partial t} = 0$, absence of body forces $\rho(\vec{V}.\vec{f}) = 0$, and using the tensor notation the equation becomes:

$$\frac{\partial}{\partial t}\Big[\rho\big(e + \frac{u_k u_k}{2}\big)\Big] + \frac{\partial}{\partial x_j}\Big[\rho u_j\big(e + \frac{u_k u_k}{2}\big)\Big] = -\frac{\partial q_j}{\partial x_j} - \frac{\partial}{\partial x_j}(u_j p) + \frac{\partial}{\partial x_j}(u_i \tau_{ij}) \quad (2.9)$$

For a Newtonian fluid with Stokes hypothesis and with the assumption of Fourier heat conduction, $q_j = -\lambda\frac{\partial T}{\partial x_j} \equiv -c_p\frac{\mu}{P_r}\frac{\partial T}{\partial x_j}$, the equation takes the following form:

$$\begin{aligned}\frac{\partial}{\partial t}\Big[\rho\big(e + \frac{u_k u_k}{2}\big)\Big] + \frac{\partial}{\partial x_j}\Big[\rho u_j\big(e + \frac{u_k u_k}{2}\big)\Big] &= c_p\frac{\mu}{P_r}\frac{\partial T}{\partial x_j} - \frac{\partial}{\partial x_j}(u_j p) \\ &+ \frac{\partial}{\partial x_j}\Big[\mu\Big(\frac{\partial u_i}{\partial x_j} + \frac{\partial u_j}{\partial x_i}\Big)\Big] - \frac{\partial}{\partial x_j}\Big[\frac{2}{3}\mu\Big(\frac{\partial u_k}{\partial x_k}\Big)\Big] \quad (2.10)\end{aligned}$$

2.3 Reynolds Averaged Navier-Stokes Equations

Turbulent flows are characterized by a range of apparently random and chaotic, three-dimensional velocity fluctuations, the velocity fluctuation arise obviously also fluctuations in other flow properties. The cause for the phenomenon of turbulence is attributed to the destabilizing effect that viscosity arises in all fluids [57].

The energy cascade hypotheses establishes turbulence as being composed of eddies of different sizes. Large eddies are characterized by a lengthscale comparable to the flow scale, these are the scales responsible for the large flow fluctuations. Large eddies are unstable and break up, transferring their energy to smaller eddies which in turn transfer also their energy to even smaller eddies. This energy cascade continues until the Reynolds number is sufficiently small that the eddy motion is stable and molecular viscosity is effective in dissipating the kinetic energy. The Kolmogorov hypotheses gives the lengthscale of the smallest, dissipative eddies, the Kolmogorov scales [32]. These scales are in practice extremely small, and to solve them numerically very fine grids must be used. This leads to solutions very expensive to be obtained in terms of computational resources. However, as explained in the first chapter, solving all the scales of motion would give by far the most accurate results, and this approach is called DNS.
There are alternatives for the treatment of turbulent flows which do not involve the resolution of all the scales of motion. As stated, turbulence is characterized by the existence of random and chaotic fluctuations, however, by averaging the fluctuating values of a property in a given time a mean value of the property can be obtained. Thus, a transformation can be performed in which a variable is decomposed into its time averaged value $\overline{\phi}$ and the fluctuation ϕ', this procedure takes the name of Reynolds decomposition:

$$\phi = \overline{\phi} + \phi' \quad (2.11)$$

Where ϕ is time averaged in the following way:

$$\overline{\phi} = \frac{1}{t}\int_t \phi(t)dt \quad (2.12)$$

Applying the Reynolds decomposition for each of the flow's variables in the equations of fluid motion for conservation of mass and momentum for an incompressible and Newtonian fluid, the so called Reynolds Averaged Navier-Stokes equations are obtained.

2.3.1 Reynolds Averaged Conservation of Mass

Applying the Reynolds decomposition of equation 2.11 to the average velocity in the continuity equation 2.3, one obtains the Reynolds Averaged Continuity Equation for an incompressible fluid:

$$\frac{\partial}{\partial x_i}(\overline{\rho u_i}) = \frac{\partial}{\partial x_i}\left(\rho(\overline{\overline{u_i} + u_i'})\right) = \frac{\partial}{\partial x_i}\left(\rho(\overline{\overline{u_i}} + \overline{u_i'})\right) \quad (2.13)$$

Since in incompressible flow ρ is constant, and the average of a constant is the constant itself, ρ can be excluded from the averaging process. By definition the average of a fluctuation is equal to zero, also the average of an average is the average itself, so:

$$\overline{u_i'} = 0 \quad (2.14)$$

and,

$$\overline{\overline{u_i}} = \overline{u_i} \quad (2.15)$$

Thus, the Reynolds averaged continuity equation stays:

$$\frac{\partial}{\partial x_i}(\rho\overline{u_i}) = 0 \quad (2.16)$$

2.3.2 Reynolds Averaged Conservation of Linear Momentum

The same procedure can be applied to the momentum equation 2.5 while neglecting the existence of body forces $\rho f_i = 0$:

$$\frac{\partial}{\partial x_i}\overline{(\rho u_i)} + \frac{\partial}{\partial x_i}\overline{(\rho u_i u_j)} = -\frac{\partial \overline{p}}{\partial x_i} + \frac{\partial}{\partial x_i}\overline{\tau_{ij}} \Leftrightarrow \quad (2.17)$$

$$\Leftrightarrow \frac{\partial}{\partial x_i}\rho\overline{(\overline{u_i} + u_i')} + \frac{\partial}{\partial x_i}\rho\overline{(\overline{u_i u_j} + u_i' u_j')} = -\frac{\partial}{\partial x_i}\overline{(\overline{p} + p')} + \frac{\partial}{\partial x_i}\overline{(\overline{\tau_{ij}} + \tau_{ij}')} \Leftrightarrow \quad (2.18)$$

$$\Leftrightarrow \frac{\partial}{\partial x_i}\rho\big(\overline{\overline{u_i}} + \overline{u_i'}\big) + \frac{\partial}{\partial x_i}\rho\overline{\big(\overline{u_i u_j} + u_i' u_j'\big)} = -\frac{\partial}{\partial x_i}\big(\overline{\overline{p}} + \overline{p'}\big) + \frac{\partial}{\partial x_i}\big(\overline{\overline{\tau_{ij}}} + \overline{\tau_{ij}'}\big) \quad (2.19)$$

Applying equations 2.14 and 2.15 the equation 2.19 transforms into:

$$\frac{\partial}{\partial x_i}(\rho\overline{u_i}) + \frac{\partial}{\partial x_i}(\rho\overline{u_i u_i}) + \frac{\partial}{\partial x_i}(\rho\overline{u_i' u_j'}) = \frac{\partial \overline{p}}{\partial x_i} + \frac{\partial \overline{\tau_{ij}}}{\partial x_i} \quad (2.20)$$

The application of Reynolds Averaging to the momentum equation leads to the appearance of the averaged product of velocity fluctuations $\overline{u_i' u_j'}$, these velocity covariances are called Reynolds stresses. Unlike the term $\overline{u_i'}$ the Reynold stresses are not zero and must be determined, since the very different behaviour of u_i and $\overline{u_i}$ are attributable to the effect of the Reynolds stresses [32]. As already affirmed in Chapter 1 Reynolds stresses have a difficult physical interpretation and must be related to the average flow in order to obtain closure. Several

different models exist, in the present work was employed a $k-\varepsilon$ model which will be shortly described later.

2.3.3 Other considerations

The Reynolds averaging procedure can also be employed to the energy equation. However for an incompressible flow, where ρ is constant the primary flow-field variables are p and V. The continuity and momentum equations obtained above are two equations in terms of the two unknowns p and V. Hence, for a study of an incompressible flow, the continuity and momentum equations are sufficient tools [58]. Also the application of the Reynolds averaging to the equation energy bring with it an extra number of terms for which no straight solution exists, thus having to be modelled somehow.
It happens that for the flow of interest ρ is far from being constant, the same can also be said about all other fluid properties. Previously the Reynolds averaging was employed assuming always incompressible flow, with ρ constant, thus $\overline{\rho} = \rho$. However, for compressible flow the Reynolds averaging of continuity and momentum equation gives quite more complex terms than the ones obtained for incompressible flow. As an example we can employ the same procedure to the continuity equation for compressible flow 2.2:

$$\frac{\partial \overline{\rho}}{\partial t} + \frac{\partial}{\partial x_i}\overline{(\rho u_i)} = \frac{\partial \overline{\overline{\rho} + \rho'}}{\partial t} + \frac{\partial}{\partial x_i}(\overline{\overline{\rho u_i} + \rho' u_i'}) \quad (2.21)$$

Applying equations 2.14 and 2.15, the equation becomes:

$$\frac{\partial \overline{\rho}}{\partial t} + \frac{\partial}{\partial x_i}(\overline{\rho u_i}) + \frac{\partial}{\partial x_i}(\overline{\rho' u_i'}) = 0 \quad (2.22)$$

The term $\overline{\rho' u_i'}$ cannot be assumed as zero and because has no direct physical interpretation must be modelled in some way. The Reynolds averaged momentum equation for compressible flow brings even more complex terms connected with density fluctuations. The task of modelling all these terms turns out to be quite difficult and time consuming. And for this reason other averaging process is employed for compressible flows which will be presented next.

2.4 Favre Averaged Navier-Stokes Equations

The density fluctuations pose an increase complexity when using the Reynolds Averaged Navier-Stokes equations for flows without constant density. The way to overcome those challenges is by the use of different kind of averaging for the Navier-Stokes equations, specifically a density weighted average. This kind of average, called Favre Averaging, has the advantage of suppressing terms containing correlations involving the density fluctuations, thus leading to a significant simplification of the averaged equations [59]. Analogous to the Reynolds averaging a decomposition is performed to the generic variable ϕ:

$$\phi = \tilde{\phi} + \phi'' \quad (2.23)$$

However, for this procedure the density weighted averaged variable $\tilde{\phi}$ is given by:

$$\tilde{\phi} = \frac{\frac{1}{t}\int_t \rho(t)\phi(t)dt}{\frac{1}{t}\int_t \rho(t)dt} = \frac{\overline{\rho\phi}}{\overline{\rho}} \quad (2.24)$$

Contrasting with Reynolds Averaging, the average of the Favre fluctuation is not zero:

$$\overline{\phi''} \neq 0 \quad (2.25)$$

But,

$$\overline{\rho\phi''} = 0 \quad (2.26)$$

As was already presented in the equation 2.21, applying the Reynolds averaging to the $\rho\phi$ term, is obtained:

$$\overline{\rho\phi} = \overline{\overline{\rho\phi} + \rho'\phi'} \Rightarrow \overline{\rho\phi} = \overline{\rho}.\overline{\phi} + \overline{\rho'\phi'} \quad (2.27)$$

Analogous to the Reynolds decomposition, the Favre decomposition can also be employed into the averaging procedure of the same term:

$$\overline{\rho}\tilde{\phi} = \overline{\overline{\rho\tilde{\phi}} + \rho\phi''} = \overline{\rho}\tilde{\phi} + \overline{\rho\phi''} \underset{\overline{\rho\phi''}=0}{\Longrightarrow} \overline{\rho.\phi} = \overline{\rho}\tilde{\phi} \quad (2.28)$$

From the combination of equations 2.27 and 2.28 the following relation between the Reynolds

averaging and the Favre averaging can be obtained:

$$\overline{\rho}\tilde{\phi} = \overline{\rho}.\overline{\phi} + \overline{\rho'\phi'} \Rightarrow \tilde{\phi} = \overline{\phi} + \frac{\overline{\rho'\phi'}}{\overline{\rho}} \quad (2.29)$$

The fluctuation from the Favre averaging is denoted by:

$$\phi'' = \phi - \tilde{\phi} \quad (2.30)$$

The value of the Favre fluctuation can be determined applying equation 2.29 into equation 2.30:

$$\phi'' = \phi - \tilde{\phi} = \phi - \left(\overline{\phi} + \frac{\overline{\rho'\phi'}}{\overline{\rho}}\right) \Rightarrow \phi'' = \phi - \overline{\phi} - \frac{\overline{\rho'\phi'}}{\overline{\rho}} \quad (2.31)$$

Thus, the average of the Favre fluctuation is:

$$\overline{\phi''} = \overline{\phi - \overline{\phi} - \frac{\overline{\rho'\phi'}}{\overline{\rho}}} \Rightarrow \overline{\phi''} = \overline{\phi} - \overline{\phi} - \frac{\overline{\rho'\phi'}}{\overline{\rho}} \Rightarrow \overline{\phi''} = \frac{\overline{\rho'\phi'}}{\overline{\rho}} \quad (2.32)$$

This last deduction besides allowing the determination the value of $\overline{\phi''}$ also proves the inequality from equation 2.25.
After obtaining comprehension of the Favre averaging process, it can be applied to the governing equations of fluid dynamics, conservation of mass, 2.2, conservation of momentum, 2.6, and conservation of energy, 2.10. The Favre Averaged Navier-Stokes equations will be now presented.

2.4.1 Favre Averaged Conservation of Mass

Employing the time averaging procedure to the continuity equation, 2.2, is obtained equation 2.21, from equation 2.29, using the relation $\overline{\rho}\tilde{\phi} = \overline{\rho}.\overline{\phi} + \overline{\rho'\phi'}$, the Reynolds averaged equation can be transformed into the Favre averaged conservation of mass equation:

$$\frac{\partial\overline{\rho} + \overline{\rho'}}{\partial t} + \frac{\partial}{\partial x_i}\left(\overline{\overline{\rho u_i} + \rho' u_i'}\right) = 0 \Rightarrow \frac{\partial\overline{\rho}}{\partial t} + \frac{\partial}{\partial x_i}\left(\overline{\rho}.\tilde{u_i}\right) = 0 \quad (2.33)$$

As can be observed the employment of the Favre averaging transformation allows the elimination of the average term of the product of density and velocity fluctuations, $\overline{\rho' u_i'}$. Otherwise, this term would have to be determined, the averaged continuity equation offer by this method a simplified treatment.
Because in the current work the flow is considered to be steady, the equation 2.33 can be further simplified eliminating the temporary term.

$$\frac{\partial}{\partial x_i}\left(\overline{\rho}.\tilde{u_i}\right) = 0 \quad \textbf{(2.34)}$$

2.4.2 Favre Averaged Conservation of Linear Momentum

An analogous process to the one which was done for the Reynolds averaging in 2.3.2, can now be applied to equation 2.17, which represents the average of momentum equation, here written with slightly different presentation for the sake of compactness:

$$\frac{\partial}{\partial t}\left(\overline{\rho.u_i}\right) + \frac{\partial}{\partial x_j}\left[\overline{\rho.u_i.u_j + p.\delta_{ij} - \tau_{ij}}\right] = 0 \quad \textbf{(2.35)}$$

The $\overline{\rho.u_i}$ term is treated the same form as it was done for the conservation of mass, and so the equation becomes:

$$\frac{\partial}{\partial t}\left(\overline{\rho}.\tilde{u_i}\right) + \frac{\partial}{\partial x_j}\left[\overline{\rho.u_i.u_j} + \overline{p.\delta_{ij}} - \overline{\tau_{ij}}\right] = 0 \quad \textbf{(2.36)}$$

Applying the Favre decomposition to the rest of the terms, the Favre Averaged Conservation of Linear Momentum equation is:

$$\frac{\partial}{\partial t}\left(\overline{\rho}.\tilde{u_i}\right) + \frac{\partial}{\partial x_j}\left[\overline{\rho}.\tilde{u_i}.\tilde{u_j} + \frac{\partial}{\partial x_j}\left[\overline{\rho.u_i''.u_j''} + \overline{p}.\delta_{ij} - \tilde{\tau}_{ij} - \overline{\tau_{ij}''}\right] = 0 \quad \textbf{(2.37)}\right.$$

This equation has two complex terms, $\overline{\rho.u_i''.u_j''}$ and $\overline{\tau_{ij}''}$, that result from the averaging process and will have to be modelled. For steady flow conditions the equation becomes:

$$\frac{\partial}{\partial x_j}\left[\overline{\rho}.\tilde{u_i}.\tilde{u_j} + \frac{\partial}{\partial x_j}\left[\overline{\rho.u_i''.u_j''} + \overline{p}.\delta_{ij} - \tilde{\tau}_{ij} - \overline{\tau_{ij}''}\right] = 0 \quad (2.38)$$

2.4.3 Favre Averaged Conservation of Energy

The Favre Averaged Conservation of Energy equation can be obtained applying the same Favre decomposition to the time average conservation equation. However, in present work, the main objective from the use of energy equation is not to obtain the total energy in each point of the domain but in fact to determine the temperature field. Thus, some manipulations of the energy equation will be performed in order to obtain the temperature. Equations which establish the relation between temperature and enery and allow to obtain the temperature from the energy equation will be presented.

The total energy, here for a finite volume, is given by the sum of the internal energy and kinetic energy.

$$e_t = e + \frac{u_k.u_k}{2} \quad (2.39)$$

Enthalpy can be defined as the maximum heat content of a system, and it is equal to the sum of internal energy and the product of pressure with volume. Applied to a finite volume formulation is given by:

$$h = e + \frac{p}{\rho} \quad (2.40)$$

The variation of enthalpy for a given system can directly associated with the variation of temperature by means of the specific heat.

$$\Delta h = c_p.\Delta T \Leftrightarrow \Delta T = \frac{\Delta h}{c_p} \quad (2.41)$$

The time averaged energy equation can be written applying the time averaging to equation 2.9.

$$\frac{\partial}{\partial t}\left[\overline{\rho(e+\frac{u_k.u_k}{2})}\right]+\frac{\partial}{\partial x_j}\left[\overline{\rho u_j(e+\frac{u_k u_k}{2})+q_j+u_j.p-u_i.\tau_{ij}}\right]=0 \quad \textbf{(2.42)}$$

Multiplying and dividing the term $u_j.p$ by ρ, appears $\frac{p}{\rho}$.

$$\frac{\partial}{\partial t}\left[\overline{\rho(e+\frac{u_k.u_k}{2})}\right]+\frac{\partial}{\partial x_j}\left[\overline{\rho u_j(e+\frac{u_k u_k}{2})+q_j+\rho u_j.\frac{p}{\rho}-u_i.\tau_{ij}}\right]=0 \quad \textbf{(2.43)}$$

Combining this term with the internal energy, e.

$$\frac{\partial}{\partial t}\left[\overline{\rho(e+\frac{u_k.u_k}{2})}\right]+\frac{\partial}{\partial x_j}\left[\overline{\rho u_j\Big(\underbrace{e+\frac{p}{\rho}}_{h}+\frac{u_k u_k}{2}\Big)+q_j-u_i.\tau_{ij}}\right]=0 \quad \textbf{(2.44)}$$

From equation 2.40 this two terms are equal to enthalpy.

$$\frac{\partial}{\partial t}\left[\overline{\rho(e+\frac{u_k.u_k}{2})}\right]+\frac{\partial}{\partial x_j}\left[\overline{\rho u_j(h+\frac{u_k u_k}{2})+q_j-u_i.\tau_{ij}}\right]=0 \quad \textbf{(2.45)}$$

Employing now the Favre decomposition too all the terms of the previous equation together with some mathematical manipulation.

$$\begin{aligned}\frac{\partial}{\partial t}\left[\overline{\rho}(\tilde{e}+\frac{\tilde{u_k}.\tilde{u_k}}{2})\right]+\frac{\partial}{\partial x_j}\Big[&\overline{\rho}\tilde{u_j}\tilde{h}+\overline{\rho u_j''h''}+\frac{\overline{\rho}\tilde{u_j}\tilde{u_k}\tilde{u_k}}{2}+\frac{\tilde{u_j}\overline{\rho u_k''u_k''}}{2}+\tilde{u_k}\overline{\rho u_k''u_k''}\\&+\frac{\overline{\rho u_j''u_k''u_k''}}{2}+\tilde{q_j}+q_j''-\tilde{u_i}\tilde{\tau_{ij}}-\overline{u_i''\tau_{ij}}+\tilde{u_i}\overline{\tau_{ij}''}\Big]=0 \quad \textbf{(2.46)}\end{aligned}$$

Substituting enthalpy by the use of equation 2.41, and applying Fourier heat conduction law,

$$\begin{aligned}\frac{\partial}{\partial t}\left[\overline{\rho}(\tilde{e}+\frac{\tilde{u_k}.\tilde{u_k}}{2})\right]+\frac{\partial}{\partial x_j}\Big[&\overline{\rho}\tilde{u_j}\tilde{T}+\overline{\rho u_j''T''}+\frac{\overline{\rho}\tilde{u_j}\tilde{u_k}\tilde{u_k}}{2}+\frac{\tilde{u_j}\overline{\rho u_k''u_k''}}{2}+\tilde{u_k}\overline{\rho u_k''u_k''}\\&+\frac{\overline{\rho u_j''u_k''u_k''}}{2}+c_p\frac{\mu}{P_r}\frac{\partial\tilde{T}}{x_j}+c_p\frac{\mu}{P_r}\frac{\partial T''}{x_j}-\tilde{u_i}\tilde{\tau_{ij}}-\overline{u_i''\tau_{ij}}+\tilde{u_i}\overline{\tau_{ij}''}\Big]=0 \quad \textbf{(2.47)}\end{aligned}$$

In this equation a number of terms consisting on velocity and temperature fluctuations arose for which there is no direct solution. These terms represent the influence of turbulence on the flow and must be modelled. The modelling of such terms will depend on the method chosen for the treatment of turbulence which is reserved for the next section.
For the current case of study, the flow is assumed as steady, due to it the temporal term of equation can be neglected.

$$\frac{\partial}{\partial x_j}\Big[\overline{\rho}\tilde{u_j}\tilde{T} + \overline{\rho u_j'' T''} + \frac{\overline{\rho}\tilde{u_j}\tilde{u_k}\tilde{u_k}}{2} + \frac{\tilde{u_j}\overline{\rho u_k'' u_k''}}{2} + \tilde{u_k}\overline{\rho u_k'' u_k''} + \frac{\overline{\rho u_j'' u_k'' u_k''}}{2} + c_p\frac{\mu}{P_r}\frac{\partial \tilde{T}}{x_j} + c_p\frac{\mu}{P_r}\frac{\partial T''}{x_j} - \tilde{u_i}\tilde{\tau_{ij}} - \overline{u_i''\tau_{ij}} + \tilde{u_i}\overline{\tau_{ij}''}\Big] = 0 \quad (2.48)$$

2.5 Treatment of Turbulence

As was shown in the previous sections the time averaging process generates a number of fluctuation correlations which are not equal to zero. These terms can't also be neglected since they are responsible for the effects of turbulence in the flow, and, in order to find closure to the system of equation, they must be determined. Different strategies exist to find solution for these terms.
For the Reynolds Averaging of the equation of continuity and linear momentum only the correlations of velocity called Reynolds stresses, $\overline{u_i' u_j'}$, appear. Two main methodologies can be used to obtain solution for these terms as was already exemplified in Chapter 1. The Reynolds-stress models (RSM) solve a transport equation for the Reynolds stresses, this is a possible way to determine the Reynolds stresses, but not the only one. In the present work was instead used a much more common method, a turbulent-viscosity model. The objective is to associate the Reynolds stresses to some quantity of the mean flow. A quantity of the turbulent flows that is introduced is the turbulent kinetic energy, k, its mean value is defined to be half the trace of the Reynolds stresses tensor, $\overline{u_i' u_i'}$ [32].

$$\overline{k} = \frac{1}{2}\overline{u_i' u_i'} \quad (2.49)$$

According to the turbulent-viscosity hypothesis, the Reynolds stresses are given by

$$\overline{u_i' u_j'} = \frac{2}{3}\overline{k}\delta_{ij} - \mu_t\left(\frac{\partial \overline{u_i}}{\partial x_j} + \frac{\partial \overline{u_j}}{\partial x_i}\right) \quad (2.50)$$

In order for equations 2.49 and 2.50 to be used, the value of k must be known or estimated. Kolmogorov and Prandtl suggested achieving this by solving a model transport equation for k [32].

$$\frac{\partial \overline{k}}{t} + \frac{\partial \overline{u_i}\overline{k}}{x_i} = P_k - \overline{\varepsilon} + \frac{\partial}{\partial x_i}\left(\frac{\mu_t}{\sigma_k}\frac{\partial \overline{k}}{\partial x_i}\right) \quad (2.51)$$

In this equation P_k represents the production of turbulent kinetic energy which is given by

$$P_k = -\overline{u_i' u_j'}\frac{\partial \overline{u_j}}{x_i} = \mu_t\left(\frac{\partial \overline{u_i}}{\partial x_j} + \frac{\partial \overline{u_j}}{\partial x_i}\right)\frac{\partial \overline{u_i}}{\partial x_j} \quad (2.52)$$

ε is the dissipation of turbulent kinetic energy and σ_k is a model constant which must be given. Models that make use of the equation 2.51 are called the Turbulent-kinetic-energy models. Several of these models exist, the distinction between them is made by the way the turbulent viscosity, μ_t, and the dissipation, ε, are determined. For one equation model these quantities must be obtained by a relation with a lengthscale which has to be initially specified, usually depending on the kind of flow. Because of the need to specify a lenghtscale, one equation models are classified as incomplete.
For the current investigation the $k-\varepsilon$ model was used. This model belongs to a class of two-equations models, in which a model transport equation is solved not only for the turbulent kinetic energy, k, but also for its dissipation quantity , ε. For this model the turbulent viscosity is given by

$$\mu_t = C_\mu \frac{k^2}{\varepsilon} \quad (2.53)$$

Where C_μ is one of the five model constants. The dissipation is determined by the model transport equation

$$\frac{\partial \overline{\varepsilon}}{\partial t} + \frac{\partial \overline{u_i \varepsilon}}{\partial x_i} = \frac{\partial}{\partial x_i}\left(\frac{\mu_t}{\sigma_\varepsilon}\frac{\partial \overline{\varepsilon}}{\partial x_i}\right) + \frac{\overline{\varepsilon}}{\overline{k}}\left(C_{\varepsilon 1}P_k - C_{\varepsilon 2}\overline{\varepsilon}\right) \quad (2.54)$$

Observing the previous equation one can still notice the existence of unknown values. These are in fact model constants, their value is obtained empirically and, for the standard $k-\varepsilon$

Table 2.1: Model constants of the $k-\varepsilon$ turbulence model.

Model	C_μ	$C_{\varepsilon 1}$	$C_{\varepsilon 2}$	σ_k	σ_ε
Standard $k-\varepsilon$	0.09	1.44	1.92	1.0	1.3

model, these quantities are defined in table 2.1.
The $k-\varepsilon$ model is arguably the simplest complete turbulence model, is the most widely used, being incorporated in most commercial CFD codes. Its fatherhood is credited to Jones and Launder [60] in 1972 and has since then been developed and improved [32].

2.5.1 Modeling of favre fluctuation correlations

Having introduced the turbulence model which will be used in the present investigation, the unknown terms from the favre averaged linear momentum and energy equations can be modelled. Starting from the averaged equations 2.38 and 2.48 the unknown terms can be identified and numbered. Also, from equation 2.49, the term $\frac{\tilde{u_j}\overline{\rho u_k'' u_k''}}{2}$ in the energy equation 2.48 can be turned into $\overline{\rho}\tilde{u_j}\tilde{k}$.

$$\frac{\partial}{\partial x_j}\left[\overline{\rho}.\tilde{u_i}.\tilde{u_j} + \underbrace{\overline{\rho.u_i''.u_j''}}_{(1)} + \overline{p}.\delta_{ij} - \tilde{\tau_{ij}} - \underbrace{\overline{\tau_{ij}''}}_{(2)}\right] = 0 \quad \textbf{(2.55)}$$

$$\frac{\partial}{\partial x_j}\Big[\overline{\rho}.\tilde{u_j}.c_p.\tilde{T} + c_p.\underbrace{\overline{\rho.u_j''.T''}}_{(3)} + \frac{\overline{\rho}\tilde{u_j}\tilde{u_k}\tilde{u_k}}{2} + \overline{\rho}\tilde{u_j}\tilde{k} + \underbrace{\tilde{u_k}\overline{\rho u_j'' u_k''}}_{(4)} + \underbrace{\frac{\overline{\rho u_j'' u_k'' u_k''}}{2}}_{(5)}$$
$$+c_p\frac{\mu}{Pr}\frac{\partial\tilde{T}}{\partial x_j} + \underbrace{c_p\frac{\mu}{Pr}\frac{\partial T''}{\partial x_j}}_{(6)} - \tilde{u_i}\tilde{\tau_{ij}} - \underbrace{\overline{u_i''\tau_{ij}}}_{(7)} + \underbrace{\tilde{u_i}\overline{\tau_{ij}''}}_{(8)}\Big] = 0 \quad \textbf{(2.56)}$$

The terms (1) and (4) are obtained from the turbulent-viscosity hypothesis expressed in equation 2.50, here applied to the favre fluctuations.

$$\overline{\rho u_i'' u_j''} \approx \frac{2}{3}\rho\tilde{k}\delta_{ij} - \mu_t\Big(\frac{\partial\tilde{u_i}}{\partial x_j} + \frac{\partial\tilde{u_j}}{\partial x_i} - \frac{2}{3}\frac{\partial\tilde{u_k}}{\partial x_k}\delta_{ij}\Big) \quad \textbf{(2.57)}$$

Terms (2) and (8) can be neglected if $|\tilde{\tau_{ij}}| \gg |\overline{\tau_{ij}''}|$, and this is true to virtually all flows. Term (3), corresponding to turbulent transport of heat, can be modelled using a gradient approximation

for the turbulent heat-flux:

$$q_j^{turb} \equiv c_p \overline{\rho u_j'' T''} \approx -c_p \frac{\mu_t}{Pr_t} \frac{\partial \tilde{T}}{\partial x_j} \quad (2.58)$$

In equation 2.58 Pr_t is the turbulent Prandtl number, defined as constant in the present investigation, however, some authors [38] suggest its variability in the flow. Through out all the simulations performed in the present investigation the turbulent Prandtl number took the value of 0.7.

Terms (5) and (7), corresponding to turbulent transport and molecular diffusion of turbulent energy, can be neglected if the turbulent energy is small compared to the enthalpy, $k \ll \tilde{h}$. This is a reasonable approximation for most flows below the hyper-sonic regime. A better approximation might be a gradient expression of the form:

$$\frac{\overline{\rho u_j'' u_k'' u_k''}}{2} - \overline{u_i'' \tau_{ij}} \approx -\Big(\mu + \frac{\mu_t}{\sigma_k}\Big) \frac{\partial k}{\partial x_k} \quad (2.59)$$

Term (6) is an artefact from the Favre averaging. It is related to heat conduction effects associated with temperature fluctuations. It can be neglected if $\left|\frac{\partial^2 \bar{T}}{\partial x_j^2}\right| \ll \left|\frac{\partial^2 \overline{T''}}{\partial x_j^2}\right|$, which is also true for virtually all flows.

2.6 Governing Equations for the axisymmetric flow of study

The equations deduced in the previous sections constitute the theoretical base which supports the mathematical approach used in the present study. However, the present mathematical approach constitutes a modification to the variable density model for axisymmetric isothermal turbulent jets developed by Sanders [34] in 1997. Thus, the specific governing equations employed will be now described.

For the governing equation which will be solved numerically, the standard parabolic truncation is employed. The continuity equation for the axisymmetric two-dimensional geometry can be written in cylindrical polar coordinates, and is given by

$$\frac{\partial \overline{\rho}.\tilde{U}}{\partial x} + \frac{1}{r} \frac{\partial r \overline{\rho}.\tilde{V}}{\partial r} = 0 \quad (2.60)$$

The momentum equations for axial and radial direction take the form

$$\frac{\partial \overline{\rho}.\widetilde{UU}}{\partial x} + \frac{1}{r} \frac{\partial r \overline{\rho}.\widetilde{VU}}{\partial r} = -\frac{\partial \overline{p}}{\partial x} - \frac{1}{r} \frac{\partial r \overline{\rho}.\widetilde{u''v''}}{\partial r} \quad (2.61)$$

and

$$\frac{\partial \overline{\rho}.\widetilde{UV}}{\partial x} + \frac{1}{r}\frac{\partial r\overline{\rho}.\widetilde{VV}}{\partial r} = -\frac{\partial \overline{p}}{\partial x} - \frac{1}{r}\frac{\partial r\overline{\rho}.\widetilde{v''v''}}{\partial r} + \frac{\rho.\widetilde{w''w''}}{r} \quad (2.62)$$

The mixing of different fluids is described by introducing the scalar property of mixture fraction, F, this variable represents the mass fraction of the fluid at the injector. It obeys a convection-diffusion equation of the form

$$\frac{\partial \overline{\rho}.\widetilde{UF}}{\partial x} + \frac{1}{r}\frac{\partial r\overline{\rho}.\widetilde{VF}}{\partial r} = -\frac{1}{r}\frac{\partial r\overline{\rho}.\widetilde{v''f''}}{\partial r} \quad (2.63)$$

From the $k-\varepsilon$ model described in the previous section the Reynolds stresses from the favre averaging, equation 2.57, can be expressed in terms of the local strain rate:

$$-\overline{\rho}\widetilde{u_i''u_j''} = \overline{\rho}(\mu_t+\mu)\left(\frac{\partial \tilde{u_i}}{\partial x_j} + \frac{\partial \tilde{u_j}}{\partial x_i}\right) - \frac{2}{3}\delta_{ij}\left[\overline{\rho}\tilde{k} + \overline{\rho}(\mu_t+\mu)\frac{\partial \tilde{u_k}}{\partial x_k}\right] \quad (2.64)$$

Where the turbulent viscosity, μ_t, is obtained from equation 2.53. The scalar flux in equation 2.63 is approximated with a gradient transport assumption

$$-\overline{\rho}\widetilde{u_i''f''} = -\frac{\mu_f}{\sigma_f}\frac{\partial \overline{F}}{\partial x_i} \quad (2.65)$$

Finally, the generalized equation for the for the parabolized set of equation in cylindrical coordinates takes the form of

$$\frac{\partial}{\partial x}\left(\overline{\rho}.\tilde{U}\tilde{\phi}\right) + \frac{1}{r}\frac{\partial}{\partial r}\left(r\overline{\rho}.\tilde{V}\tilde{\phi}\right) = -\frac{1}{r}\frac{\partial}{\partial r}\left(r\overline{\rho}\Gamma\frac{\partial \tilde{\phi}}{\partial r}\right) + S_\phi \quad (2.66)$$

Where ϕ can stand for any of the velocities, turbulent kinetic energy, dissipation, or scalar property, and S_ϕ, which takes on different values for each particular $\tilde{\phi}$, is given in Table 2.2.
In Table 2.2 P_k is given by equation 2.52 and the buoyancy term, G, is neglected for the present study.
For the conservation of energy equation, since it didn't exist in the original model of Sanders

Table 2.2: Source terms in the generalized equation 2.66.

Variable	S_ϕ
k	$P_k + G + \overline{\rho}\varepsilon$
ε	$\frac{\varepsilon}{k}(C_{\varepsilon 1}(P_k + G) - C_{\varepsilon 2}\overline{\rho}\varepsilon)$

[34] it had to be implemented in the current model. To do so the deduced energy equation, 2.52, was adapted to cylindrical coordinated assuming a similar form to the generalized transport equation, 2.66, for the source terms were used exactly like described above in subsection 2.5.1.

2.7 Wall Treatment

Existence of solid walls strongly influence the behaviour of fluid flows, thus a special attention must be given in order to obtain good accuracy from modelling. At the wall, the boundary condition defines the tangential velocity as zero, this dictates that all Reynolds stresses are zero. Consequently, the wall shear stress is due entirely to the viscous contribution.

$$\tau_w \equiv \rho\mu\left(\frac{\overline{du}}{dy}\right)_{y=0} \quad (2.67)$$

The fact that viscous stress dominates the flow close to the wall contrasts to the situation in free shear flow. There, at high Reynolds number, the viscous stresses are everywhere negligibly small compared with the Reynolds stresses [32]. The higher prevalence of the viscous stress near to the wall leads to a very small local Reynolds number, this becomes an issue for the $k-\varepsilon$ model which, due to its limitations, is better fitted for high Reynolds number flows. Both this fact and steep variation of properties near walls arise the need of a dedicated calculation method.

It is evident that close to the wall the viscosity μ and the wall shear stress τ_w are important parameters. From these quantities (and ρ) viscous scales can be defined, which are the appropriate velocity scaled and lengthscales in the near-wall region. These are the friction velocity

$$u_\tau \equiv \sqrt{\frac{\tau_w}{\rho}} \quad (2.68)$$

and the viscous lengthscale

$$\delta_\tau \equiv \mu\sqrt{\frac{\tau_w}{\rho}} = \frac{\mu}{u_\tau} \quad (2.69)$$

The Reynolds number based on the viscous scale $u_\tau\delta_\mu/\mu$ is identically unity, while the friction Reynolds number is defined by

$$Re_\tau \equiv \frac{u_\tau\delta}{\mu} = \frac{\delta}{\delta_\mu} \quad (2.70)$$

The distance from the wall measured in viscous lengths is denoted by

$$y^+ \equiv \frac{y}{\delta_\mu} = \frac{u_\tau y}{\mu} \quad (2.71)$$

2.7.1 The Law of the Wall

Based on the previous relations a dimensionless velocity, u^+, can be defined based on the friction velocity, u_τ,

$$u^+ \equiv \frac{\overline{u}}{u_\tau} \quad (2.72)$$

The law of the wall describes the dimensionless velocity as function of the distance from the wall measures in viscous lengths y^+

$$u^+ = f_w(y^+) \quad (2.73)$$

The question that arises is what function to use. The near-wall space can be divided in several regions and layers where the flow will show different behaviour. The inner layer, $y/\delta < 0.1$, where the mean velocity is determined by u_τ and y^+, and the outer layer, $y^+ > 50$, where the direct effects of viscosity on $\overline{u}$ are negligible. The inner layer can itself be divided in three regions, the viscous sublayer, $y^+ < 5$, the buffer layer, $5 < y^+ < 30$, and the log-law region, $y^+ > 30$.
In the viscous sublayer the Reynolds shear stress is negligible compared with the viscous stress, this region is dominated by viscosity and the flow is almost laminar, for this region a linear relation is used.

$$u^+ = y^+ \qquad \text{for } y^+ \leq 11.63 \quad (2.74)$$

The departures from the linear relation are negligible in the viscous sublayer, but become significant (greater than 25 %) for $y^+ > 12$. For the log-law region where the flow is dominated by turbulence the velocity is given by a logarithmic relation.

$$u^+ = \frac{1}{K} \ln y^+ + B \qquad \text{for } y^+ > 11.63 \quad (2.75)$$

K=0.4187, is the von Karman constant and B is given by

$$B \equiv \frac{1}{K} \ln \left(E y^+ \right) \quad (2.76)$$

Where in the present model E=9.793, represent the roughness and shear stress variation.

The buffer layer, which is the transition region between the viscosity-dominated and the turbulence-dominated parts of the flow, is in this approach divided by the two other regions. For the y^+ of division between the two other regions is taken the value of 11.63 that was already presented in equations 2.74 and 2.75.

2.7.2 Law of the Wall for Scalar Transport

The same treatment can be extended for other scalar variables, here for example the temperature, T:

$$T^+ = \sigma_\phi y^+ \qquad \text{for } y^+ \leq 11.63 \quad (2.77)$$

and,

$$T^+ = \frac{\sigma_{\phi,t}}{K} \ln y^+ + c_T\left(\sigma_\phi\right) \qquad \text{for } y^+ > 11.63 \quad (2.78)$$

Where,

$$\sigma_\phi = Pr = \frac{c_p \mu}{\lambda}, \quad (2.79)$$

$$c_T(\sigma_\phi) \equiv \sigma_{\phi,t}\left[u^+ + P\Big(\frac{\sigma_\phi}{\sigma_{\phi,t}}\Big)\right], \quad (2.80)$$

$$T^+ = \frac{\rho u_\tau c_p (T_w - T)}{\dot{q}''_w}, \quad (2.81)$$

$$\frac{\dot{q}''}{\dot{q}''_w} = \left(\frac{\Gamma}{\mu} + \frac{\Gamma_t}{\mu_t}\right)\frac{dT^+}{dy^+}, \quad (2.82)$$

and,

$$\dot{q}''(\Gamma + \Gamma_t) c_p \frac{dT}{dy}, \quad (2.83)$$

Finally, $\sigma_{\phi,t}$ is, for the case of temperature, the turbulent Prandtl number and the P-function for impermeable, smooth walls is:

$$P\left(\frac{\sigma_\phi}{\sigma_{\phi,t}}\right) \cong 9.24\left[\left(\frac{\sigma_\phi}{\sigma_{\phi,t}}\right)^{3/4} + 1\right] \quad (2.84)$$

2.7.3 Wall treatment for k and ε equations

The approach adopted for the treatment of k and ε is strictly valid only for the inertial sublayer where the flow is assumed to be completely turbulent: $y^+ > 30$, but sufficiently close to the wall so that the assumption of constant shear stress applies ($y^+ < 400$). In this region, the local rate of production of turbulence is balanced by the viscous dissipation rate ε. This local equilibrium forms the main basis for our wall treatment.
The turbulence energy equation reduces to a simple form that yields expression for both the

shear stress $\tau_I (\cong \tau_w)$ and the dissipation rate ε within the inertial sublayer.

$$k = \frac{\frac{\tau_I}{\rho}}{C_\mu^{1/2}} \quad (2.85)$$

$$\varepsilon^{++} = \frac{C_\mu^{3/4} K^{3/2}}{Ky} \quad (2.86)$$

The ε-equation reduces to a form which indicates modification of σ_ε for this region.

$$C_1 = C_2 - \frac{K^2}{\sigma_\varepsilon C_\mu^{1/2}} \quad (2.87)$$

Thus,

$$\sigma_\varepsilon = \frac{K^2}{\left(C_2 - C_1\right) C_\mu^{1/2}} \quad (2.88)$$

More details over the specificities of the wall treatment employed in the present work can be found in the TEACH-T computer program documentation.

Chapter 3

Real Fluid Thermodynamics

3.1 Introduction

In Chapter 1 was given a great amount of importance to the highly transient nature of the physical properties of fluids at conditions around the thermodynamic critical point. In order to correctly address jet flows at the conditions intended for the present, work the used model must be able to make use of values of properties which are the closest possible to the real value for those conditions. The properties of interest for the study of transcritical and supercritical fluids are the density, ρ, viscosity, μ, specific heat at constant pressure, c_p, and thermal conductivity, λ. These are the thermodynamic properties which are directly used by the several governing equations deduced in the previous chapter, and for which a value must be attributed in order to perform the calculations of the flow field. For relatively simpler models these properties are assumed as constant over all the domain of study, and so, just one value is taken in the beginning of the calculation and not changed during the course of it. This is in fact a valid assumption for a large range of flows. Incompressible, isothermal, and single-specie flows are a kind of flows for which all these properties can be taken as constants without inducing relevant errors to the calculations. This isn't however the case for the present conditions of study. Thus an effort must be made in order to approximate the value used in calculation the closest possible to the reality. And, as the flow characteristics change not only along the domain but also during the course of the calculation procedure, the value of these properties should be actualized by means of models dependent on the flows variables.
Under a determined set of thermodynamic conditions, gases can be treated in a simplified manner, as ideal gases. This is valid, as was shown in Figure 1.1 of Chapter 1, for pressures bellow the critical point and temperatures above the critical point. For most common gases of atmosphere this happens at conditions around the standard temperature and pressure, STP. STP conditions are established as a temperature of 273.15 K and an absolute pressure of 100 kPa. The present investigation intends to study conditions around the thermodynamic critical point, in Table 3.1, which shows the critical values of temperature and pressure for nitrogen, we can see that these values are very far from STP conditions. As a consequence, the employment of ideal gas thermodynamics to the present approach can be proved to be inadequate, as it will be shown next. For this, real fluid thermodynamics, which are expected to be valid over a larger range of conditions is preferred for the studied problematic. The current chapter will be focused on the employment of real fluid thermodynamics to the model as well as explaining the flaws which could emerge from the use of a simpler ideal gas hypothesis.

3.2 Equation of State

The first property to focus on is the fluid density. Obtaining a correct value of this property is essential since it plays a key role in all the conservation equations. When the problematic of study doesn't allow to set the density as constant, a technique must be employed to obtain its

Table 3.1: Physical Properties of Nitrogen.

Nitrogen, N_2			
M_n	Molar Mass	28.01348	$g.mol^{-1}$
p_c	Critical Pressure	3.3958	MPa
T_c	Critical Temperature	126.192	K
ρ_c	Critical Pressure	3.3958	$mol.dm^{-3}$

correct values, employing an equation of state is very often the procedure to take. An equation of state is a thermodynamic equation which relates several state variables such as pressure, p, temperature, T, volume, $\vee$, or amount of substance, n. By the use of an equation of state, the density is possible to be obtained as long as pressure and temperature are known variables.
In the present work several equations of state were tested and employed in the modelling with the objective of testing which one appears to perform better.

3.2.1 Amagat's law

The original mathematical approach from which the used model is based on, determines the mean density directly from the mean mixture fraction using the following equation of state:

$$\frac{1}{\overline{\rho}} = \frac{F}{\rho_0} + \frac{1-F}{\rho_\infty} \quad (3.1)$$

This equation of state is based on the Amagat's law which describes the properties of mixtures of ideal gases. The equation is only valid for constant pressure and temperature. It is allowed in isothermal jets because the instantaneous density, for which the equation is exact, is approximately a linear function of the instantaneous mixture fraction [34].
Previous investigations [7], [8] proved this equation of state to be able to provide quite good agreement with experimental data. However, limitations to this equation of state can be easily recognized. For instance, the heat exchange between the jet fluid and the chamber fluid, and its resulting variation of density are neglected. Also, with this equation of state is not taken into account the thermodynamic singularity represented by the critical point. As referred in Chapter 1, at conditions around critical point fluid properties suffer vigorous changes which must be addressed in order to provide a realistic approach to the objective of study. To reach this objective, an equation of state should be able to reflect to the value of density changes of pressure and temperature.
Even with the limitations concluded above, in the present work attention was also given to the approach which employs this equation of state. As said previously good agreement was found in the past, thus, the first approach in the present work was made exactly with this equation, as a mean of comparison with following approaches, and also to conclude if the assumption of

gaseous isothermal jet would be reasonable until some extent.

3.2.2 Ideal gas law

An ideal gas is a theoretical gas in which its molecules don't suffer forces of attraction or repulsion between each other. Interactions between molecules are neglected with the exception of elastic collision. Also, in an ideal gas de volume of molecules is neglected when compared with the volume of the container. Despite in nature nothing truly behaving like an ideal gas, the variations from its behaviour can be neglected in calculations for a reasonable range of temperatures and pressures [61]. The ideal gas concept obeys to the ideal gas law, a simplified equation of state which correlates four different fluid properties, pressure, p, temperature, T, volume, V, or amount of substance, n. This equation of state includes also a gas constant, $R = 8.314472 J.K^{-}1.mol^{-}1$.

$$PV = nRT \quad (3.2)$$

Multiplying this equation by molar mass, M_n, mass can appear in the equation,

$$PVM_n = nM_nRT \Rightarrow P \vee M_n = mRT \quad (3.3)$$

Finally, density, ρ, can be given by,

$$\rho = \frac{PM_n}{RT} \quad (3.4)$$

Equation 3.4 allows the determination of density for different values of pressure and temperature. Unlike equation 3.1, it is not limited to conditions of constant pressure and temperature. However, as said above, this equation of state relies on a theory which is not valid for all values of pressure and temperature, but instead to a reasonable, but limited, range of STP conditions. Conditions in the present investigation are far from STP and as shown in Figure 3.1, the ideal gas equation of state fails to predict the correct value of nitrogen density for temperatures below 200 K at pressures ranging from 3.0 to 5.0 MPa when compared with experimental data [62]. This proves that for the conditions of study, the employment of an ideal gas equation of state would provide incorrect values of density. Since the ideal gas equation of state is found not to be suitable for usage at the current work conditions, a different equation of state, which is able to provide good results of density around the critical point and at supercritical conditions, must be employed.

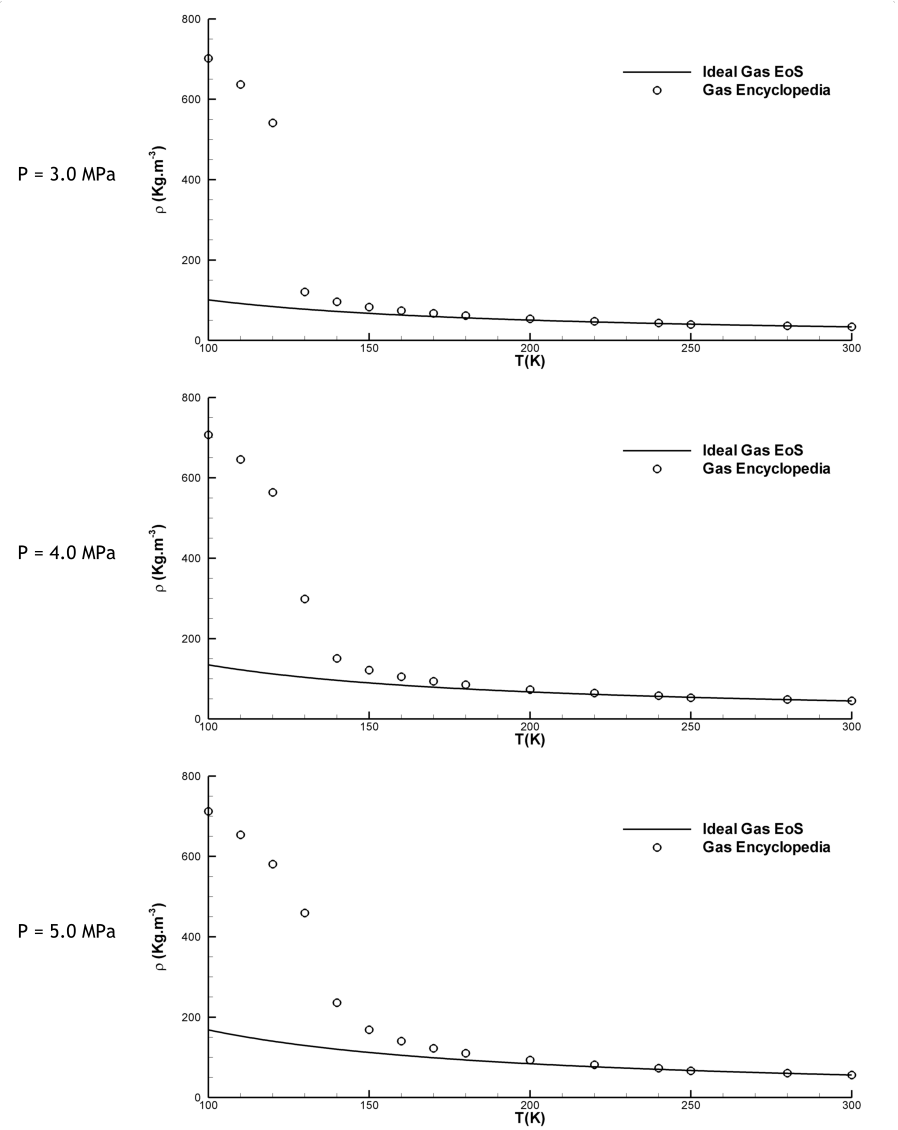

Figure 3.1: Nitrogen Density comparison of Ideal Gas Equation of State with data from Gas Encyclopedia [62] for a range of temperature at 3.0, 4.0, and 5.0 MPa.

3.2.3 Real fluid equation of state

To study with precision real gases, some modifications to the ideal gas equation are required in order to take into account intermolecular forces as well as the finite volume of molecules. This kind of analysis was done for the first time in 1873 by J.D. van der Waals. Van der Waals suggested that the pressure exerted by an ideal gas, P_{ideal}, was related with the pressure measured by experimental means, P_{real}.

$$P_{ideal} = P_{real} + \frac{an^2}{V^2} \quad (3.5)$$

Where the correction term a is a proportionality constant. The correction term can be explained by the fact that the interaction of molecules which leads to the departure from the ideal

behaviour, depends of the frequency on which to molecules approach each other. The amount of encounters increases with the square of the number of molecules per unit of volume. The ideal pressure, P_{ideal}, is the pressure which would be measured if no intermolecular attractions existed.
Another proposed correction concerns the volume occupied by the gas molecules. The quantity of V, in the ideal gas equation, represents the container 's volume. However, while very small, each individual molecule occupies its own finite volume. So the effective gas volume becomes equal to $V - nb$, where b is a constant as well. The term nb represents the volume occupied by n molecules of gas. Adding these corrections to the ideal gas equation of state, 3.2, one obtains the van der Waals equation of state:

$$\left(P + \frac{an^2}{V^2}\right)(V - nb) = nRT \quad (3.6)$$

The van der Waals constants a and b are chosen for each gas in a manner to obtain the best possible agreement between the equation 3.6 and the behaviour of that gas in particular [61]. This formula revolutionized the study of equations of state, and while its modelling of real fluid behaviour is not sufficient for many applications, it opened the path for the appearance of new, cubic, equations of state like for example the Redlich-Kwong equation of state of 1949 [63]. Directly based on the van der Walls formulation, this is a two-parameters equation, which, besides being essentially empirical, was generally recognized as holding a good degree of accuracy for calculation of volumetric and thermal properties of pure compounds and of mixtures [52]. This equation, as proposed originally by Otto Redlich and Joseph Kwong in 1949, has the following formulation [63].

$$P = \frac{RT}{V_m - b} - \frac{a}{\sqrt{T}V_m(V_m + b)} \quad (3.7)$$

Here V_m stands for molar volume. The constants a and b are different depending on which gas is being analysed and are calculated from the critical point of gases,

$$a = 0.4278\frac{R^2T_c^{2.5}}{P_c}, \quad (3.8)$$

$$b = 0.0867\frac{RT_c}{P_c} \quad (3.9)$$

In order to obtain the density from equation 3.7, it has to assume a different form. The Redlich-Kwong equation of state can be represented in order to the compressibility factor, Z:

$$Z = \frac{1}{1-H} - \frac{A^2}{B}\frac{H}{1-H} \quad (3.10)$$

Where,

$$A^2 = \frac{a}{R^2 T^{2.5}}, \quad (3.11)$$

$$B = \frac{b}{RT} \quad (3.12)$$

and,

$$H = \frac{BP}{Z} \quad (3.13)$$

This form of the equation of state only gives the compressibility factor, Z, as function of pressure, P, and temperature, T, in an implicit way, however the equation can be easily solved numerically or by graphical interpolation.
The compressibility factor, Z, can be defined as the ratio between the molar volume of a gas and the molar volume of an ideal gas at the same pressure and temperature. It indicates the degree to which a gas deviates from the ideal gas behaviour [64]. For an ideal gas the compressibility factor takes the value of 1. The compressibility factor can also be expressed in the following way:

$$Z = \frac{PV_m}{RT} \quad (3.14)$$

From this equation the value of density can now be obtaining with a small modification using the definition of molar volume, $V_m = M_n/\rho$,

$$Z = \frac{PM_n}{RT\rho} \Rightarrow \rho = \frac{PM_n}{RTZ} \quad (3.15)$$

Since its introduction in 1949 the Redlich-Kwong equation of state was considered one of the

most successful equations of state originating, since that time, numerous modified formulations based on it [51]. In the present work a modified version of this equation was employed and tested.

3.2.4 Soave-Redlich-Kwong Equation of State

Giorgio Soave introduced in 1972 a modification of the Redlich-Kwong equation of state with the objective of obtaining a closer reproduction of vapour pressures of pure compounds. The modification consisted on assuming the parameter a in the original equation as temperature dependent. For this, the $a/\sqrt{T}$ term in the original equation, 3.7, has been replaced by a more general temperature dependent term $a(T)$. The Soave-Readlich-Kwong equation of state assumes the following shape,

$$P = \frac{RT}{V_m - b} - \frac{a(T)}{V_m(V_m + b)} \quad (3.16)$$

Where the parameter $a(T)$ is given by the multiplication of the parameter at the critical point, $a_c = a(T_c)$, and a non-dimensional factor, $\alpha(T)$, which corrects the value of $a(T)$ for other temperatures different from critical.

$$a(T) = a_c.\alpha(T) \quad (3.17)$$

The term a_c is calculated from the critical values of pressure and temperature,

$$a_c = 0.42747\frac{R^2T_c^2}{P_c} \quad (3.18)$$

As well as the parameter b,

$$b = b_c = 0.08664\frac{R^2T_c^2}{P_c} \quad (3.19)$$

The non-dimensional factor $\alpha(T)$ is given by,

$$\alpha(T) = \left(1 + (0.480 + 1.574\omega + 0.176\omega^2).(1 - \sqrt{T_r})\right)^2 \quad (3.20)$$

Where ω is the acentric factor of the substance, the acentric factor can be defined as a measure of the non-sphericity of the molecules which compose the substance. T_r is the reduced temperature and is given by,

$$T_r = \frac{T}{T_c} \quad (3.21)$$

Like the original Redlich-Kwong equation of state, this Soave's modification can also be written in terms of the compressibility factor:

$$Z^3 - Z^2 + Z(A - B - B^2) - AB = 0 \quad (3.22)$$

With,

$$A = \frac{\alpha(T)P}{R^2T^2} \quad (3.23)$$

and,

$$B = \frac{bP}{RT} \quad (3.24)$$

Equation 3.22 is a cubic polynomial, to obtain the compressibility factor, Z, the roots of the polynomial must be found. Being of degree 3 it will result in one or three different results for Z. From the three possible solutions only one will represent a physically realistic value of density, will be this value the selected one. The density is obtained from the compressibility factor by application of equation 3.15, exactly the same way as for the original Redlich-Kwong equation of state.

3.2.5 Peng-Robinson Equation of State

Another formulation based on the van der Waals equation of state was introduced in 1976 by Ding-Yo Peng and Donald B. Robison through modification of the attraction pressure term [51]. This equation of state was created with four main goals in mind, that the parameters of equation should be expressed only in terms of the critical properties and the accentric factor, the model should provide reasonable accuracy for the critical point, mixing rules should be only dependent on one binary parameter, and that the equation should be applicable to all calculations of all fluid properties in natural gas processes.
The equation of state was also design to keep the same level of simplicity of the Soave-Redlich-K-

wong equation of state, while providing satisfactory density values for the liquid phase, as this was, in the author's opinion, the biggest handicap of the SRK equation of state [51]. The result was a formulation in many ways resembling the Soave-Redlich-Kwong equation of state,

$$P = \frac{RT}{V_m - b} - \frac{a(T)}{V_m(V_m + b) + b(V_m - b)} \quad \textbf{(3.25)}$$

The equation parameters are calculated in a very similar way to the one found for the Soave-Redlich-Kwong equation of state,

$$a(T) = a(T_c).\alpha(T) \quad \textbf{(3.26)}$$

With,

$$a(T_c) = 0.45724\frac{R^2T_c^2}{P_c}, \quad \textbf{(3.27)}$$

$$\alpha(T) = \left(1 + (0.37464 + 1.54226\omega - 0.26992\omega^2).(1 - \sqrt{T_r})\right)^2 \quad \textbf{(3.28)}$$

and,

$$b = b_c = 0.07780\frac{R^2T_c^2}{P_c}. \quad \textbf{(3.29)}$$

Once again, this equation of state can also be rewritten in terms of the compressibility factor:

$$Z^3 - (1 - B)Z^2 + (A - 2B - 3B^2)Z - (AB - B^2 - B^3) = 0 \quad \textbf{(3.30)}$$

With the A and B parameters having exactly the same formulation proposed in the Soave-Redlich-Kwong equation of state - equations 3.23 and 3.24. Like before, the equation 3.30 yields one or three roots depending upon the number of phases in the system. In the two-phase region, the largest root is for the compressibility factor of the vapour while the smallest positive root corresponds to that of the liquid [51]. Density can then be obtained from equation 3.15.

3.2.6 Equation of state comparison

In order to select the best suited equation of state for the conditions of study they must be compared against experimental data. Figures 3.2, 3.3, and 3.4 show the variation of the density value along a range of temperatures between 100K and 200K, for the pressures of 3, 4, and 5 MPa respectively. In the figures the Soave-Redlich-Kwong equation of state together with the Peng-Robinson equation are compared against the experimental data provided by the Gas Encyclopaedia [62]. The results from the ideal gas equation of state are once more presented just as reference.

Looking to Figure 3.2, with a pressure of 3 MPa, and analyzing from the highest to the lowest temperature, it can be observed that from 300K to 200K all equations of state are able to provide good results of density. Below 200K the ideal gas equation is no longer able to predict the density values. The two real fluid equations of state present similar results, both in very good agreement with the experimental data until a temperature of 130K. Bellow this mark the Peng-Robinson (PR) is able to provide better result at 120K, but lower that this is the Soave-Redlich-Kwong (SRK) which shows better agreement.

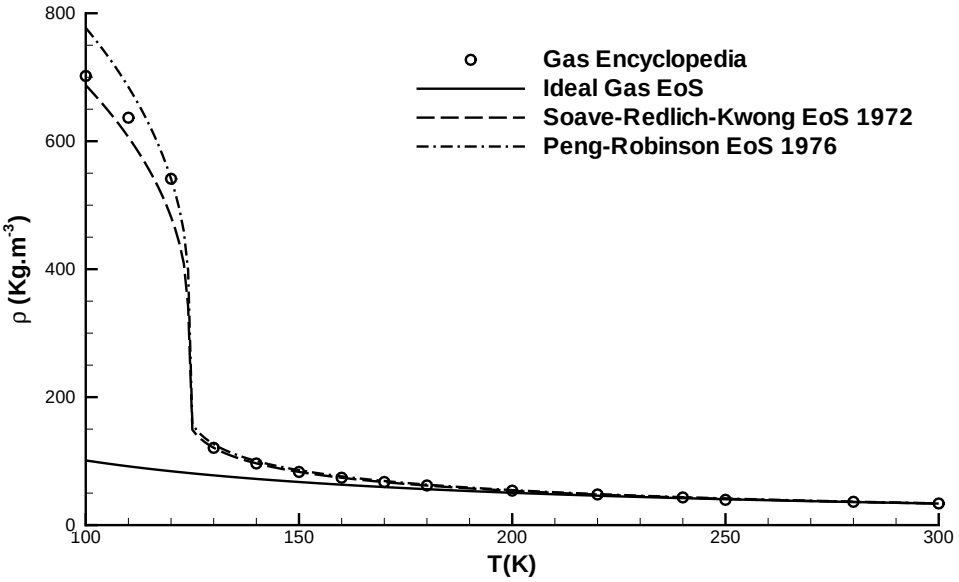

Figure 3.2: Comparison of the performance of the Ideal Gas, Soave-Redlich-Kwong, and Peng-Robinson equations of state for a pressure of 3 MPa.

Similar conclusion can be taken in Figure 3.3 at a pressure of 4MPa. From 300K to 200K all equations provide good predictions. From 200K to 130K both SRK and PR equation provide very similar results. The differences appear bellow 130K with PR equation being more accurate until 120K and bellow this the SRK can in fact provide a closer agreement.

Figure 3.4 shows similar results, for a pressure of 5 MPa. In this case the departure between the two real fluid equations of state starts a little bit earlier (when analysing from high to low temperatures) at 140K. Again the PR is more accurate until 120K and bellow this the agreement with SRK is better.

For the present work the temperatures of interest range between 126.9K and 298K. For this range of temperatures, the Peng-Robinson equation of state is indeed able to provide better accuracy, as demonstrated by the Figures 3.2 to 3.4, being this way the obvious choice for the model.

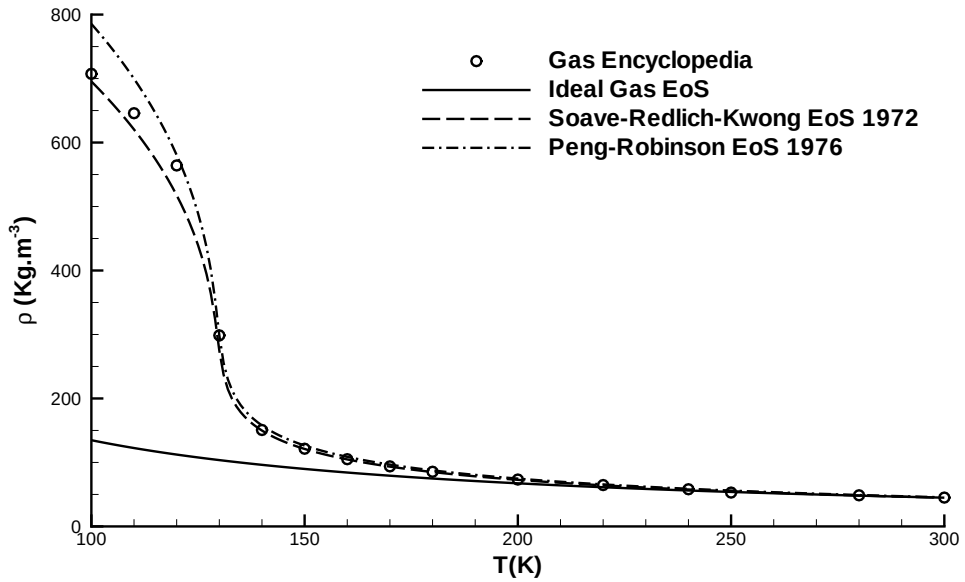

Figure 3.3: Comparison of the performance of the Ideal Gas, Soave-Redlich-Kwong, and Peng-Robinson equations of state for a pressure of 4 MPa.

3.3 Determination of Viscosity

The viscosity of a fluid is a property used to describe the response of a fluid to the imposed shearing forces [56]. The correct determination of the viscosity, μ, is of great interest since it intervenes in the conservation equations of momentum and energy. A formulation which would allow to obtain the viscosity through the state variable pressure, p, and temperature, T, analogously to the equation of state would be ideal. However, very often, more simplistic methods are employed. In the present section the several distinct approaches used to obtain the value of viscosity will be present.

3.3.1 Assumption of Viscosity as constant

The most simplistic method to treat the viscosity is by the assumption of a constant value. This is the approach followed in the model proposed by Sanders [34] and also the first methodology used in the present work. This approach is justified by Sanders from the fact that the flow is assumed as an isothermal jet. However, as it happens with density, also the viscosity suffers variations with pressure and temperature. In order to cope with such variation different approaches are tested and employed in the present work.

3.3.2 Sutherland's law

Perhaps the most commonly used relation for dilute gases is the Sutherland's law, which was published by William Sutherland in 1893, and establishes the relation between the dynamic viscosity, μ, and the temperature, T. The relation is expressed by the following formulation [56].

$$\mu = c_1 \frac{T^{3/2}}{T + c_2} \quad (3.31)$$

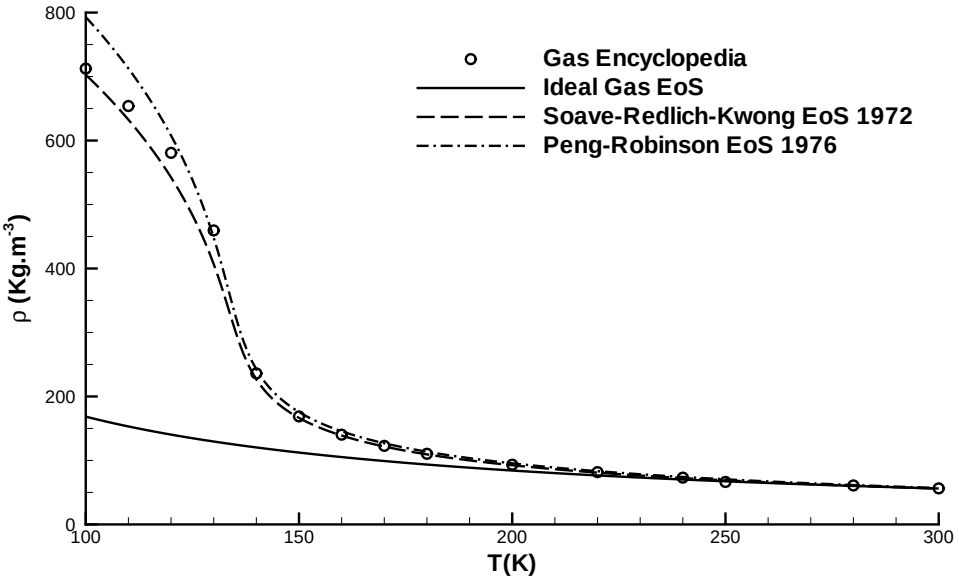

Figure 3.4: Comparison of the performance of the Ideal Gas, Soave-Redlich-Kwong, and Peng-Robinson equations of state for a pressure of 5 MPa.

Where c_1 and c_2 are constants which depend on the substance, for gaseous Nitrogen they take the values of, $c_1 = 1.390 \times 10^{-6} kg.sec^{-1}.m^{-1}.K^{-1/2}$ and $c_2 = 102.0K$. However, this relation is only valid for ideal gases, and as shown in Figure 3.5 the equation loses the ability to provide accurate results of viscosity as the temperature decreases and pressure increases. Showing poorer agreement with the data from a pressure of 5 MPa and total inability to predict the viscosity for temperatures below 150K at the analysed pressures. Another argument against the Sutherland's law is that it doesn't provide any relation with pressure, however, as can be seen in Figure 3.5, pressure does influence the value of viscosity when at lower temperatures. Until recently, no single functional relation $\mu = \mu(p, T)$ existed which could describe any large class of fluids. Thus, typically, a set of tables and/or charts where used to determine the appropriate value of viscosity at a given pressure and temperature [56].

3.3.3 Determination of Viscosity from experimental data

As said above another way to obtain the value of viscosity is by the interpolation of values given by experimental measurements. In the present work data from the Gas Encyclopaedia [62] was used to generate a linear function defined by parts which tries to fit in a simplistic way the existent experimental data.

$$\mu(T) = \begin{cases} -1.2768 \times 10^{-6}.T + 2.04 \times 10^{-4}, & T < 150 \\ \\ 4.12 \times 10^{-6}.T + 6.14 \times 10^{-6}, & T \geq 150 \end{cases} \tag{3.32}$$

This set of functions provide closer agreement with experimental data for a pressure of 4 MPa

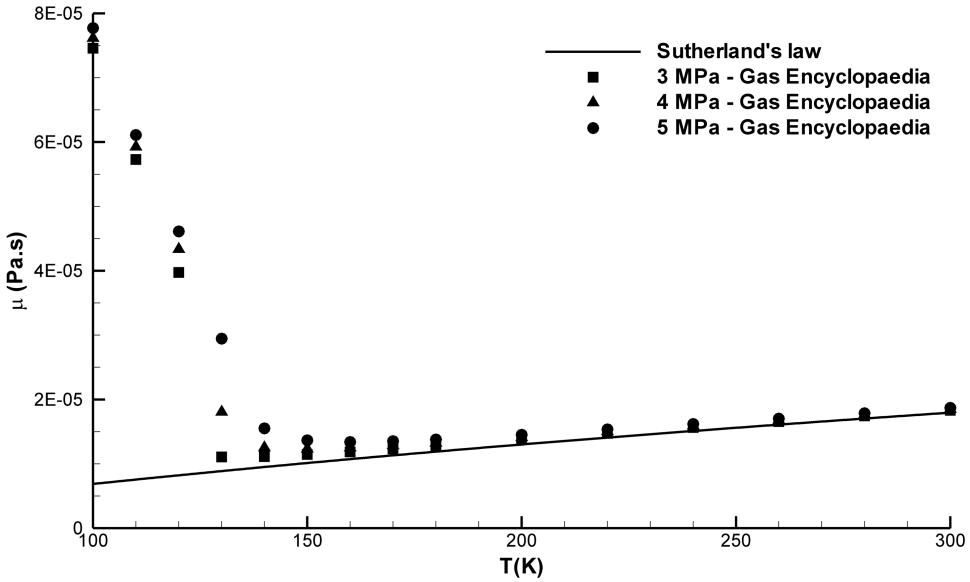

Figure 3.5: Comparison of the Sutherland's law performance with the experimental data for 3, 4, and 5 MPa.

than the Sutherland's law, as can be seen by Figure 3.6.

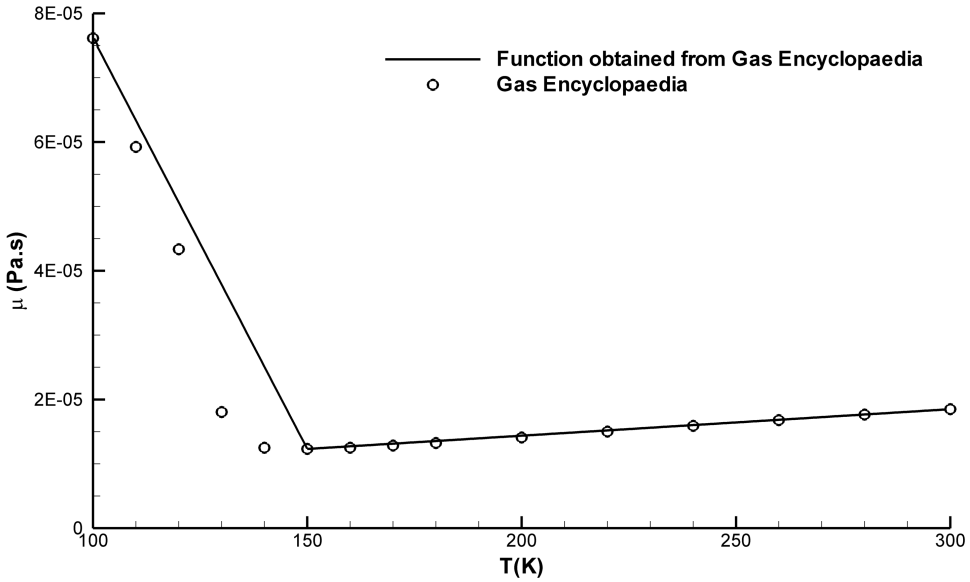

Figure 3.6: Comparison between data from Gas Encyclopaedia and the function by parts obtained from it for a pressure of 4 MPa.

Still, the determination of viscosity doesn't offer the desired agreement for temperatures below 150K, also, this presents itself as a less elegant solution then a single function which could provide the values of viscosity for several classes of fluids at different conditions.

3.3.4 Real fluid equation for viscosity

A new formulation that allows the determination of not only the viscosity but also the thermal conductivity of Nitrogen, Oxygen, Argon, and Air was proposed more recently by Lemmon and

Jacobsen [65]. According to the authors, these equations are valid over all liquid and vapour states, and the uncertainties of calculated values from the equations are generally within 2% for nitrogen. These equations constitute the base of the REFPROP 7.1 software from the National Institute of Standards and Technology, NIST. The viscosity of nitrogen, argon, oxygen, and air are expressed by the following equation.

$$\mu = \mu^0(T) + \mu^r(\tau, \delta) \quad (3.33)$$

Where the viscosity, μ, is given in $\mu Pa.s$, μ^0 is the dilute gas viscosity, μ^r is the residual fluid viscosity, $\tau = T_c/T$, and $\delta = \rho/\rho_c$. The critical parameters T_c and ρ_c are given in Table 3.1. Since the effects of the critical region behaviour on viscosity are, according to the authors, negligible for most of the practical states, no enhancement for the critical region viscosity was used in this formulation. The dilute gas contribution is given by

$$\mu^0 = \frac{0.0266958\sqrt{M_n T}}{\sigma^2 \Omega(T^*)}, \quad (3.34)$$

where σ is the Lennar-Jones size parameter and Ω is the collision integral, given by

$$\Omega(T^*) = \exp\left(\sum_{i=0}^{4} b_i \big[\ln(T^*)\big]^i\right), \quad (3.35)$$

where $T^* = T/(\varepsilon/k)$ and ε/k is the Lennard-Jones energy parameter. The Lennard-Jones parameters are given in Table 3.2, and the coefficients b_i (fitted in this work to the experimental data) are given in Table 3.3. The residual fluid contribution to the viscosity is given (in $\mu Pa.s$) by

$$\mu^r(\tau, \delta) = \sum_{i=1}^{n} N_i \tau^{t_i} \delta^{d_i} \exp\big(-\gamma_i \delta^{l_i}\big), \quad (3.36)$$

where γ_i is zero when l_i is zero and one when l_i is not zero. The coefficients and exponents of this equation are given in Table 3.4 [66].

Figures 3.7, 3.8, and 3.9 show the performance of this formulation for the pressures of respectively 3, 4, and 5 MPa, in a set of temperatures ranging from 100 to 300K. The viscosities were calculated both with the Peng-Robinson and the Soave-Redlich-Kwong equations of state. Calculations were compared with the data from Gas Encyclopaedia [62]. The results clearly show much better agreement with the experimental data that any of the previous methodologies

Table 3.2: Parameters of the Viscosity and Thermal Conductivity Equations for N2 [66].

Nitrogen, N_2			
ε/k	Lennard-Jones energy parameter	98.94	K
σ	Lennard-Jones size parameter	0.3656	nm
ξ_0	Constant for correlation length	0.17	nm
Γ	Constant for correlation length	0.055	
q_D	Constant for correlation length	0.40	nm
T_{ref}	Reference temperature	252.384	K

Table 3.3: Coefficients of the Collision Integral Equation [66].

i	b_i
0	0.431
1	-0.4623
2	0.08406
3	0.005341
4	-0.00331

Table 3.4: Coefficients of the Collision Integral Equation [66].

i	N_i	t_i	d_i	l_i
1	10.72	0.1	2	0
2	0.03989	0.25	10	1
3	0.001208	3.2	12	1
4	-7.402	0.9	2	2
5	4.620	0.3	1	3

used for the determination of viscosity. Moreover, by including in the equations the value of density, this formulation clearly takes into consideration the effects of pressure into the value of viscosity and not only the temperature like it happened with the Sutherland's law. By depending on the value of density this formulation depends also on the choice of the equation of state employed. The Figures 3.7 to 3.8 show distinct variations of the viscosity values depending on if was used the SRK or the PR equations of state to calculate the density. Curiously, the results obtained by the use of the Soave-Redlich-Kwong equation of state seem to be more accurate than the ones obtained with the Peng-Robison equation. The Lemmon-Jacobsen formulation also presents equations for the calculation of thermal conductivity, which will be treated in the next section.

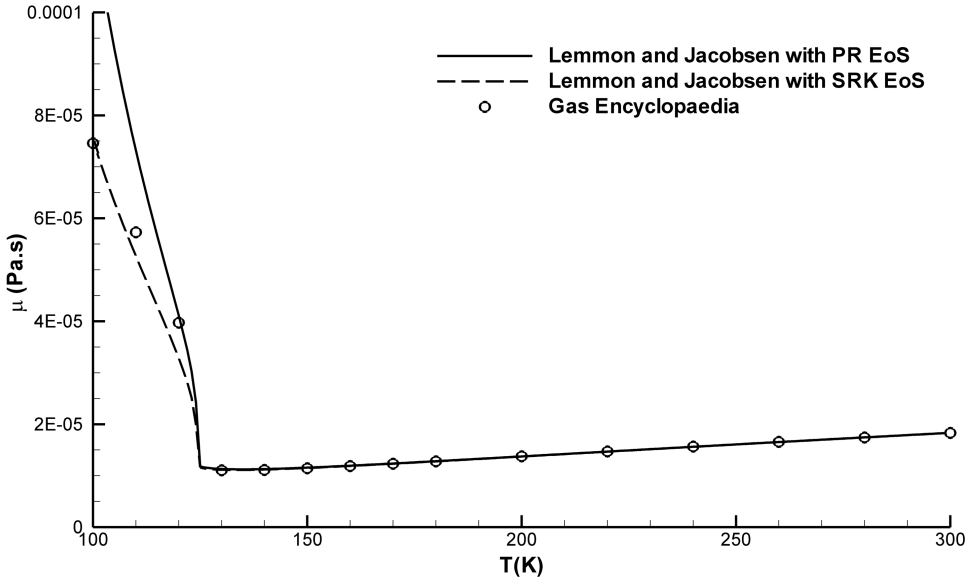

Figure 3.7: Comparison against experimental data, of the Lemmon/Jacobsen's formulation for viscosity determination with the PR and SRK equations of state for a pressure of 3 MPa.

3.4 Determination of Thermal Conductivity

The thermal conductivity, λ, plays a very important role in the diffusion term of the energy equation. Thus its correct determination is essential in order to obtain a realistic temperature field. Like for viscosity, the desired methodology would be a formulation capable of providing a correct value of thermal conductivity for different conditions of pressure and temperature. Unlike viscosity, the initial approach of Sanders [34], which didn't include the energy equation or the determination of the temperature, did not depend on the thermal conductivity value, and this variable was not taken in consideration.

The simpler approach would be to assume the value of thermal conductivity as constant. This could be a valid approach for condition of standard temperature and pressure, it isn't however, as will be shown next, a valid approach for the extremely variable conditions around the thermodynamic critical point. Thus, other approaches had to be considered.

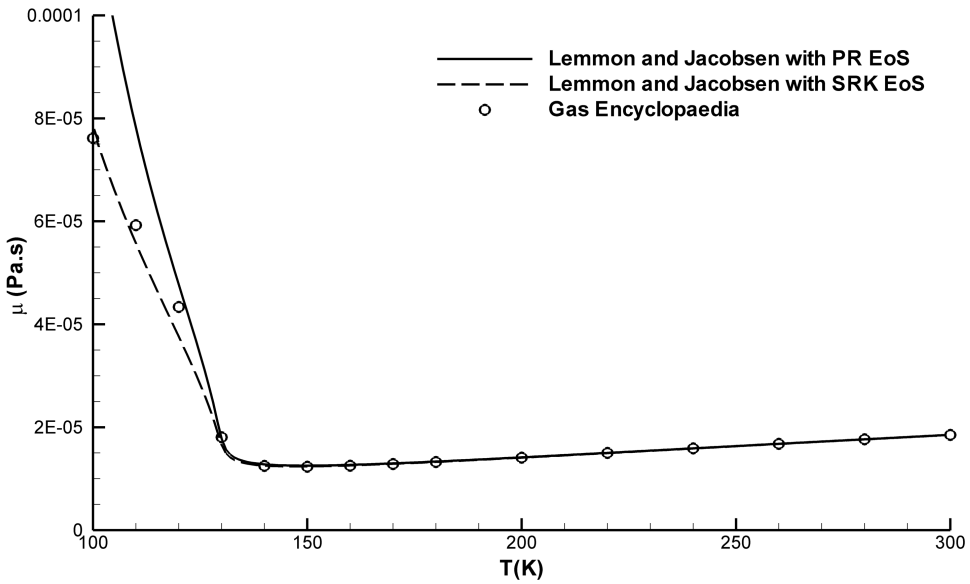

Figure 3.8: Comparison against experimental data, of the Lemmon/Jacobsen's formulation for viscosity determination with the PR and SRK equations of state for a pressure of 4 MPa.

3.4.1 Sutherland's law

Just as for viscosity, Sutherland's law can be used to determine the thermal conductivity of dilute gases. Once again this formulation doesn't take in consideration the pressure variation since, as for viscosity, its influence on thermal conductivity at lower pressures is secondary [56]. The formulation is given by

$$\frac{\lambda}{\lambda_0} = \left(\frac{T}{T_0}\right)^{3/2} \frac{T_0 + S}{T + S} \quad (3.37)$$

Where λ_0, T_0, and S are constants dependent on the gas of study. For nitrogen, N_2, $\lambda_0 = 0.0242 W.m^{-1}.K^{-1}$, $T_0 = 273.1K$, and $S = 166.7K$. The results of the Suderland's relation for the thermal conductivity can be observed in Figure 3.10, compared with the data from Gas Encyclopaedia [62] for 3, 4, and 5 MPa of pressure across a range of temperatures between 100 and 300K. The results show that while being able to provide acceptable results at higher pressures, like for viscosity, it fails when temperatures get closer to the critical value.

3.4.2 Determination of thermal conductivity from experimental data

As viscosity, also thermal conductivity can be obtained from experimental data. A linear function defined by parts presents itself as a simplistic method to obtain better agreement for the thermal conductivity values,

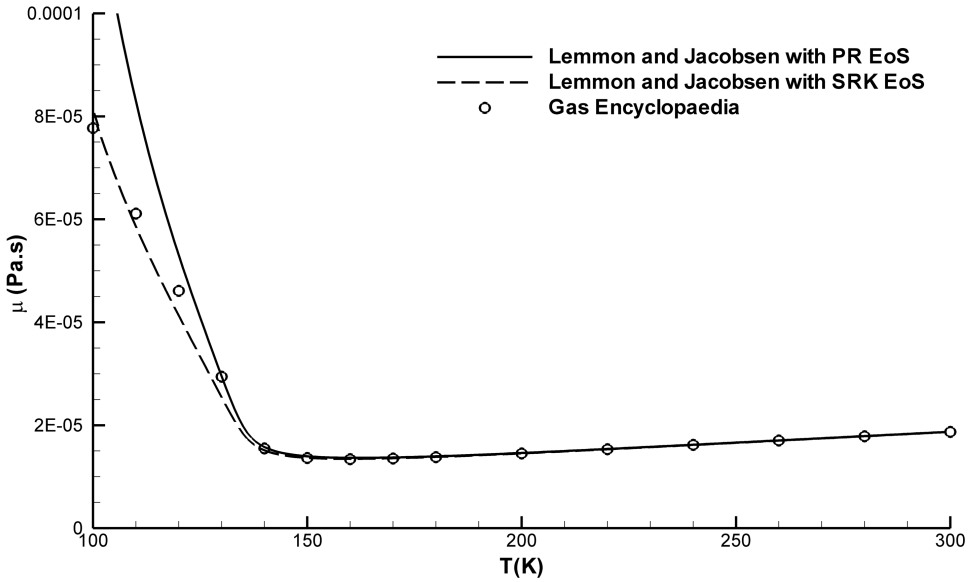

Figure 3.9: Comparison against experimental data, of the Lemmon/Jacobsen's formulation for viscosity determination with the PR and SRK equations of state for a pressure of 5 MPa.

$$\lambda(T) = \begin{cases} -2.108 \times 10^{-3}.T + 3.1618 \times 10^{-1}, & T \leq 140 \\ \\ 4.3688 \times 10^{-5}.T + 1.4944 \times 10^{-6}, & T > 140 \end{cases} \quad (3.38)$$

This set of functions provide closer agreement with experimental data for a pressure of 4 MPa than the Sutherland's relation, as can be seen by Figure 3.11.
Still, as for viscosity, this present itself as a solution which can provide values for different pressures and offers a great deal of uncertainty for the range of temperatures close to the critical point. Thus a better approach would be desired.

3.4.3 Real fluid equation for thermal conductivity

The Lemmon and Jacobsen [65] approach presented in sub-section 3.3.4 also provides equations for the calculation of thermal conductivity. In this formulation the thermal conductivity, λ, is obtain from a model similar to the one for viscosity, being expressed as function of temperature and density:

$$\lambda = \lambda^0(T) + \lambda^r(\tau, \delta) + \lambda^c(\tau, \delta), \quad (3.39)$$

where λ is the thermal conductivity in $mW.m^{-1}.K^{-1}$, λ^0 is the dilute gas thermal conductivity, λ^r is the residual fluid thermal conductivity, λ^c is the thermal conductivity critical enhancement, $\tau = T_c/T$, and $\delta = \rho/\rho_0$. The critical parameters T_c and ρ_c are given in Table 3.1. The

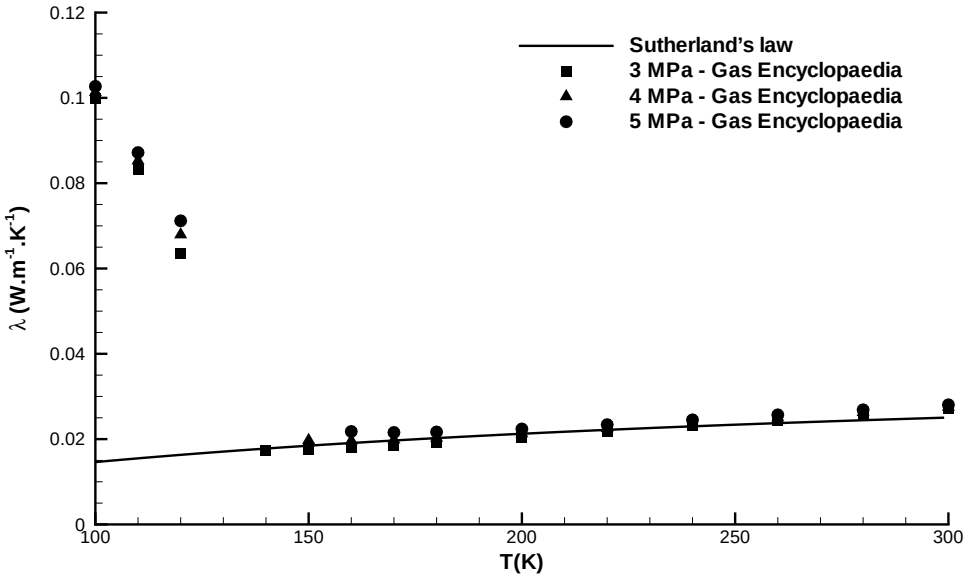

Figure 3.10: Comparison of the Sutherland's law performance for thermal conductivity with the experimental data for 3, 4, and 5 MPa.

dilute gas contribution is given by

$$\lambda^0 = N_1 \left[\frac{\mu^0(T)}{1\mu Pa.s} \right] + N_2 \tau^{t_2} + N_3 \tau^{t_3}, \quad (3.40)$$

where μ^0 is the dilute gas viscosity described previously. The coefficients and exponents are given in Table 3.5. The residual contribution to the thermal conductivity is given (in $mW\Delta m^{-1}\Delta K^{-1}$) by

$$\lambda^r = \sum_{i=4}^{n} N_i \tau^{t_i} \delta^{d_i} \exp\big(-\gamma_i \delta^{l_i}\big), \quad (3.41)$$

where γ_i is zero when l_i is zero and one when l_i is not zero. The coefficients and exponents of this equation are given in Table 3.5.

The term λ^c represents the critical enhancement model of Olchowy and Sengers [66] which is used to calculate the fluid properties in the critical region:

$$\lambda^c = \rho c_p \frac{kR_0T}{6\pi\xi\mu(T,\rho)} \big(\tilde{\Omega} - \tilde{\Omega_0}\big), \quad (3.42)$$

where

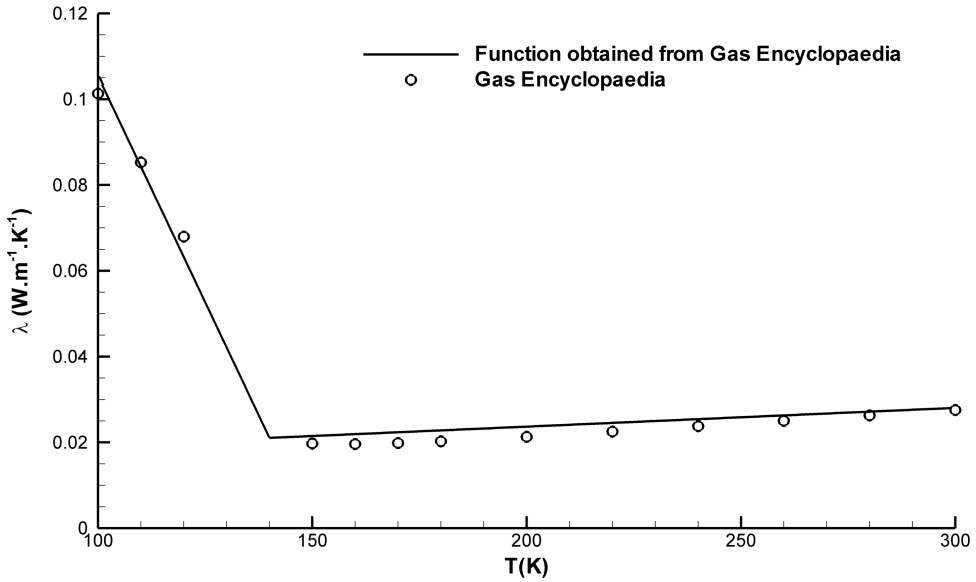

Figure 3.11: Comparison between data from Gas Encyclopaedia and the function by parts obtained from it for a pressure of 4 MPa.

$$\tilde{\Omega} = \frac{2}{\pi}\left[\left(\frac{c_p - c_v}{c_p}\right)\tan^{-1}(\xi/q_D) + \frac{c_v}{c_p}(\xi/q_D)\right] \quad (3.43)$$

$$\tilde{\Omega}_0 = \frac{2}{\pi}\left\{1 - \exp\left[\frac{-1}{(\xi/q_D)^{-1} + \frac{1}{3}(\xi/q_D)^2(\rho_c/\rho)^2}\right]\right\} \quad (3.44)$$

The correlation length ξ is given by

$$\xi = \xi_0\left[\frac{\tilde{\chi}(T,\rho) - \tilde{\chi}(T_{ref},\rho)\frac{T_{ref}}{T}}{\Gamma}\right]^{\nu/\gamma} \quad (3.45)$$

where

$$\tilde{\chi}(T,\rho) = \frac{p_c\rho}{\rho_c^2}\left(\frac{\partial\rho}{\partial p}\right)_T. \quad (3.46)$$

In these equations, k is Boltzmann's constant ($1.380658 \times 10^{-23} J.K^{-1}$), and R_0, ν, and γ are theoretically based constants with values of $R_0 = 1.01$, $\nu = 0.63$, and $\gamma = 1.2415$. The terms

Table 3.5: Coefficients and Exponents of the Residual Fluid Thermal Conductivity Equations for N_2 [65]

i	N_i	t_i	d_i	l_i
1	1.511			
2	2.117	-1.0		
3	-3.332	-0.7		
4	8.862	0.0	1	0
5	31.11	0.03	2	0
6	-73.13	0.2	3	1
7	20.03	0.8	4	2
8	-0.7096	0.6	8	2
9	0.2672	1.9	10	2

q_D, ξ_0 , and Γ are fluid-specific (fitted) terms, and T_{ref} is a reference temperature that is significantly above the critical temperature (T_{ref} was taken as twice the critical temperature as this was also the choice of the authors of the present formulation [65]). The values of these terms are given in Table 3.2. The value of λ_c should be set to zero when the bracketed term in Equation 3.45 is negative (usually at high temperatures) or zero. The isochoric heat capacity (c_v), isobaric heat capacity (c_p), and the first derivative of density with respect to pressure are calculated from the equation of state at the specified temperature and density.

The results from this formulation provided by Lemmon and Jacobsen coped with the two real fluid equations of state, PR and SRK, tested in the present work can be observed in Figures 3.12, 3.13, and 3.14 for respectively the pressures of 3, 4, and 5 MPa. The results show an agreement very similar to the one already obtained for the viscosity. Once again, it can be observed that the choice of equation of state is the responsible for the greatest departures from the experimental data. Is important also to reefer that in the observed results the thermal conductivity critical enhancement term, λ^c, was not employed in the calculations, due to the extra complexity that it brings with it. However, conclusions from its effect would be difficult to obtain since the data from gas encyclopaedia doesn't provide value of thermal conductivity for values close to critical.

Nevertheless, the results obtained provide a very good agreement with experimental data, representing a big step forward when compared with other approaches for obtaining the correct value of thermal conductivity.

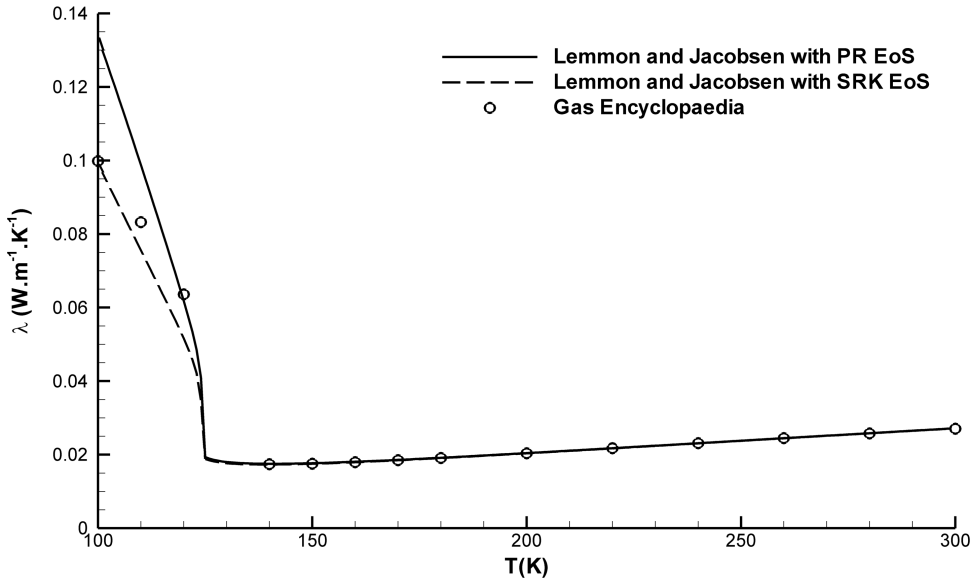

Figure 3.12: Comparison against experimental data, of the Lemmon/Jacobsen's formulation for thermal conductivity determination with the PR and SRK equations of state for a pressure of 3 MPa.

3.5 Determination of specific heat

Specific heat represents the amount of heat required to produce a variation in the temperature of a substance. In the present work it translates the transferences of energy in the flow into variation of temperature of the fluid of study. Using its correct value is essential in order to obtain a correct temperature field. For a calorically perfect gas, the specific heat is constant [56]. It happens, however, as already state in the Chapter 1, that the specific heat suffers strong variations when around the critical point. These variations hold a strong effect over the flow behaviour and must this way be taking in consideration. Thus, the assumption of the specific heat as a constant value is, for the present work, not a desirable approach. Specific heat at constant pressure is defined as

$$c_p = \left(\frac{\partial h}{\partial T}\right)_p \quad (3.47)$$

And specific heat at constant volume is defined as

$$c_v = \left(\frac{\partial e}{\partial T}\right)_v \quad (3.48)$$

The ratio of specific heat is defined as

$$\gamma = \frac{c_p}{c_v} \quad (3.49)$$

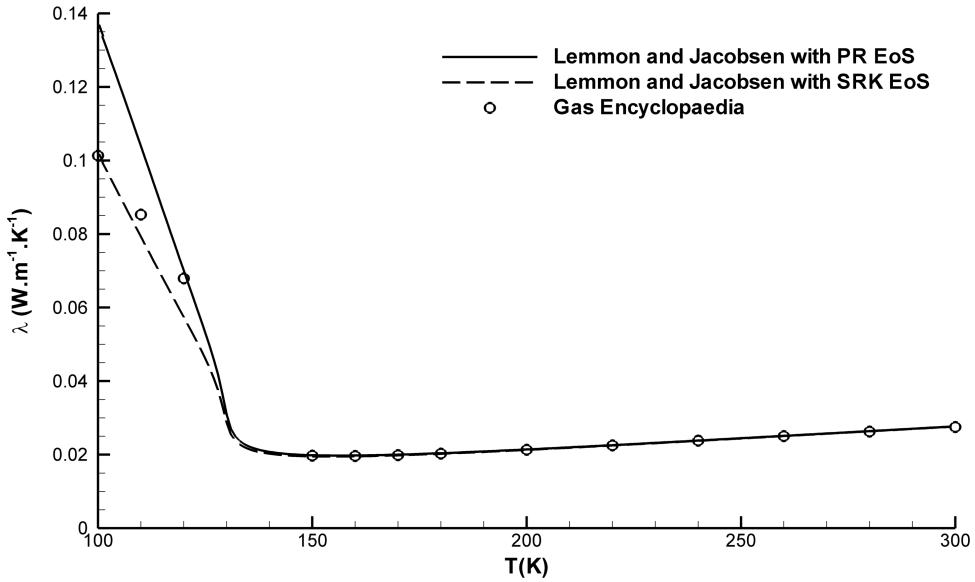

Figure 3.13: Comparison against experimental data, of the Lemmon/Jacobsen's formulation for thermal conductivity determination with the PR and SRK equations of state for a pressure of 4 MPa.

In the current work the interest is to obtain the specific heat at constant pressure, c_p, since it's the one to be used in the energy equation. Unlike for viscosity and thermal conductivity, the Sunderland's law doesn't provide any equation for the determination of the specific heat, so other methodologies have to be used.

3.5.1 Determination of specific heat from experimental data

As for viscosity and thermal conductivity, one method which can be used for obtaining the specific heat in by the use of data from tables, like for example the Gas Encyclopaedia [62]. Data from this source allow the definition of a set of linear functions which are meant to fit the experimental data,

$$c_p(T) = \begin{cases} 43.0952T - 2149.48, & T < 120 \\ 1240.68T - 145859, & 120 \leq T < 130 \\ -1278.55T + 181641, & 130 \leq T < 140 \\ -53.1159T + 145859, & 140 \leq T < 160 \\ -3.41594T + 2128.52 & T \geq 160 \end{cases} \quad (3.50)$$

Figure 3.15 allow to see the comparison between the function by parts 3.50 and the data from gas encyclopaedia at 4 MPa, the results show a close fitting.

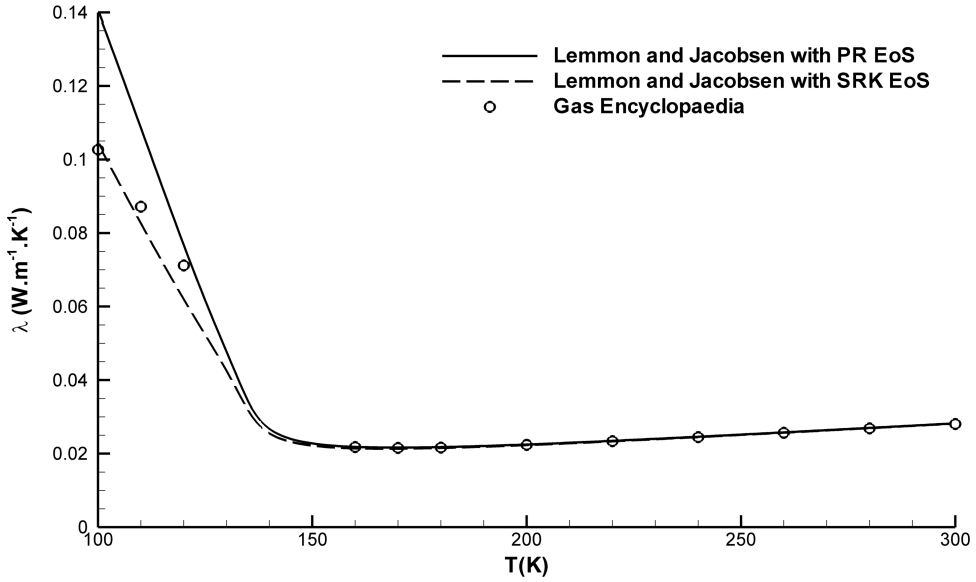

Figure 3.14: Comparison against experimental data, of the Lemmon/Jacobsen's formulation for thermal conductivity determination with the PR and SRK equations of state for a pressure of 5 MPa.

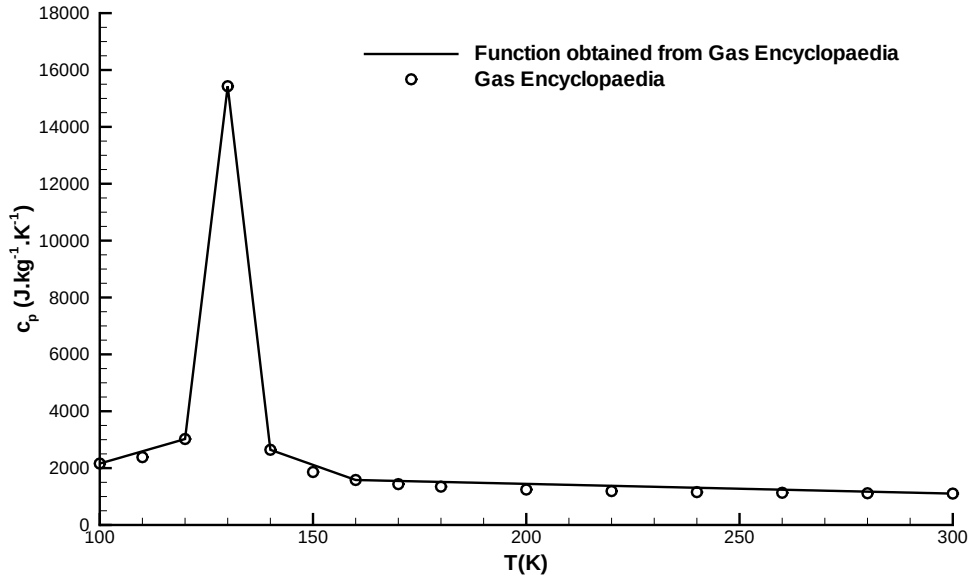

Figure 3.15: Comparison between data from Gas Encyclopaedia and the function by parts obtained from it for a pressure of 4 MPa.

Chapter 4

Numerical Approach

4.1 Introduction

The present chapter describes the numerical approach to solve the equations presented in the previous two chapters for the flow of interest. The governing equations presented in chapter 2 won't be solved analytically. Instead, they will be discretized in order to obtain linear equations which can be solved numerically, this methodology will be described in section 4.2. Then, the configuration of the flow of interest for this investigation will be presented, which will also expose the boundary conditions imposed in the present numerical approach. After describing the flow configuration, the thermodynamic conditions imposed by the chosen cases of study will be presented. Finally, a numerical approach depends on the discretization of the domain of study into a numerical grid, to perform a correct choice of grid, the effects that it has on the solution must be evaluated, for this a grid dependency test was performed and the results are express in the last section.

4.2 Numerical Method

The conservation equations of mass, momentum, and energy cannot be solved analytically with currently known methods except for a very limited number of flows. The known solutions are extremely useful in helping to understand fluid flows but can rarely be used directly in engineering analysis or design [67]. Another approach must then be used to solve the governing equations. Numerical methods can be used as tools to find solutions for these equations. In order to solve the differential equations in a numerical manner, one must initially discretize them into algebraic linear equations.

4.2.1 Discretization of differential equations

Several methods exist for the approximation of the differential equations by a system of algebraic equations for the variables at some set of discrete locations in space and time. The most important approaches are the finite differences, finite volume, and finite element methods. The present numerical approach makes use of the finite volume method, which involves the integration of the differential governing equations in each volume of control defined by the grid [68]. The generalized transport equations of momentum, energy, k, and ε can be expressed by equation 2.66 presented in chapter 2,

$$\frac{\partial}{\partial x}\left(\overline{\rho}\tilde{U}\tilde{\phi}\right)+\frac{1}{r}\frac{\partial}{\partial r}\left(r\overline{\rho}\tilde{V}\tilde{\phi}\right)=-\frac{1}{r}\frac{\partial}{\partial r}\left(r\overline{\rho}\Gamma\frac{\partial\tilde{\phi}}{\partial r}\right)+S_{\phi} \quad (4.1)$$

In order to discretize the equation above, first, the domain of study must be divided into discrete volumes of control centred around the grid nodes. Figure 4.1 shows the control volume, the grey area, centred around the node P and surrounded by the neighbour nodes, N, S, W, and E. Each node will have its own control volume, in Figure 4.1 is just represented the control volume of P. All fluid variable described in the previous chapters are located in the point P with exception of velocities which are positioned between each two nodes in the border between control volumes, this configuration is called staggered grid. After the integration of the equations to the control volume and the use of a numerical scheme, an algebraic equation, which relates the variable values in P with the neighbour nodes [68], this equation is represented for the two-dimensional of the present work by,

$$A_P\phi_P = A_N\phi_N + A_S\phi_S + A_S\phi_S + A_W\phi_W + A_E\phi_E + S_U^\phi \quad (4.2)$$

Where

$$A_P = A_N + A_S + A_W + A_E - S_P^\phi \quad (4.3)$$

S_U^ϕ and S_P^ϕ are the coefficients of the source term which can be written as,

$$S_\phi \Delta x \Delta r = S_U^\phi + S_P^\phi \quad (4.4)$$

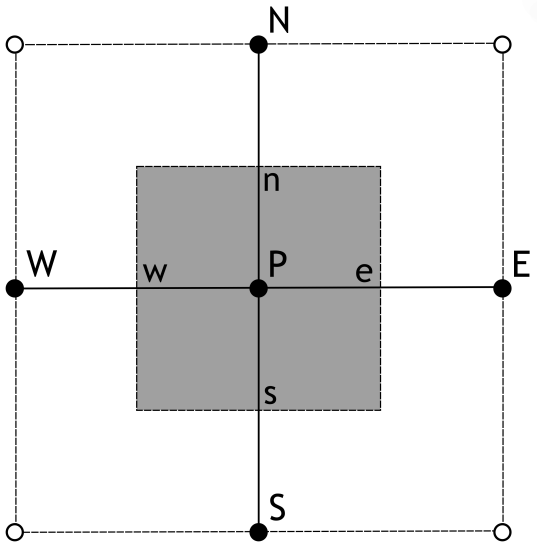

Figure 4.1: Node configuration for a control volume centered in P.

4.2.2 Numerical Scheme

To calculate the convective and diffusive fluxes, the value of the variable ϕ and its gradient normal to the cell face at one or more locations on the control volume surface are needed. The numerical interpolation scheme defines how the value of variables is represented in the face of each control volume, as they have to be expressed in terms of the nodal values by interpolation. Numerous possibilities are available, in the present work the hybrid scheme was selected has it offers good accuracy for the present flow of study while keeping a low computational cost when compared with more advanced schemes such as the power-law scheme. To explain the general principals of the hybrid scheme lets considerate a steady one-dimensional situation in which only the convection and diffusion terms are present

$$\frac{d}{dx}(\rho U\phi) = \frac{d}{dx}\left(\Gamma\frac{d\phi}{dx}\right) \quad (4.5)$$

Integration of equation 4.5 over the control volume of Figure 4.1 in the horizontal dimension, using the same formulation of equation 4.2, its obtained

$$(\rho U\phi)_e - (\rho U\phi)_w = \left(\Gamma\frac{d\phi}{dx}\right)_e - \left(\Gamma\frac{d\phi}{dx}\right)_w \quad (4.6)$$

The hybrid scheme uses the central-differences for $\left|P_e = \frac{\rho U\Delta x}{\Gamma}\right| < 2$, which consists in the representation of the values of ϕ on the faces of the control volume by a linear interpolation between the closest nodes. Assuming a constant grid size, equal to Δx, one obtains

$$\phi_e = \frac{\phi_E + \phi_P}{2} \quad (4.7)$$

and,

$$\phi_e = \frac{\phi_E + \phi_P}{2} \quad (4.8)$$

This way, the discretized form of equation 4.6 takes the shape of

$$A_P\phi_P = A_W\phi_W + A_E\phi_E \quad (4.9)$$

where,

$$A_E = \frac{\Gamma_e}{\Delta x} - \frac{\rho U_e}{2}, \quad (4.10)$$

$$A_W = \frac{\Gamma_w}{\Delta x} - \frac{\rho U_w}{2}, \quad (4.11)$$

and

$$A_P = A_E + A_W \quad (4.12)$$

From the analysis of equations 4.10 to 4.12, can be concluded that for Pecler number, Pe, greater than 2, the coefficients A_E and A_W can become negative bringing with it possible instabilities. Due to this the hybrid scheme applies the upwind scheme whenever $|P_e| > 2$. The upwind scheme neglects the diffusion term, which is much smaller than the convection term, and this way the unstable behaviour of the central-differences is avoid and the coefficients never assume negative values. For the upwind scheme the values of ϕ on the face e of the control volume is given by

$$\phi_e = \phi_P \quad \text{if} \quad U_e > 0 \quad (4.13)$$

$$\phi_e = \phi_E \quad \text{if} \quad U_e < 0 \quad (4.14)$$

The conjunction of the central-differences scheme and the upwind scheme gives the hybrid scheme, for which the coefficients A_E and A_W are expressed by

$$A_E = max(-\rho U_e, 0) \quad (4.15)$$

and

$$A_W = max(-\rho U_w, 0) \quad (4.16)$$

4.2.3 Algorithm

The finite volume algebraic equations must be solved for all differential equations described in chapter 2, however, the order to solve these equations is all but random. An algorithm for the solution has to be employed not only for the differential equations but also for the other variables treated in chapter 3. The numerical approach used in the present work is the same employed by Sanders [34] and uses a parabolized marching algorithm which resembles the (elliptic) TEACH code. The TEACH code in its turn makes use of the SIMPLE algorithm which is a widely used numerical procedure to solve the Reynolds averaged Navier-Stokes equations [69]. The computations are performed by using the continuity equation to obtain the radial velocity V. Using the radial momentum equation for V and solving a pressure correction equation in the radial direction did not show any difference with the use of only the continuity equation [34].
The computer code was not written for transcritical and supercritical jets. This kind of flows are known to have high-density gradients which cause to this formulation, oscillations and very often the iterative process diverges. Due to this high under relaxation for the momentum equations was used (up to 90%) as well as special attention with grids which will be referred later [7]. These instabilities of the numerical procedure were aggravated by the introduction of a real fluid equation of state together with the real fluid functions for the other fluid properties. The used algorithm is described in detail in Figure 4.2.
Some variations of the resolution exist between the original approach and one that includes the real fluid thermodynamics. The later approach, after solving the transport equations for k, ε, and F also solves the energy equation to obtained the thermal field, updates the values of viscosity, thermal conductivity and specific heat are also performed in this step. The system of discretized equations obtain from the finite volumes for each differential equation are solved using a line by line procedure employing the Thomas Tridiagonal Matrix Algorithm.

4.3 Flow Configuration and Boundary Conditions

The flow configuration modelled in the present investigation is shown in Figure 4.3. Cold nitrogen is injected into a cylindrical chamber filled with gaseous, warmer, nitrogen. The injector has an inner diameter of 2.2 mm, the chamber is 250 mm long and 122 mm wide as shown in the figure. Since the flow is axisymmetric only half of the domain was modelled, as represented in Figure 4.3.
The computational domain contains four boundaries as shown in Figure 4.4. The north boundary is set as a constant temperature wall, and is applied the law of the wall described in chapter 2. The fixed value of temperature is the same as the chamber temperature.
The west boundary is an adiabatic wall, where it is also applied the law of the wall but for the energy equation is defined a flux equal to zero.
In the south boundary which represents the axis of symmetry, the normal velocity vanishes, and the normal derivatives of the other variables are zero.

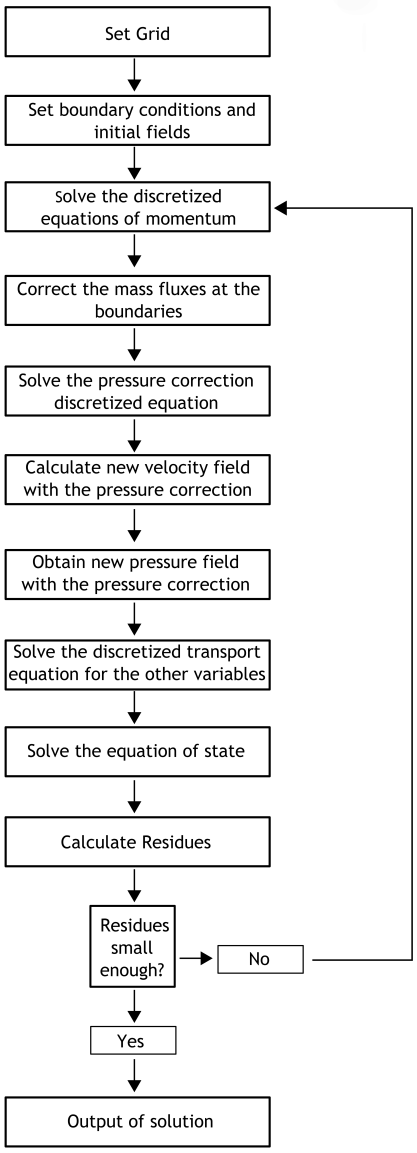

Figure 4.2: Algorithm for the sequence of resolution of the numerical approach.

At the outlet the gradients of the dependent variables in the axial direction are set to zero. For the axial velocity component a second global mass conservation adjustment is done so that the pressure correction has a solution [7].
Finally, at the injector the properties of the injection fluid and constant velocity are imposed.

4.4 Cases of Study

In the present investigation, two different test cases were modelled. The choice of the test cases was made firstly to fit the thermodynamic conditions of interest for the present work. Other factors for this choice were not only the existence of experimental data for these conditions but also the existence of investigations performing numerical simulations by other authors which provide a big amount of data for comparison.
The two different conditions represent two different thermodynamic regimes for the injection

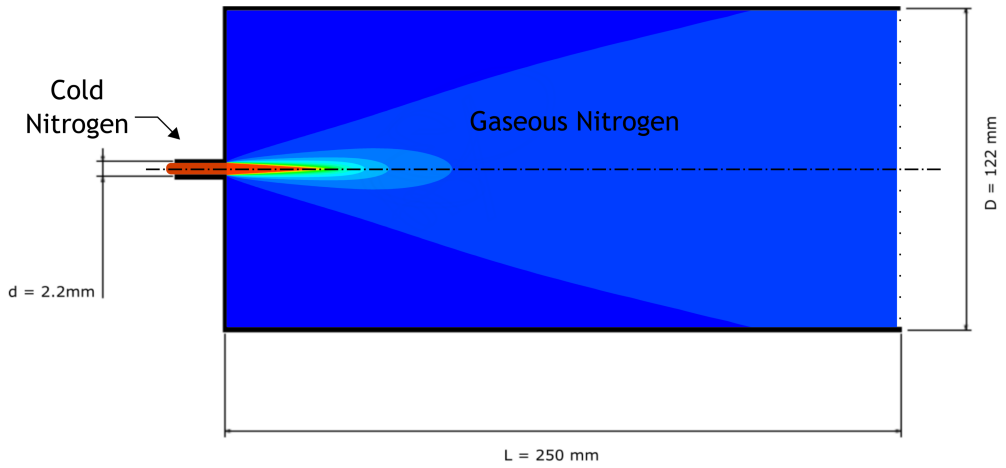

Figure 4.3: Flow configuration.

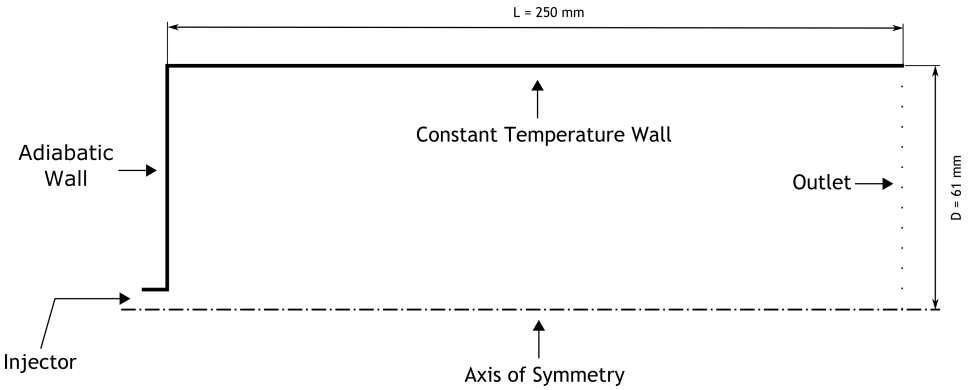

Figure 4.4: Boundary Conditions.

fluid, the transcritical regime and the supercritical regime. In both cases the chamber fluid is at supercritical conditions due to pressure and temperature being both above its critical points. The test cases chosen represent the cases 3 and 4 of the experimental research of Mayer et al. [26], and these cases were also tested by Schmitt et al. [40] and Jarczyk and Pfitzner [44] by the use of Large Eddy Simulation. The conditions of the test cases are presented in Table 4.1, the case 3 represents transcritical conditions of injection fluid while case 4 represents supercritical conditions. As can be seen in Table 4.1, the only different between test case 3 and 4 is the injection temperature which is lower in the first case, this offers, however, an important distinction between the two cases. Since the injected fluid in the case 3 enters the chamber at a temperature bellow critical and then, as it warms, makes a transition to supercritical values, while, for case 4, it already enters the chamber at supercritical temperature not facing the same transition of regime. Figure 4.5 represents the position of the test cases according to the thermodynamic regime. T stands for transcritical, case 3, and S for supercritical, case 4.

4.5 Grid

The discretization of the differential equations relies on a discretized domain. The domain is discretized through a computational grid which divides the space into a generally large number

Table 4.1: Conditions of the test cases.

Condition	Case 3 Transcritical	Case 4 Supercritical
Chamber Temperature $[K]$	298	298
Chamber Pressure $[MPa]$	3.97	3.97
Injection Temperature $[K]$	126.9	137
Injection Velocity $[m/s]$	4.9	5.4
$\rho_0[kg/m^3]$	435	171
$\rho_\infty[kg/m^3]$	45.5	45.5
ω	0.1046	0.2661

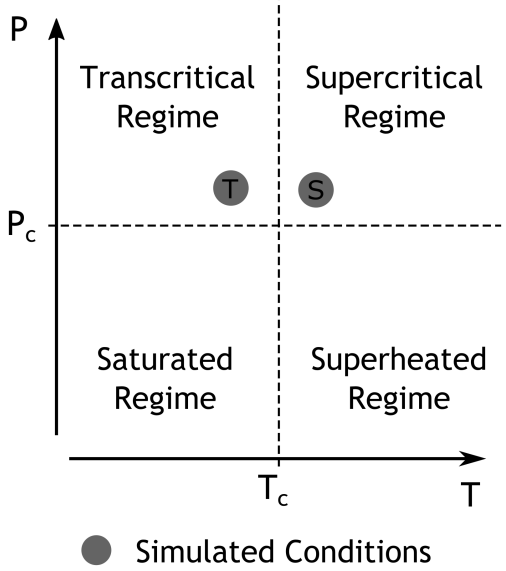

Figure 4.5: conditions in the thermodynamic regime chart.

of nodes, each one of the nodes is the centre of a control volume which was already defined above. This group of points constitutes what can be called a computational grid, or mesh. The choice of the grid is of extreme importance in order to assure numerical stability of the computational approach, assuring that convergence to a solution is achieved, as well as guaranteeing that the converged solution is physically realistic.

The present computational approach is especially sensitive to the choice of grid due the appearance of oscillations in the iterative process, very often, during calculation, the approach would not converge to a solution due to an incorrect choice of grid. A significant amount of time was indeed used in developing and testing of new grids which could provide stability, guaranty of convergence and also, very importantly, a solution independent from the grid. This was one of the most challenging tasks of the present work as there were tested uniform grids, grids with expansion by steps, grids with expansion just in one direction, and grids with constant expansion coefficients.

From the grid tests was possible to conclude that the computational approach presents a strong sensibility to the grid size for the axial direction close to injector, special care had to be taken for this region.

Finally, the choice fell over an expansive grid in both directions, making it more refined when close to injector. In the axial direction a constant expansion rate is impose, as well as the domain length, due to this, the initial grid size is calculated by the grid construction routine. The determination of points in the radial direction is somewhat more complex. For the width of the injector, a fixed amount of points was set, which establishes a constant distance between nodes. Outside of the injector radial size, the grid routine determines the expansion rate in order to fit the remaining points into the radial domain of the configuration. The grid has a size of 150 by 65 points, for the injector width are set 13 points in the radial direction. The rate of expansion in the axial direction is set as 2%. The used grid is shown in Figure 4.6

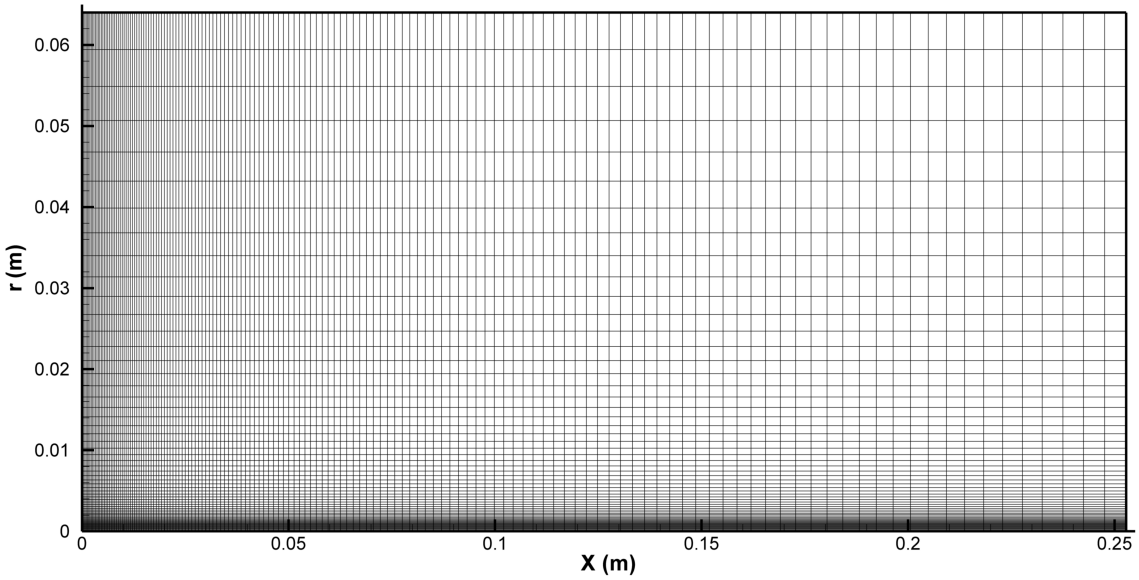

Figure 4.6: Computational grid.

In order to evaluate the influence of the grid on the converged solution grid dependency tests had to be performed. Figure 4.7 shows the grid dependency test for the original approach. The used grid, of 150x65 points is compared with a more refined grid of 212x92 points and with a coarser grid of 106x46 points. The results used for comparison are the axial density variation in the centreline The results shown barely any difference between the three tested grids. A test had also to be performed for the case which makes use of real fluid thermodynamics since its inclusion increases the oscillations and instabilities of the iterative process. Results are shown in Figure 4.8, and like for the original approach they also prove the results to be independent of the grid size.

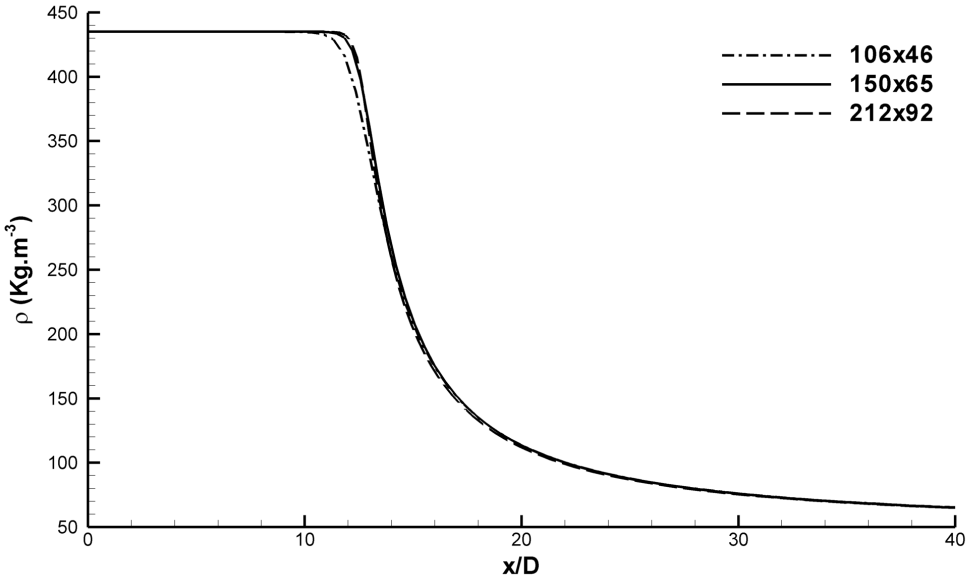

Figure 4.7: Grid dependency test based on the axial density distribution in the centreline for the original approach.

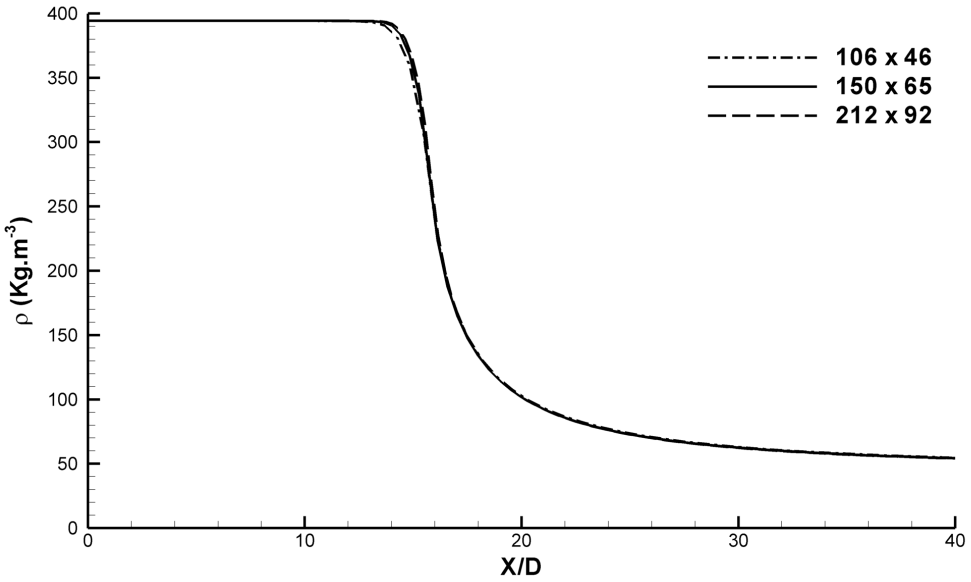

Figure 4.8: Grid dependency test based on the axial density distribution in the centreline for the approach with real fluid thermodynamics.

Chapter 5

Results

5.1 Introduction

In the present chapter, will be presented the results obtained by the implementation of the computational model described previously to the cases of study. The different approaches for modelling of transcritical and supercritical jets which were implemented and tested under the scope of the present investigation will be presented here. This includes the comparison of equations of state as well as the different methodologies for obtaining the flow properties at such transient conditions.

Firstly, the next section presents the results obtained by the approach using the Amagat's law to compute the mean density from the mean mixture fraction

Section 5.3 introduces the approach in which the density is obtained through real fluid equations of state, namely the Soave-Redlich-Kwong and the Peng-Robinson equations of state presented in Chapter 3. An extra conservative equation was introduced which concerns to energy and allow the determination of the temperature field, essential for the density determination. For this second approach the viscosity, thermal conductivity and specific heat at constant pressure are set as constant.

Section 5.4 shows the results of the third approach of the present work. This approach distinguishes itself from the second approach only by the fact that introduced variable values of viscosity, thermal conductivity and specific heat at constant pressure, obtained from the data provided from [62].

The fourth numerical approach of the present investigation has its results exposed in section 5.5, this approach is very similar to the third approach with the two only differences being the way viscosity and thermal conductivity are obtained. For the fourth approach the formulation provided by Lemmon and Jacobsen [65] is employed.

Finally, last section contains a brief summary of the numerical results.

5.2 Fraction Mixture Based Equation of State

The original approach introduced by Sanders [34] in 1997, and applied by Barata [7] to cryogenic jets at supercritical conditions, calculates the density from the mixture fraction, by the use of Amagat's law, as was described in chapter 3. This approach doesn't take into consideration the real fluid thermodynamics and established viscosity, μ, as a constant. Also, this approach does not integrate the energy equation in its formulation, so no thermal field is calculated, for this reason the temperature can't be imposed neither on the initial conditions or the boundary conditions. The numerical results obtained by this approach are presented in this section and compared with the experimental data o Mayer et al. [26] as well as with the large eddy simulations of Schmitt et al. [40], and of Jarczyk and Pfitzner [44].

5.2.1 Flow Fields

Figures 5.1, 5.2 and 5.3 show the velocity, mixture fraction, and density fields for transcritical and supercritical cases respectively. Its allow us to obtain a general picture of the flow geometry. Comparison between both cases shows very similar jet structures. Nevertheless, the supercritical case presents a faster reduction of the density and mixture fraction value than the transcritical case. Similar conclusions are obtained in the previous studies of Schmitt et al. [40] and Jarczyk and Pfitzner [44], with the LES visualizations showing similar variations between the two cases. These results also suggest the existence of a smaller potential core for the supercritical conditions. This characteristic, in particular, will be discussed later.

Figure 5.1 shows the velocity fields obtained in each of the test cases. It is visible in both cases the appearance of an entrainment close to the injector exit with ambient nitrogen being pulled into the jet stream. This phenomenon appears to be slightly more intense in transcritical regime even having a slower injection velocity. This is probably due to the higher jet momentum caused by higher injection fluid density. It is also visible that further away from the injector, the velocity is higher in the transcritical case than in the supercritical due not only to the higher injection velocity but by the higher fluid density. The injection density appears to be determinant to the distance that a jet can reach.

In Figure 5.2 the mixture fraction fields are shown for both tested cases. The value of mixture fraction is one for the injection fluid and zero for the ambient gaseous nitrogen in chamber. The images show a high concentration of injected fluid close to the injector exit which decreases as the distance to the injector in both radial and axial direction increases. Comparison between the two cases shows a faster decrease of the mixture fraction along the jet in supercritical conditions than in transcritical. However, it is important to note that this faster decrease does not mean a better mixture of the jet fluid with the chamber fluid. In fact, there are higher mixture fraction gradients at supercritical conditions. Close to the injector the mixture fraction quickly decreases in value but then, in the rest of the injection chamber, the flow is dominated by mixture fraction values bellow 0.5. In the transcritical case, even though it evidences a slower decrease of mixture fraction and bigger penetration of injection fluid (apparently showing a slower mixture at the beginning of the jet), a better mixture is still visible as the mixture fraction values close to 0.5 are found in most of the domain. These results of the apparently better mixture in the case with smaller temperature and at which the difference between injection density and chamber density is higher can be considered in some way surprising. However, the reason for this can once more be appointed to the higher flow momentum at lower temperature that causes the injected fluid to travel further in the chamber.

The density fields are shown in Figure 5.3. Once more, the results show similar jet structure for both cases. The transcritical case, however, shows a longer dense core than the one observed at supercritical conditions. Having the transcritical situation a higher density gradient between injected and chamber fluid and a lower injection velocity, one could expect it to have a shorter dense core as well as a smaller jet penetration than supercritical case. However, the opposite occurs. The explanation found by the authors of the present research is that the value of fluid density, due to its influence in fluid momentum, rules the jet dynamics. Although the jet in transcritical conditions has a slower injection velocity, it has, in fact, a higher momentum which results in a deeper penetration length. The higher jet momentum is also responsible for the more intense entrainment at the jet exit in this case. The entrainment phenomenon is important for the fluid mixing. This explains the better mixing at transcritical conditions

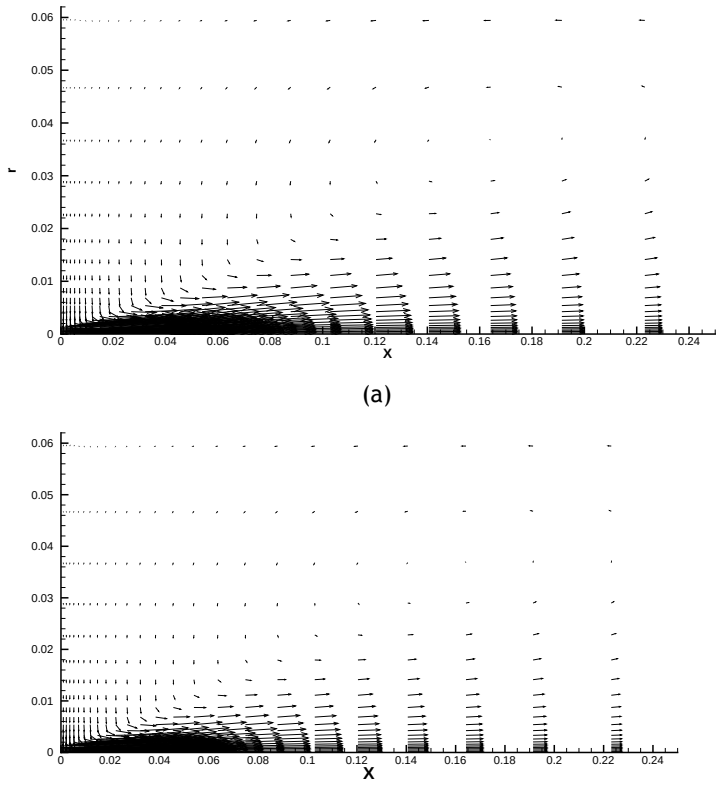

(a)

(b)

Figure 5.1: Velocity field of the jet for a) transcritical and b) supercritical conditions.

when compared to supercritical. These results obtained by the present numerical approach are corroborated in the LES results of Schmitt et al. [40] where the case 3, transcritical conditions, also shows a longer jet length and a denser core than case 4, supercritical conditions.
The results obtained by the velocity and scalar fields also give us the evidence that the jet behaviour is mostly dominated by the convective terms while diffusion plays a minor role. In turn, convection is strongly influenced by the density variations. The calculation of density appears this way as a key factor in the modelling of this kind of flows.

5.2.2 Axial Density Distribution

The axial density distributions of transcritical and supercritical cases are shown in Figures 5.4 and 5.5, respectively. The numerical model of the original approach is evaluated against experimental and numerical results of other authors. Potential core length is one of the most relevant characteristics of a jet as it is generally used by other authors to help quantifying it. Schmitt et al.[40] defines the potential core length as the axial distance at which the centreline density is 99% of the injected density. Generally, potential core length is expressed in multiples of injector diameters. In the present investigation, it was decided to use the same definition of potential core already used by Schmitt [40].
The results obtained for the transcritical case in the present investigation show a potential core of 11.8 injector diameters. It is longer when compared with the results of other authors. Schmitt et al. [40] for example shows a potential core length of 7.9 diameters, whereas Jarczyk and Pfitzner [44] identifies a length of around 9 diameters . The Large Eddy Simulation performed by Schmitt et al. [40] shows the best agreement with the experimental data from

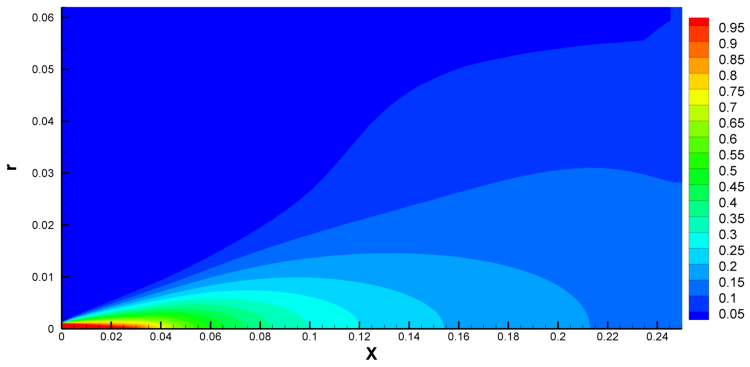

(a)

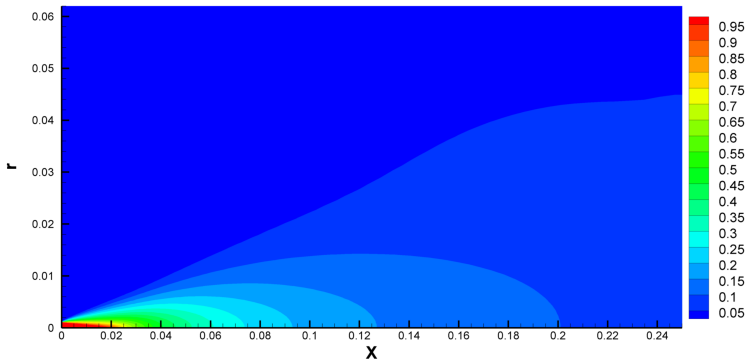

(b)

Figure 5.2: Mixture fraction field of the jet for a) transcritical and b) supercritical conditions.

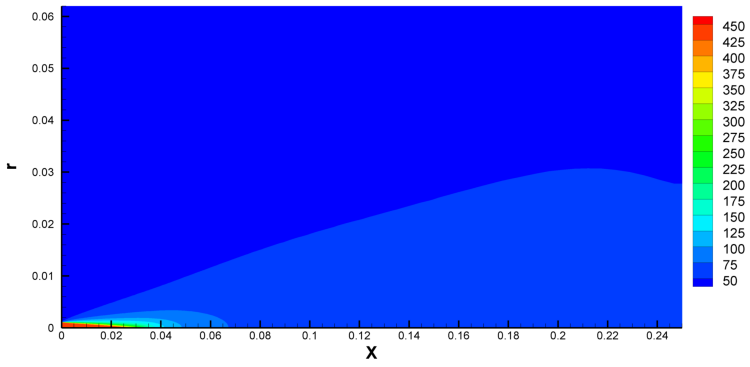

(a)

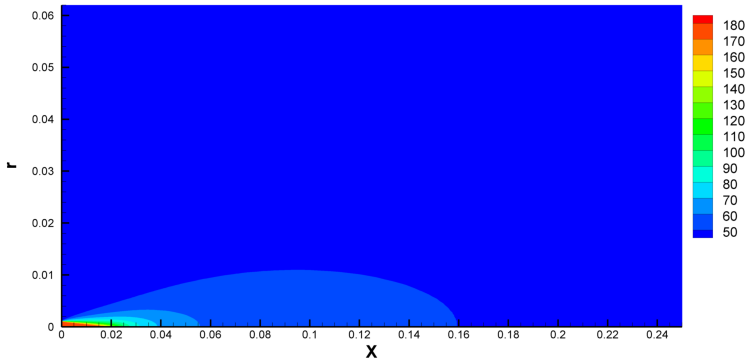

(b)

Figure 5.3: Density field of the jet for a) transcritical and b) supercritical conditions.

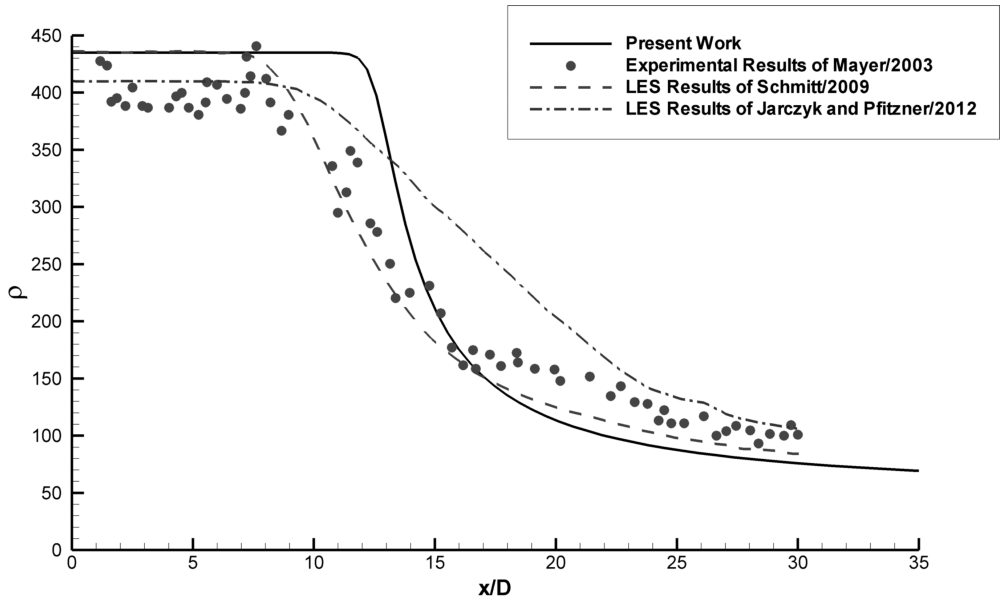

Figure 5.4: Axial density distribution for transcritical case and comparisons with different authors' results.

all the numerical approaches. The Large Eddy Simulation of Jarczyk and Pfitzner [44] overestimates the value of the density for a large range of the visible domain, from the potential core, and only getting closer to the experimental values at an axial distance of around 25 jet diameters. The current approach, after clearly overestimating the potential core, gets closer to the experimental data for a distance of 15 x/D, however, diverges from the experiments after 17 x/D. The results are nevertheless in line with the other investigations. The same kind of centreline density distribution profile was obtained for supercritical conditions in Figure 5.5. The potential core obtained of around 7.8 diameters is bigger than the one obtained with the two LES results which are 5.1 diameters in the work of Schmitt et al. [40] and around 6 jet diameters for Jarczyk and Pfitzner [44]. Analysing experimental data of Mayer et al. [26] there is little amount of evidence of the existence of a potential core for this test case.
For the supercritical test case, the numerical approach published by Jarczyk and Pfitzner [44] provides the results with the closest agreement with the experimental data. The numerical results of Schmitt et al. [40] under-predict the density value at the centreline for all the visible domain with the exception of the points closest to the injector. The results of the present approach, after the overestimation of the potential core, under predict slightly the density value, it gives, however, closer results to experimental data than Schmitt [40]. Further away from the injector the current results reach total agreement with the data from Schmitt.

5.2.3 Radial Density Distribution

Figures 5.6 and 5.7 show the radial density distribution of three different axial distances for transcritical and supercritical cases respectively. In both figures a), b) and c) illustrate respectively the axial distance of 1.2, 5 and 25 injector diameters. Figure 5.6 a) shows quite good agreement with experimental data of Mayer [26]. For the same axial distance for supercritical conditions in Figure 5.7 a) the agreement is also good, showing even a coincidence of experimental and numerical data during some range of the domain. For the axial distance of 5 x/D, in transcritical case, Figure 5.6 b), the experimental data show a decrease of density close to the

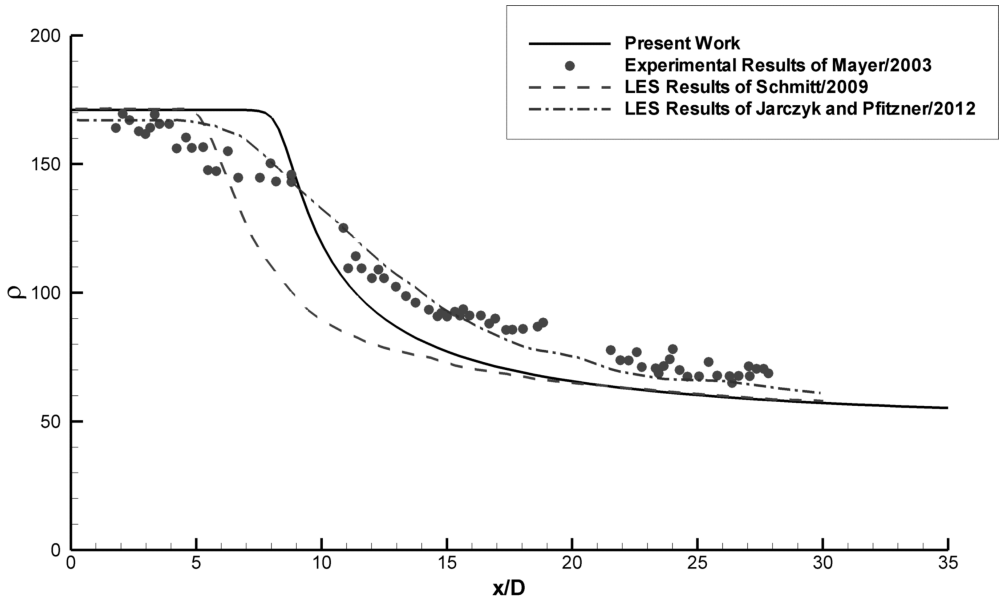

Figure 5.5: Axial density distribution for supercritical case and comparisons with different authors' results.

centreline that is not observed in the current results. These results are naturally attributed to the longer potential core, obtained in the current approach, which have already been visualized in Figure 5.4. Farther away from the centreline the numerical results find much better agreement with the experiments. For the same case in Figure 5.6 c), at an axial distance of 25 x/D, the agreement obtained is not as good, since the numerical results are not able to replicate the flattened bell shape of the experimental data which shows an almost constant value of density along the radial direction with only a slight decrease. For supercritical case, it can be observed that the results follow the same trend of case 3 and a similar agreement is expected. The comparison between present results and experimental data shows a fair agreement between both, with some differences identified further downstream in the domain, showing some difficulty of the current approach to provide correct values of density in this zone.

5.2.4 Jets Spreading Rate

The spreading angle of the jet is one of the most important parameters available for the use of a researcher when his objective is to characterize a jet flow. In order to determine the spreading of a jet, it becomes necessary to define its radial border. Several authors, [40], [44], assume that the border of the jet is in the radial position where the density is the average between the maximum value (located in the centreline position, at the same axial distance) and minimum value (the chamber density). This is how the Full Width of Half Maximum of Density (FWHM of Density) is defined. In the work of Schmitt et al. [40] the tangent of the spreading angle of density was obtained by linear interpolation of the FWHM of Density between x/D = 15 and x/D = 25. In the present work, it was decided to use the exact same method.

Figure 5.8 shows the FWHM of Density for test transcritical conditions obtained in the present work and is compared against the Raman measurements of Mayer et al. [26]. It can be observed that the numerical results obtained in the present work follow a similar trend as the one obtained in the experimental data. The chart initially shows a decrease of the full width that extends up to 10 x/D in the experimental data, whereas in the present numerical data it

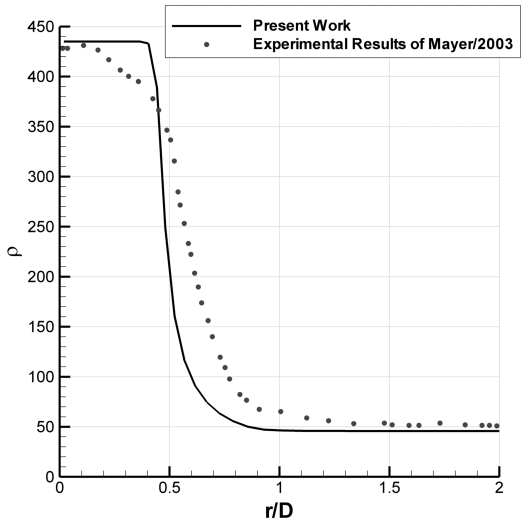

(a)

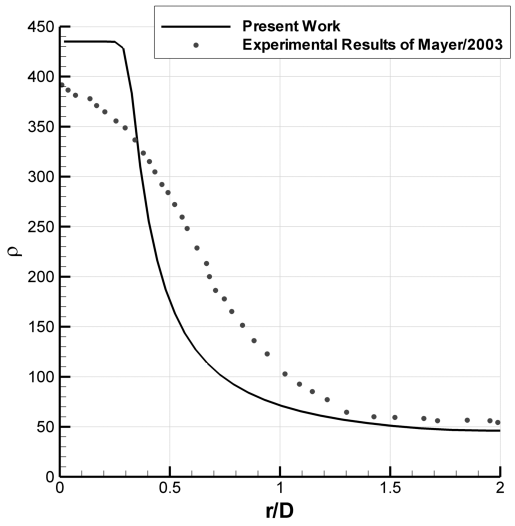

(b)

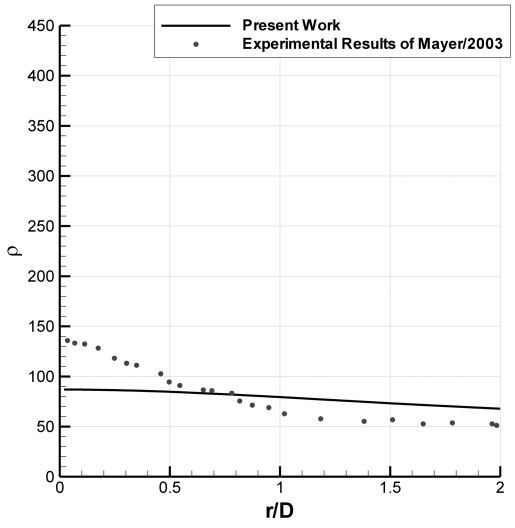

(c)

Figure 5.6: Radial Density Distribution for transcritical case. a) x/D = 1.2; b) x/D = 5; c) x/D = 25

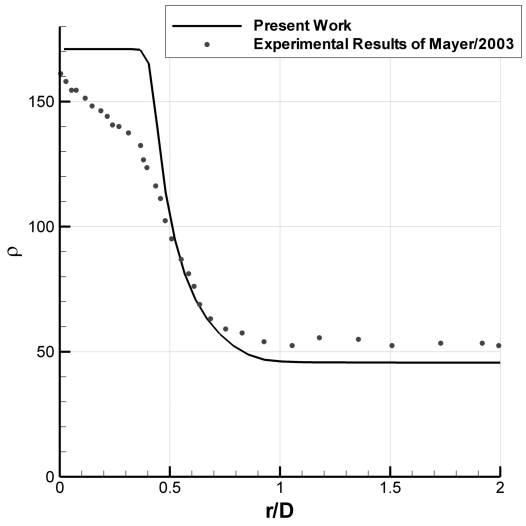

(a)

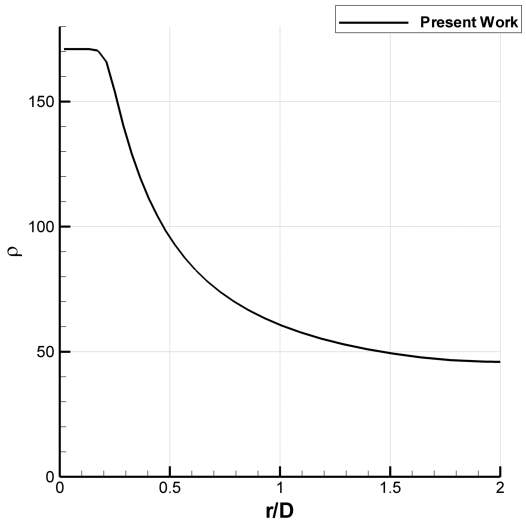

(b)

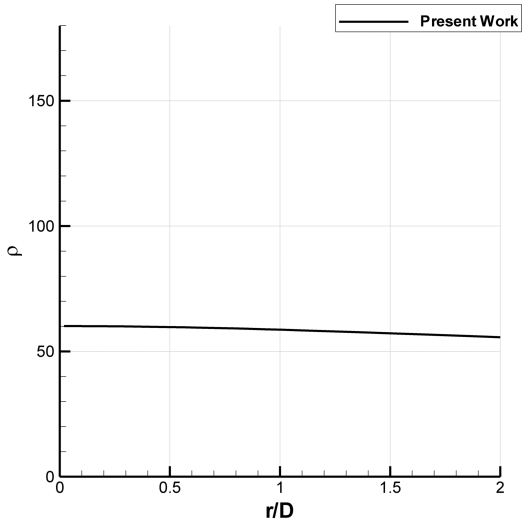

(c)

Figure 5.7: Radial Density Distribution for supercritical case. a) x/D = 1.2; b) x/D = 5; c) x/D = 25

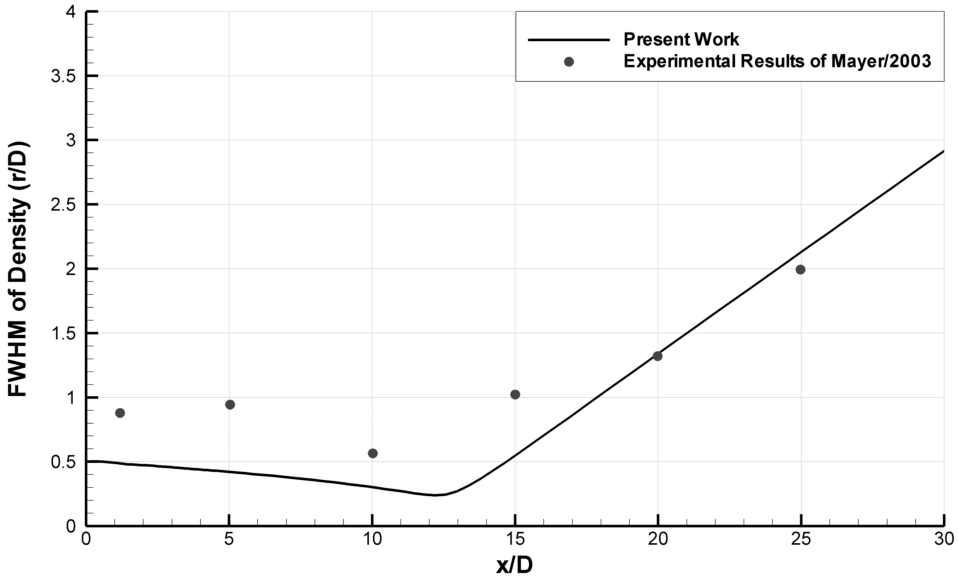

Figure 5.8: Full Width of Half Maximum of Density for transcritical case and comparison with experimental data of Mayer et al.[26].

decreases until approximately 12 x/D, but always with a smaller width than in the experimental data. After this point, the full width of the jet starts increasing, showing that the jet is spreading. The observed numerical spreading rate is very much in line with the Raman measurements. The jet spreading rate is 0.196 for the experimental data of Mayer [26] and 0.206 for the experimental data of Oschwald and Micci [25]. The present approach has a jet spreading rate of 0.316, which represents a difference of 62.8 percent to [26] and of 53.4 percent to [25]. For the same case the LES simulation of Schmitt et al.[40] presents a tangent of the spreading angle of 0.227 which is a little higher than experimental data [26] with a different of around 15.8 percent, a closer result than the one obtained in the present work.

Figure 5.9 shows the FWHM of Density for the supercritical case. For this case there were no available experimental data from the Raman measurements of Mayer et al. [26] and for this reason Figure 5.9 only shows the results obtained in the present work. In the chart, it is possible to observe at the beginning of the jet a very slow decrease of the jet width until an axial length of around 8 x/D. After this mark, there is an increase of the jet width following a tangent of the spreading angle of around 0.310. Existing experimental data [25] shows a value of 0.312 which shows the very close agreement achieved by this numerical approach for supercritical injection conditions. For the same test case Schmitt [40] provided a tangent of the spreading angle of 0.241, clearly getting a worse agreement that the one provided by the approach of present section.

5.3 Real Fluid Equation of State with Constant Properties

The second approach of the present investigation was to introduce a real fluid equation of state into the original approach already presented in the previous section. To do so, the Favre averaged energy equation had to be solved additionally as was already described in Chapter 2. As introduced in Chapter 3, the simplest methodology to obtained the fluid properties of viscosity, μ, thermal conductivity, λ, and specific heat at constant pressure, c_p, was by assuming

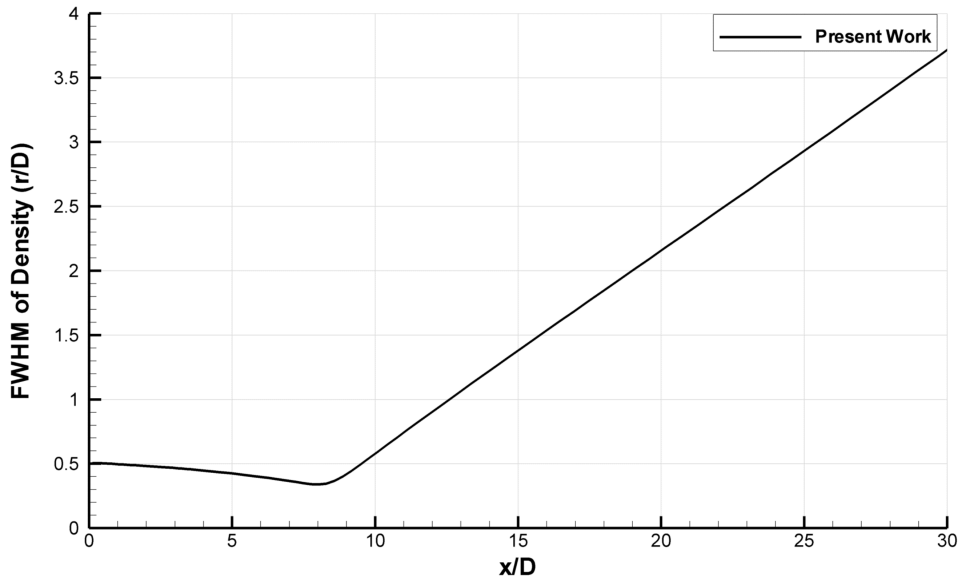

Figure 5.9: Full Width of Half Maximum of Density for supercritical case.

them as constants. The results of this assumption will be presented along this section.

5.3.1 Properties at Different Temperatures

The assumption of a constant value of properties demands the choice of suitable values for the simulated test conditions. For this, different values of the properties corresponding to different nitrogen temperatures were employed and tested. Figure 5.10 shows the axial density variation for both test conditions with the use of the Soave-Redlich-Kwong equation of state for properties at five different temperatures and compared with the experimental data of Mayer [26]. The results show a very small influence of the value of properties for the given range of temperatures established on the results. Similar conclusion is obtained when analysing the results of the FWHM of Density in Figures 5.11 a) and b).

Figures 5.12 and 5.13 show the same results expressed above while using the Peng-Robinson equation of state instead of the Soave-Redlich-Kwong. Concerning the effects of the variation of the value of the properties, the results are in everything similar to those obtained for the SRK equation of state. The employment of values of the properties corresponding to a range of different temperatures between 150K and 300K shows to have very little influence over the results. This can in part be explained by the fact that between this range of temperatures the variation of the properties is rather small as could be seen in Figures 3.5, 3.10, and 3.15 of Chapter 3. The biggest variations of the fluid properties happen closer to the critical temperature, however the nitrogen data provided by the Gas Encyclopaedia [62] doesn't include values close to critical temperature.

These results also seem to suggest that the biggest contribution for the dissipation term comes in fact from the turbulent viscosity and the turbulent thermal conductivity obtained from the turbulent Prandtl number.

Since the value of properties for this range of temperatures has so little influence for the results, for this approach with constant value of properties, it will be always used the value of properties for a temperature of 150K.

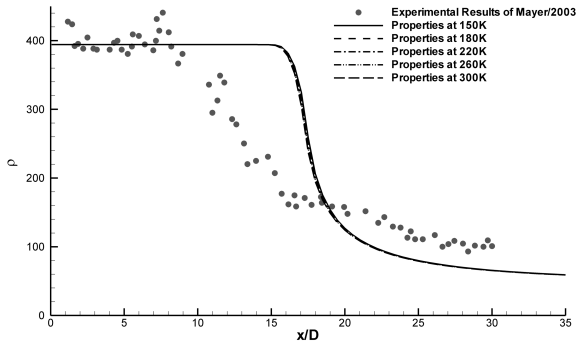

(a)

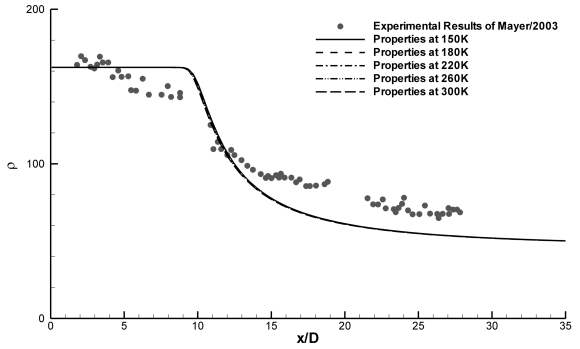

(b)

Figure 5.10: Axial density distribution for the transcritical case a), and supercritical case, b), with the use of Soave Redlich-Kwong Equation of State.

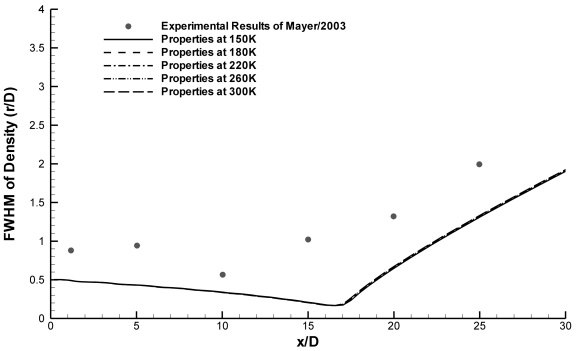

(a)

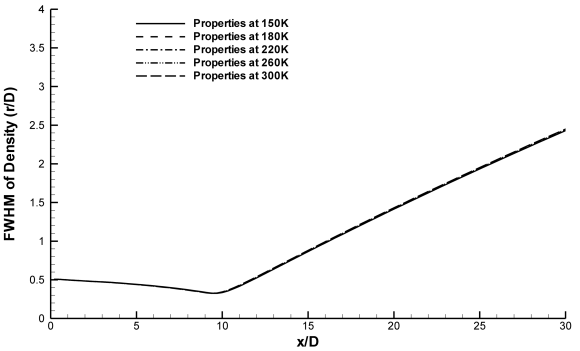

(b)

Figure 5.11: Full Width of Half Maximum of Density for the transcritical case a), and supercritical case, b), with the use of Soave Redlich-Kwong Equation of State.

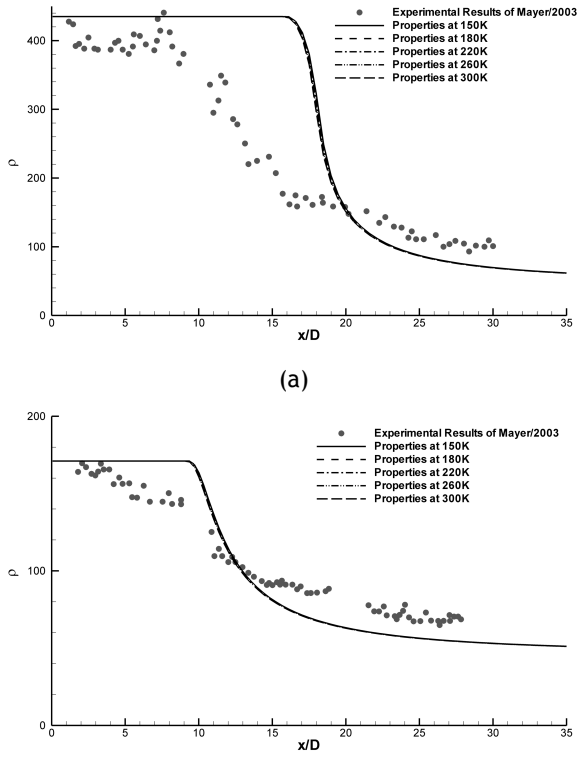

(a)

(b)

Figure 5.12: Axial density distribution for the transcritical case a), and supercritical case, b), with the use of Peng-Robinson Equation of State.

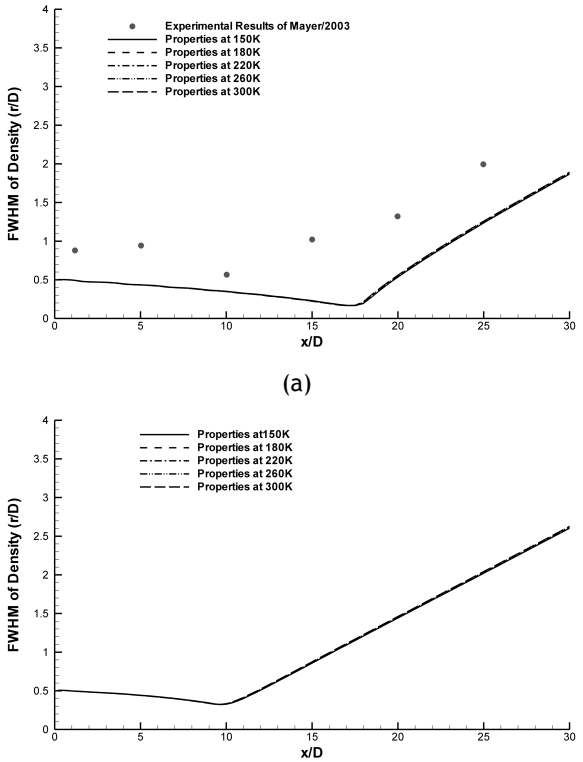

(a)

(b)

Figure 5.13: Full Width of Half Maximum of Density for the transcritical case a), and supercritical case, b), with the use of Peng-Robison Equation of State.

5.3.2 Flow Fields

Figures 5.14, 5.15, and 5.16 show the velocity, mixture fraction, and density fields for this approach with the use of the Soave-Redlich-Kwong equation of state. For all figures the chart a) represents the transcritical injection case while the chart b) shows the supercritical case. Comparing the velocity field, Figure 5.14, for both cases with the results obtained with the approach employing Amagat's law of the previous section, one can observe a very similar flow behaviour. Once again there is the appearance of entrainment close to the injector, which looks like to be more intense in the transcritical case. The existence of a recirculation further away from injector is also observed, the existence of such recirculation was also visible on Figure 5.1 of the previous numerical approach.

The mixture fraction field observed in Figure 5.15 shows also a similar result to the one obtained by the use of an equation of state based on Amagat's law. However, as it can be observed, the potential core is longer for both test cases. Like before, also with this approach there's a faster reduction of the mixture fraction value for the supercritical case showing shallower penetration of jet like was already concluded for the previous approach.

Similar comparison can be made for the density field visible in Figure 5.16. A longer potential core is observed when compared with Figure 5.3, however the value of density with the use of the Soave-Redlich-Kwong equation of state is lower in most of the domain when compared with the first approach. This leads to an apparent smaller penetration of the injected fluid into the chamber if just the density field is analysed However, when compared with the mixture fraction field, which does not show a smaller penetration of the jet, the results can simply suggest that the density values obtained from this equation of state are generally lower.

Figures 5.17, 5.18, and 5.19 express the flow fields obtained by the use of the Peng-Robison equation of state. The results for the velocity field, Figure 5.17, show that the vectors are slightly bigger when the Peng-Robinson equation is used, nevertheless, both results are similar. The mixture fraction field obtained with Peng-Robinson equation is also very similar to the one obtained with the Soave-Redlich-Kwong equation. A slightly higher potential core is obtained, this agrees with the fact that the velocity vectors are also slightly bigger. The results also seem to suggest that the degree of mixture between the injected fluid and the chamber's fluid is higher when the Peng-Robinson equation is employed.

The biggest differences between the use of different equations of state are the values of the density at lower temperature ranges. The density field for the Peng-Robinson equation of state shows higher values of density for the coldest regions of the jet closer to the injector. This may constitute the reason why velocity vectors are bigger for this equation of state. Since the density of the injected fluid is higher, the momentum is also higher (as injection velocity remains the same). This way, due to higher inertia, there's a lower loss of axial velocity which increases the potential core and jet penetration. The phenomenon of entrainment is also enhanced by the higher injection momentum, this may lead to an increased mixture. Finally, the results of density field obtained by the two equations of state are in not far agreement with the results obtained previously by the method originally introduced by Sanders [34], and the same can be concluded to the other flow fields.

5.3.3 Axial Density Distribution

Figure 5.20 shows the axial density distribution for the transcritical case. In this figure are shown the results of this approach with the use of the Soave-Redlich-Kwong equation of state

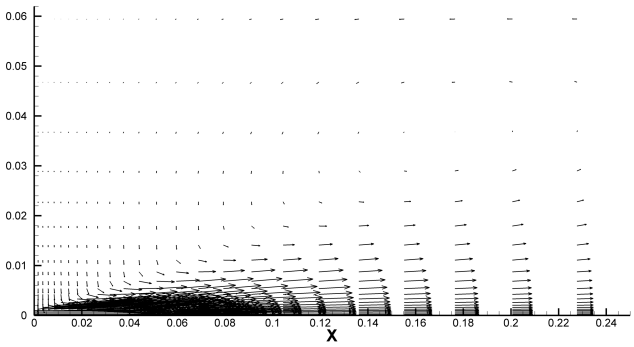

(a)

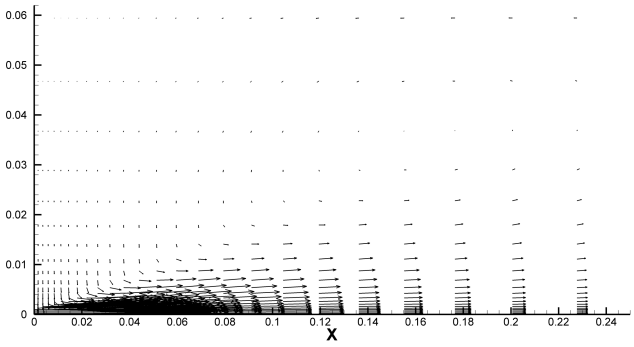

(b)

Figure 5.14: Velocity field of the jet for a) transcritical and b) supercritical conditions with the use of the Soave-Redlich-Kwong equation of state and with constant fluid properties.

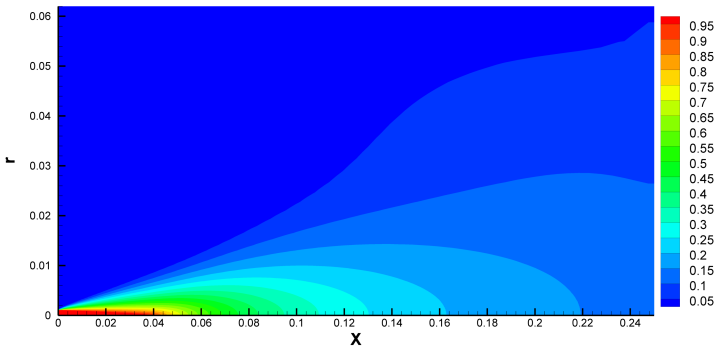

(a)

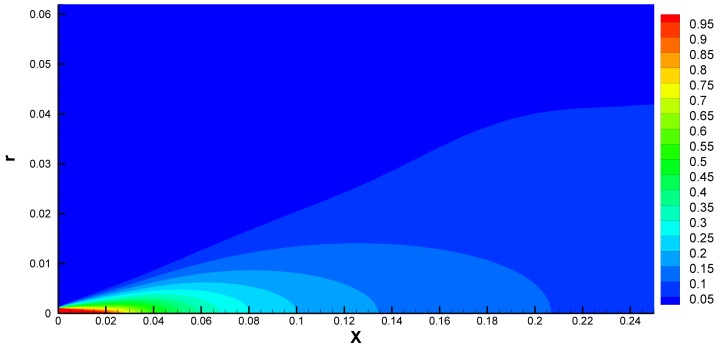

(b)

Figure 5.15: Mixture fraction field of the jet for a) transcritical and b) supercritical conditions with the use of the Soave-Redlich-Kwong equation of state and with constant fluid properties.

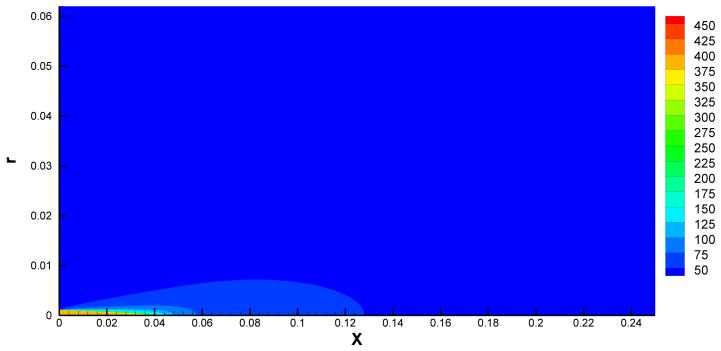

(a)

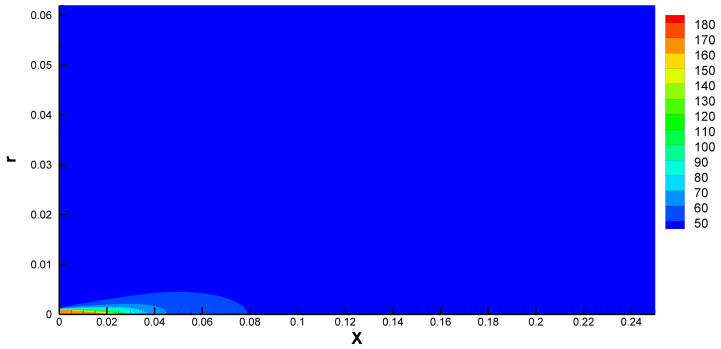

(b)

Figure 5.16: Density field of the jet for a) transcritical and b) supercritical conditions with the use of the Soave-Redlich-Kwong equation of state and with constant fluid properties.

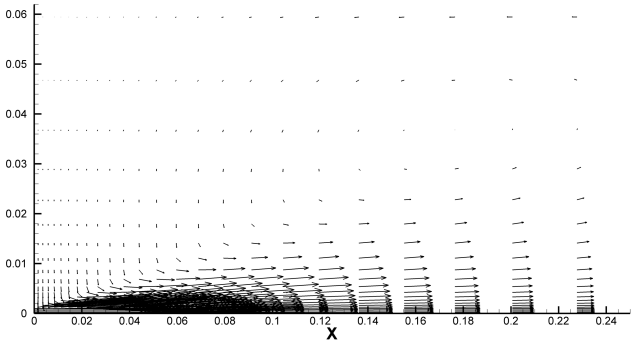

(a)

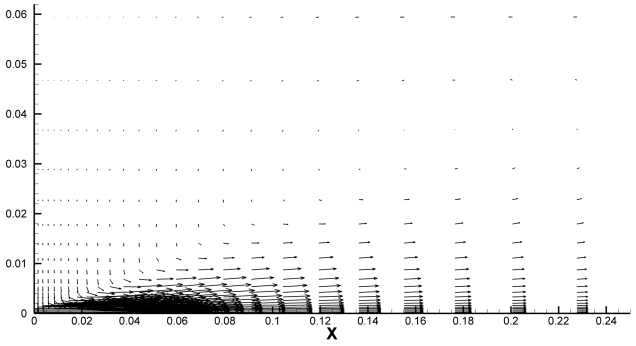

(b)

Figure 5.17: Velocity field of the jet for a) transcritical and b) supercritical conditions with the use of the Peng-Robinson equation of state and with constant fluid properties.

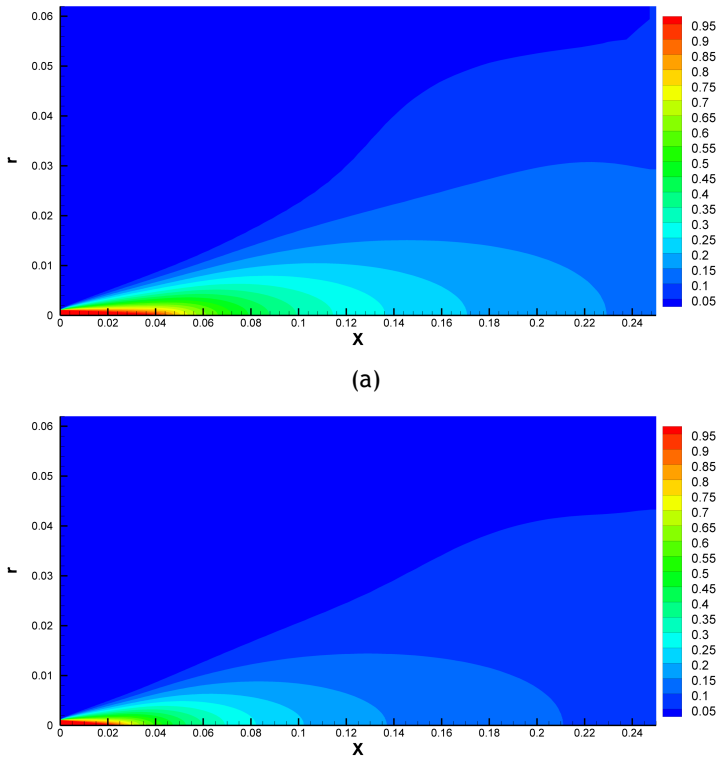

(a)

(b)

Figure 5.18: Mixture fraction field of the jet for a) transcritical and b) supercritical conditions with the use of the Peng-Robinson equation of state and with constant fluid properties.

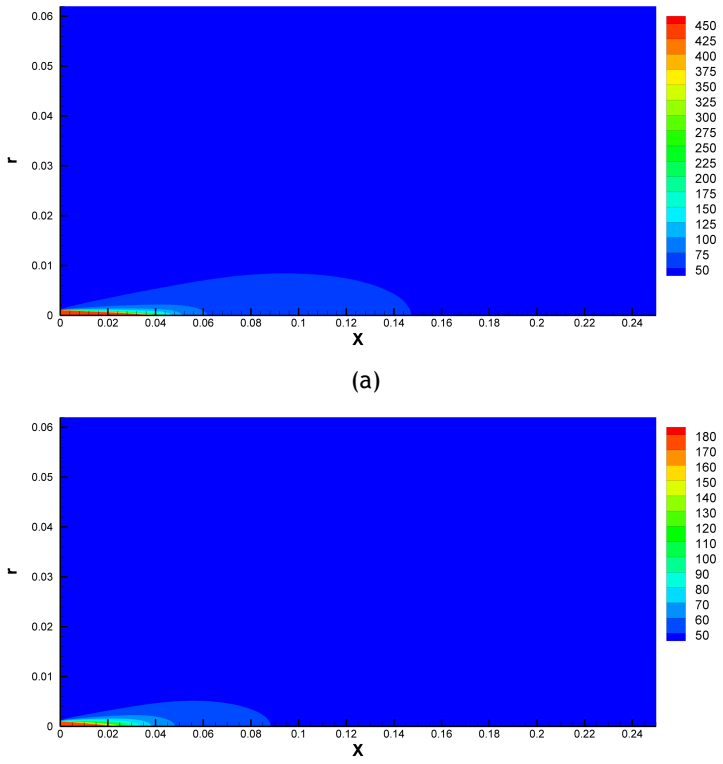

(a)

(b)

Figure 5.19: Density field of the jet for a) transcritical and b) supercritical conditions with the use of the Peng-Robinson equation of state and with constant fluid properties.

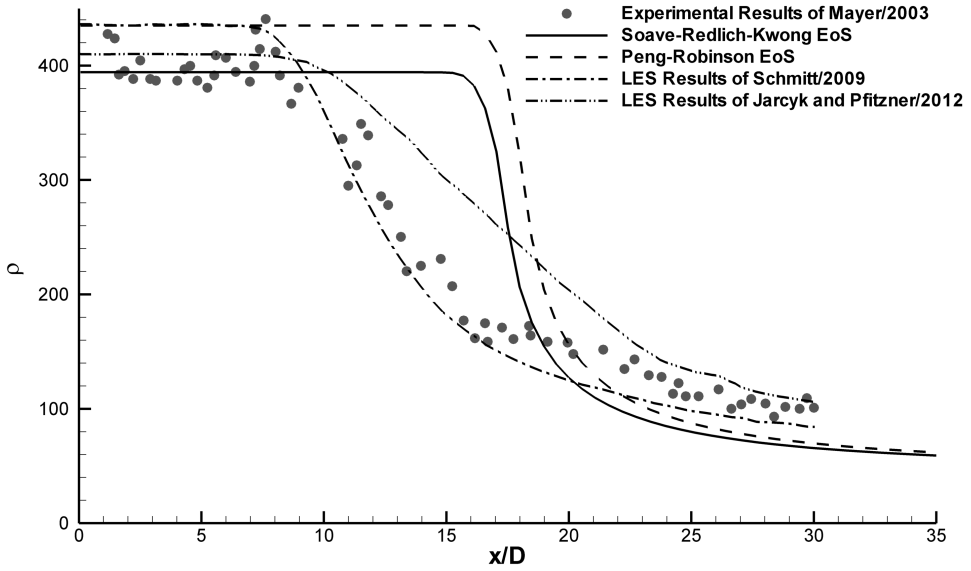

Figure 5.20: Axial density distribution for transcritical case and comparisons with different authors results.

as well as with the Peng-Robinson equation. There, are also shown the experimental results of Mayer et al. [26] and the large eddy simulations of Schmitt et al. [40] and also of Jarczyk and Pfitzner [44]. Both results of the different equations of state for the current approach show a much larger potential core than the one observed in the results of the other authors. With the Soave-Redlich-Kwong equation of state is obtained a potential core of 15.7 injector diameters, as for the Peng-Robinson equation a potential core of 16.4 injector diameters is obtained. These values of potential core length are even longer than the already long potential core obtained by the initial approach treated in section 5.2. Further downstream the current approach keeps the difficulty in fitting the experimental data or the other LES investigations.

The axial density distribution for the supercritical case is represented in Figure 5.21. Again, the current approach employing the two different equations of state is compared with experimental and LES data. For the supercritical case a closer agreement with experimental data is obtained but the over prediction of the potential core length didn't cease to exist. When using the Soave-Redlich-Kwong equation a potential core with a length of 9.4 injector diameters is observed, with the Peng-Robinson equation it increases to a length of 9.6 injector diameters. Downstream of the potential core is obtained a better agreement with experiments between 10 and 15 diameters but then there is a departure from the data provided by Mayer [26]. Still, for this condition, the LES from Schmitt et al. [40] is not able to provide superior agreement.

5.3.4 Radial Density Distribution

The radial density distribution for three different axial distances is represented in Figures 5.22 and 5.23 for respectively the transcritical and supercritical test case. The charts a), b), and c) correspond respectively to the axial distances of 1.2, 5, and 25 injector diameters. In this figures the current approach for each equation of state is compared with the data from Mayer [26]. In Figure 5.22 a) it can be observed that this approach is able to provide close agreement with experimental data, for this case the approach using the Peng-Robinson equation of state has superior agreement being able to predict the correct centreline of the density, on

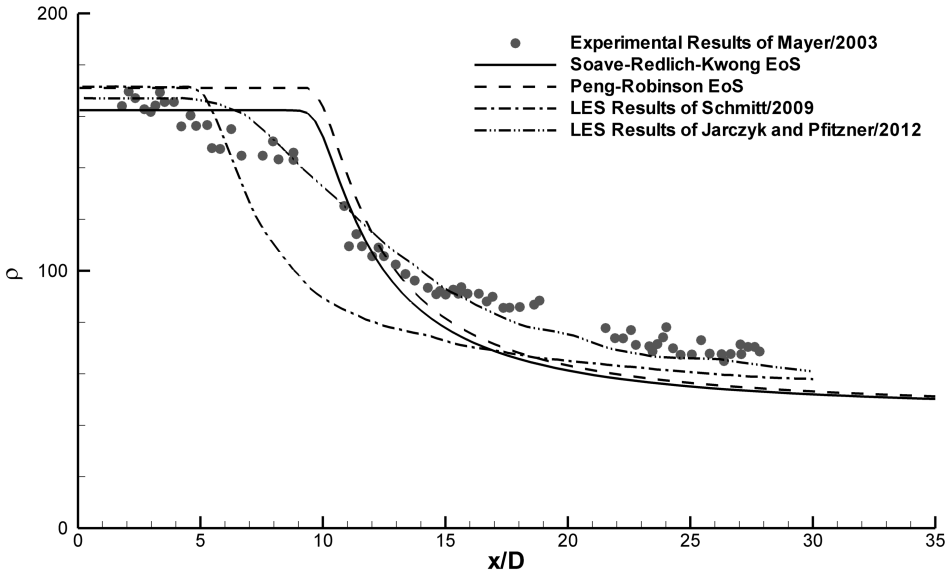

Figure 5.21: Axial density distribution for supercritical case and comparisons with different authors results.

the other hand, with the Soave-Redlich-Kwong equation the predicted density is lower than experiments. The opposite seems to happen for supercritical case at the same axial distance, the approach using Soave-Redlich-Kwong equation predicts more accurately the value of density in centreline while the Peng-Robinson equation over predicts it. Figure 5.22 b), for an axial distance of 5 x/D, shows the approach using the Soave-Redlich-Kwong equation of state being able to reach a closer agreement of the centreline density than the Peng-Robinson equation. For this distance the current approach shows a faster decrease along the radial distance than the experiments, still the agreement is obtained in good degree. For the axial distance of 25 x/D neither approaches are able to predict the correct value of density in the centreline, however the agreement is relatively close. As was already observed above the Peng-Robison equation of state provides always higher values of density than the Soave-Redlich-Kwong equation. The results are very much in line to those achieved by the previous approach.

5.3.5 Jet Spreading Rate

The FWHM of Density for the transcritical conditions for the current approach with both equations of state and the experimental data of Mayer [26] is shown in Figure 5.24. While the same trend already observed in the first approach is also observed here, the longer potential core obtained with this approach causes the expansion of the jet to start more than 5 injector diameters after what observed experimentally. Using a similar methodology to obtain the jet spreading rate as was employed before, the tangent of the spreading rate achieves the value of 0.250 when employing the Soave-Redlich-Kwong equation of state and 0.267 when using the Peng-Robinson equation. For the transcritical case, it is visible that the jet is not yet expanding at an axial distance of 15 x/D, thus, for this case, the calculation of the jet spreading rate is performed between 20 and 30 x/D.

Figure 5.25 shows the FWHM of Density for the current approach with both equation of state at supercritical injection conditions. For this case the two equations of state give very similar results of the jet spreading rate. The Soave-Redlich-Kwong equation provides a tangent of

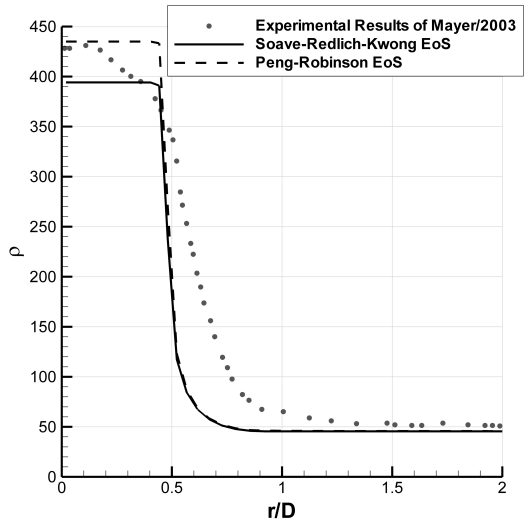

(a)

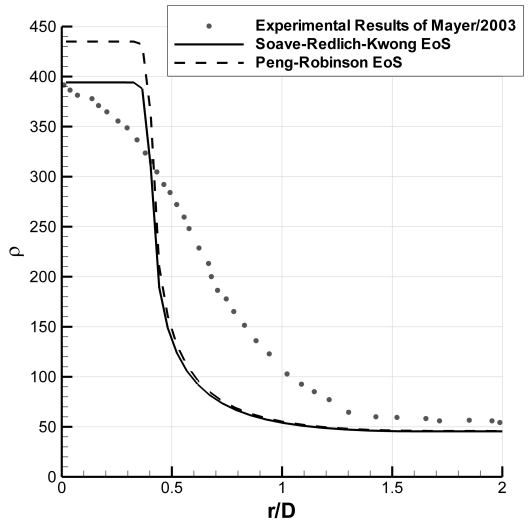

(b)

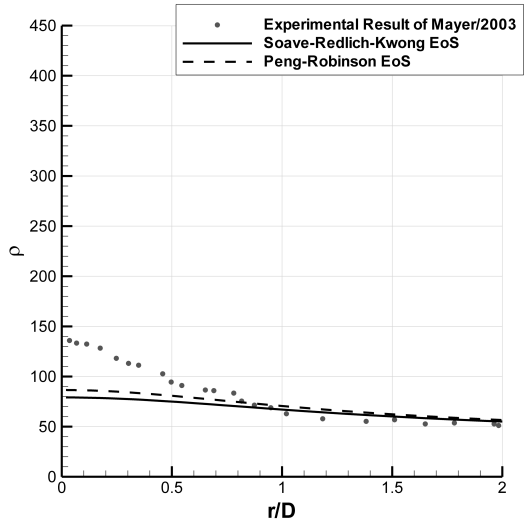

(c)

Figure 5.22: Radial Density Distribution for transcritical case. a) x/D = 1.2; b) x/D = 5; c) x/D = 25

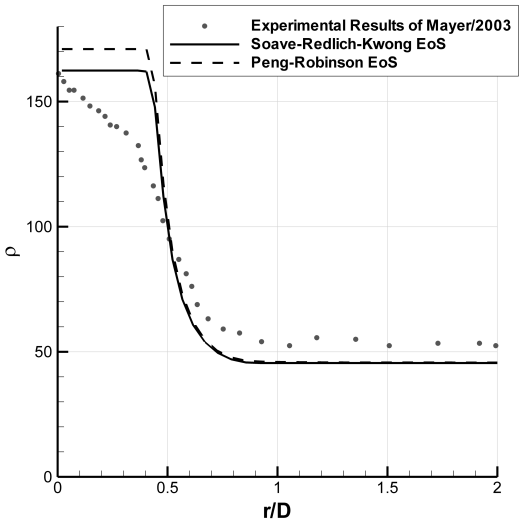

(a)

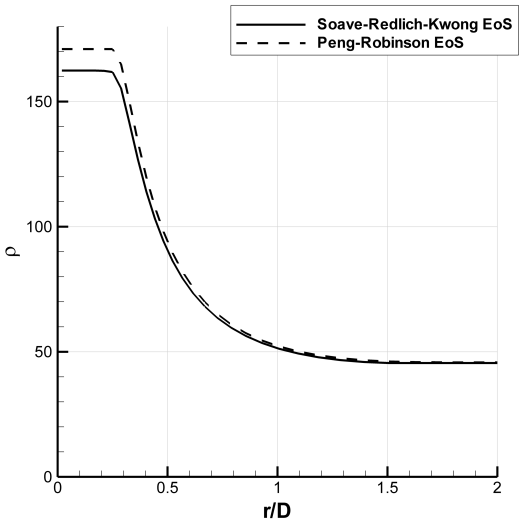

(b)

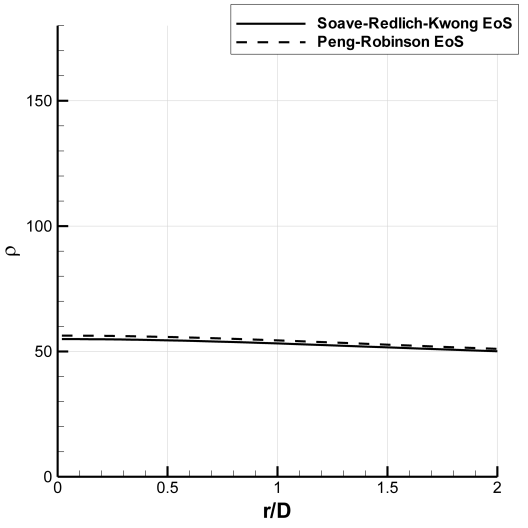

(c)

Figure 5.23: Radial Density Distribution for supercritical case. a) x/D = 1.2; b) x/D = 5; c) x/D = 25

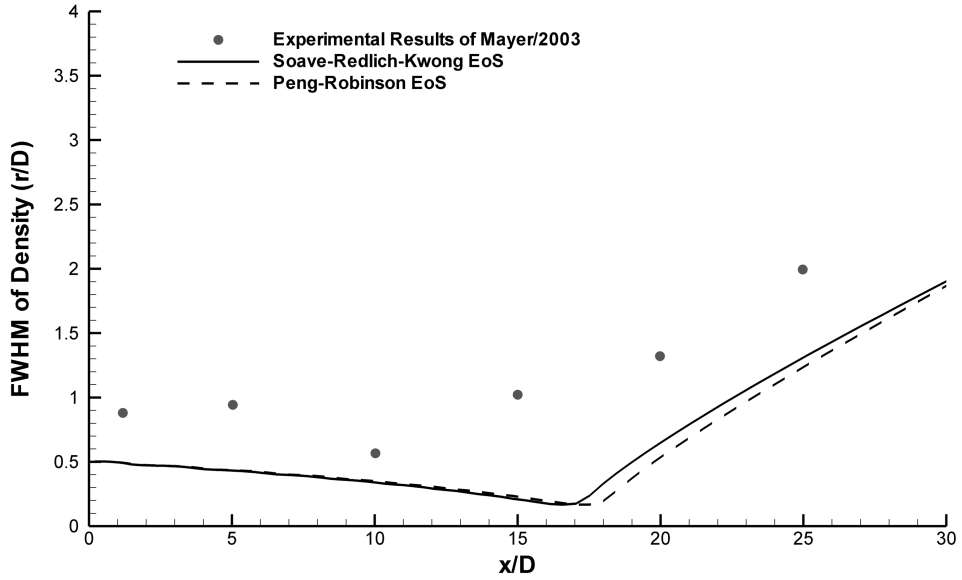

Figure 5.24: Full Width of Half Maximum of Density for transcritical case and comparison with experimental data of Mayer et al. [26].

the spreading rate of 0.214, using the Peng-Robinson equation of state a tangent of 0.232 was obtained. Contrary to what happened at transcritical injection conditions, for the supercritical case the Peng-Robinson equation of state provides a higher spreading of the jet which is closer to the experimental data [25].

For transcritical case this approach is able to provide better agreement of the jet spreading rate than what was obtained by the original approach proposed by Sanders et al. [34]. For the transcritical case the best agreement is obtained when employing the SRK equation, the achieved results have a variation of 27.5% from the experimental results of Mayer et al. [26] as well as to those of Oschwald and Micci [25], variation of 21.4%, much closer than the 61.2% and 53.4% of variation achieved before and a variation from the results of Schmitt of 10.1%. In the supercritical case this approach provides a clear reduction of agreement when compared with experimental data and the values of jet spreading rate become close to those provided by the LES data of Schmitt et al. [40]. The result using the PR EoS shows a variation from experiment [25] of 25.6% and a different of merely 3.9% to the large eddy simulation of Schmitt et al.

Relating to the performance given by the two different equations of state one can conclude that under this approach there is none of them which can without doubts perform better than the other. The results show that the best performance alternates between both equations with one performing better in some aspects and worst in others.

5.4 Real Fluid Equation of State with fluid properties obtained from experimental data

A more realistic methodology to obtain the values of viscosity, thermal conductivity, and specific heat at constant pressure is to make those values depend on the temperature using experimental data, in the form of tables, taken from the Gas Encyclopaedia [62]. From these tables, a linear function defined by parts was created as was already described in Chapter 3, subsections 3.3.3 and 3.4.2. This conducts to a simplistic yet more accurate manner to obtain the proper-

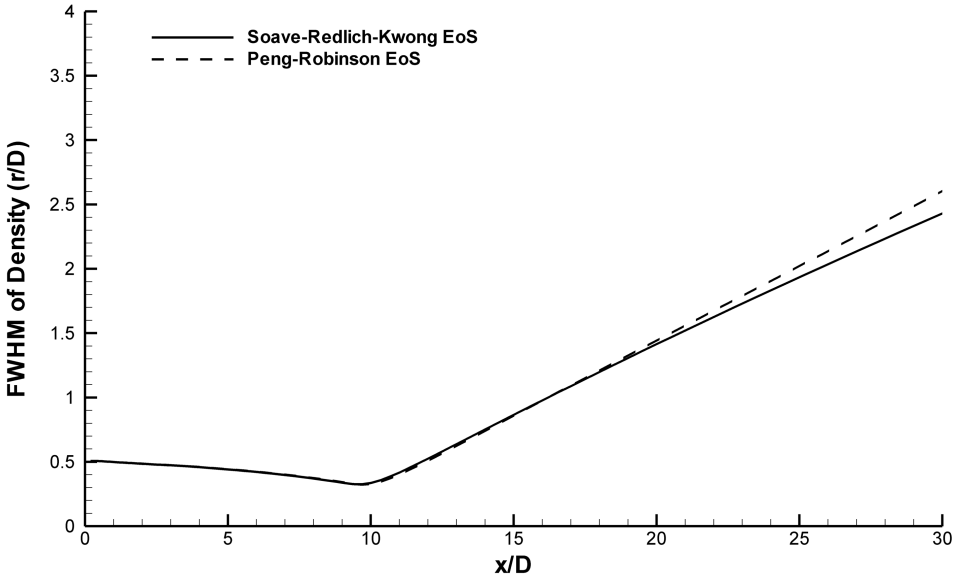

Figure 5.25: Full Width of Half Maximum of Density for supercritical case.

ties values. The results obtained using this methodology will be presented along the present section. Apart from the determination of properties, this methodology is in everything similar to the one presented in the previous section. For this approach the results will be presented for the two real fluid equations of state, allowing a performance comparison between both.

5.4.1 Flow Fields

The velocity, mixture fraction, and density field for the Soave-Redlich-Kwong equation of state are shown respectively in Figures 5.26, 5.27, and 5.28. As before, chart a) represents the transcritical case while b) stands for the supercritical injection condition. The results for all flow fields show very similar results to those already obtained before with previous approaches, however, small variations between them can be observed. In the case of the velocity field, expressed in Figure 5.26, for both cases extremely small differences exist when comparing with the second approach, thus making all the analysis made for the previous approach also valid now. The same conclusions can be taken for the mixture fraction field, in Figure 5.27 as well as for the density field, Figure 5.28.

Figures 5.29, 5.30, and 5.31 show the flow fields which were obtained employing the Peng-Robinson equation of state. The velocity field obtained by the use of the PR equation of state, Figure 5.29, shows like was already seen in previous section a very slight increase of vector size in the axial direction when compared of the SRK equation, this is probably due to the highest value of density obtained with the PR equation which increases momentum of the jet. Nevertheless, the results between both equations of state are nearly identical.

The Peng-Robinson equation of state produces a mixture fraction field, Figure 5.30, which is all identical to the one produced by the other equation of state. As before, a slightly higher potential core is obtained which agrees with the fact that the velocity vectors are also slightly bigger. The Peng-Robinson also seems to predict enhanced mixture when compared with Soave-Redlich-Kwong equation.

The analysis of the density field for the Peng-Robinson equation of state, Figure 5.31, and its comparison to the one obtained for the with the Soave-Redlich-Kwong equation of state

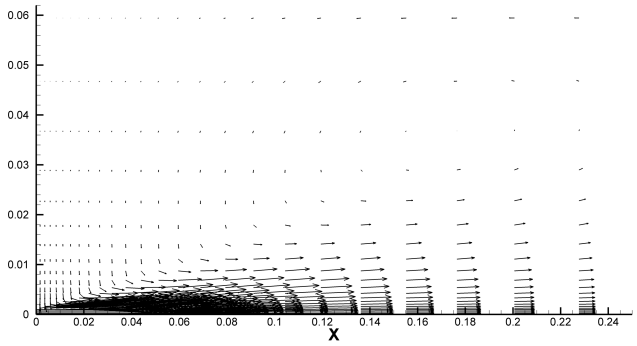

(a)

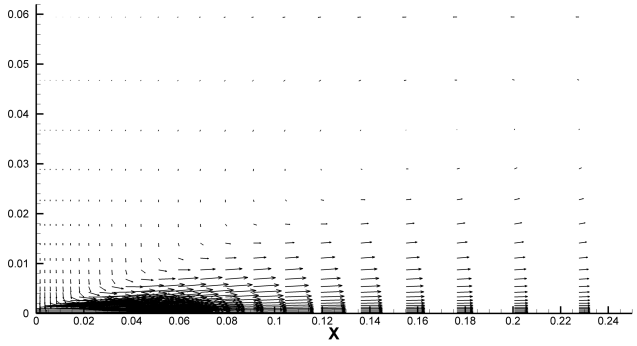

(b)

Figure 5.26: Velocity field of the jet for a) transcritical and b) supercritical conditions with the use of the Soave-Redlich-Kwong equation of state and with variable fluid properties.

shows once again that the PR equation predicts higher values of density. It's also apparent the existence of a higher jet penetration as well as a widening of the jet. Like for the mixture fraction, these results seem to suggest an increased mixture when compared with the SRK equation.

5.4.2 Axial Density Distribution

The axial density distribution for the transcritical case using the present approach is shown in Figure 5.32. There are shown the results obtained with both equations of state as well as the experimental results of Mayer et al. [26] and the large eddy simulations of Schmitt et al. [40] and of Jarczyk and Pfitzner [44]. The potential core obtained with the Soave-Redlich-Kwong has the length of 15.5 injector diameters, for the Peng-Robinson equation of state the potential core has the length of 16.2 injector diameters. These values are slightly closer to the ones obtained by other authors when compared with the results from the approach that uses constant value of the properties in section 5.3. Further downstream the evolution of the axial density distribution follows the same trend already observed for the previous approach with constant properties.
Figure 5.33 represents the axial density distribution for the supercritical case for the approach of with variable properties using both equations of state. The obtained results are also compared with the experimental and LES results. Like in the previous approach, for this one, a better agreement with experimental results is obtained than in the transcritical case. The potential core using the SRK equation as a length of 9.3 injector diameters while when employing the PR equation of state, a length of 9.5 is reached. These results are for both cases 0.2 x/D shorter than the one obtained with constant properties, this puts it slightly closer to experimen-

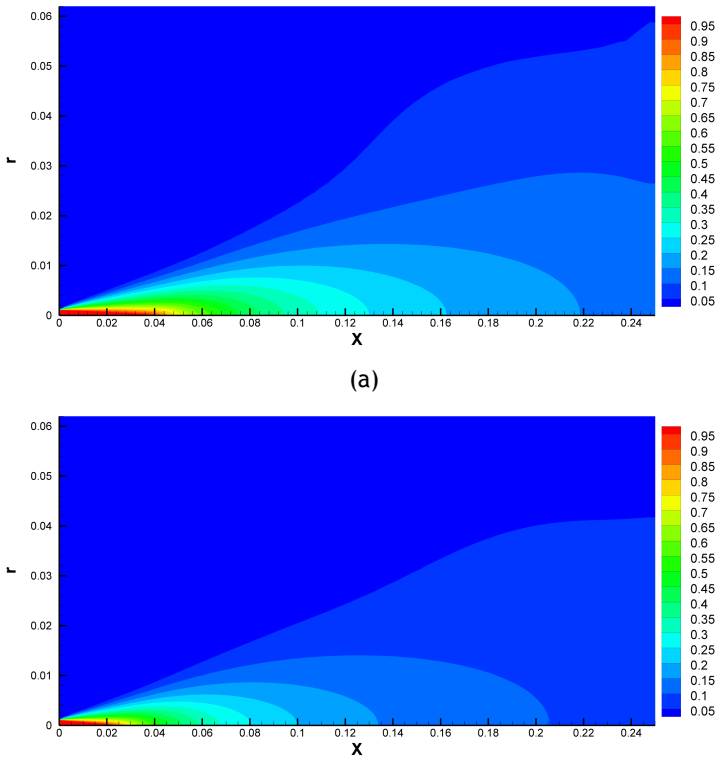

(a)

(b)

Figure 5.27: Mixture fraction field of the jet for a) transcritical and b) supercritical conditions with the use of the Soave-Redlich-Kwong equation of state and with variable fluid properties.

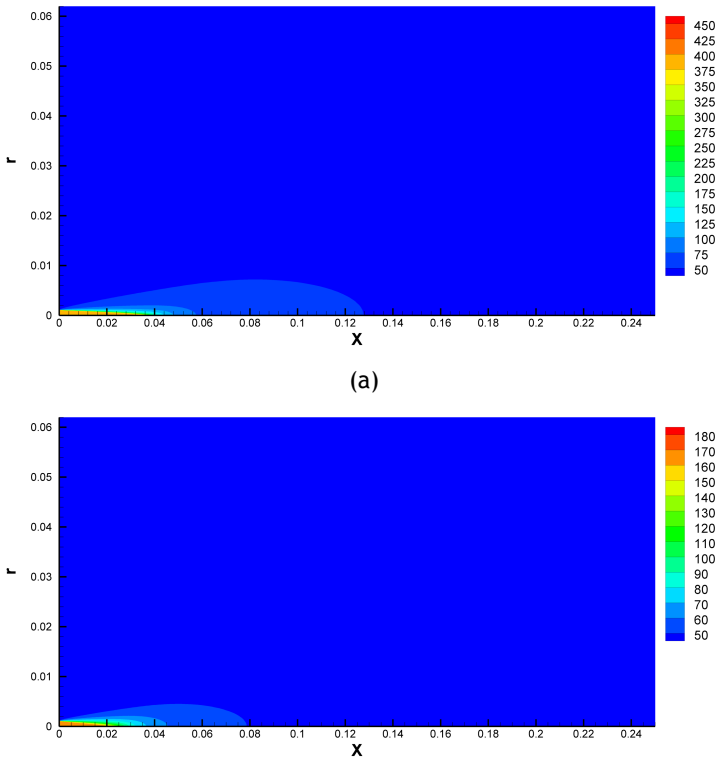

(a)

(b)

Figure 5.28: Density field of the jet for a) transcritical and b) supercritical conditions with the use of the Soave-Redlich-Kwong equation of state and with variable fluid properties.

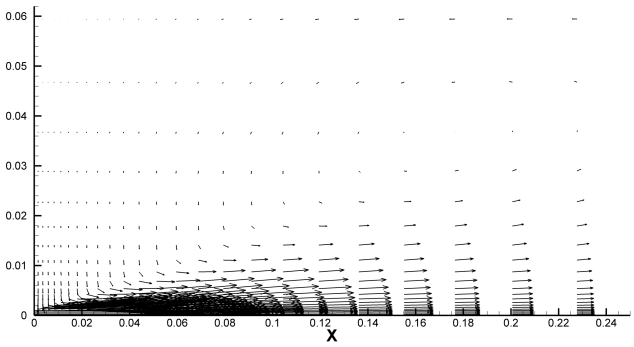

(a)

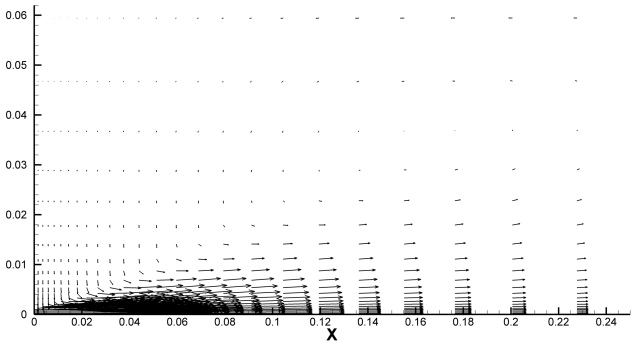

(b)

Figure 5.29: Velocity field of the jet for a) transcritical and b) supercritical conditions with the use of the Peng-Robinson equation of state and with variable fluid properties.

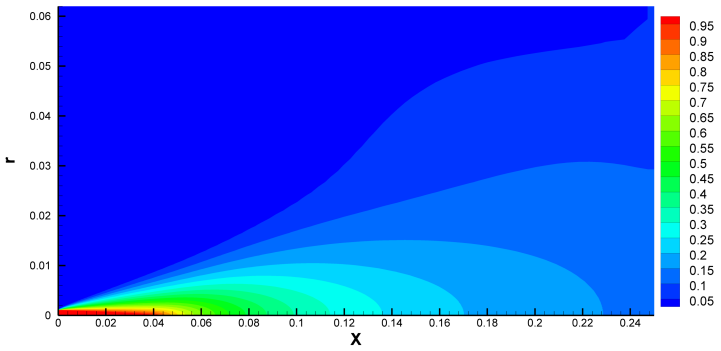

(a)

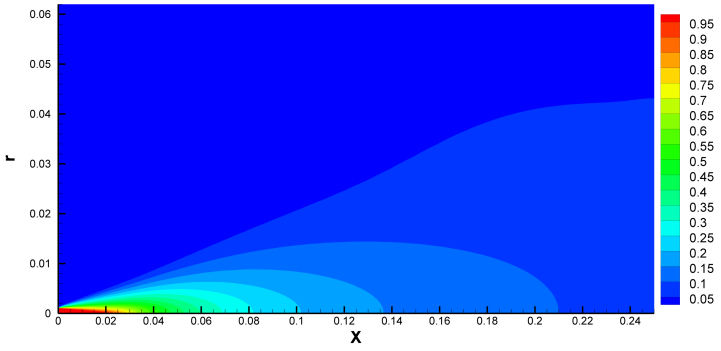

(b)

Figure 5.30: Mixture fraction field of the jet for a) transcritical and b) supercritical conditions with the use of the Peng-Robinson equation of state and with variable fluid properties.

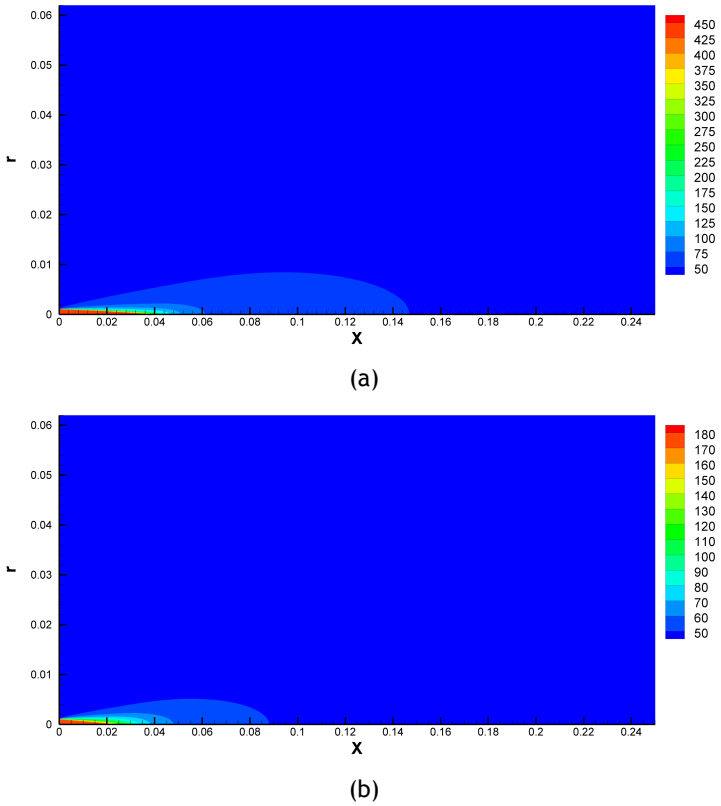

Figure 5.31: Density field of the jet for a) transcritical and b) supercritical conditions with the use of the Peng-Robinson equation of state and with variable fluid properties.

tal data, as well to the large eddy simulations of other authors. Downstream of the potential core, similar conclusions to those obtained with the approach of section 5.3 are reached. For this test case this approach is able to outperform the results of Schmitt [40] during a large portion of the domain.

5.4.3 Radial Density Distribution

The radial density distribution for the transcritical case is shown in Figure 5.34 for three different axial distances of 1.2 x/D, 5 x/D, and 25 x/D which correspond respectively to charts a), b), and c). In these figures the experimental results of Mayer et al. [26] are compared with the results obtained by the present approach using both real fluid equations of state. The obtained results are very much identical to those already obtained before for numerical approach in which viscosity, thermal conductivity, and specific heat are set as constants. The general agreement is good for 1.2 and 5 injector diameters, Peng-Robinson performs better at the shorter distance while the Soave-Redlich-Kwong equation predicts a more accurate centreline density for 5 injector diameters. At 25 injector diameters both equations give similar results which less accurately predict the experimental data.
Figure 5.35 shows the same results for the supercritical case. The Soave-Redlich-Kwong predict a closer maximum density at 1.2 x/D, but both equations have a similar evolution which agrees quite well with the experimental data. As before the main difference between the results of both equations is that in the higher range of densities the Peng-Robinson equation tends to provide higher values of it. However, the following evolution of density in radial direction is quite similar between both equations of state.

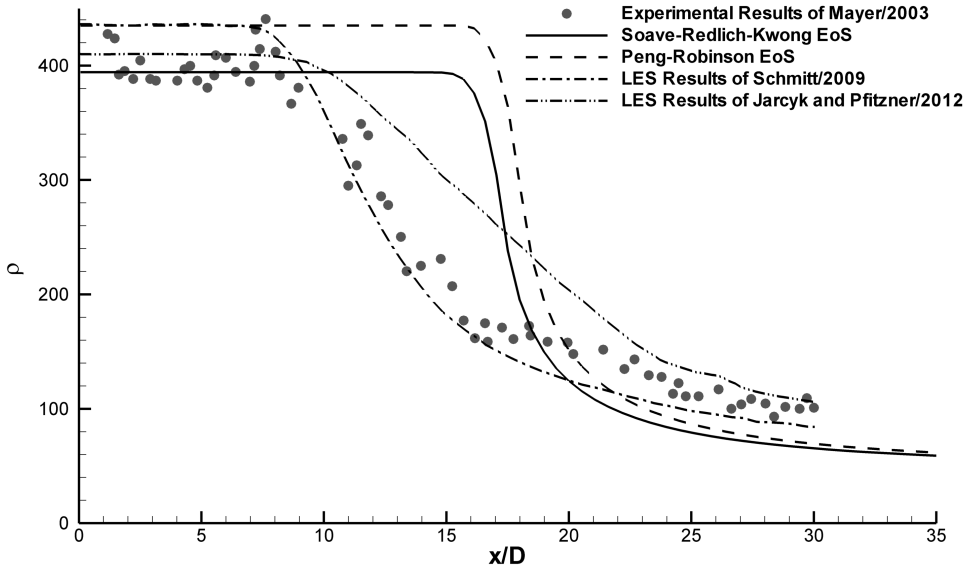

Figure 5.32: Axial density distribution for transcritical case and comparisons with different authors results.

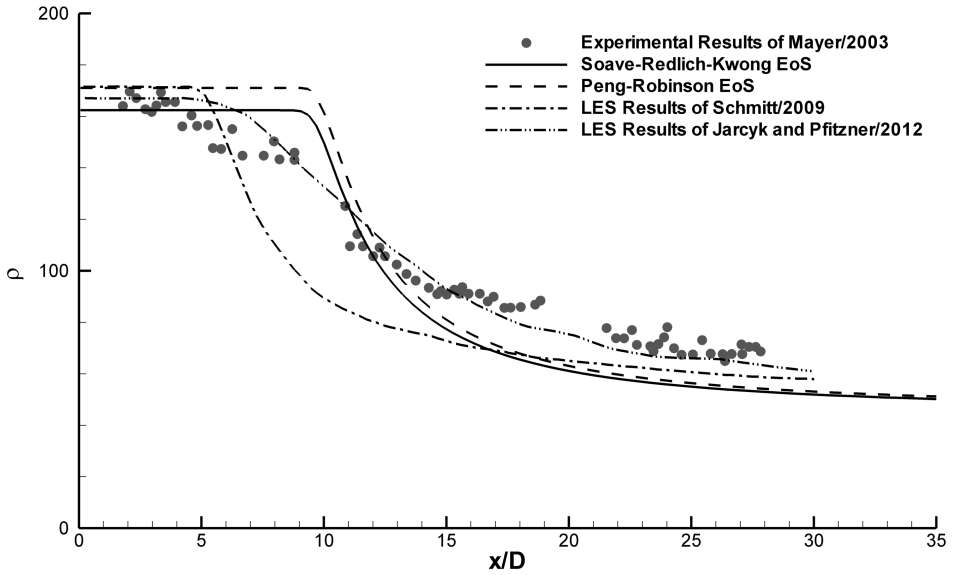

Figure 5.33: Axial density distribution for supercritical case and comparisons with different authors results.

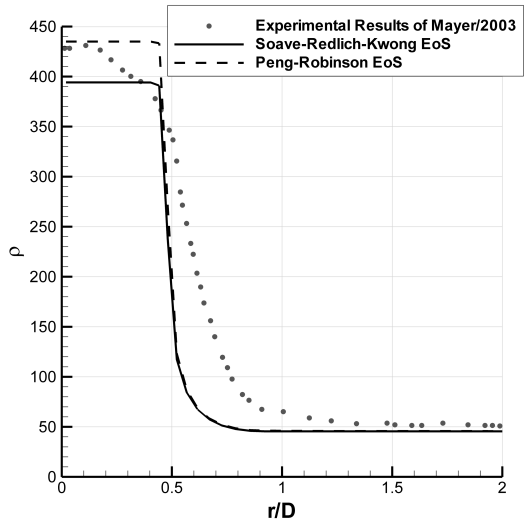

(a)

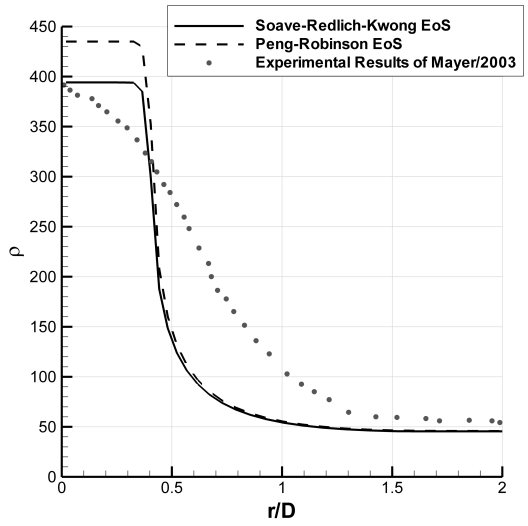

(b)

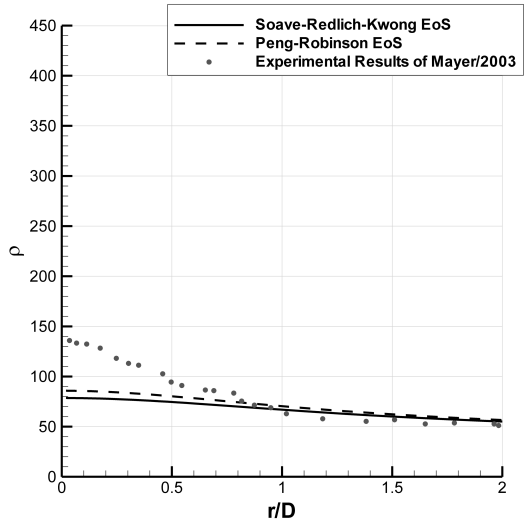

(c)

Figure 5.34: Radial Density Distribution for transcritical case. a) x/D = 1.2; b) x/D = 5; c) x/D = 25

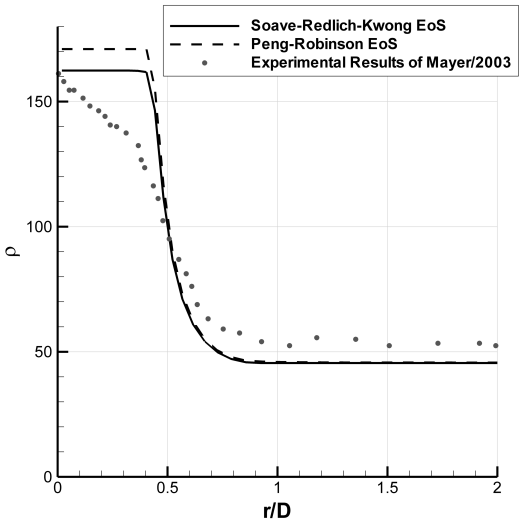

(a)

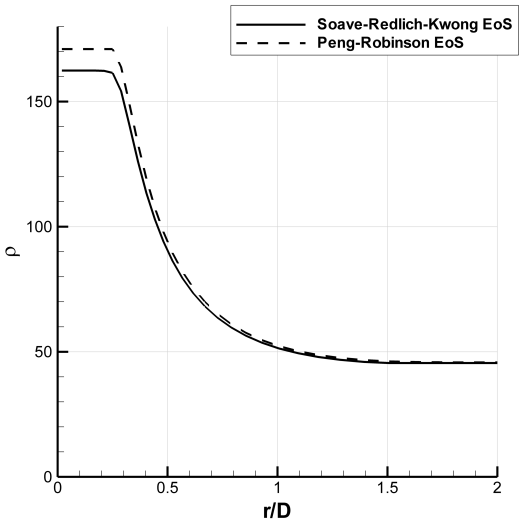

(b)

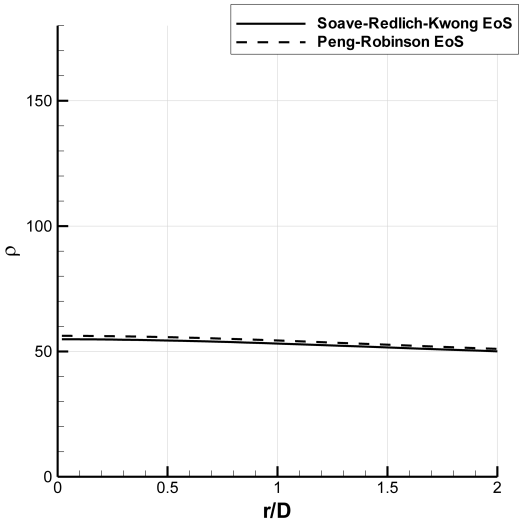

(c)

Figure 5.35: Radial Density Distribution for supercritical case. a) x/D = 1.2; b) x/D = 5; c) x/D = 25

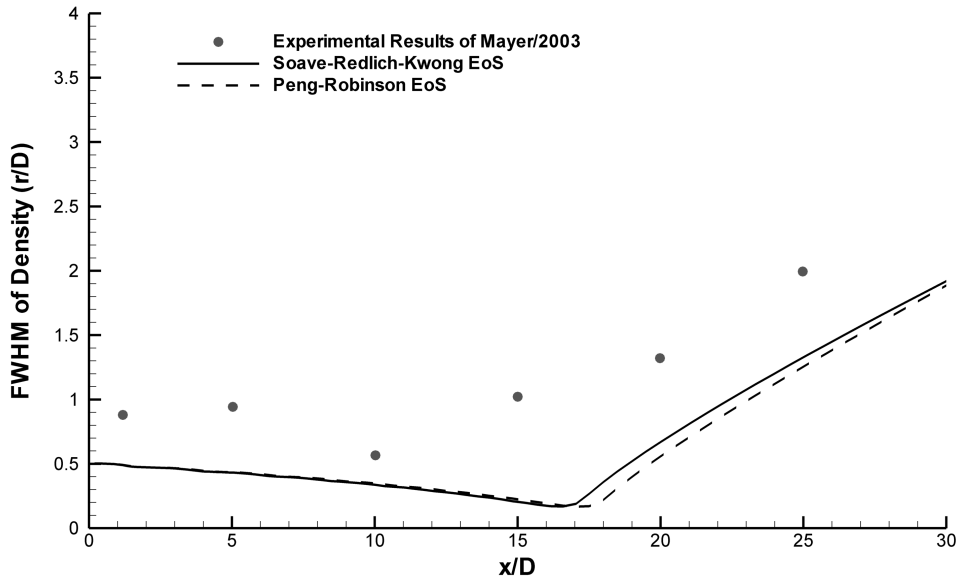

Figure 5.36: Full Width of Half Maximum of Density for transcritical case and comparison with experimental data of Mayer et al. [26].

5.4.4 Jet Spreading Rate

Figure 5.36 shows the FWHM of Density at transcritical injection conditions obtained by the presents approach, for the two equations of state, as well as for the experimental data of Mayer [26]. Like in the previous approach, the calculation of the spreading rate is done for the transcritical case between 20 and 30 jet diameters and the evolution of the profile obtained is similar to that already obtained before. For the Soave-Redlich-Kwong equation of state, the jet spreading rate holds a tangent with a value of 0.250 which is the same that was observed for the approach with constant value of the fluid properties, the value shows the same level of agreement with experiments being very close to what was obtained with the LES approach of Schmitt. For the same test case the Peng-Robinson equation of state is able to provide a jet spreading rate with a tangent of 0.266, this is a result in worse agreement to the experimental data when compared with results obtained through the use of the SRK equation of state, still is slightly closer when compared with the approach with constant value of properties.

Figure 5.37 shows the FWHM of Density for the supercritical case using both equations of state. After initial jet spreading decrease which lasts until an axial distance of approximately 8 injector diameters the jet starts spreading starts increasing at a rate with a tangent of 0.214 for the Soave-Redlich-Kwong equation of state and of 0.234 for the Peng-Robinson. This results are almost the same obtained with the approach of section 5.3.

As a general conclusion the results obtained with this approach which makes use of variable values of fluid properties seems to reach the same degree of agreement with experiments as the approach treated in section 5.3 which assumes viscosity, thermal conductivity, and specific heat as constant values.

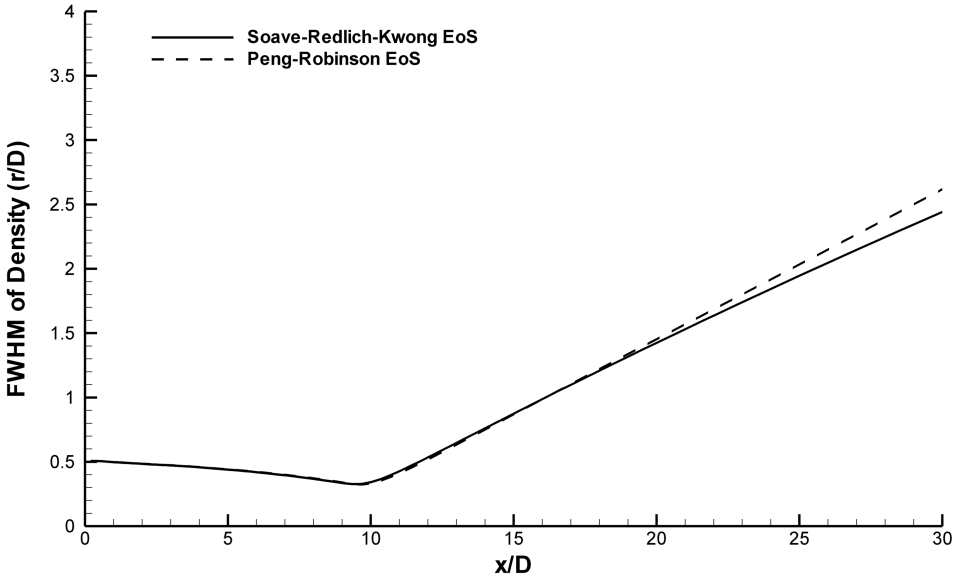

Figure 5.37: Full Width of Half Maximum of Density for supercritical case.

5.5 Real Fluid Equation of State with viscosity and thermal conductivity obtained from Lemmon and Jacobsen

In Chapter 3 was presented the formulation provided by Lemmon and Jacobsen [65] which allows the determination of viscosity and thermal conductivity for different values of temperature and pressure. This formulation provides a higher degree of agreement with the values provided by the Gas Encyclopaedia [62] than any other of the methodologies investigated in the present work.

The approach treated in the present section makes use of the Lemmon and Jacobsen [65] formulation for the calculation of viscosity and thermal conductivity. As for the specific heat at constant pressure the same methodology employed in the previous section and described in the section 3.5.1 of Chapter 3 is employed. Besides the different methodology for the calculation of viscosity and thermal conductivity, the approach presented in the present section has no other difference to the third approach, treated in previous section, and as before, results will be present and compared for both Soave-Redlich-Kwong and Peng-Robinson equations of state.

5.5.1 Flow Fields

Figures 5.38, 5.39, and 5.40 show the velocity, mixture fraction, and density fields when employing the Soave-Redlich-Kwong equation of state for the transcritical, a), and the supercritical, b), test cases. Analysing the velocity field for this approach in the transcritical case, Figure 5.38 a), and comparing to what was obtained by the approach of the previous section, Figure 5.26 a), can be concluded that the vectors seem to have a smaller size in the axial direction. However, the entrainment phenomenon seems to be more intense, this appears to suggest a higher interaction between the injected fluid and the one present in the chamber.

Comparing the mixture fraction field of this approach and transcritical, Figure 5.39 a), with the one obtained in previously, Figure 5.27 a), can be observed a smaller potential core as well as a widening of the jet. A similar conclusion is obtained when comparing the density fields of the

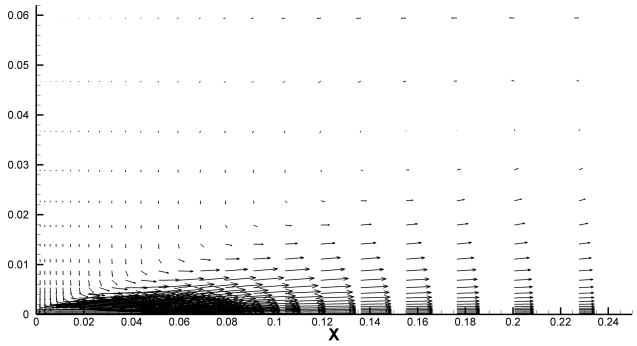

(a)

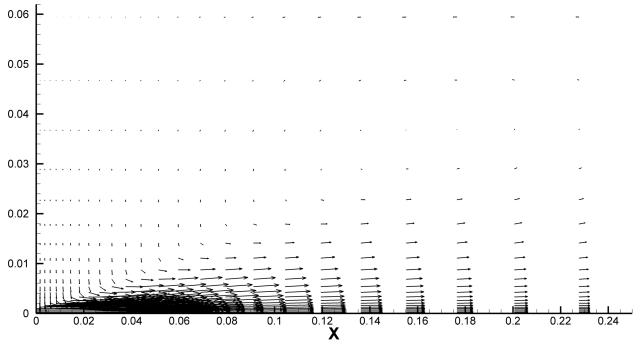

(b)

Figure 5.38: Velocity field of the jet for a) transcritical and b) supercritical conditions with the use of the Soave-Redlich-Kwong equation of state and with fluid properties obtained from [65].

two approaches.
By comparing the same flow fields for the supercritical case, identical results are found between the two approaches. The same happens when comparing the results obtained with the Peng-Robinson equation of state. Figures 5.41, 5.42, and 5.43 show the velocity, mixture fraction, and density fields when employing the Peng-Robinson equation of state. The results are virtually identical to those observed in section 5.4, and the same conclusions presented before can be applied for this approach.

5.5.2 Axial Density Distribution

Figure 5.44 shows the axial density distribution for the transcritical case for the present approach. Are shown the results obtained with both equations of state as well as the experimental results of Mayer et al. [26] and the large eddy simulations of Schmitt et al. [40] and of Jarczyk and Pfitzner [44]. The potential core obtained with the Soave-Redlich-Kwong has the length of 14.0 injector diameters, for the Peng-Robinson equation of state the potential core has the length of 16.3 injector diameters. For the transcritical case the results are in better agreement with experimental then the results obtained by the approaches of sections 5.3 and 5.4. The Peng-Robinson equation shows essentially the same result already obtained in section 5.4.
In Figure 5.45 are shown the same results but for supercritical injection conditions. The results are very similar, if not identical to what was obtained in section 5.3. The potential core using the SRK equation as a length of 9.4 injector diameters while when employing the PR equation of state, a length of 9.6 is obtained. The results are barely the same that were obtained before

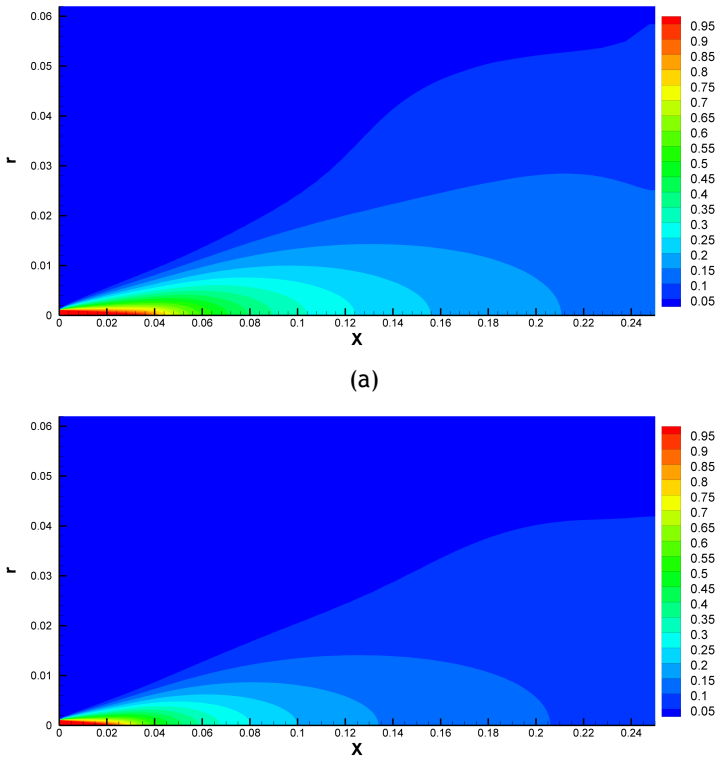

(a)

(b)

Figure 5.39: Mixture fraction field of the jet for a) transcritical and b) supercritical conditions with the use of the Soave-Redlich-Kwong equation of state and with fluid properties obtained from [65].

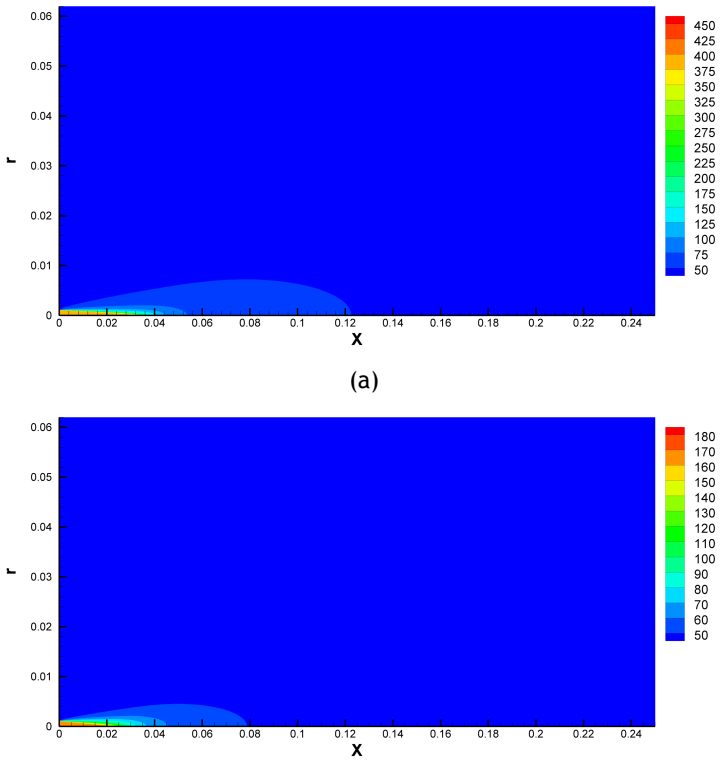

(a)

(b)

Figure 5.40: Density field of the jet for a) transcritical and b) supercritical conditions with the use of the Soave-Redlich-Kwong equation of state and with fluid properties obtained from [65].

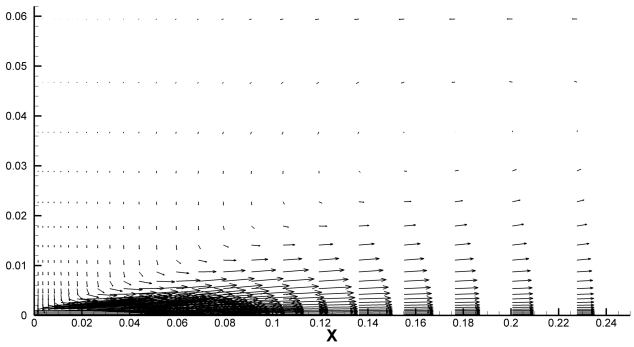

(a)

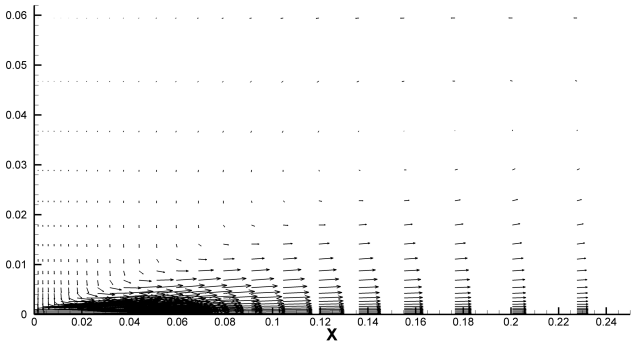

(b)

Figure 5.41: Velocity field of the jet for a) transcritical and b) supercritical conditions with the use of the Peng-Robinson equation of state and with fluid properties obtained from [65].

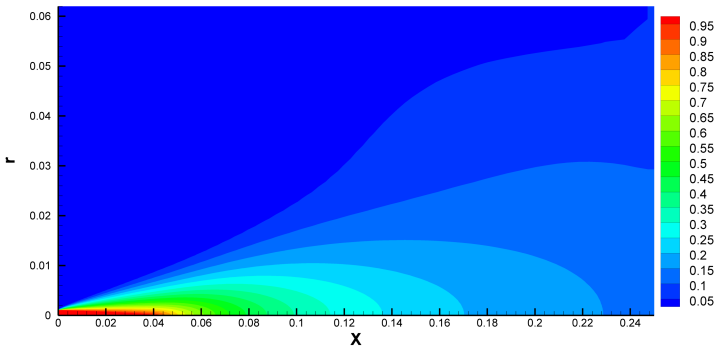

(a)

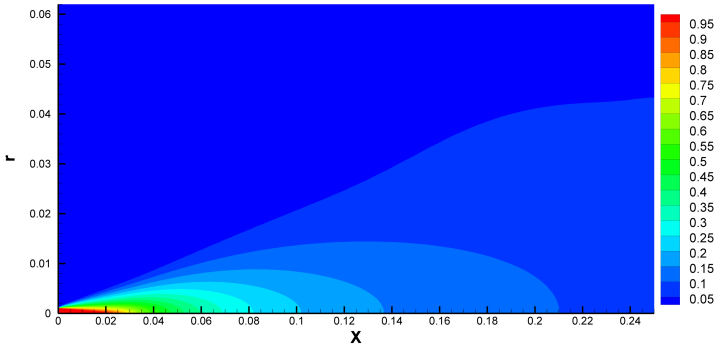

(b)

Figure 5.42: Mixture fraction field of the jet for a) transcritical and b) supercritical conditions with the use of the Peng-Robinson equation of state and with fluid properties obtained from [65].

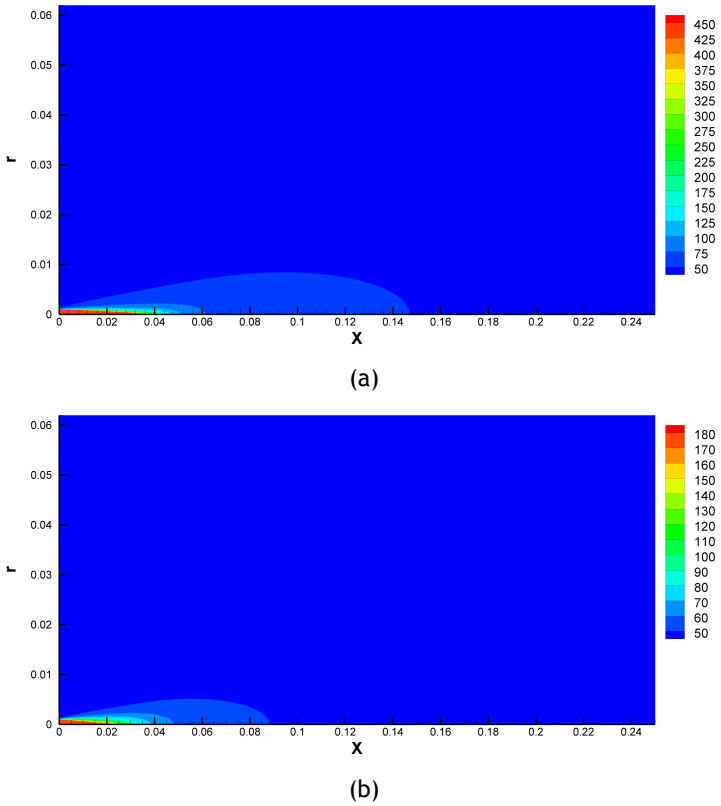

Figure 5.43: Density field of the jet for a) transcritical and b) supercritical conditions with the use of the Peng-Robinson equation of state and with fluid properties obtained from [65].

with only an increase of 0.1 x/D.

5.5.3 Radial Density Distribution

Figure 5.46 shows the radial density distribution using the current approach for the transcritical case. No visible differences are observed between the results obtained in section 5.4 as the results are identical. The same can be conclude for the supercritical case, Figure 5.47 shows the same results for all the axial distances already obtained in the previous section as can be observed in Figure 5.35.

5.5.4 Jet Spreading Rate

The FWHM of Density for the transcritical case obtained employing the present approach is shown in Figure 5.48. Comparing both equations of state, it can be observed that the SRK equation produces a smaller potential core, which is closer to what the experimental data of Mayer et al. [26] expresses. Analysing the jet spreading rate, the Soave-Redlich-Kwong equation of state shows a tangent of 0.249, a variation of 27% and 20.8% when compared respectively with both experiments [26] and [25] closer than the variation of 35.7% and 29.1% obtained with the Peng-Robinson equation which gives a tangent of 0.266. This also shows that while for this approach the SRK equation produces a result slightly in closer agreement with experimental when compared with the previous approach, the PR equation produces barely the same result obtained with the approach of section 5.4.

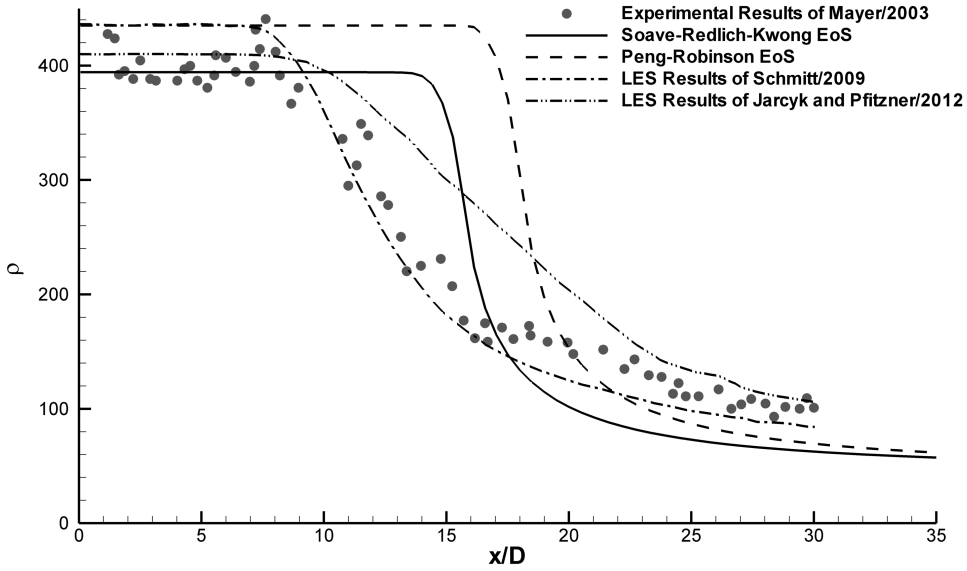

Figure 5.44: Axial density distribution for transcritical case and comparisons with different authors results.

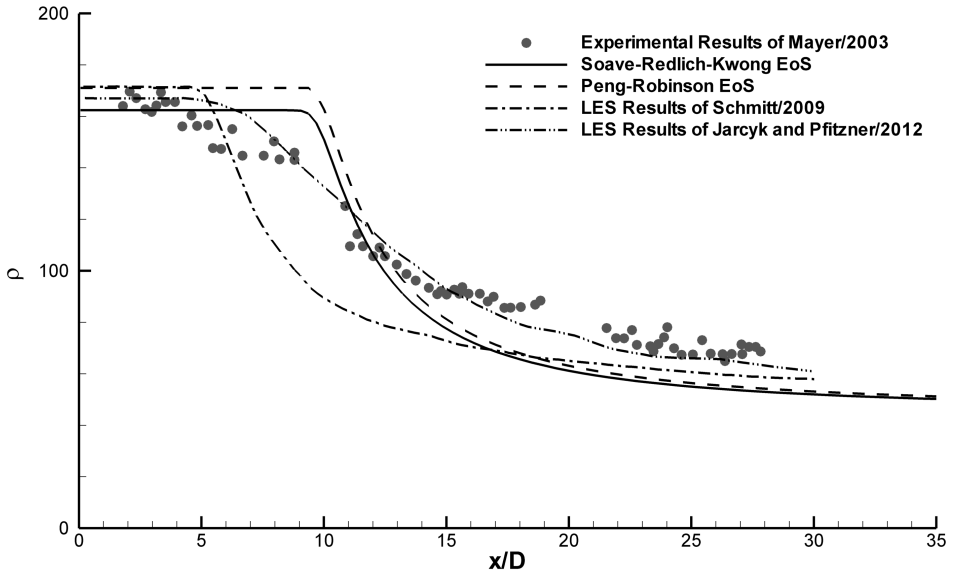

Figure 5.45: Axial density distribution for supercritical case and comparisons with different authors results.

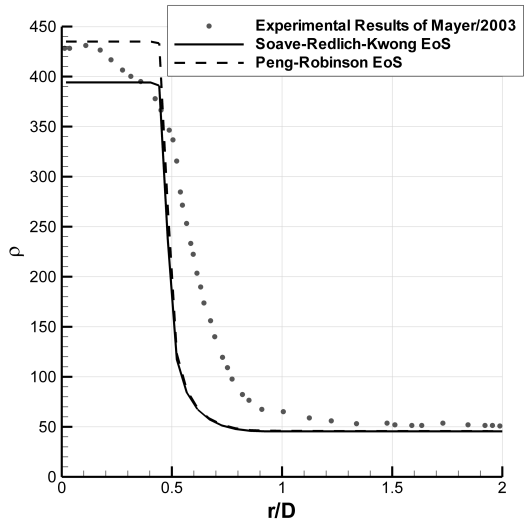

(a)

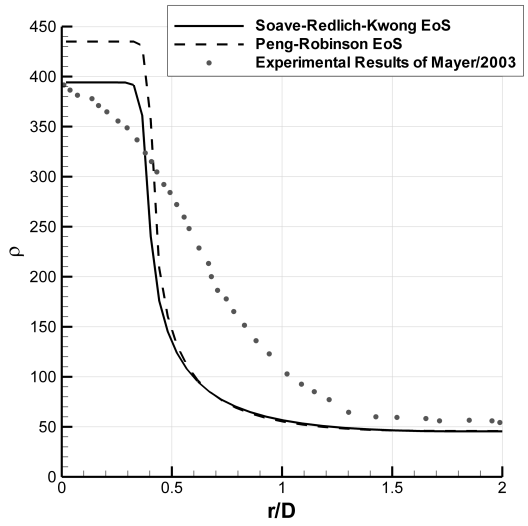

(b)

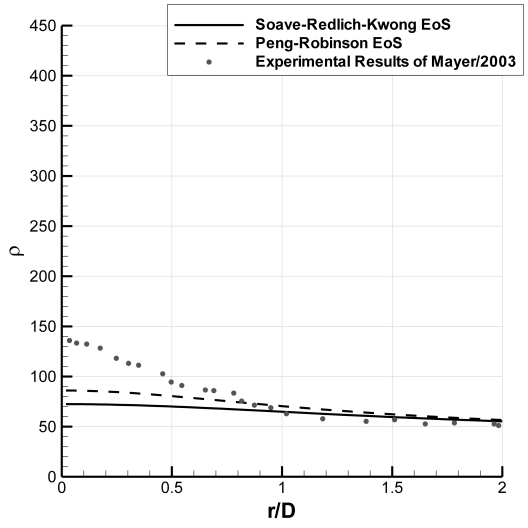

(c)

Figure 5.46: Radial Density Distribution for transcritical case. a) x/D = 1.2; b) x/D = 5; c) x/D = 25

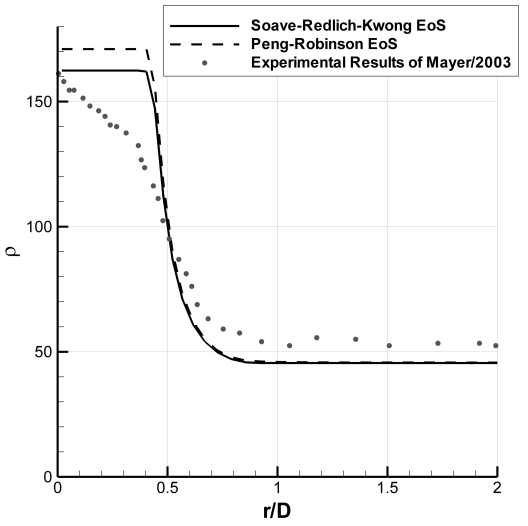

(a)

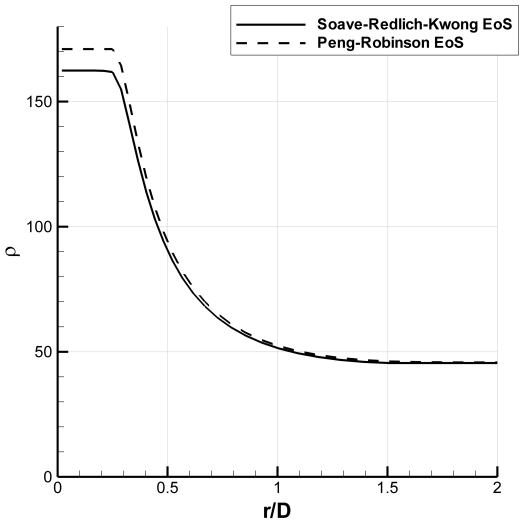

(b)

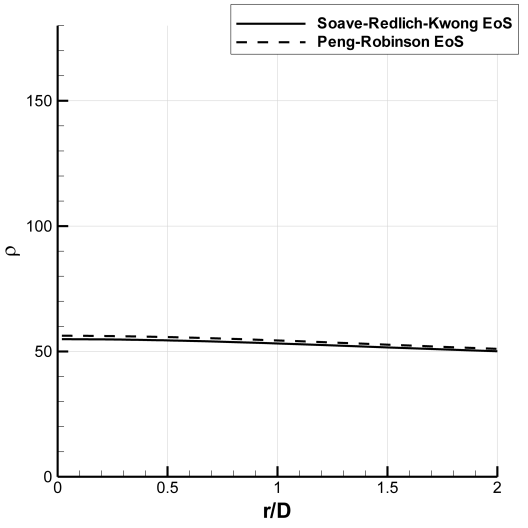

(c)

Figure 5.47: Radial Density Distribution for supercritical case. a) x/D = 1.2; b) x/D = 5; c) x/D = 25

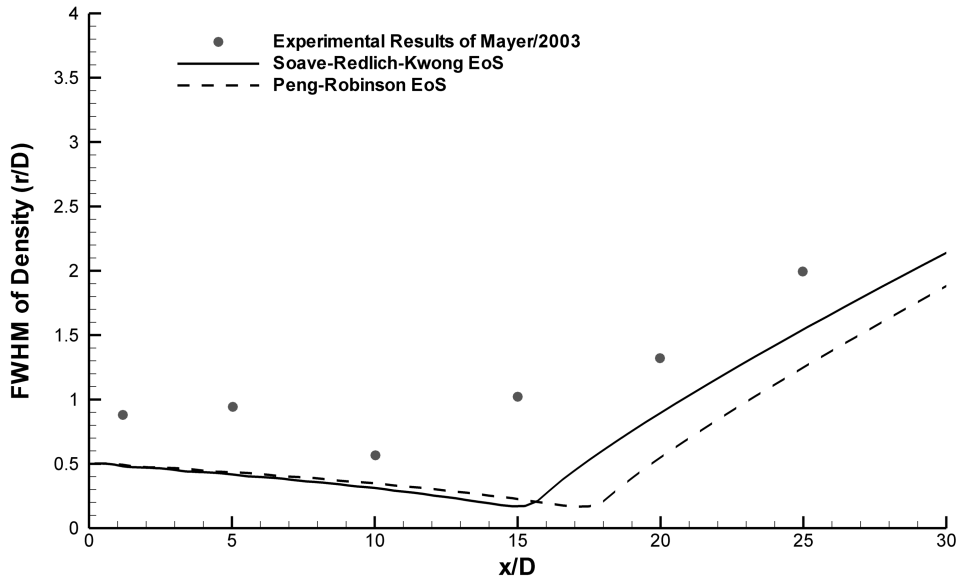

Figure 5.48: Full Width of Half Maximum of Density for transcritical case and comparison with experimental data of Mayer et al. [26].

Figure 5.49 shows the FWHM of Density for the supercritical case using both equations of state for the present approach. The results are identical to those obtained by the previous approach expressing a jet spreading rate exactly with the same value as obtained in section 5.4. The obtained results, when compared with the spreading rates obtained by Schmitt et al. [40] represent a variation of 12.6% when employing the SRK equation of state and of merely 3.0% density is obtained from PR equation. However, when compared with the experimental data [25] bigger variation of results is found.

5.6 Summary

The results from all the tested approaches in the present investigation are summarized in Tables 5.1 and 5.2. The results for potential core show that the original approach which determines the density through mixture fraction is indeed the one which is able to provide better agreement with the large eddy simulations as well as with experiment. The approaches which introduce real fluid thermodynamics show difficulty in fitting the experimental and LES data, also, the very small difference between the approaches which use different methods of determination of fluid properties seem to indicate a small impact that the molecular properties have on the flow, suggesting that are probably the turbulence characteristics which have more relevance. As for the jet spreading rate results, a different conclusion can be taken.

The employment of a real fluid equation of state in order to determine the density field provides results of jet spreading rate for the transcritical case significantly closer to experiments [70, 25] and the large eddy simulation [40] than the original approach which calculated density from mixture fraction. However, there's a decrease of agreement with experimental [25] spreading rate for the supercritical case when compared with the results of first approach.

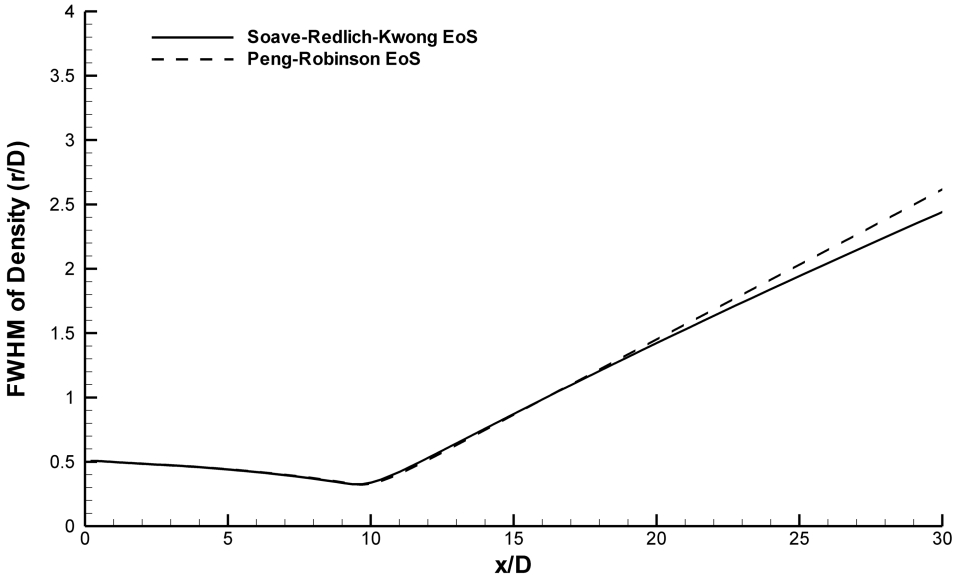

Figure 5.49: Full Width of Half Maximum of Density for supercritical case.

Table 5.1: Potential core x/D.

	Schmitt et al. [40]	Jarczyk and Pfitzner [44]	First Approach	Second Approach		Third Approach		Fourth Approach	
				SRK	PR	SRK	PR	SRK	PR
Transcritical case	7.9	9.0	11.8	15.7	16.4	15.5	16.2	14.0	16.3
Supercritical case	5.1	6.0	7.8	9.4	9.6	9.3	9.5	9.4	9.6

Table 5.2: Tangent of the Jet Spreading Rate.

	Oschwald and Micci [25]	Mayer et al. [26]	Schmitt et al. [40]	First Approach	Second Approach		Third Approach		Fourth Approach	
					SRK	PR	SRK	PR	SRK	PR
Transcritical case	0.206	0.196	0.227	0.316	0.250	0.267	0.250	0.266	0.249	0.266
Supercritical case	0.312	-	0.241	0.310	0.214	0.232	0.214	0.234	0.214	0.234

Chapter 6

Conclusions

This chapter will present the most important conclusions achieved in the present work for the study of different methodologies in the modelling of transcritical and supercritical jets. Basing on the conclusions of the present study, future investigations will also be proposed in order to achieve objectives not possible be reached in the present work, as well as new ones which proved to be relevant.

In Chapter 1, the different behaviour which characterizes jets at conditions around the critical point as well as at supercritical conditions was put in evidence. The work of different research teams pointed in the direction of using real fluid thermodynamics as a mean to take in consideration the different fluid behaviour observed at such conditions. Previously, a variable density approach, originally developed for gaseous isothermal jets had been evaluated for modelling cryogenic jets under supercritical conditions. This approach was evaluated again in the present investigation for the study of transcritical and supercritical jets. The results shown to be promising despite this approach neglecting real fluid thermodynamics as well as the heat exchange in the flow. The inclusion of real fluid thermodynamics and heat exchange in an approach which had already presented an acceptable agreement with experimental data constituted a very interesting approach.

The inclusion of a Favre averaged equation of energy to the already existing mathematical approach was presented. It allowed the calculation of the temperature field which had in consideration the heat exchange present in the flow.

From the analysis of different equations of state, it was concluded that both Soave-Redlich-Kwong and Peng-Robinson equations of state allow a close approximation to the correct value of density at a given pressure and temperature for the conditions of interest in the present work. The two equations of state have a very similar behaviour at temperatures above 130K. Bellow these temperatures a departure from experimental data is observed for both formulations. While the Peng-Robinson equation shows a value higher than experimental, the Soave-Redlich-Kwong equation shows lower values of density. The viscosity and thermal conductivity were also very closely approached by a new formulation proposed by Lemmon and Jacobsen [65]. As for the specific heat at constant pressure, linear relations obtained from experimental data were developed and permit a nice fitting of the values for the given pressure.

The comparison of the different computational approaches in Chapter 5 shows that for the approaches which make use of real fluid thermodynamics the employment of different methodologies of determination of molecular viscosity, thermal conductivity, and specific heat has a very limited effect on the obtained results. This results are interesting since they seem to be contrary to what was generally defended in the literature, which gives big relevance to use of real fluid thermodynamics. In fact, this seems to suggest that are indeed the turbulence characteristics which play the major role in the jet behaviour. A very surprising result is that the original approach which didn't employ real fluid thermodynamics, defining the viscosity as a constant and the density from Amagat's law, was able to provide a closer agreement with the experimental results [25, 26] as well as with the two large eddy simulations provided by other authors [40, 44]. The Amagat's law approach was only outperformed by the approaches

employing real fluid thermodynamics in the determination of the jet spreading rate at transcritical injection conditions. The employment of real fluid equations of state and real fluid thermodynamics assure that this model is using the correct values of the fluid's properties. This conclusion raises the hypothesis that are the turbulent viscosity as well as the turbulent thermal conductivity, defined from the turbulent Prandtl number, the properties which apparently act as "driving forces" of the flow of study.

The comparison between the two real fluid equations of state leads to the conclusion that there isn't one which clearly performs better. When comparing the equations of state in an isolated manner in Chapter 3, the Peng-Robinson appeared to be slightly closer to the data provided by tables. However, this slight edge was not corroborated when used inside the numerical approach. In fact when used integrated with the CFD code the Soave-Redlich-Kwong was often found in closer agreement with experiments.

For all approaches the results obtained offer a quite acceptable agreement with experiments and are actually able to outperform the LES results at some conditions, this is of great relevance since this approach is undoubtedly much less computationally expensive than other approaches. The introduction of a different methodology proved to be able to improve the prediction capabilities of the jet spreading rate. These results clearly open the way to more simplistic methodologies to predict complex flows for which still little knowledge exists and which play an increasingly more important role in modern and future propulsion systems.

Improvements to the present approach are promising due to the achieved results. The biggest relevance that the turbulent characteristics appear to have on the flow behaviour when compared with the molecular properties points in the direction of giving a higher attention to the turbulent Prandtl number. In the present investigation it was always treated as a constant value. However, recent investigations have pointed in the direction of employing a variable turbulent Prandtl number [38]. The variation of this property would have an important effect in the jet behaviour, and is a new available direction of research.

Room for improvement is also present in the methodology for the specific heat determination since until now it is calculated by the use of relations obtained from tables, but a formulation similar to that existing for molecular viscosity and thermal conductivity would be preferable.

Under supercritical conditions the generality of experimental data prove the non-existence of droplets. However, this is not necessarily true for other conditions in the proximity of the critical point. The formulation developed in the present work is now able to provide real fluid values of the molecular properties of the flow. The prediction of the more accurate thermodynamic properties of fluid open the door to the capability of predicting the appearance and disappearance of droplets in the flow, which would lead to a two phases computational approach truly able to predict the transition between them.

Bibliography

[1] J. Bellan, "Supercritical (and subcritical) fluid behavior and modeling: drops, streams, shear and mixing layers, jets and sprays," *Progress in Energy and Combustion Science*, vol. 26, pp. 329–366, 2000. 1, 2, 6, 8

[2] V. Yang, "Modeling of Supercritical Vaporization , Mixing , and Combustion Processes in Liquid-Fueled Propulsion Systems," *Proceedings of the Combustion Institute*, vol. 28, no. 1, pp. 925–942, 2000. 1

[3] G. Lacaze and J. C. Oefelein, "A non-premixed combustion model based on flame structure analysis at supercritical pressures," *Combustion and Flame*, vol. 159, pp. 2087–2103, 2012. 2, 30

[4] G. P. Sutton and O. Biblarz, *Rocket Propulsion Elements*. Hoboken, New Jersey: John Wiley & Sons, Inc., 8th ed., 2010. 2

[5] B. Chehroudi, R. Cohn, and D. Talley, "Cryogenic shear layers: Experiments and phenomenological modeling of the initial growth rate under subcritical and supercritical conditions," *International Journal of Heat and Fluid Flow*, vol. 23, pp. 554–563, 2002. 3, 15

[6] K. Harstad and J. Bellan, "Isolated fuid oxygen drop behavior in fluid hydrogen at rocket chamber pressures," *International Journal of Heat and Mass Transfer*, vol. 41, pp. 3537–3550, 1998. 3, 6, 7, 10

[7] J. M. M. Barata and A. R. R. Silva, "Numerical Study of Cryogenic Jets Under Supercritical Conditions," *Journal of Propulsion and Power*, vol. 19, pp. 142–147, 2003. 3, 24, 34, 35, 60, 87, 88, 93

[8] E. L. S. F. Antunes, A. R. R. Silva, and J. M. M. Barata, "Evaluation of Numerical Variable Density Approach to Cryogenic Jets," in *50th AIAA Aerospace Sciences Meeting Including the New Horizons Forum and Aerospace Exposition*, (Nashville, Tennessee), pp. 1–14, January 2012. 3, 34, 60

[9] S. Negro and G. M. Bianchi, "Superheated fuel injection modeling: An engineering approach," *International Journal of Thermal Sciences*, vol. 50, no. 8, pp. 1460–1471, 2011. 3, 29

[10] S. D. Givler and J. Abraham, "Supercritical droplet vaporization and combustion studies," *Progress in Energy and Combustion Science*, vol. 22, pp. 1–28, 1996. 3, 4, 5, 6, 7, 8, 9, 10

[11] T. Kim, Y. Kim, and S. K. Kim, "Numerical study of cryogenic liquid nitrogen jets at supercritical pressures," *Journal of Supercritical Fluids*, vol. 56, no. 2, pp. 152–163, 2011. 4, 28, 34

[12] K. Harstad and J. Bellan, "An all-pressure fluid drop model applied to a binary mixture: Heptane in nitrogen," *International Journal of Multiphase Flow*, vol. 26, pp. 1675–1706, 2000. 6

[13] K. Harstad and J. Bellan, "Interactions of fluid oxygen drops in fluid hydrogen at rocket chamber pressures," *International Journal of Heat and Mass Transfer*, vol. 41, pp. 3551–3558, 1998. 6, 7, 10

[14] H. Zhang, V. Raghavan, and G. Gogos, "Subcritical and supercritical droplet evaporation within a zero-gravity environment: Low Weber number relative motion," *International Communications in Heat and Mass Transfer*, vol. 35, pp. 385–394, 2008. 8

[15] H. Nomura, Y. Ujiie, H. J. Rath, J. Sato, and M. Kono, "Experimental study on high-pressure droplet evaporation using microgravity conditions," *Symposium (International) on Combustion*, vol. 26, pp. 1267–1273, 1996. 8

[16] M. Tsue, H. Nomura, M. Niwa, H. Miyano, J. Sato, and M. Kono, "Evaporation of a Fuel Droplet in High Pressure High Temperature Atmosphere," *Japan Society for Aeronautical and Space Sciences, Journal*, vol. 37, no. 420, pp. 21–28, 1989. 8

[17] G. S. Zhu and S. K. Aggarwal, "Transient supercritical droplet evaporation with emphasis on the effects of equation of state," *International Journal of Heat and Mass Transfer*, vol. 43, pp. 1157–1171, 2000. 9

[18] H. Meng and V. Yang, "A unified treatment of general fluid thermodynamics and its application to a preconditioning scheme," *Journal of Computational Physics*, vol. 189, no. 1, pp. 277–304, 2003. 9

[19] C. Fieberg, L. Reichelt, D. Martin, U. Renz, and R. Kneer, "Experimental and numerical investigation of droplet evaporation under diesel engine conditions," *International Journal of Heat and Mass Transfer*, vol. 52, no. 15-16, pp. 3738–3746, 2009. 9

[20] M. Oschwald, J. J. Smith, R. Branam, J. Hussong, A. Schik, B. Chehroudi, and D. Talley, "Injection of Fluids Into Supercritical Environments," *Combustion Science and Technology*, vol. 178, no. 908038079, pp. 49–100, 2006. xvii, 10, 11, 18, 19, 26

[21] J. Newman and T. Brzustowski, "Behavior of a Liquid Jet near the Thermodynamic Critical Region," *AIAA Journal*, vol. 9, no. August, pp. 1595–1602, 1971. 12

[22] D. Papamoschou and A. Roshko, "The compressible turbulent shear layer: an experimental study," *Journal of Fluid Mechanics*, vol. 197, pp. 453–477, 1988. 12

[23] W. O. H. Mayer, A. H. A. Schik, B. Vielle, C. Chauveau, I. Gökalp, D. G. Talley, and R. D. Woodward, "Atomization and Breakup of Cryogenic Propellants Under High-Pressure Subcritical and Supercritical Conditions," *Journal of Propulsion and Power*, vol. 14, no. 5, pp. 835–842, 1998. xvii, 13, 15

[24] M. Oschwald and A. Schik, "Supercritical nitrogen free jet investigated by spontaneous Raman scattering," *Experiments in Fluids*, vol. 27, pp. 497–506, 1999. 14

[25] M. Oschwald and M. Micci, "Spreading angle and centerline variation of density of supercritical Nitrogen Jets," *Atomization and Sprays*, vol. 12, no. 1-3, pp. 91–106, 2002. 16, 100, 111, 124, 127, 128, 129

[26] W. Mayer, J. Telaar, R. Branam, G. Schneider, and J. Hussong, "Raman measurements of cryogenic injection at supercritical pressure," *Heat and Mass Transfer*, vol. 39, pp. 709–719, 2003. xviii, xix, xx, 16, 18, 19, 25, 26, 27, 30, 33, 35, 89, 93, 97, 98, 100, 101, 108, 109, 111, 113, 116, 119, 121, 124, 127, 128, 129

[27] B. Chehroudi, S.-H. Chen, F. Bracco, and Y. Onuma, "On the Intact Core of Full-Cone Sprays," *SAE Technical Paper Series*, no. 850126, pp. 1–10, 1985. 19

[28] A. M. Star, J. R. Edwards, K. Lin, S. Cox-Stouffer, and T. A. Jackson, "Numerical Simulation of Injection of Supercritical Ethylene into Nitrogen," *Journal of Propulsion and Power*, vol. 22, no. 4, pp. 809–819, 2006. 20, 27

[29] S. Martínez-Martínez, F. A. Sánchez-Cruz, J. M. Riesco-Ávila, A. Gallegos-Muñoz, and S. M. Aceves, "Liquid penetration length in direct diesel fuel injection," *Applied Thermal Engineering*, vol. 28, pp. 1756–1762, 2008. 20

[30] C. Segal and S. A. Polikhov, "Subcritical to supercritical mixing," *Physics of Fluids*, vol. 20, pp. 1–7, 2008. 21

[31] T. Schmitt, J. Rodriguez, I. A. Leyva, and S. Candel, "Experiments and numerical simulation of mixing under supercritical conditions," *Physics of Fluids*, vol. 24, 2012. 21, 32, 35

[32] S. B. Pope, *Turbulent Flows*. 2000. 23, 40, 41, 48, 49, 50, 53

[33] A. Favre, "Équations des gaz turbulents compressibles. I Formes générales.," *Journal de Mécanique*, vol. 4, no. 3, pp. 361–390, 1965. 24

[34] J. Sanders, B. Sarh, and I. Gökalp, "Variable density effects in axisymmetric isothermal turbulent jets: a comparison between a first- and a second-order turbulence model," *International Journal of Heat and Mass Transfer*, vol. 40, pp. 823–842, 1997. 24, 51, 53, 60, 69, 74, 87, 93, 104, 111

[35] B. Chehroudi, D. Talley, and E. Coy, "Visual characteristics and initial growth rates of round cryogenic jets at subcritical and supercritical pressures," *Physics of Fluids*, vol. 14, no. 2, pp. 850–861, 2002. 25, 27

[36] N. Zong, H. Meng, S. Y. Hsieh, and V. Yang, "A numerical study of cryogenic fluid injection and mixing under supercritical conditions," *Physics of Fluids*, vol. 16, pp. 4248–4261, 2004. xvii, 25, 26, 35

[37] N. Zong and V. Yang, "Cryogenic Fluid Jets and Mixing Layers in Transcritical and Supercritical Environments," *Combustion Science and Technology*, vol. 178, no. 908038079, pp. 193–227, 2006. 26, 35

[38] M. Aouissi, A. Bounif, and K. Bensayah, "Scalar turbulence model investigation with variable turbulent Prandtl number in heated jets and diffusion flames," *Heat and Mass Transfer*, vol. 44, no. 9, pp. 1065–1077, 2008. 28, 35, 51, 130

[39] T. S. Park, "LES and RANS simulations of cryogenic liquid nitrogen jets," *Journal of Supercritical Fluids*, vol. 72, pp. 232–247, 2012. 28, 31, 34, 35

[40] T. Schmitt, L. Selle, B. Cuenot, and T. Poinsot, "Large-Eddy Simulation of transcritical flows," *Comptes Rendus - Mecanique*, vol. 337, no. 6-7, pp. 528–538, 2009. 28, 32, 35, 89, 93, 94, 95, 97, 98, 100, 108, 111, 113, 116, 121, 127, 128, 129

[41] J. Telaar, G. Schneider, J. Hussong, and W.Mayer, "Cryogenic jet injection: description of test case RCM 1," in *2nd International Workshop on Rocket Combustion Modeling*, (Heilbronn, Germany), pp. 25–27. 29

[42] L. Zhou, M.-Z. Xie, M. Jia, and J.-R. Shi, "Large eddy simulation of fuel injection and mixing process in a diesel engine," *Acta Mechanica Sinica*, vol. 27, pp. 519–530, 2011. 29

[43] J. Shinjo and A. Umemura, "Surface instability and primary atomization characteristics of straight liquid jet sprays," *International Journal of Multiphase Flow*, vol. 37, no. 10, pp. 1294–1304, 2011. 30

[44] M. Jarczyk and M. Pfitzner, "Large Eddy Simulation of Supercritical Nitrogen Jets," in *50th AIAA Aerospace Sciences Meeting Including the New Horizons Forum and Aerospace Exposition*, pp. 1–13, January 2012. 30, 35, 89, 93, 94, 95, 97, 98, 108, 113, 121, 128, 129

[45] H. Terashima and M. Koshi, "Approach for simulating gas-liquid-like flows under supercritical pressures using a high-order central differencing scheme," *Journal of Computational Physics*, vol. 231, no. 20, pp. 6907–6923, 2012. 31

[46] H. Terashima and M. Koshi, "Strategy for simulating supercritical cryogenic jets using high--order schemes," *Computers and Fluids*, vol. 85, pp. 39–46, 2013. 31

[47] M. J. Schuler, T. Rothenfluh, and P. Rudolf Von Rohr, "Simulation of the thermal field of submerged supercritical water jets at near-critical pressures," *Journal of Supercritical Fluids*, vol. 75, pp. 128–137, 2013. 32, 35

[48] T. Rothenfluh, M. J. Schuler, and P. R. Von Rohr, "Penetration length studies of supercritical water jets submerged in a subcritical water environment using a novel optical Schlieren method," *Journal of Supercritical Fluids*, vol. 57, no. 2, pp. 175–182, 2011. 32

[49] T.-H. Chung, M. Ajlan, L. L. Lee, and K. E. Starling, "Generalized multiparameter correlation for nonpolar and polar fluid transport properties," *Industrial and Engineering Chemistry Research*, vol. 27, no. 4, pp. 671–679, 1988. 32, 33, 34

[50] X. Petit, G. Ribert, G. Lartigue, and P. Domingo, "Large-eddy simulation of supercritical fluid injection," *Journal of Supercritical Fluids*, vol. 84, pp. 61–73, 2013. 33, 34, 35

[51] D.-Y. Peng and D. B. Robinson, "A New Two-Constant Equation of State," *Industrial and Engineering Chemistry: Fundamentals*, vol. 15, no. 1, pp. 59–64, 1976. 33, 65, 66, 67

[52] G. Soave, "Equilibrium constants from a modified Redlich-Kwong equation of state," *Chemical Engineering Science*, vol. 27, no. 6, pp. 1197–1203, 1972. 33, 63

[53] S. K. Kim, H. S. Choi, and Y. Kim, "Thermodynamic modeling based on a generalized cubic equation of state for kerosene/LOx rocket combustion," *Combustion and Flame*, vol. 159, no. 3, pp. 1351–1365, 2012. 34

[54] S. K. Kim and Y. Kim, "Thermophysical properties of dimethyl ether at near- and supercritical pressures using generalized cubic EoS," *Journal of Supercritical Fluids*, vol. 92, pp. 16–23, 2014. 34

[55] M. Cismondi and J. Mollerup, "Development and application of a three-parameter RK-PR equation of state," *Fluid Phase Equilibria*, vol. 232, no. 1-2, pp. 74–89, 2005. 34

[56] K. A. Hoffman, S. T. Chiang, S. Siddiqui, and M. Papadakis, *Fundamental Equations of Fluid Mechanics*. Wichita, Kansas: Engineering Education System, 1996. 37, 69, 70, 75, 80

[57] F. M. White, *Fluid Mechanics*. McGraw-Hill Higher Education, 4th editio ed., 1998. 39

[58] J. D. Anderson, *Fundamentals of Aerodynamics*. McGraw-Hill, 2nd ed., 1991. 42

[59] R. Cant and E. Mastorakos, *An introduction to Turbulent Reacting Flows*. Imperial College Press, 2007. 42

[60] W. P. Jones and B. E. Launder, "The Prediction of Laminarization with a Two-Equation Model of Turbulence," *International Journal of Heat and Mass Transfer*, vol. 15, no. 2, pp. 301–314, 1972. 50

[61] R. Chang, *Chemistry, Eighth Edition*. McGraw-Hill, 8th ed., 2003. 61, 63

[62] L. Medard, *Gas Encyclopaedia*. Amsterdam: Elsevier Science, 1 ed., 1976. 61, 68, 70, 72, 81, 93, 101, 111, 120

[63] O. Redlich and J. N. S. Kwong, "On the Thermodynamics of Solutions. V. An Equation of State. Fugacities of Gaseous Solutions.," *Chemical Reviews*, vol. 44, no. 1, pp. 233–244, 1949. 63

[64] J. C. Oefelein, "Thermophysical characteristics of shear-coaxial LOX-H2 flames at supercritical pressure," *Proceedings of the Combustion Institute*, vol. 30, no. 2, pp. 2929–2937, 2005. 64

[65] E. W. Lemmon and R. T. Jacobsen, "Viscosity and Thermal Conductivity Equations for Nitrogen, Oxygen, Argon, and Air," vol. 25, no. 1, 2004. xix, xx, xxi, 72, 76, 79, 93, 120, 121, 122, 123, 124, 129

[66] G. A. Olchowy and J. V. Sengers, "A simplified representation for the thermal conductivity of fluids in the critical region," *International Journal of Thermophysics*, vol. 10, no. 2, pp. 417–426, 1989. 77

[67] J. H. Ferziger and M. Peric, *Computational Methods for fluid Dynamics*. New York: Springer-Verlag, 3rd ed., 2002. 83

[68] J. M. M. Barata, *Estudo Numérico e Experimental de Jactos Incidentes sobre Placas Planas através de um Escoamento Cruzado*. PhD thesis, Universidade Técnica de Lisboa, 1989. 83, 84

[69] S. V. Patankar and D. B. Spalding, "A Calculation Procedure for Heat, Mass and Momentum Transfer in Three- Dimensional Parabolic Flows," *International Journal of Heat and Mass Transfer*, vol. 15, no. 10, pp. 1787–1806, 1972. 87

[70] W. Mayer and J. Telaar, "Investigation of Breakup of Turbulent Cryogenic Variable-Density Jets," *Atomization and Sprays*, vol. 12, pp. 651–666, 2002. 127

Appendix A

Scientific Communications

A.1 Paper Presented in 50th AIAA Aerospace Science Meeting including the New Horizons Forum and Aerospace Exposition

https://arc.aiaa.org/doi/abs/10.2514/6.2012-1282

50th AIAA Aerospace Sciences Meeting including the New Horizons Forum and Aerospace Exposition
09 - 12 January 2012, Nashville, Tennessee

AIAA 2012-1282

Evaluation of Numerical Variable Density Approach to Cryogenic Jets

Eduardo L.S.F. Antunes[1], André R. R. Silva[2], Jorge M. M. Barata[3]
Universidade da Beira Interior, 6200-001 Covilhã, Portugal

The present work is devoted to study cryogenic nitrogen jets in high subcritical conditions. Fuel injection is one of the great challenges in engineering of diesel engines, gas turbines and rocket engines, combining in the last one also the injection of oxidizer. It is widely known that the increase of operation pressures and temperatures increases engine efficiency and reduces fuel specific consumption. Thus, it is a general trend in modern engines the operation in increasingly higher pressures. However at higher chamber pressures the injected fluids may experience ambient conditions exceeding the critical values. Several authors stated that at these conditions the injected fluids suffers a change of its properties, and the traditional two-phase flow models cannot correctly predict the jet behavior at these conditions, thus new computational models are needed for these specific conditions. Barata et al. [18] performed a numerical investigation aimed to evaluate the applicability of an incompressible but variable density model in liquid jets under sub-to-supercritical conditions. The results achieved agree well with the experimental data but they only considered intermediate density ratios from 0.05 to 0.14. The objective of the present work was to extend the investigation of Ref. 18 to lower density ratios from 0.025 to 0.045 which correspond to cases with subcritical chamber pressures. The obtained results agree well with the experimental and numerical data of Chehroudi *et al.* presented in Ref. 18. It was also found in this work that the computational model does not offers valid results for density ratios lower than 0.025.

Nomenclature

B	= transfer number
β_v	= evaporation rate
C_μ	= coefficient in turbulence model
d_0	= initial droplet diameter
d	= droplet diameter
D	= injector diameter [m], normalized droplet diameter (d(t) / d_0)
ε	= dissipation rate of turbulent energy
f	= mixture fraction
F	= mean mixture fraction
i	= axial direction index
j	= radial direction index
k	= turbulent kinetic energy
ϕ	= generalized variable
ω	= chamber-to-injection fluid density ratio (ρ_∞/ρ_0)
P_{cr}	= critical pressure [MPa]
P_∞	= chamber ambient pressure [MPa]
P_r	= reduced pressure (P_∞/P_{cr})
ρ	= density [kg.m^{-3}]
ρ_0	= injected fluid density [kg.m^{-3}]
ρ_∞	= injection chamber's fluid density [kg.m^{-3}]
r	= radial coordinate [m]
R/D	= radial distance normalized by injector diameter
R_{diam}	= injector radius [m]
R_e	= Reynolds Number
S_ϕ	= source term
t	= time [s]
T	= temperature [K]
u	= axial velocity [m.s^{-1}]

[1] MEng Student, Aerospace Sciences Department, Rua Marques Avila e Bolama, AIAA Student Member.
[2] Assistant Professor, Aerospace Sciences Department, AIAA Member.
[3] Full Professor, Aerospace Sciences Department, AIAA Associate Fellow.

U = mean axial velocity [m.s^{-1}]
U_{in} = injection axial velocity [m.s^{-1}]
v = radial velocity [m.s^{-1}]
ν_t = turbulent kinematic viscosity
V = mean radial velocity [m.s^{-1}]
X = axial coordinate [m]
X/D = axial distance normalized by injector diameter

I. Introduction

FUEL injection presents itself as one of the great challenges in engineering of diesel engines, gas turbines and rocket engines, combining in the last one also the injection of oxidizer. It is widely known that the increase of operating pressure and temperatures in combustion chamber, or thrust chamber in rocket engines, leads to an increase of engine efficiency, reducing this way the fuel consumption. Thereby is a general trend in new engine designs to operate with higher chamber pressures and temperatures. Also the appearance of new and more resistant materials is other reason that could make grow this tendency. As a result of these increasingly higher pressures, the injected fluids may experience ambient conditions exceeding the critical values. The Space Shuttle Main Engine and the Vulcain with thrust chamber pressures of respectively 22.3 MPa and 28.2 MPa are both examples of engines in which the chamber pressure exceeds the critical pressure of P_{cr} = 5.043 MPa for liquid oxygen and P_{cr} = 1.28 MPa for liquid hydrogen[1]. In these application, the initial temperature of the oxygen can initially be below the critical temperature of the oxygen (T_{cr} = 154.58 K) but it then undergoes into a transition, when in the combustion chamber, reaching supercritical temperatures. At these conditions the liquid fuel is on supercritical conditions and its physical state is named as fluid. As the fluid reach pressure and temperature values exceeding the critical ones it suffers significantly changes in its properties. The effective mass diffusivity, the surface tension and the latent heat of the liquid all vanish in critical conditions. On the other hand, the heat capacity at constant pressure, Cp, the isentropic compressibility, κ_s, and the thermal conductivity, λ , all become infinite[2]. These changes in the fluid behavior cause the inapplicability of the traditional two-phase flow models used in fuel injection under subcritical conditions, thus there is a need to develop new models with can correctly be applied to supercritical fuel injection.

Several authors investigated the fuel injection in supercritical condition both in experimentally and numerically[3-22]. The first experimental investigations performed used techniques like photography and shadowgraphy, and had as principal objective the study of the visual structure of the jet without obtaining any quantitative result[1,6], these investigations observed that the jet structure suffers significantly changes as the pressure increases, firstly the surface tension reduction leads to the formations of jet ligaments and droplets that detach from the main jet structure and a further increase of the chamber pressure into supercritical conditions leads to gas-gas like structure of the jet. In more recent experimental works, along with qualitative characterization, were made quantitative studies in which results like the jet spreading angle, density and temperature were obtained[4,7,15,16]. These quantitative experimental results allowed the comparison with the results obtained in numerical studies and this way validate the numerical models[17-22].

Barata *et al.*[18] performed an initial investigation aimed to evaluate the capabilities of a computational method developed for incompressible but variable density flows when applied to supercritical conditions. Their results have show a good agreement with the experimental data, but they only considered intermediate density ratios from 0.05 to 0.14. The present work extends the investigation of Ref. 18 to lower density ratios, corresponding to sub/near-critical conditions, and investigates the limits of application of the variable density approach to supercritical jets. An injection velocity study was also performed in the present work with the intend of better characterize the variable density approach.

II. Mathematical Model

A. Governing Equations

The method to solve variable density jet flows is based on the solution of the conservation equations for momentum and mass. Turbulence is modeled with the "k~ε" turbulence model. A similar method has been used for three-dimensional or axisymmetric flows and only the main features are summarized here.

In the conservation equations, mass weighted averaging is applied to avoid the appearance of many terms involving density fluctuations for which additional models are needed. A mass averaged quantity is defined as

$$\tilde{\phi} = \frac{\overline{\rho\phi}}{\bar{\rho}} \qquad (1)$$

For the governing equations the standard parabolic truncation is employed. The mass averaged partial differential equations governing the steady, variable density axisymmetric flow may be written in cylindrical polar coordinates as

$$\frac{\partial \bar{\rho} UU}{\partial x} + \frac{1}{r}\frac{\partial r\bar{\rho} UV}{\partial r} = -\frac{\partial \bar{p}}{\partial x} - \frac{1}{r}\frac{\partial r\bar{\rho}\,\overset{\sim}{\overline{u'v'}}}{\partial r} \qquad (2)$$

$$\frac{\partial \bar{\rho} UV}{\partial x} + \frac{1}{r}\frac{\partial r\bar{\rho} VV}{\partial r} = -\frac{\partial \bar{p}}{\partial x} - \frac{1}{r}\frac{\partial r\bar{\rho}\,\overset{\sim}{\overline{v'v'}}}{\partial r} + \bar{\rho}\frac{\overset{\sim}{\overline{w'w'}}}{r} \qquad (3)$$

and the continuity equation as

$$\frac{\partial \bar{\rho} U}{\partial x} + \frac{1}{r}\frac{\partial r\bar{\rho} V}{\partial r} = 0 \qquad (4)$$

To describe mixing of gases, the mixture fraction *F*, that represents the mass fraction of the nozzle fluid, is introduced. It obeys a convection-diffusion equation of the form

$$\frac{\partial \bar{\rho} UF}{\partial x} + \frac{1}{r}\frac{\partial r\bar{\rho} VF}{\partial r} = -\frac{1}{r}\frac{\partial r\bar{\rho}\,\overset{\sim}{\overline{v'f'}}}{\partial r} \qquad (5)$$

In "k~ε" turbulence model, the Reynolds stresses are expressed in terms of the local strain rate:

$$-\bar{\rho}\,\overset{\sim}{\overline{u'_i u'_j}} = \bar{\rho}(\nu_t + \nu)\left(\frac{\partial \tilde{u}_i}{\partial x_j} + \frac{\partial \tilde{u}_j}{\partial x_i}\right) - \frac{2}{3}\delta_{ij}\left(\bar{\rho}k + \bar{\rho}(\nu_t + \nu)\frac{\partial \tilde{u}_j}{\partial x_j}\right) \qquad (6)$$

with

$$\nu_t = C_\mu \frac{k^2}{\varepsilon} \qquad (7)$$

The scalar flux in equation (5) is approximated with a gradient transport assumption

$$\overset{\sim}{\overline{u'_i f'}} = -\frac{\nu_t}{\sigma_f}\frac{\partial F}{\partial x_i} \qquad (8)$$

From the foregoing we can deduced the parabolized set of equations in cylindrical coordinates where the generalized equation is

$$\frac{\partial}{\partial x}\left(\bar{\rho} U\tilde{\phi}\right) + \frac{1}{r}\frac{\partial}{\partial r}\left(r\bar{\rho}\tilde{\phi}\right) = \frac{1}{r}\frac{\partial}{\partial r}\left(r\bar{\rho} D\frac{\partial \tilde{\phi}}{dr}\right) + S_\phi \qquad (9)$$

where $\tilde{\phi}$ may stand for any of the velocities, turbulent kinetic energy, dissipation, or scalar property, and S_ϕ take on different values for each particular $\tilde{\phi}$, described in detail by Sanders et al[17].

The mean density can be obtained from the mean mixture fraction using the equation state. With constant pressure this leads to

$$\frac{1}{\bar{\rho}} = \frac{F}{\rho_o} + \frac{1-F}{\rho_\infty} \qquad (10)$$

where density fluctuations have been neglected. This is allowed in isothermal jets because the instantaneous density, for which equation (10) is exact, is approximately a linear function of the instantaneous mixture fraction[18].

B. Numerical Method

The governing equations are solved using a parabolized marching algorithm which resembles the (elliptic) TEACH code.[17] The computations are performed by using the continuity equation to obtain the radial velocity (*V*). Using the radial momentum equation for *V* and solving a pressure correction equation for *V* in radial direction did not show any difference with the use of the continuity equation.[17] In this approach the numerical model was applied to variable density jets and for the present case it was used for the study of liquid cryogenic jets under sub-near critical pressures, and sub to supercritical temperatures.

In order to determine the tangent of the jet spreading angle is used the Half Width of Half Maximum of the Velocity (HWHMV), this routine has the function of determine the radial distance from the centerline (*r*) at which the axial mean velocity (*U*) is half of the maximum velocity localized in the centerline. This routine analysis all the points in the radial direction comparing them with half of the centerline velocity, when the routine finds a point bellow this value it saves the point before that.

C. Boundary Conditions

There are four boundaries in the computational domain, in these boundaries dependent variables are specified: an inlet and outlet plane, a symmetry axis and a free boundary parallel to the axis. The sensitivity of the solutions to the locations of the boundaries was investigated in previous works, and their final position is sufficiently far away from the jet so that the influence on the computed results is negligible[18]. At the inlet boundary the 1/7th power law turbulent velocity profile was used for the axial velocity at the jet exit.

$$U = U_{in}.\left(1 - \frac{r}{R_{diam}}\right)^{\frac{1}{7}} \qquad (11)$$

The radial velocity is zero at the jet exit and in ambient. The mixture fraction is one at the jet exit and zero in the ambient. On the symmetry axis, the normal velocity vanishes, and the normal derivatives of the other variables are zero. At the outflow boundary, the gradients of dependent variables in the axial direction are set to zero.

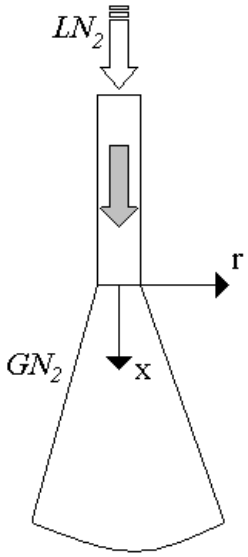

Figure 1 – Flow Configuration

The flow configuration can be observed in Figure 1. The injector nozzle has a diameter of 2.54×10^{-4} m while the domain of study has an axial length of 1.77×10^{-2} m and a radial length of 3.49×10^{-3} m. The test conditions for the present study of different densities ratios are presented in Table 1.

It was also performed a parallel study with the objective of evaluate the numerical model for different injection velocities, the test conditions used are summarized in Table 2.

The mathematical program underwent small changes from its original form in order to avoid the flow reversion verified next to the outlet when at high injection velocities.

Table 1. Summary of test conditions

Case	Pr	U_{in} [m/s]	Re	T_0 [K]	ρ_0 [Kg/m^3]	ρ_∞ [Kg/m^3]	ω
1	0,583	3.0	72060	100	700	17,5	0,025
2	0,642	3.0	72060	100	700	24,5	0,035
3	0,825	3.0	72060	100	700	31,5	0,045

Table 2. Summary of test conditions for the injection velocity study

Case	Pr	U_{in} [m/s]	Re	T_0 [K]	ρ_0 [Kg/m^3]	ρ_∞ [Kg/m^3]	ω
4	0,583	3.0	72060	100	700	17,5	0,025
5	0,583	5.0	120100	100	700	17,5	0,025
6	0,583	10.0	240200	100	700	17,5	0,025
7	0,583	20.0	480400	100	700	17,5	0,025

III. Results and discussion

In this section are presented the numerical results obtained at the present work and compared with the results exposed by Barata *et al*.[18]. The main objective is to extend the analysis performed by Barata *et al*.[18] to lower density ratios and then compare them with the experimental data in order to investigate the applicability of the variable density approach to liquid jet injection into a gaseous ambient under subcritical chamber pressures. The parameter used to compare the numerical results obtained in the present work with the results exposed in Ref. 18 is the jet growth rate. The jet growth rate is calculated by the tangent of the half with of half maximum of the velocity (HWHMV), this parameter is given by the calculation at each axial point of the radial distance to the centerline at which the axial velocity (U) is half of the velocity at the centerline. However other parameters were used in the characterization of the jet allowing also some interesting conclusions and are shown in the present paper.

Figures 2 and 3 show the typical velocity and scalar fields of the jet for test conditions 1 (Figure 2) and 3 (Figure 3) of Table 1. In both cases the jet structure is very similar, in the velocity field is visible the appearance of the entrainment phenomena close to the injector, with the jet fluid dragging the ambient fluid. This phenomenon causes the appearance of a vortex above the jet. It's visible that the position of the center of the vortex is influenced by the density ratio, when the density ratio increases the vortex center moves downstream. The mixture fraction and density scalar field show the rapid change of the jet structure at the injector exit. The density scalar field shows a faster decrease after the injector than the mixture fraction scalar field. This suggests that the density rapid decreased is not caused by the mixture of injected fluid with the less dense ambient fluid but indeed by a rapid expansion that the injected fluid may experiences as it exits the injector.

Figure 4 shows the axial variation of the centerline density in a logarithmic scale for cases 1 to 3 of Table 1. It is visible that the centerline density has a very similar behavior for the three cases with a first stage of almost constant density followed by a stage with a fast decrease of the centerline density and then stabilization around the ambient density value. A closer look to the graphic allows however to perceive that the case with a higher ambient pressure has a slightly higher decrease rate which is in agreement with the density scalar field observed in Figures 2 and 3. The length of the potential core based on the density is defined by the initial, almost constant, stage of the axial variation of the centerline density which lasts until an approximately length of X/D = 3 to 5 diameters for the three studied cases.

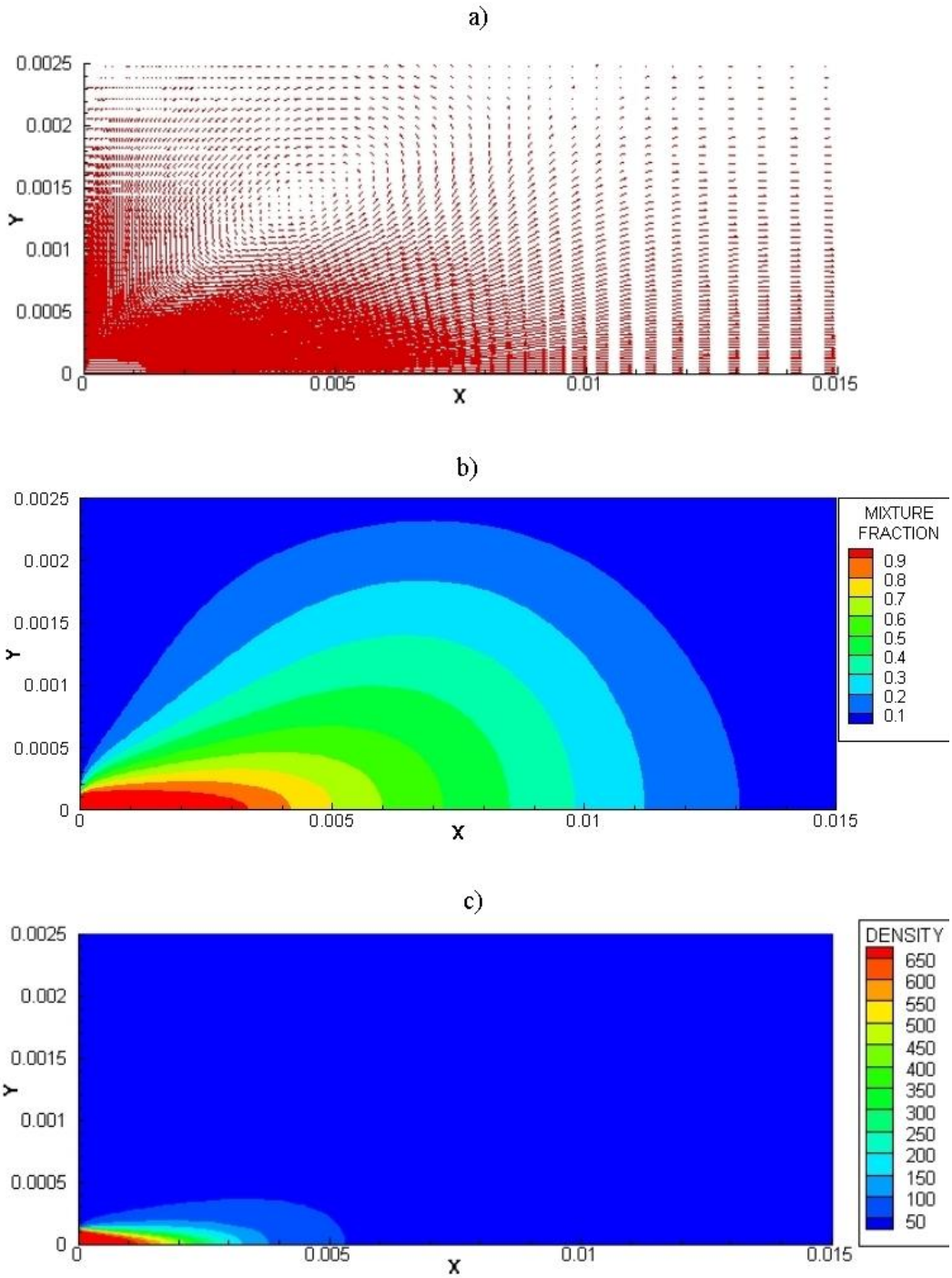

Figure 2 - Velocity and scalar fields of the jet with a density ratio of ω = 0.025 and a chamber pressure of Pr = 0.583, (a) Velocity vectors, (b) Mixture fraction contours, (c) Density contours.

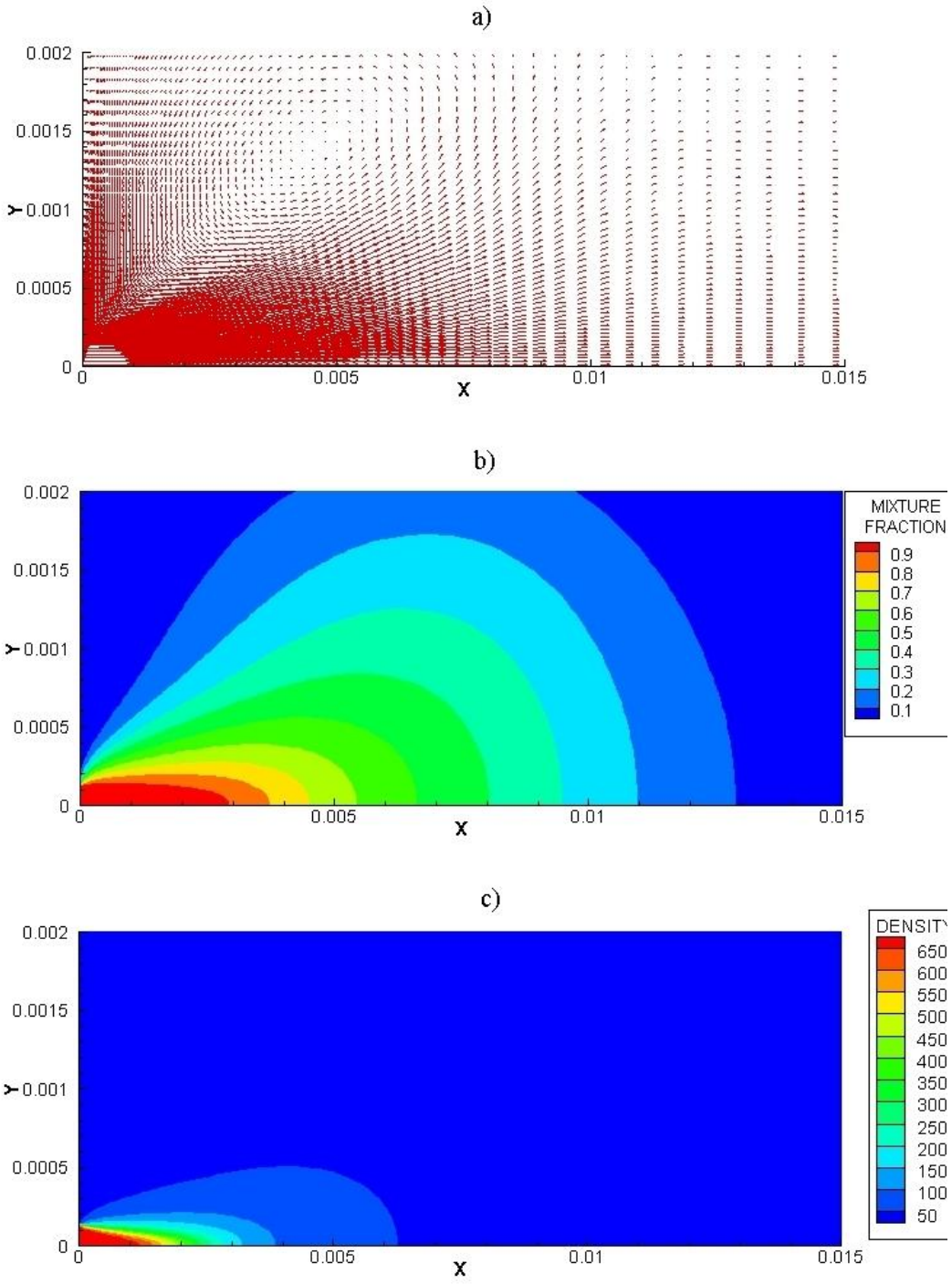

Figure 3 - Velocity and scalar fields of the jet with a density ratio of ω = 0.035 and a chamber pressure of Pr = 0.642, (a) Velocity vectors, (b) Mixture fraction contours, (c) Density contours.

The centerline velocity decay is shown in Figure 5 for the cases 1, 2 and 3. The velocity decay has a similar profile for the three cases with a first stage with almost no decay followed by a stage with a higher rate of decay and finally a stabilization like observed in Figure 4 for the variation of density. A higher rate of velocity decay is observed for the cases with higher ambient pressure indicating a greater interaction between the injection and ambient fluids. The length of the potential core based on the velocity decay is defined in the present work by the axial distance to the injector at which the centerline velocity has decayed 10%. The length of the potential core is between X/D = 7.9 and X/D = 7.47 diameters respectively for cases 1 and 3. Thus it is verified that the length of the potential core based on centerline velocity decay has a substantially different value that the approximately X/D = 3 diameters found for the potential core based on the centerline density. This is an interesting result, as in previous works the length of the potential core based on the density has approximately the same value as the one based on the velocity decay, and hypothesizes that the injected, possibly identify by the observation of the scalar fields, may contribute with kinetic energy to the jet.

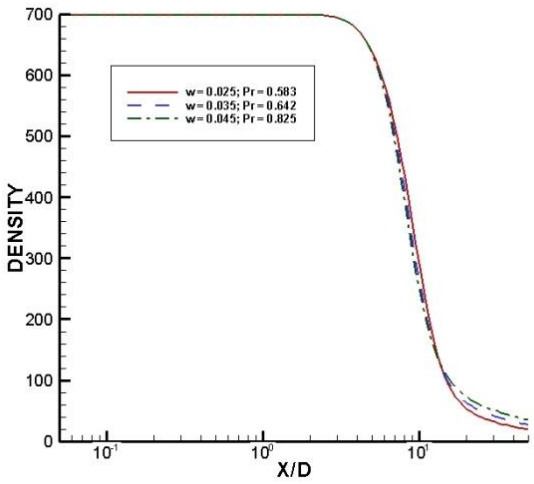

Figure 4 – Axial variation of the centerline density.

Figure 6 shows the half width of the half maximum of the velocity (HWHMV) for the cases 1, 2 and 3 of Table 1. The three cases have a similar evolution of the HWHMV across the domain of study with an almost linear first stage and a second non linear stage. The tangent of the slope of the almost linear stage corresponds to the jet growing rate. Observing the graphic it is possible to conclude that the jet growing rate is very similar for the three studied cases with only a slightly decrease as the chamber pressure increases. This was however not an expected result as in several previous work the increase of the chamber pressure causes an increase in the jet growing rate.

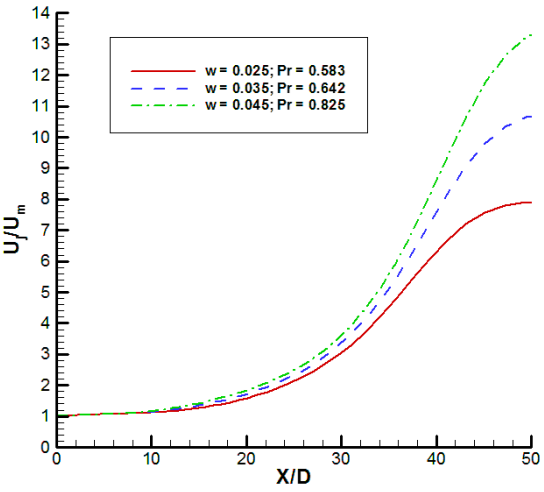

Figure 5 – Centerline velocity decay.

In Figure 7 are shown the decay rates of velocity and density after the potential core for the cases of Table 1. For both velocity and density an increase in the injection chamber pressure has as result an increase of the decay rate which is in agreement with previous works from other authors, however this effect is more pronounced in the velocity decay. The velocity also shows for the three cases a higher decay rate then the density although is important to remember that the density decay starts earlier then the velocity decay due to the longer potential core obtained for the velocity.

Figure 8 is similar to the graphic presented by Barata *et al.*[18] and shows the tangent of the jet spreading angle, calculated by the half width of half maximum of the velocity, in order to the density ratio. In addition to the three cases of Table 1 the graphic contains also results obtained by other authors in previous investigations including the results of Barata *et al.*[18], the investigation which the present work pretends to extend. The results achieved in the present work are represented in red while those achieved by other authors are represented in black. Obversing the graphic it is visible that the result obtained for a density ratio of $\omega = 0.025$ agree very well with the experimental result obtained by Chehroudi *et al.*[23], the result obtained for a density $\omega = 0.035$ is in total agreement with the modeling results of the same author. The $\omega = 0.045$ density ratio case shows a slight divergence from previous result but is still very close to

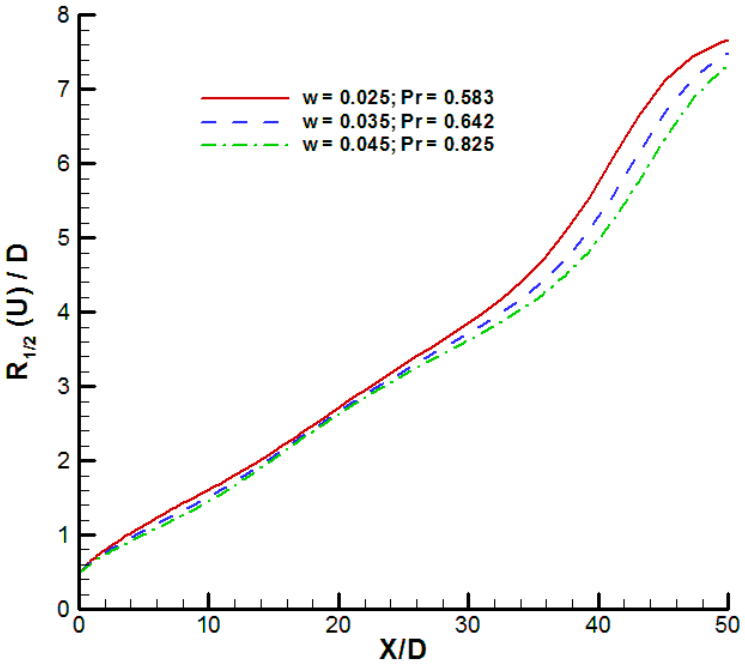

Figure 6 – Half width of half maximum of the velocity.

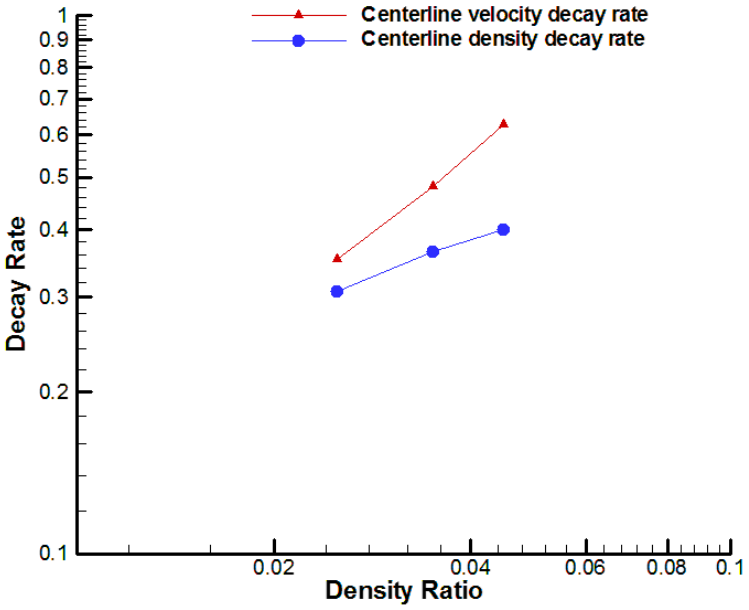

Figure 7 – Decay rate of the centerline velocity and density.

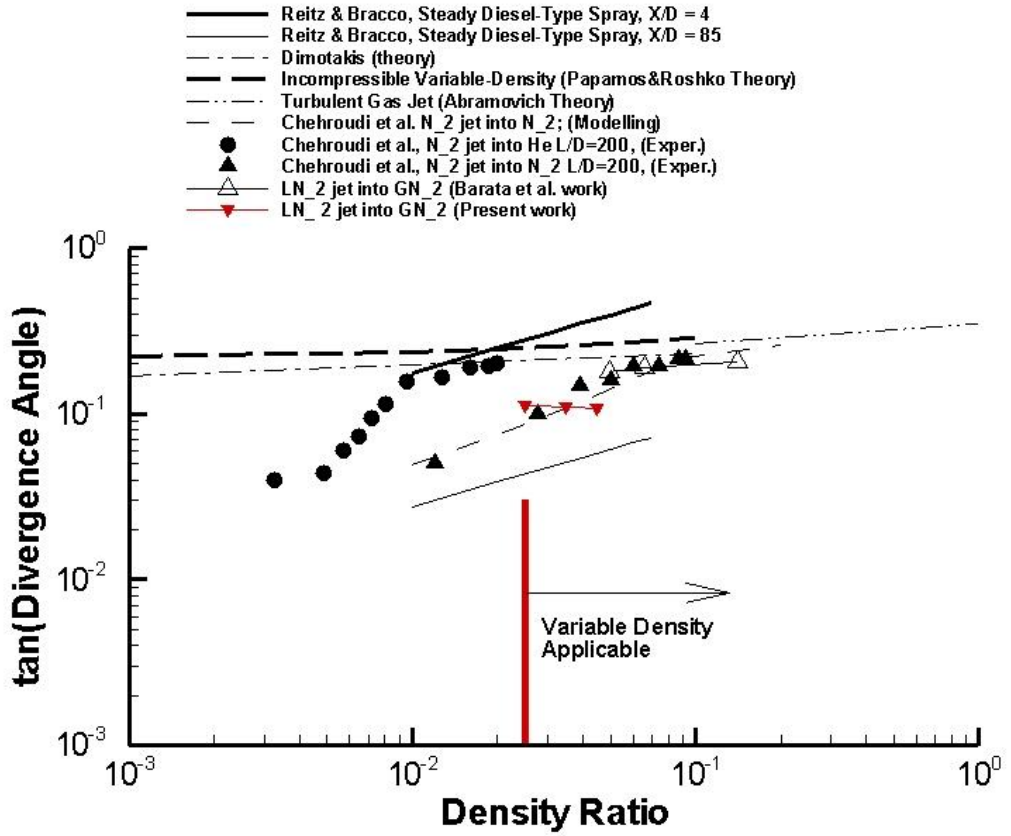

Figure 8 - Tangent of the spreading angle versus the chamber-to-injectant density ratio and representation if limit of applicability of the Variable Density approach.

the modeling result of Chehroudi *et al.*[23]. The test of the present variable density approach to lower density ratios, which are not presented here, allow the conclusion that the density ratio of $\omega = 0.025$ is the lowest value liable to be modeled by the present mathematical model. This conclusion is represented in Figure 8 by the vertical red line that marks the limit of applicability of the variable density approach.

The influence of the injection velocity in jet behavior was also subject of analysis at the present investigation. The objective was to perform a better characterization of the mathematical model. In order to achieve this objective the variable density approach was tested for different injection velocities as presented in Table 2.

Figure 9 shows the velocity and scalar fields for the test case 7 of Table 2. It is visible that the jet has the same structure found in Figure 2 corresponding to the case 4 of Table 2. It's however possible to verify that the vortex center appears in localization further downstream, also the mixture fraction and density show a slower evolution across the centerline when compared with the case with slower injection velocity. The axial variation of the centerline density shown in Figure 10 corroborates the observation stated above. The centerline density shows a slower decrease for higher injection velocities. One interesting observation is the increase of the potential core based on density as the injection velocity increases. Similar observations are made for the centerline velocity decay. As the injection velocity increases the potential core based on the velocity decay increases and the centerline velocity shows a lower rate of decay, this is somehow contrary to the expected since an increase in the injection velocity should lead to an increase of drag forces between the injected and the ambient fluid and this way increase the velocity decay rate. Like in the axial variation of the centerline also for the centerline velocity decay the case 5 with an injection velocity of $U_{in} = 5$ m.s^{-1} shows a behavior different from the tendency followed by the other three cases.

The half width of half maximum of the velocity is shown in Figure 11. Again the case 4 of Table 2 shows a different HWHMV structure then the other three cases not having an almost linear stage. By the observation of the graphic can be concluded that an increase of the injection velocity causes a decrease in the jet spreading angle.

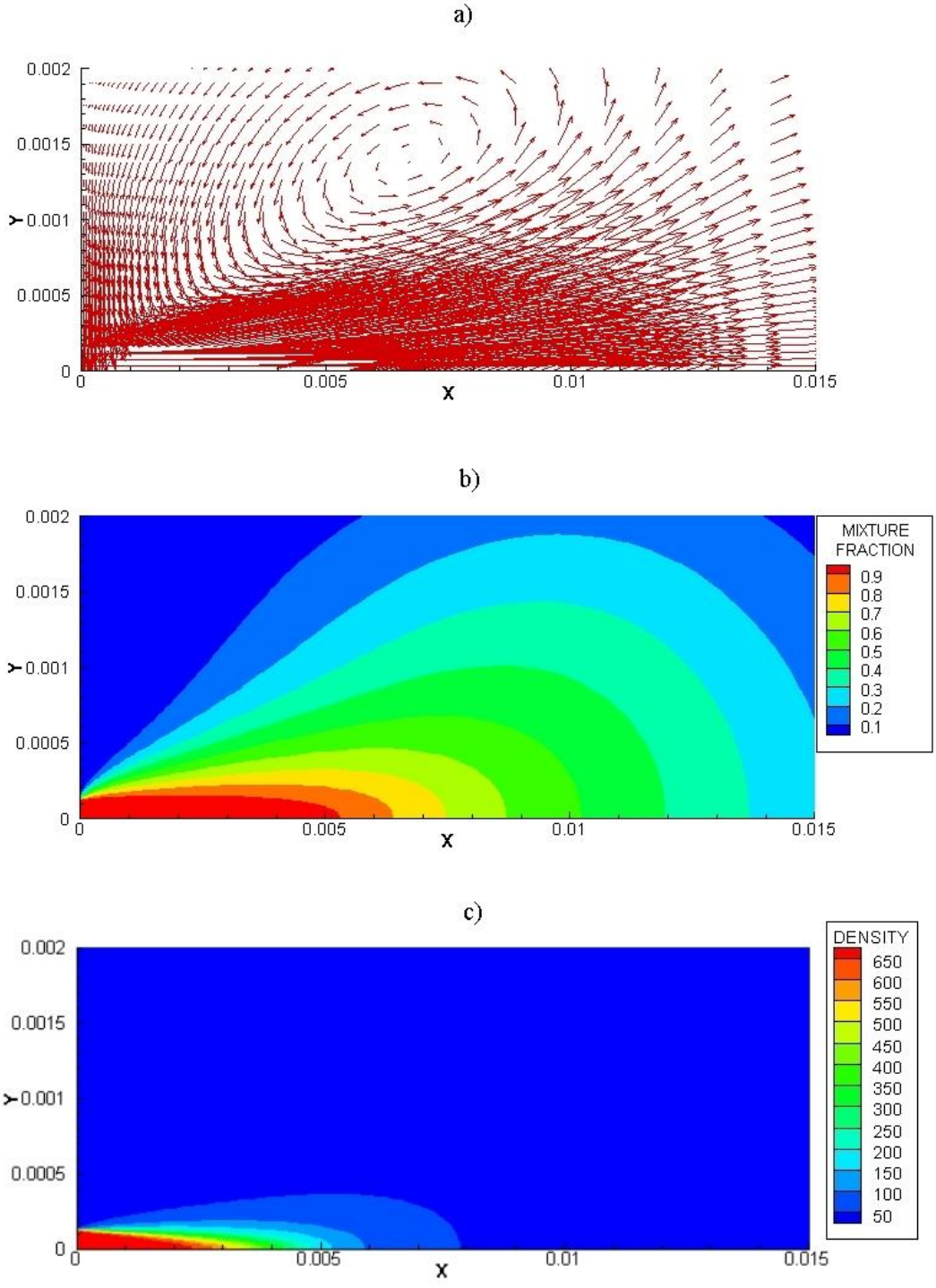

Figure 9 - Velocity and scalar fields of the jet with a density ratio of ω = 0.025 and an injection velocity of U_{in} = 20 m.s^{-1}, (a) Velocity vectors, (b) Mixture fraction contours, (c) Density contours.

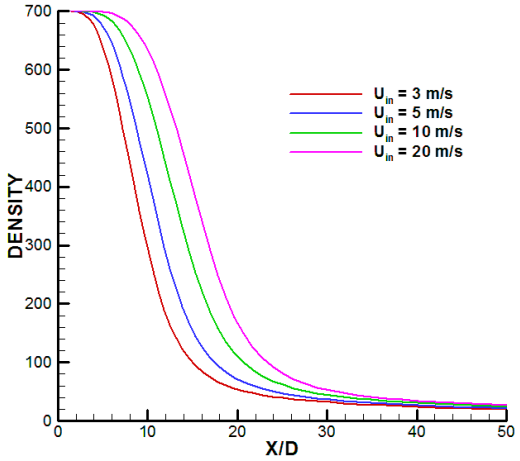

Figure 10 - Axial variation of the centerline density for the cases 4, 5, 6 and 7 of the Table 2.

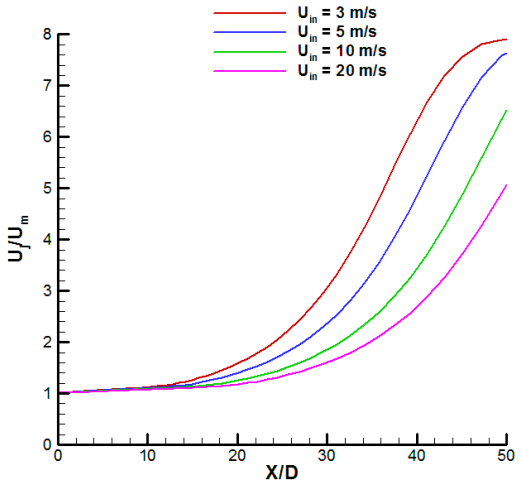

Figure 11 - Centerline velocity decay for the cases 4, 5, 6 and 7 of the Table 2.

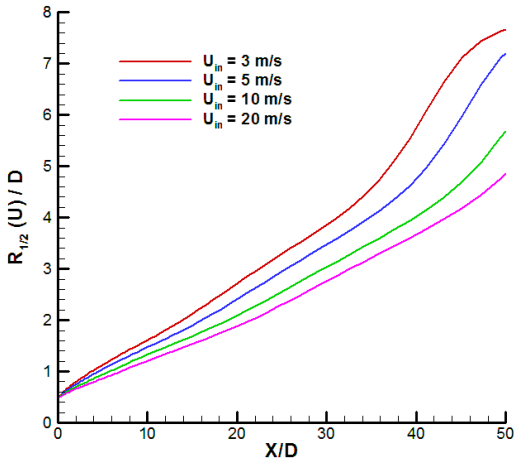

Figure 12 - Half width of half maximum of the velocity for the cases 4, 5, 6 and 7 of the Table 2.

IV. Conclusions

Barata *et al.* [18] had concluded that the variable density mathematical model could be successfully used in the study of cryogenic jets injected initially at subcritical temperatures into an environment at a supercritical temperature over a range of subcritical and supercritical pressures [18]. The objective of the present work was to extend the study performed by Barata *et al.* [18] to lower chamber-to-injection fluid density ratios. Like in Barata *et al.* [18], for this investigation an injection of cryogenic liquid nitrogen into a gaseous nitrogen environment was simulated.

In the analysis of the obtained result were identified some interesting new results. The fastest mixture fraction scalar field evolution when compared with the density scalar field together with the difference between the potential core based on density and the one based on velocity decay, suggests that a vigorous expansion of the injected fluid happens as it enters the injection chamber. And the longer potential core based on the velocity decay indicated that expansion may somehow contribute with kinetic energy to the jet.

The results of the half with of half maximum of the velocity allowed the determination of the jet growth rate which is in general agreement with the results obtained by Chehroudi *et al.*[23] described in Ref. 18. By the analysis of the results of the HWHMV obtained to density ratios lower than $\omega = 0.025$, it was concluded that below this value no more agreement was found with previous experimental and numerical results. This establishes the limit of applicability of the variable density approach to cryogenic liquid jet into a supercritical temperature and subcritical pressure ambient.

Finally it was concluded that the injection velocity has influence on the results obtained by the variable density approach. A faster injection velocity has as result a delay in mixture process and density decrease. The potential core based both on density and velocity decay increases as the injection velocity increases while the jet growth rate suffers a decrease. This way, the injection velocity must be taken into account when applying the variable density approach to a case study.

References

[1]Chehroudi, B., Cohn, R., and Talley, D., "Visual Characteristics and Initial Growth Rates of Round Cryogenic Jets at Subcritical and Supercritical Pressures," *Physics of Fluids*, Vol. 14, No. 2, 2002, pp. 850-861.

[2]Bellan, J., "Supercritical (and Subcritical) Fluid Behavior and Modeling: Drops, Streams, Shear and Mixing Layers, Jets and Sprays," *Progress in Energy and Combustion Science*, Vol. 26, Issues 4-6, 2000, pp. 329-366.

[3]Yang, V., "Modeling of Supercritical Vaporization, Mixing, and Combustion Processes in Liquid-Fueled Propulsion Systems," *Proceedings Of the Combustion Institute*, Vol. 28, 2000, pp. 925-942.

[4]Segal, C., and Polikhov, S.A., "Subcritical to Supercritical Mixing," *Physics of Fluids*, Vol. 20, Issue 5, 2008, pp. 052101-1-052101-7.

[5]Oschwald, M., Smith, J. J., Branam, R., Hussong, J., Schik, A., Chehroudi, B. and Talley, D. (2006) "Injection of Fluids into Supercritical Environments", *Combustion Science and Technology*, 178: 1, 49-100.

[6]Mayer, W.O.H., Schick, A. H. A., Vielle, B., Chauveau, C., Gökalp, I., Talley, D.G., and Woodward, R.D., "Atomization and Breakup of Cryogenic Propellants under High-Pressure Subcritical and Supercritical Conditions," *Journal of Propulsion and Power*, Vol.14, No.5, 1998, pp.835-842.

[7]Chehroudi, B., Cohn, R., and Talley, D., "Cryogenic Shear Layers: Experiments and Phenomenological Modeling of the Initial Growth Rate under Subcritical and Supercritical Conditions," *International Journal of Heat and Fluid Flow*, Vol. 23, Issue 5, 2002, pp. 554-563.

[8]Givler, S.D., John Abraham, J., "Supercritical Droplet Vaporization and Combustion Studies," *Progress in Energy and Combustion Science*, Vol. 22, Issue 1, 1996, pp. l-28.

[9]Zhang, H., Raghavan, V., Gogos, G., "Subcritical and Supercritical Droplet Evaporation within a Zero-Gravity Environment: Low Weber Number Relative Motion," *International Communications in Heat and Mass Transfer*, Vol. 35, Issue 4, 2008, pp. 385–394.

[10]Nomura, H., Ujiie, Y., Rath, H.J., Sato, J., Kono, M., "Experimental Study of High-Pressure Droplet Evaporation using Microgravity Conditions," *Twenty-Sixth Symposium (International) on Combustion/The Combustion Institute*, 1996, pp. 1267–1273.

[11]Tsue, M., Nomur, H., Niwa, M., Miyano, H., Sato, J., Kono, M., "Evaporation of a Fuel Droplet in a High Pressure High Temperature Atmosphere," *Japan Society for Aeronautical and Space Sciences*, Journal (ISSN 0021-4663), Vol. 37, No. 420, 1989, pp. 21-28.

[12]Fieberg, C., Reichelt, L., Martin, D., Renz, U., and Kneer, R., "Experimental and Numerical Investigation of Droplet Evaporation under Diesel Engines Conditions," *International Journal of Heat and Mass Transfer*, Vol. 52, Issues 15-16, 2009, pp. 3738-3746.

[13]Zhu, G.S., and Aggarwal, S.K., "Transient Supercritical Droplet Evaporation with emphasis on the Effects of Equation of State", *International Journal of Heat and Mass Transfer*, Vol. 43, Issue 7, 2000, pp. 1157-1171.

[14]Emekwuru, N.G., Watkins, P., "Analysis of a Two-Fluid Sprayer and its Use to Develop the Number Size Distribution Moments Spray Model Part II: Computational Analysis," *Atomization and Sprays*, Vol. 20, Issue 8, 2010, pp. 653-672.

[15]Oschwald, M., and Schik, A., "Supercritical Nitrogen Free Jet Investigated by Spontaneous Raman Scattering," *Experiments in Fluids*, Vol. 27, No. 6, 1999, pp. 497-506.

[16]Mayer, W., and Telaar, J., "Investigation of Breakup of Turbulent Cryogenic Variable-Density Jets," *Atomization and Sprays*, Vol. 12, Issue 5-6, 2002, pp. 651-666.

[17]Sanders, J. P. H., B. Sarh, B., Gokalp, I., "Variable Density Effects in Axisymmetric Isothermal Turbulent jets: a Comparison Between a First- and a Second-order Turbulence Model," *Int. J. Heat Mass Transfer*. Vol. 40, No. 4, 1997, pp. 823-842.

[18]Barata, J.M.M., Gokalp, I., Silva, A.R.R., "Numerical Study of Cryogenic Jets under Supercritical Conditions," *Journal of Propulsion and Power*, Vol. 19, No.1, 2003, pp. 142-147.

[19]Zong, N., Meng, H., Hsieh, S., and Yang, V., "A Numerical Study of Cryogenic Fluid Injection and Mixing under Supercritical Conditions," *Physics of Fluids*, Vol. 16, No. 12, 2004, pp. 4248-4261.

[20]Sierra-Pallares, J., Parra-Santos, M.T., García-Serna, J., Castro, F., Cocero, M.J., "Numerical Analysis of High-pressure Fluid Jets: Application to RTD Prediction in Supercritical Reactors", *Journal of Supercritical Fluids*, Vol. 49, 2009, pp. 249-255.

[21]Schmitt, T., Selle, L., Cuenot, B., and Poinsot, T., "Large-Eddy Simulation of Transcritical Flows", *Comptes Rendus Mécanique*, Vol. 337, Issues 6-7, June-July 2009, pp. 528-538.

[22]Kim, T., Kim, Y., Kim, S., "Numerical study of cryogenic liquid nitrogen jets at supercritical pressures," *The Journal of Supercritical Fluids*, Vol. 56, Issue 2, 2011, pp. 152-163.

[23]Chehroudi, B., Cohn, R., and Talley, D., "Spray/Gas Behaviour of Cryogenic Fluids under Sub- and Supercritical Conditions", Eighth International Conference on Liquid Atomization & Sprays Systems, ICLASS-2000, Pasadena, California, USA, July 16-20, 2000.

A.2 Paper Presented in 53th AIAA Aerospace Science Meeting

https://arc.aiaa.org/doi/abs/10.2514/6.2015-0469

AIAA SciTech
5-9 January 2015, Kissimmee, Florida
53rd AIAA Aerospace Sciences Meeting

RANS Modeling of Transcritical and Supercritical Nitrogen Jets

Eduardo L.S.F. Antunes*, André R. R. Silva†, Jorge M. M. Barata‡
Universidade da Beira Interior, Covilhã, 6201-1, Portugal

The present work is dedicated to the study of cryogenic nitrogen jets under supercritical chamber conditions with the objective of simulating the process of fuel injection inside a combustion engine. In order to do so, a numerical simulation using a RANS model was performed over two case studies previously analyzed by other authors both in experimental and numerical studies. The result obtained by the present numerical approach were then compared with previous results and this way accessed the capabilities of RANS approach using a k-ε turbulence model in which the density is calculated through the mixture fraction value to correctly model cryogenic jets at supercritical conditions. The results show the ability to achieve good agreement with other studies for the axial density distribution however for other parameters like the jet spreading angle the same agreement was not found.

Nomenclature

B = transfer number
β_v = evaporation rate
C_μ = coefficient in turbulence model
d_0 = initial droplet diameter
d = droplet diameter
D = injector diameter [m], normalized droplet diameter (d(t) / d_0)
ε = dissipation rate of turbulent energy
f = mixture fraction
F = mean mixture fraction
i = axial direction index
j = radial direction index
k = turbulent kinetic energy
ϕ = generalized variable
ω = chamber-to-injection fluid density ratio (ρ_∞/ρ_0)
P_{cr} = critical pressure [MPa]
P_∞ = chamber ambient pressure [MPa]
P_r = reduced pressure (P_∞/P_{cr})
ρ = density [kg.m^{-3}]
ρ_0 = injected fluid density [kg.m^{-3}]
ρ_∞ = injection chamber's fluid density [kg.m^{-3}]
r = radial coordinate [m]
R/D = radial distance normalized by injector diameter
R_{diam} = injector radius [m]
R_e = Reynolds Number
S_ϕ = source term
t = time [s]
T = temperature [K]
u = axial velocity [m.s^{-1}]
U = mean axial velocity [m.s^{-1}]

* PhD Student, Aerospace Sciences Department, AIAA Student Member.
† Assistant Professor, Aerospace Sciences Department, AIAA Member.
‡ Full Professor, Aerospace Sciences Department, Associate Fellow of AIAA.

U_{in} = injection axial velocity [m.s^{-1}]
v = radial velocity [m.s^{-1}]
v_t = turbulent kinematic viscosity
V = mean radial velocity [m.s^{-1}]
X = axial coordinate [m]
X/D = axial distance normalized by injector diameter

I. Introduction

HUMAN kind finds itself today in a moment in history were it is strongly dependent on fossil fuels, while other alternative sources of energy have not yet been found, to sustain and further increase the achieved development. However, these fossil fuels are not unlimited, and a more efficient use of them must be found in the meanwhile. Also, we live in a planet that relies in a very fragile balance of its ecosystem. Pollution originated by the burning of fossil fuels are proved to be able to destabilize this fragile balance with possible disastrous consequences. This way a less harmful way of burning these fuels must be found, or at least a way of while fulfilling our energetic demands, burning those fuels in less quantity.

One way of fulfilling the exposed objectives is by the development and adoption of more efficient combustion power systems. Fuel injection plays one of the most important roles in the subject of combustion. The way fuel and oxidizer mix inside the combustion chamber of the several kinds of engines is key for the degree of combustion efficiency in power production. Other important factors in the efficiency of a combustion engine are the combustion chamber's temperature and pressure. Increasing the operating temperatures and pressure of power systems like diesel engines, gas turbines and rocket engines is a known way of increasing the fuel efficiency of such engines. And this increase is turned in the past years into a important trend in designing of new power units.

Thus appears as an important issue, in recent combustion engines, the investigation of fuel (and oxidizer) injection into combustion chambers at high values of temperature and pressure. However it happens that when operating pressure and temperature increase, the fuels and oxidizers used by the propulsion systems may experience the exceeding of their critical values. The issue is that, under conditions of pressure and temperature that exceed or are around the critical values, fluids have shown to have quite distinct behavior from the usually observed behavior while at conditions far from these.

Several author have investigated the fluid behavior under and near supercritical conditions both by experimental and numerical approaches which resulted in the production of extensive bibliography[1-27]. As far as today, some conclusions have been already taken and validated about the changes in the physical properties of fluids when around and above critical conditions. According to Bellan[25], under supercritical conditions, which in the present work are characterize by both pressure and temperature being over the critical values, mass diffusivity, surface tension and latent heat vanish. On the other hand the heat capacity at constant pressure, Cp, the isentropic compressibility, k_s and the thermal conductivity, λ, all become infinite. In terms of flow behavior is observed a change in the jet structure from a liquid-gas injection to a gas-gas like injection[4,15,17,18]. However bigger questions about fluid behavior appear in conditions near critical for which is still unknown if the fluid a behavior closer to gas behavior, liquid behavior or a mix of the two behavior which appears to be the most probable possibility[27].

In previous works[10,11] was made the attempt to evaluate the applicability of a numerical variable density approach to cryogenic nitrogen jets injected into nitrogen gaseous environment at different chamber-to-injectant density ratio (ω). The results obtained shown agreement of the jet spreading angle with the experimental work of Chehroudi et al.[3] for chamber-to-injectant ratios between 0.025 and 0.1408.

The objective of the present work is to study, evaluate and develop numerical methods to better describe injection process around and beyond critical condition. In the present paper is described the injection of liquid nitrogen into gaseous nitrogen environment modeling, resorting to a RANS approach using a k-ε turbulence model initially developed for incompressible but variable density flows. Two different test cases were simulated using the same injector and chamber geometry shown in Figure 1. The cases were named as case 3 and 4 in order to follow the same nomenclature already used by previous authors and its conditions are shown in Table 1. The only difference between case 3 and 4 is the injection temperature, however this different puts the first one in transcritical conditions (supercritical pressure but subcritical temperature) while the second in supercritical injection conditions. The modeled cases were then compared with the experimental data of Mayer et al.[16] and the Large Eddy Simulations of Schmitt et al.[20] and of Jarczyk and Pfitzner[24].

With these two tests, and joining them with the knowledge obtained in previous work, is expected to be achieved better insight over the injection performed at conditions close to critical in order obtain more clues of the better strategy to model these flows.

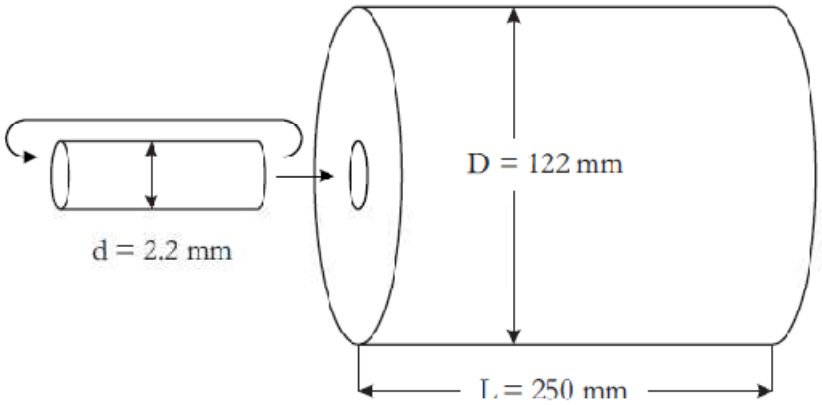

Figure 1. Chamber geometry[20].

	Case 3	Case 4
Chamber Pressure [MPa]	3.97	3.97
Chamber Temperature [K]	298	298
Injection Temperature [K]	126.9	137
Injection Velocity [m/s]	4.9	5.4
ρ_∞ [kg/m^3]	435	171
ρ_{inj} [kg/m^3]	45.5	45.5
ω	0.1046	0.2661

Table 1 - Conditions of the test cases.

II. Mathematical Model

In the present work was used the same mathematical model and numerical approach already used by Barata et al. [10] and in the previous work [11]. However some modifications were introduced in the grid and the boundary conditions in order to provide the numerical approach the ability to test the same conditions present in the works of Mayer et al.[16], Schmitt et al.[20] and Jarczyk and Pfitzner[24].

A. Governing Equations

The method to solve is based on the solution of the conservation equations for momentum and mass. Turbulence is modeled with the "k~ε" turbulence model. A similar method has been used for three-dimensional or axisymmetric flows and only the main features are summarized here.

In the conservation equations, mass weighted averaging is applied to avoid the appearance of many terms involving density fluctuations for which additional models are needed. A mass averaged quantity is defined as

$$\tilde{\phi} = \frac{\overline{\rho\phi}}{\overline{\rho}} \qquad (1)$$

For the governing equations the standard parabolic truncation is employed. The mass averaged partial differential equations governing the steady, variable density axisymmetric flow may be written in cylindrical polar coordinates as

$$\frac{\partial \bar{\rho} UU}{\partial x} + \frac{1}{r}\frac{\partial r\bar{\rho} UV}{\partial r} = -\frac{\partial \bar{p}}{\partial x} - \frac{1}{r}\frac{\partial r\bar{\rho}\,\overline{\tilde{u'v'}}}{\partial r} \quad (2)$$

$$\frac{\partial \bar{\rho} UV}{\partial x} + \frac{1}{r}\frac{\partial r\bar{\rho} VV}{\partial r} = -\frac{\partial \bar{p}}{\partial x} - \frac{1}{r}\frac{\partial r\bar{\rho}\,\overline{\tilde{v'v'}}}{\partial r} + \bar{\rho}\frac{\overline{\tilde{w'w'}}}{r} \quad (3)$$

and the continuity equation as

$$\frac{\partial \bar{\rho} U}{\partial x} + \frac{1}{r}\frac{\partial r\bar{\rho} V}{\partial r} = 0 \qquad (4)$$

To describe mixing of gases, the mixture fraction *F*, that represents the mass fraction of the nozzle fluid, is introduced. It obeys a convection-diffusion equation of the form

$$\frac{\partial \bar{\rho} UF}{\partial x} + \frac{1}{r}\frac{\partial r\bar{\rho} VF}{\partial r} = -\frac{1}{r}\frac{\partial r\bar{\rho}\,\overline{\tilde{v'f'}}}{\partial r} \qquad (5)$$

In "k~ε" turbulence model, the Reynolds stresses are expressed in terms of the local strain rate:

$$-\bar{\rho}\,\overline{\tilde{u'_i u'_j}} = \bar{\rho}(\nu_t + \nu)\left(\frac{\partial \tilde{u}_i}{\partial x_j} + \frac{\partial \tilde{u}_j}{\partial x_i}\right) - \frac{2}{3}\delta_{ij}\left(\bar{\rho}k + \bar{\rho}(\nu_t + \nu)\frac{\partial \tilde{u}_j}{\partial x_j}\right) \qquad (6)$$

with

$$\nu_t = C_\mu \frac{k^2}{\varepsilon} \qquad (7)$$

The scalar flux in equation (5) is approximated with a gradient transport assumption

$$\overline{\tilde{u'_i f'}} = -\frac{\nu_t}{\sigma_f}\frac{\partial F}{\partial x_i} \qquad (8)$$

From the foregoing we can deduced the parabolized set of equations in cylindrical coordinates where the generalized equation is

$$\frac{\partial}{\partial x}\left(\bar{\rho} U\tilde{\phi}\right) + \frac{1}{r}\frac{\partial}{\partial r}\left(r\bar{\rho}\tilde{\phi}\right) = \frac{1}{r}\frac{\partial}{\partial r}\left(r\bar{\rho} D\frac{\partial \tilde{\phi}}{dr}\right) + S_\phi \qquad (9)$$

where $\tilde{\phi}$ may stand for any of the velocities, turbulent kinetic energy, dissipation, or scalar property, and S_ϕ take on different values for each particular $\tilde{\phi}$, described in detail by Sanders et al.[9].

The mean density can be obtained from the mean mixture fraction using the equation state. With constant pressure this leads to

$$\frac{1}{\bar{\rho}} = \frac{F}{\rho_o} + \frac{1-F}{\rho_\infty} \qquad (10)$$

where density fluctuations have been neglected. This is allowed in isothermal jets because the instantaneous density, for which equation (10) is exact, is approximately a linear function of the instantaneous mixture fraction[10].

B. Numerical Method

The governing equations are solved using a parabolized marching algorithm which resembles the (elliptic) TEACH code [9]. The computations are performed by using the continuity equation to obtain the radial velocity (V). Using the radial momentum equation for V and solving a pressure correction equation for V in radial direction did not show any difference with the use of the continuity equation[9]. In this approach the numerical model was applied to variable density jets and for the present case it was used for the study of liquid cryogenic jets under sub-near critical pressures, and sub to supercritical temperatures.

In order to determine the tangent of the jet spreading angle is used the Half Width of Half Maximum of the Density (HWHM of Density), this routine has the function of determine the radial distance from the centerline (r) at which the axial mean density (ρ) is half of the maximum density in the centerline. This routine analysis all the points in the radial direction comparing them with half of the centerline velocity, when the routine finds a point bellow this value it saves the point before that.

C. Computational grid

The flow configuration can be observed in Figure 1, with the cold nitrogen being injected through a round injector with 2.2 mm of diameter into a cylindrical chamber with a diameter of 122 mm and a length of 250 mm. For this numerical approach was used a grid that represents half of the domain since the symmetry until the external wall. Making this way a numerical domain of 250 mm long and 61 mm width. Was used a grid of 250 points in the axial direction and 100 points in the radial direction making a total of 25000 points.

The grid is represented in Figure 2. In order to allow the setting of the desired numbers of points in one direction and at the same time keep the defined length and width of the domain was not used the same method of constant expansion of grid dimensions used in previous works[10,11]. Instead was programmed a new grid subroutine that allows to define the number of points and domain, while still being more refined close to the injector. In the axial direction the grid was defined by dividing 50% of the grid points between 30% of the domain length close to the injector, the other 50% of grid point are shared between 70% of the length domain more far from injector.

In radial direction a similar strategy was followed but in this case was first defined 20 grid points in the inlet region (1.1 mm) and the remaining 80 points were defined 40 (50%) to the first 30% of domain and the rest (40 points) for the last 70% of domain. All of these features are visible in Figure 2.

Because a new grid was used and no other previous works had used it before, a grid dependency test was performed. The axial velocity decay was used to test the grid dependency of the computations. Figure 3 compares evolution along the symmetry axis of the velocity decay for 3 different grid sizes and even for a grid with 125x50 point, one quarter of the size (in total number of points), the results are very close to the used grid (250x100). And for the grid with approximately 65% of number of points (200x80) the difference is negligible.

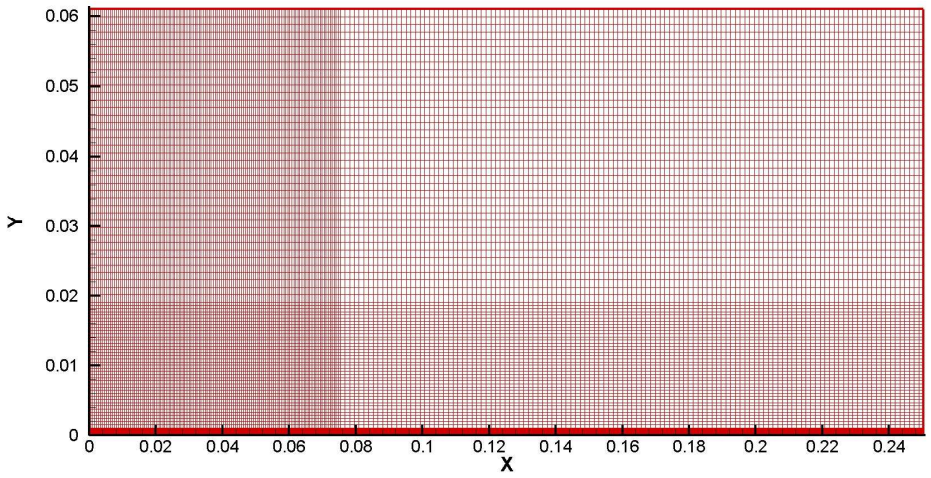

Figure 2. Grid Geometry (both axis are in meters).

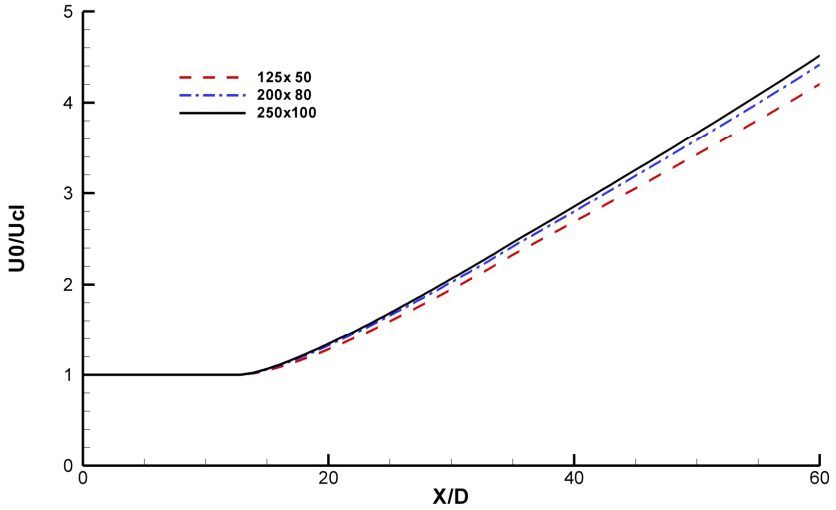

Figure 3. Grid size dependency test based on the axial velocity decay.

III. Results and Discussion

Numerical results obtained in the present work are presented in this section and compared with the experimental data of Mayer et al.[16] and the large eddy simulations of Schmitt et al.[20] and of Jarczyk and Pfitzner[24]. A discussion is also provided in order to reach the conclusions exposed in the next section.

Figures 4 and 5 show the velocity, mixture fraction and density fields for cases 3 and 4 respectively. These two charts allow us to obtain a general picture of the flow geometry. As said before, and described in Table 1, the two test cases only vary in the injection temperature (and by consequence the density) and velocity, while the chamber conditions remain the same for both cases. Nevertheless the difference in the injection temperature between the two cases is enough to position them in different thermodynamic regimes. The test case 3 is at transcritical conditions, regime at which there's supercritical pressure but subcritical temperature, while case 4 in supercritical injection conditions at which both pressure and temperature are supercritical.

Comparison between both cases show a very similar jet structure with the case 4 showing a faster reduction of density and mixture fraction value than case 3. Similar conclusions are obtain in the previous studies of Schmitt et al.[20] and Jarczyk and Pfitzner[24], with the LES visualizations showing similar variations between the two cases. These result also suggest the existence of a smaller potential core for the case 4, this characteristic in particular will be discussed later.

Figures 4 and 5 a) show the velocity field obtained in the present simulation. It is visible in both cases the appearence of entrainment close to the injector exit with ambient nitrogen being pulled into the jet stream. This phenomenon appears to be slightly more intense in test case 3 even this case slower injection velocity, this is probably due to the higher jet momentum caused by higher injection fluid density. It is also visible that more far from the injector the velocity vectors are bigger in case 3 than in case 4 that has higher injection velocity. The injection density appears to be determinant to the distance that a jet can reach.

In Figures 4 and 5 b) is shown the mixture fraction field for test cases 3 and 4. The images show a high concentration of injected fluid close to the injector exit and decreasing along the domain while getting far from the injector in both radial and axial direction. Comparison between the two cases show a faster decrease of the mixture fraction along the jet in case 4, this faster decrease however doesn't mean better mixture of the jet fluid with the chamber fluid. In fact there are bigger mixture fraction gradients in case 4, close to the injector the mixture fraction quickly decreases value but then, in the rest of the injection chamber, the ambience is dominated by mixture fraction values bellow 0.5. In case 3 even showing a slower decrease of mixture fraction and bigger penetration of injection fluid (apparently showing a slower mixture in beginning of jet) shows however better mixture having in most of domain mixture fraction values close to 0.5. These results of apparently better mixture in the case with smaller temperature and at which difference between injection density and chamber density is bigger can be considering in some way surprising.

Density field is shown in Figures 4 and 5 c) for test cases 3 and 4 respectively. Again the results show similar jet structure for both cases. Case 3 however shows a longer dense core than case 4. Having case 3 bigger density gradient between injected and chamber fluid and a lower injection velocity one could expect it to have a shorter dense core as well as a smaller jet penetration than case 4. However it happens the opposite, the explanation found by the authors of the present paper is that the fluid density due to its influence in fluid momentum rules the jet dynamics. The jet in case 3 even having slower injection velocity has in fact higher momentum and this causes it to have bigger penetration length. The higher jet momentum is also responsible for the more intense entrainment at the jet exit in case 3, the entrainment phenomenon is important for the fluid mixing, this explain the better mixing in case 3 when compared to case 4 observed in mixture fraction field. These results obtained by the present numerical approach are corroborated in the LES results of Schmitt et al.[20] where case 3 also shows to have a longer jet length and dense core than case 4.

The results obtained by the velocity and scalar fields also give us the proves that the jet behavior is mostly dominated by the convection terms while diffusion plays a minor role. In turn, convection is mostly dominated by the density. The calculation of density appear this way as a key factor in the modeling of this kind of flows.

The axial density distribution of cases 3 and 4 is shown in Figures 6 and 7 respectively for the present work modeling and also for the experimental and numerical results of other authors. Potential core length is one important characteristic of a jet, generally used by other authors to help quantifying it. Schmitt et al.[20] defines the potential core length as the axial distance at which the centerline density is 99% of the injected density, generally potential core length is expresses in multiples of injector diameters. In the present investigation was decided to use the same definition of potential core already used by Schmitt[20].

The results obtained for case 3 in the present investigation show a potential core of 12.3 injector diameters. It is longer when compared with the results of other authors, Schmitt et al.[20] for example shows a potential core length of 7.9 diameters and Jarczyk and Pfitzner[24] a length of around 9 diameters, it can however be observed that the obtained profile of the centerline density distribution follows the general trend found in the previous works. While until an axial distance of around 15 x/D the present results are not able to get a very good agreement with the experimental and even LES data, after this distance the presently numerical results are able to get in a exceptionally good proximity with the experimental data of Mayer [16], showing better agreement than both LES results. The same kind of centerline density distribution profile was obtained to case 4 in the present work. The potential core obtained of around 7.5 diameters is bigger than the one obtain by the two LES results which are 5.1 diameters in the work of Schmitt et al.[20] and around 6 jet diameters for Jarczyk and Pfitzner[24]. Analyzing experimental data of Mayer et al.[16] shows however little amount of evidence of the existence of a potential core for this test case.

During a big portion of the observed domain, since 9 jet diameters until around an axial distance of 20 x/D, the present results are positioned between the both LES works and very close to the experimental data. After this distance, the obtained results are the ones that more close agreement share with the experimental data until the end of the observed domain, once again outperforming the LES approaches in the last part of domain. The general agreement in the axial density distribution with LES results and experimental data can be classified as quite good taking in consideration the limitations of the present numerical approach when compared with other simulation techniques, being even able to overcome the results of LES in the end of the exposed domain.

The spreading angle of the jet is one of the most important parameters available to the use of a researcher when his objective is to characterize a jet. In order to determine the spreading of a jet becomes necessary to define the radial border of it. Several authors, including those cited in the present paper[20,24], assume that the border of the jet is in the radial position where the density is half of the value in the centerline position at the same axial distance. This way is defined the Full Width of Half Maximum of Density (FWHM of Density) and also the Half Maximum of Half Width of Density which has a value half of the FWHM and was used in work due to the fact that only half of the domain was simulated. In the work of Schmitt et al.[20] the tangent of the spreading angle of density was obtained by linear interpolation of the FWHM of Density between x/D = 15 and x/D = 25. In the present work was decided to use the same method but adapting it to the Half Width of Half Maximum of Density obtained in the present work. However care was always taken in order to never directly compare directly FWHM with HWHM without the proper conversion between both.

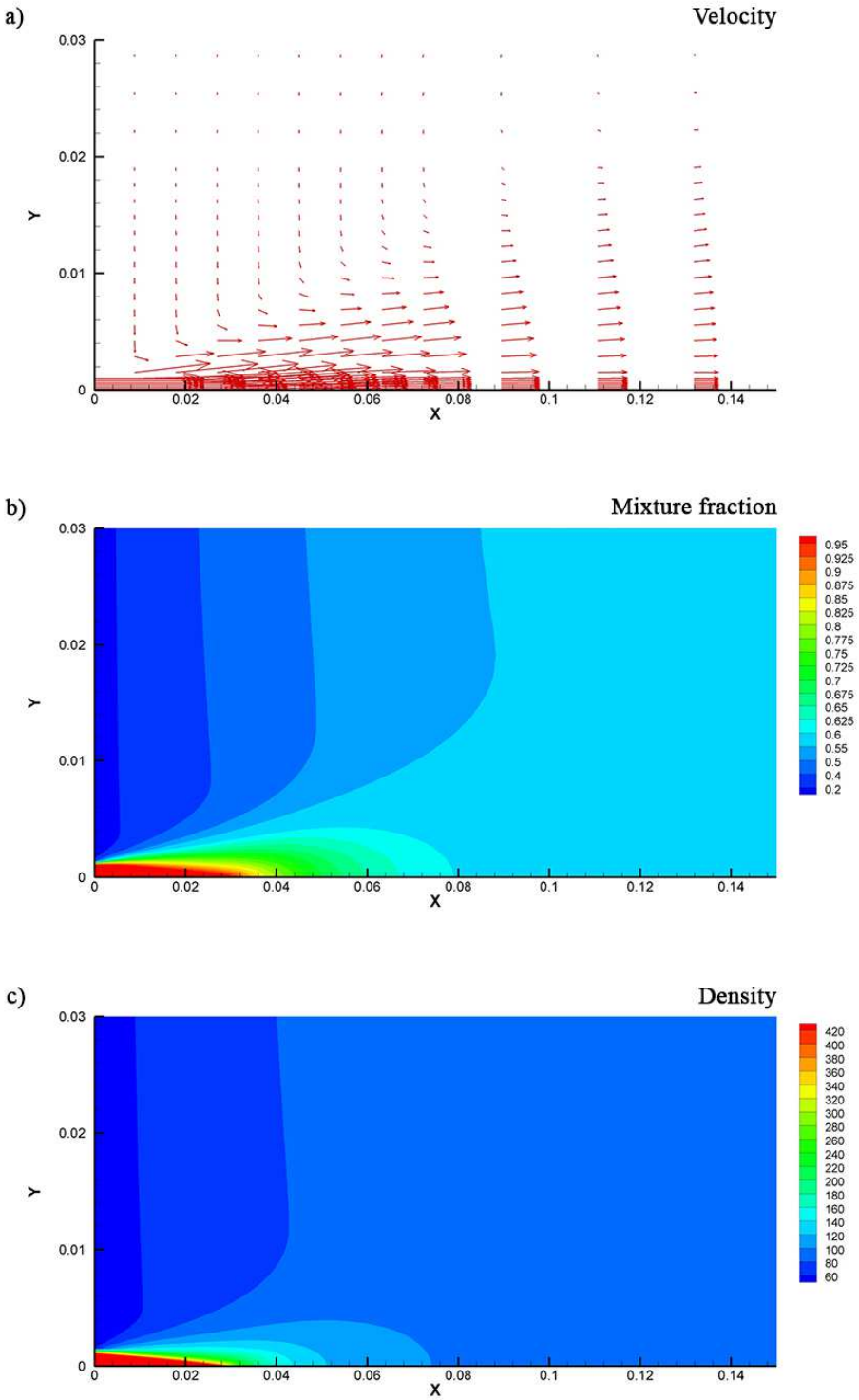

Figure 4. Velocity and scalar fields of the jet for test case 3. a) Velocity Vectors; b) Mixture Fraction contours; c) Density contours.

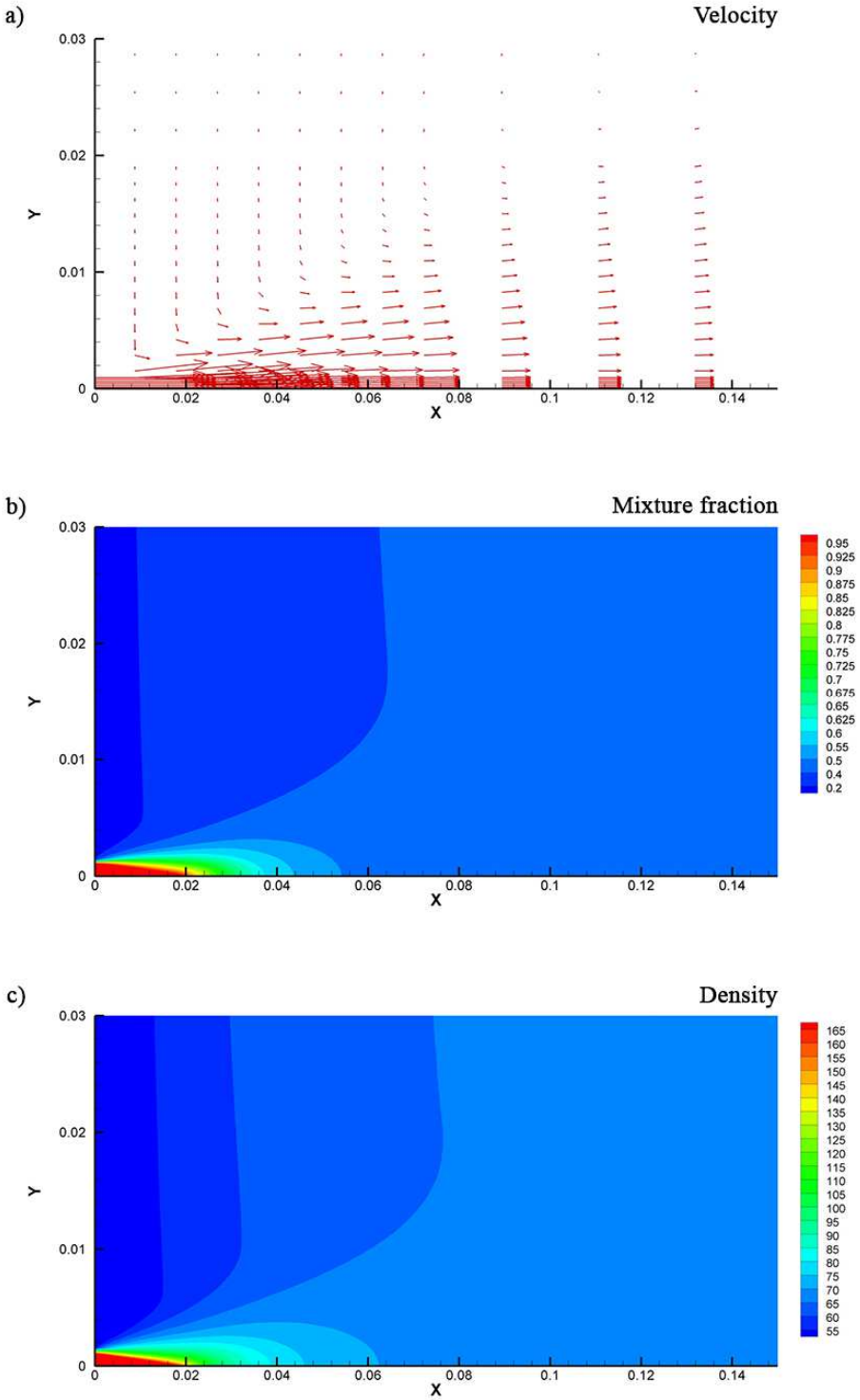

Figure 5. Velocity and scalar fields of the jet for test case 4. a) Velocity Vectors; b) Mixture Fraction contours; c) Density contours.

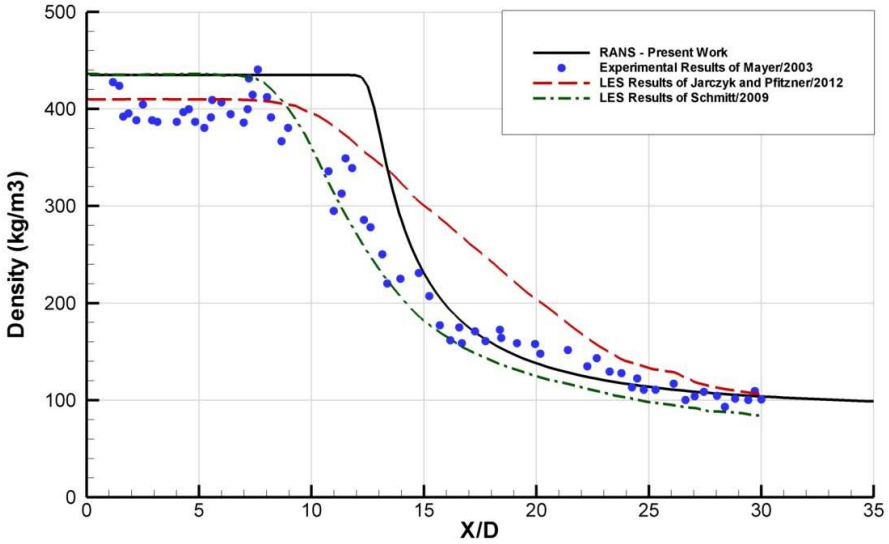

Figure 6 - Axial density distribution for Case 3 and comparisons with different authors results.

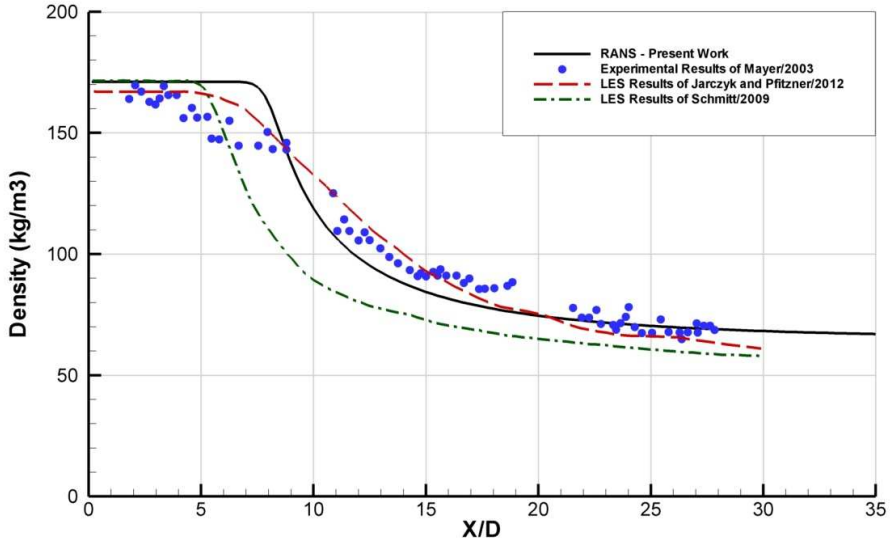

Figure 7 - Axial density distribution for Case 4 and comparisons with different authors results.

Figure 8 shows the HWHM of Density for test case 3 obtained in the present work and compared with the Raman measurements of Mayer et al.[16]. It can be observed that numerical results obtain in the present work follow a similar trend to the one obtained in the experimental data. The chart initially shows a decreasing of the half width that extends for the experimental data until 10 x/D and in present numerical data until approximately 12 x/D, while always smaller width in numerical data. After this point the half width of the jet starts increasing, showing that the

jet is spreading, however the observed spreading is much bigger in the numerical data than in the Raman measurements. The tangent of spreading angle using the FWHM of Density is 0.196 for the experimental data and 1.441 in the present numerical approach, approximately 7 times bigger. For the same case the LES simulation of Schmitt et al.[20] present a tangent of the spreading angle of 0.227 which slightly higher than experimental results but still much closer than the ones obtained in the present investigation.

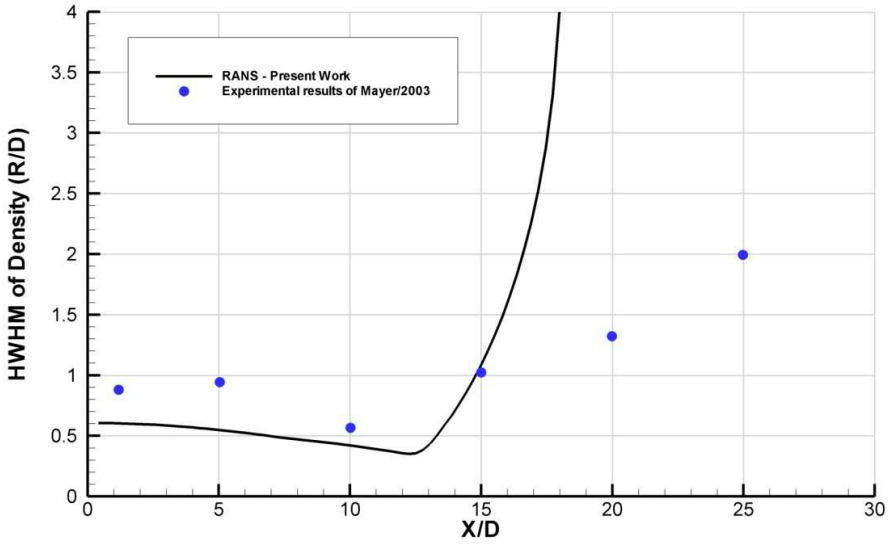

Figure 8 - Half Width of Half Maximum of Density for case 3 and comparison with experimental data of Mayer et al.[16].

In Figure 9 is shown the HWHM of Density for case 4. For these case there were no available experimental data from the Raman measurements of Mayer et al.[16] and for this reason Figure 9 only shows the results obtained on the present work. In the chart it is possible to observe in the beginning of the jet very slow increase of the of the jet width until an axial length of around 8 x/D, after this mark there's a sudden and very fast increase of jet width. Due to this sudden skyrocketing of the jet width obtain in present results, it is not possible to calculate tangent of the spreading angle by the use of the same methodology used in previous works since there weren't obtained values of the jet half width for axial length of 15 x/D and even less for 25 x/D.

Contrary to the results obtained for the axial density distribution which have shown quite good agreement with experiments and LES results, the results of the Half Width of Half Maximum of Density reached in the present investigation are very far from other experimental and LES data. Results from Schmitt et al.[20] show that for case 4 the tangent of spreading angle is around 0.241, a little bit higher than for case 3. Further improvement in the present numerical approach are required in order to provide better agreement with experimental and LES data of jet spreading angle.

Figures 10 and 11 show the Half Width of Half Maximum of Mixture Fraction for cases 3 and 4 respectively. These results are obtained with the same method used for Density but in this case for Mixture Fraction. The charts represent this way the radial distance from the centerline at which the Mixture Fraction value is half of the value in the centerline, for each point in the axial direction. The tangent of the spreading angle based on the HWHM of Mixture Fraction could be calculated by the same method used for Density, however in these cases there are no results for a axial distance of 25 x/D and this way is not possible to perform the calculation using the same two points defined in [20]. The results of case 3 show a different profile from that obtained in the HWHM of Density having an initial zone with a positive tangent of spreading angle (contrary to experimental and present work data that initially shows a negative tangent) and then an increase of the tangent to almost vertical.

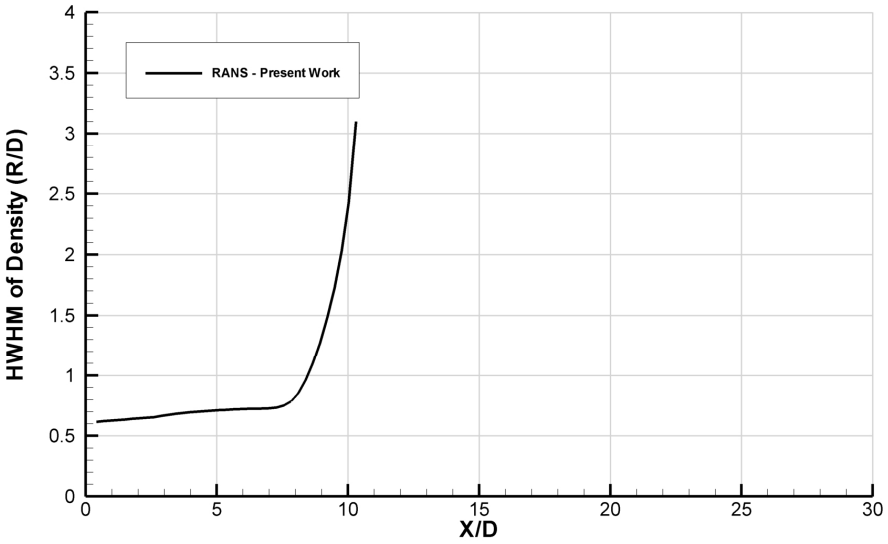

Figure 9 - Half Width of Half Maximum of Density for case 4.

IV. Conclusion

With the objective of studying, evaluating and developing numerical methods for better describing of injection process around and beyond critical condition, the present investigation has as task the evaluation of a numerical approach, originally designed to model gaseous jet flows with different densities, when used to model cryogenic jets at thermodynamic conditions near critical. As part of the task is also the goal of attempting to identify and later integrate the needed modifications to the numerical approach in order to make it more suitable to simulate the flows of interest.

With the task of evaluating the present numerical approach were modeled two test cases initially tested in a experimental work performed by Mayer et al.[16] and then numerically simulated by both Schmitt et al.[20] and Jarczyk and Pfitzner[24] using the technique of Large Eddy Simulation.

The numerical results obtained for the axial density distribution in the present investigation are in good agreement with experimental results of Mayer[16] and in some parts of the domain can even perform better than the LES investigations[20,24]. However not so good agreement was found for the jet spreading angle

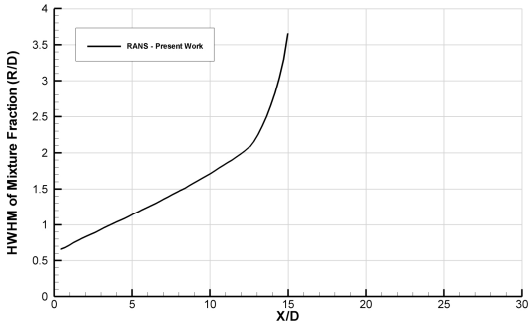

Figure 10 - Half Width of Half Maximum of Mixture Fraction for case 3.

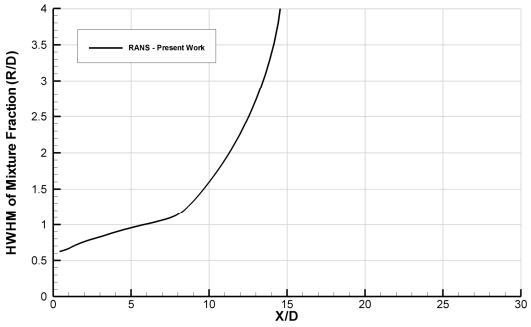

Figure 11 - Half Width of Half Maximum of Mixture Fraction for case 4.

results based on density, where the numerical approach while being able to reproduce the same shape of profile was very far from reproducing the magnitude of the jets spreading. These results lead to the conclusion that improvements must be included in the present numerical methods. There has been a trend between authors investigating jet at conditions near critical to use real gas equation of state to calculate de density[15,20,24,25]. In the present numerical approach the mean density is calculated by a equation of state that is a linear function of the mixture fraction. As stated above this method of calculation of density in allowed for isothermal jets. However in the present test cases one is not in the presence of isothermal gases, so this method of calculating density can be one of the main causes of failing to predict the jet spreading angle.

Transcritical and supercritical jets are highly transient and very sensitive to small and local changes of temperature and pressure[26]. RANS methods unlike LES use only the average terms of velocity, pressure, temperature, etc, neglecting the small fluctuations that in transcritical and supercritical jet can have huge impact in the flow behavior. This reality could in fact also consist in one of the causes for incapacity of the present numerical approach to provide accurate predictions of the studied jet spreading angle. However Park[25], in his LES and RANS investigation, concluded that the suitable adoption of a equation of state is more decisive than the selection of turbulence model for the numerical performance. On the other hand Park also stated that when compared with LES results, the spreading rates of RANS models are slightly higher.

Next works will be focused on the attempt of integrating a real gas equation of state into the present numerical formulation in order to provide the model with a different method for density calculation. With these changes the authors expect to solve the problems encountered in the present formulation and get better agreement with experimental data.

Acknowledgments

The author would like to thanks: Fundação para a Ciência e a Tecnologia (FCT), the Portuguese public agency for science and technology, for the financing of the present investigation by providing a PhD scholarship to the first author with the reference SFRH/BD/87822/2012. Also AeroG-LAETA associated laboratory, for providing integration in a research unit to the authors of the present communication. And finally to Universidade da Beira Interior - Covilhã, the host institution for the authors.

References

[1]Seebald, P., and Sojka, P.E., "Supercritical and Transcritical Injection," *Hand Book of Atomization and Sprays*, edited by N. Ashgriz, Springer Science+Business Media, 2011, pp. 255-261.

[2]Martínez- Martínez, S., Sánchez-Cruz, F.A., Riesco-Ávila, J.M., Gallegos-Munoz, A., Aceves, S.M., "Liquid Penetration Length in Direct Diesel Fuel Injection," *Applied Thermal Engineering*, Vol 28, Issues 14-15, 2008, pp. 1756-1762.

[3]Chehroudi, B., Cohn, R., and Talley, D., "Spray/Gas Behaviour of Cryogenic Fluids under Sub- and Supercritical Conditions", Eighth International Conference on Liquid Atomization & Sprays Systems, ICLASS-2000, Pasadena, California, USA, July 16-20, 2000.

[4]Chehroudi, B., Cohn, R., and Talley, D., "Cryogenic Shear Layers: Experiments and Phenomenological Modeling of the Initial Growth Rate under Subcritical and Supercritical Conditions," *International Journal of Heat and Fluid Flow*, Vol. 23, Issue 5, 2002, pp. 554-563.

[5]Chehroudi, B., Talley, D., and Coy, E., "Visual Characteristics and Initial Growth Rates of Round Cryogenic Jets at Subcritical and Supercritical Pressures," Physics of Fluids, Vol. 14, No. 2, 2002, pp. 850-861.

[6]Mayer, W.O.H., Schick, A.H.A., Vielle, B., Chauveau, C., Gökalp, I., Talley, D.G., and Woodward, R.D., "Atomization and Breakup of Cryogenic Propellants under High-Pressure Subcritical and Supercritical Conditions," *Journal of Propulsion and Power*, Vol.14, No.5, 1998, pp.835-842.

[7]Zong, N., Meng, H., Hsieh, S., Yang, V., "A numerical study of cryogenic fluid injection and mixing under supercritical conditions," *Physics of Fluids*, Vol. 16, No. 12, 2004, pp. 4248-4261.

[8]Zong, N., Yang, V., "Cryogenic Fluid Jets and Mixing Layers in Transcritical and Supercritical Environments", *Combustion Science and Technology*, Vol. 178, No 1-3, 2006, pp. 193-227.

[9]Sanders, J.P.H., Sarh, B., Gokalp, I., "Variable Density Effects in Axisymmetric Isothermal Turbulent Jets: a Comparison between a First- and a Second-order Turbulence Model," *Int. J. Heat Mass Transfer*, Vol. 40, No. 4, 1997, pp. 823-842.

[10]Barata, J.M.M., Silva, A.R.R., Golkalp, I., "Numerical Study of Cryogenic Jets under Supercritical Conditions," *40th AIAA Aerospace Sciences Meeting & Exhibit*, Reno, NV, 14-17 January 2002, AIAA 2002-0916.

[11]Antunes, E., Silva, A., Barata, J., "Evaluation of a Numerical Variable Density Approach to Cryogenic Jets," *50th AIAA Aerospace Sciences Meeting including the New Horizons Forum and Aerospace Exposition*, Nashville, TN, 09-12 January 2012, AIAA 2012-1282.

[12]Newman, J.A., and Brzustowski, T.A., "Behavior of a Liquid Jet Near the Thermodynamic Critical Region," *AIAA Journal*, Vol. 9, No. 8, 1971, pp. 1595-1602.

[13]Papamoschou, D., and Roshko, A., "The Compressible Turbulent Shear Layer: an Experimental Study," *Journal of Fluid Mechanics*, Vol. 197, 1988, pp. 453-477.
[14] Oschwald, M., and Schik, A., "Supercritical nitrogen free jet investigation by spontaneous Raman scattering," *Experiments in Fluids*, Vol 27, Issue 6, 1999, pp. 497-506.
[15]Oschwald, M., and Micci, M.M., "Spreading Angle and Centerline Variation of Density of Supercritical Nitrogen Jets" *Atomization and Sprays*, Vol. 12, Issue 1-3, 2002, pp. 91-106.
[16]Mayer, W., Telaar, J., Branam, R., Schneider, G., Hussong, J., "Raman Measurements of Cryogenic Injection at Supercritical Pressure," *Heat and Mass Transfer*, Vol. 39, Issue 8-9, 2003, pp. 709-719.
[17]Oschwald, M., Smith, J.J., Branam, R., Hussong, J., Schik, A., Chehroudi, B. and Talley, D. (2006) "Injection of Fluids into Supercritcal Environments," *Combustion Science and Technology*, Vol. 178, No. 1-3, 2006, pp. 49-100.
[18]Segal, C., and Polikhov, S.A., "Subcritical to Supercritical Mixing," *Physics of Fluids*, Vol. 20, Issue 5, 2008, pp.. 052101-1 - 052101-7.
[19]Schmitt, T., Rodriguez, J., Leyva, I.A., Candel, S., "Experiments and numerical simulation of mixing under supercritical conditions," *Physics of Fluids*, Vol 24, Issue 5, 055104, 2012.
[20]Schmitt, T., Selle, L., Cuenot, B., Poinsot, T., "Large-Eddy Simulation of transcritical flows," *Comptes Rendus Mécanique*, Vol. 337, Issue 6, 2009, pp. 528-538.
[21]Kim, T., Kim, Y., Kim, S., "Numerical study of cryogenic liquid nitrogen jets at supercritical pressures," *Journal of Supercritical Fluid*, Vol. 56, Issue 2, 2011, pp. 152-163.
[22]Zhou, L., Xie, M., Jia, M., Shi, J., "Large Eddy Simulation of Fuel Injection and Mixing Process in a Diesel Engine," Acta Mechanica Sinica, Vol. 27, Issue 4, 2011, pp. 519-530.
[23]Shinjo, J., Umemura, A., "Surface instability and primary atomization characteristics of straight liquid jet sprays," *International Journal of Multiphase Flow*, Vol. 37, Issue 10, 2011, pp. 1294-1304.
[24]Jarczyk, M., Pfitzner, M., "Large Eddy Simulation of Supercritical Nitrogen Jets," *50th AIAA Aerospace Sciences Meeting including the New Horizons Forum and Aerospace Exposition*, Nashville, TN, 09-12 January 2012, AIAA 2012-1270.
[25]Park, T.S., "LES and RANS simulations of cryogenic liquid nitrogen jets," *The Journal of Supercritical Fluids*, Vol. 72, 2012, pp. 232-247.
[26]Bellan, J., "Supercritical (and Subcritical) Fluid Behavior and Modeling: Drops, Streams, Shear and Maxing Layers, Jets and Sprays," *Progress in Energy and Combustion Institute*, Vol. 26, Issues 4-6, 2000, pp. 329-366.
[27]Lacaze, G., and Oefelein, J.C., "A non-premixed combustion model based on flame structure analysis at supercritical pressures," *Combustion and Flame*, Vol. 159, Issue 6, 2012, pp. 2087–2103.

A.3 Paper Presented in 3° Encontro de Jovens Investigadores do LAETA

https://3ejil.wordpress.com/submissoes/

3 EJIL - LAETA Young Researchers Meeting
ADAI, Coimbra, 7-8May 2015

Modeling of Transcritical and Supercritical Nitrogen Jets by the Application of a Variable Density RANS Model

Antunes E.L.S.F.[1], Silva A.R.R.[2], Barata J.M.M.[3]

Keywords: Critical Point, Cryogenic Jets, Fuel Injection, Rocket Engines, Supercritical Flows.

Abstract – *The present work is dedicated to the study of cryogenic nitrogen jets under supercritical chamber conditions with the objective of simulating the process of fuel injection inside a combustion engine. In order to do so, a numerical simulation using a RANS model was performed over two case studies previously analyzed by other authors both in experimental and numerical studies. The result obtained by the present numerical approach were then compared with previous results and this way accessed the capabilities of RANS approach using a k-ε turbulence model in which the density is calculated through the mixture fraction value to correctly model cryogenic jets at supercritical conditions. The results show the ability to achieve good agreement with other studies for the axial density distribution however for other parameters like the jet spreading angle the same agreement was not found.*

I. Introduction

Human kind finds itself today in a moment in history were it is strongly dependent on fossil fuels, while other alternative sources of energy have not yet been found, to sustain and further increase the achieved development. However, these fossil fuels are not unlimited, and a more efficient use of them must be found in the meanwhile. Also, we live in a planet that relies in a very fragile balance of its ecosystem. Pollution originated by the burning of fossil fuels are proved to be able to destabilize this fragile balance with possible disastrous consequences. This way a less harmful way of burning these fuels must be found, or at least a way of while fulfilling our energetic demands, burning those fuels in less quantity.

One way of fulfilling the exposed objectives is by the development and adoption of more efficient combustion power systems. Fuel injection plays one of the most important roles in the subject of combustion. The way fuel and oxidizer mix inside the combustion chamber of the several kinds of engines is key for the degree of combustion efficiency in power production. Other important factors in the efficiency of a combustion engine are the combustion chamber's temperature and pressure. Increasing the operating temperatures and pressure of power systems like diesel engines, gas turbines, rocket engines and others [1] is a known way of increasing the fuel efficiency of such engines. And this increase is turned in the past years into a important trend in designing of new power units.

Thus appears as an important issue, in recent combustion engines, the investigation of fuel (and oxidizer) injection into combustion chambers at high values of temperature and pressure. However it happens that when operating pressure and temperature increase, the fuels and oxidizers used by the propulsion systems may experience the exceeding of their critical values. The issue is that, under conditions of pressure and temperature that exceed, or are around the critical values, fluids have shown to have quite distinct behavior from the usually observed behavior while at conditions far from these.

Several author have investigated jet in general and in particular the fluid behavior under and near supercritical conditions both by experimental and numerical approaches which resulted in the production of extensive bibliography [2]-[29]. As far as today, some conclusions have been already taken and validated about the changes in the physical properties of fluids when around and above critical conditions. According to Bellan [27], under supercritical conditions, which in the present work

Manuscript received January 2007, revised January 2007

are characterize by both pressure and temperature being over the critical values, mass diffusivity, surface tension and latent heat vanish. On the other hand the heat capacity at constant pressure, Cp, the isentropic compressibility, k_s and the thermal conductivity, λ, all become infinite. In terms of flow behavior is observed a change in the jet structure from a liquid-gas injection to a gas-gas like injection [5], [16], [18], [19]. However bigger questions about fluid behavior appear in conditions near critical for which is still unknown if the fluid a behavior closer to gas behavior, liquid behavior or a mix of the two behavior. Recent studies have pointed in the direction of indentifying four different regions around the critical point. These regions are dependent on if both pressure and temperature are supercritical, just one of them, or none. The thermodynamic region of the flow will strongly determine its behavior [28].

In previous works [11], [12] was made the attempt to evaluate the applicability of a numerical variable density approach to cryogenic nitrogen jets injected into nitrogen gaseous environment at different chamber-to-injectant density ratio (ω). The results obtained shown agreement of the jet spreading angle with the experimental work of Chehroudi et al. [4] for chamber-to-injectant ratios between 0.025 and 0.1408.

The objective of the present work is to study, evaluate and develop numerical methods to better describe injection process around and beyond critical condition. In the present paper is described the injection of liquid nitrogen into gaseous nitrogen environment modeling, resorting to a RANS approach using a k-ε turbulence model initially developed for incompressible but variable density flows. Two different test cases were simulated using the same injector and chamber geometry shown in Fig. 1. The cases were named as case 3 and 4 in order to follow the same nomenclature already used by previous authors and its conditions are shown in Table I. The only difference between case 3 and 4 is the injection temperature, however this different puts the first one in transcritical conditions (supercritical pressure but subcritical temperature) while the second in supercritical injection conditions. The modeled cases were then compared with the experimental data of Mayer et al. [17] and the Large Eddy Simulations of Schmitt et al. [21] and of Jarczyk and Pfitzner [25].

With these two tests, and joining them with the knowledge obtained in previous work, is expected to be achieved better insight over the injection performed at conditions close to critical in order obtain more clues of the better strategy to model these flows.

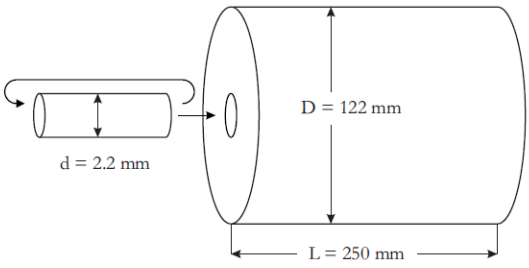

Fig. 1. Chamber geometry [21].

II. Nomenclature

B = transfer number
β_v = evaporation rate
C_μ = coefficient in turbulence model
d_0 = initial droplet diameter
d = droplet diameter
D = injector diameter [m], normalized droplet diameter (d(t) / d_0)
ε = dissipation rate of turbulent energy
f = mixture fraction
F = mean mixture fraction
i = axial direction index
j = radial direction index
k = turbulent kinetic energy
ϕ = generalized variable
ω = chamber-to-injection fluid density ratio (ρ_∞/ρ_0)
P_{cr} = critical pressure [MPa]
P_∞ = chamber ambient pressure [MPa]
P_r = reduced pressure (P_∞/P_{cr})
ρ = density [kg.m^{-3}]
ρ_0 = injected fluid density [kg.m^{-3}]
ρ_∞ = injection chamber's fluid density [kg.m^{-3}]
r = radial coordinate [m]
R/D = radial distance normalized by injector diameter
R_{diam} = injector radius [m]
R_e = Reynolds Number
S_ϕ = source term
t = time [s]
T = temperature [K]
u = axial velocity [m.s^{-1}]
U = mean axial velocity [m.s^{-1}]
U_{in} = injection axial velocity [m.s^{-1}]
v = radial velocity [m.s^{-1}]
v_t = turbulent kinematic viscosity
V = mean radial velocity [m.s^{-1}]
X = axial coordinate [m]
X/D = axial distance normalized by injector diameter

III. Mathematical Model

In the present work was used the same mathematical model and numerical approach already used by Barata et al. [11] and in the previous work [12]. However some modifications were introduced in the grid and the boundary conditions in order to provide the numerical approach the ability to test the same conditions present in the works of Mayer et al. [17], Schmitt et al. [21] and Jarczyk and Pfitzner [25].

III.1 Governing Equations

The method to solve is based on the solution of the conservation equations for momentum and mass. Turbulence is modeled with the "k~ε" turbulence model. A similar method has been used for three-dimensional or axisymmetric flows and only the main features are summarized here.

In the conservation equations, mass weighted averaging is applied to avoid the appearance of many terms involving density fluctuations for which additional models are needed. A mass averaged quantity is defined as

$$\tilde{\phi} = \frac{\overline{\rho\phi}}{\bar{\rho}} \qquad (1)$$

For the governing equations the standard parabolic truncation is employed. The mass averaged partial differential equations governing the steady, variable density axisymmetric flow may be written in cylindrical polar coordinates as

$$\frac{\partial \bar{\rho} UU}{\partial x} + \frac{1}{r}\frac{\partial r\bar{\rho} UV}{\partial r} = -\frac{\partial \bar{p}}{\partial x} - \frac{1}{r}\frac{\partial r\bar{\rho}\,\overset{\sim}{\overline{u'v'}}}{\partial r} \quad (2)$$

$$\frac{\partial \bar{\rho} UV}{\partial x} + \frac{1}{r}\frac{\partial r\bar{\rho} VV}{\partial r} = -\frac{\partial \bar{p}}{\partial x} - \frac{1}{r}\frac{\partial r\bar{\rho}\,\overset{\sim}{\overline{v'v'}}}{\partial r} + \bar{\rho}\frac{\overset{\sim}{\overline{w'w'}}}{r} \quad (3)$$

and the continuity equation as

$$\frac{\partial \bar{\rho} U}{\partial x} + \frac{1}{r}\frac{\partial r\bar{\rho} V}{\partial r} = 0 \qquad (4)$$

To describe mixing of gases, the mixture fraction *F*, that represents the mass fraction of the nozzle fluid, is introduced. It obeys a convection-diffusion equation of the form

$$\frac{\partial \bar{\rho} UF}{\partial x} + \frac{1}{r}\frac{\partial r\bar{\rho} VF}{\partial r} = -\frac{1}{r}\frac{\partial r\bar{\rho}\,\overset{\sim}{\overline{v'f'}}}{\partial r} \qquad (5)$$

In "k~ε" turbulence model, the Reynolds stresses are expressed in terms of the local strain rate:

$$-\bar{\rho}\,\overset{\sim}{\overline{u'_i u'_j}} = \bar{\rho}(\nu_t + \nu)\left(\frac{\partial \tilde{u}_i}{\partial x_j} + \frac{\partial \tilde{u}_j}{\partial x_i}\right) - \frac{2}{3}\delta_{ij}\left(\bar{\rho}k + \bar{\rho}(\nu_t + \nu)\frac{\partial \tilde{u}_j}{\partial x_j}\right) \quad (6)$$

with

$$\nu_t = C_\mu \frac{k^2}{\varepsilon} \qquad (7)$$

The scalar flux in equation (5) is approximated with a gradient transport assumption

$$\overset{\sim}{\overline{u'_i f'}} = -\frac{\nu_t}{\sigma_f}\frac{\partial F}{\partial x_i} \qquad (8)$$

From the foregoing we can deduced the parabolized set of equations in cylindrical coordinates where the generalized equation is

$$\frac{\partial}{\partial x}\left(\bar{\rho} U\tilde{\phi}\right) + \frac{1}{r}\frac{\partial}{\partial r}\left(r\bar{\rho}\tilde{\phi}\right) = \frac{1}{r}\frac{\partial}{\partial r}\left(r\bar{\rho} D\frac{\partial \tilde{\phi}}{dr}\right) + S_\phi \qquad (9)$$

where $\tilde{\phi}$ may stand for any of the velocities, turbulent kinetic energy, dissipation, or scalar property, and S_ϕ take on different values for each particular $\tilde{\phi}$, described in

TABLE I
CONDITIONS OF THE TEST CASES.

	Case 3	**Case 4**
Chamber Pressure [MPa]	3.97	3.97
Chamber Temperature [K]	298	298
Injection Temperature [K]	126.9	137
Injection Velocity [m/s]	4.9	5.4
ρ_∞ [kg/m^3]	435	171
ρ_{inj} [kg/m^3]	45.5	45.5
ω	0.1046	0.2661

detail by Sanders et al. [10].

The mean density can be obtained from the mean mixture fraction using the equation state. With constant pressure this leads to

$$\frac{1}{\overline{\rho}} = \frac{F}{\rho_o} + \frac{1-F}{\rho_\infty} \qquad (10)$$

where density fluctuations have been neglected. This is allowed in isothermal jets because the instantaneous density, for which equation (10) is exact, is approximately a linear function of the instantaneous mixture fraction [11].

III.2 Numerical Method

The governing equations are solved using a parabolized marching algorithm which resembles the (elliptic) TEACH code [10]. The computations are performed by using the continuity equation to obtain the radial velocity (*V*). Using the radial momentum equation for *V* and solving a pressure correction equation for *V* in radial direction did not show any difference with the use of the continuity equation [10]. In this approach the numerical model was applied to variable density jets and for the present case it was used for the study of liquid cryogenic jets under sub-near critical pressures, and sub to supercritical temperatures.

In order to determine the tangent of the jet spreading angle is used the Half Width of Half Maximum of the Density (HWHM of Density), this routine has the function of determine the radial distance from the centerline (r) at which the axial mean density (ρ) is half of the maximum density in the centerline. This routine analysis all the points in the radial direction comparing them with half of the centerline velocity, when the routine finds a point bellow this value it saves the point before that.

III.3 Computational grid

The flow configuration can be observed in Fig. 1, with the cold nitrogen being injected through a round injector with 2.2 mm of diameter into a cylindrical chamber with a diameter of 122 mm and a length of 250 mm. For this numerical approach was used a grid that represents half of the domain since the symmetry until the external wall. Making this way a numerical domain of 250 mm long and 61 mm width. Was used a grid of 250 points in the axial direction and 100 points in the radial direction making a total of 25000 points.

In order to allow the setting of the desired numbers of points in one direction and at the same time keep the defined length and width of the domain was not used the same method of constant expansion of grid dimensions used in previous works [11], [12]. Instead was programmed a new grid subroutine that allows to define the number of points and domain, while still being more refined close to the injector. In the axial direction the grid was defined by dividing 50% of the grid points between 30% of the domain length close to the injector, the other 50% of grid point are shared between 70% of the length domain more far from injector.

In radial direction a similar strategy was followed but in this case was first defined 20 grid points in the inlet region (1.1 mm) and the remaining 80 points were defined 40 (50%) to the first 30% of domain and the rest (40 points) for the last 70% of domain.

Because a new grid was used and no other previous works had used it before, a grid dependency test was performed. The axial velocity decay was used to test the grid dependency of the computations. Fig. 2 compares evolution along the symmetry axis of the velocity decay for 3 different grid sizes and even for a grid with 125x50 point, one quarter of the size (in total number of points), the results are very close to the used grid (250x100). And for the grid with approximately 65% of number of points (200x80) the difference is negligible.

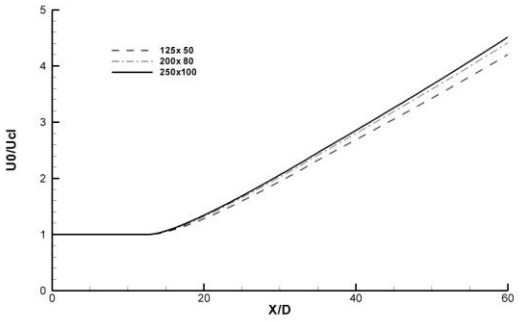

Fig. 2. Grid size dependency test based on the axial velocity decay.

IV. Results

Numerical results obtained in the present work are presented in this section and compared with the experimental data of Mayer et al. [17] and the large eddy simulations of Schmitt et al. [21] and of Jarczyk and Pfitzner [25]. A discussion is also provided in order to reach the conclusions exposed in the next section.

Figures 3 and 4 show the velocity, mixture fraction and density fields for cases 3 and 4 respectively. These two charts allow us to obtain a general picture of the flow geometry. As said before, and described in Table I, the two test cases only vary in the injection temperature (and by consequence the density) and velocity, while the chamber conditions remain the same for both cases. Nevertheless the difference in the injection temperature between the two cases is enough to position them in different thermodynamic regimes. The test case 3 is at

transcritical conditions, regime at which there's supercritical pressure but subcritical temperature, while case 4 in supercritical injection conditions at which both pressure and temperature are supercritical.

Comparison between both cases show a very similar jet structure with the case 4 showing a faster reduction of density and mixture fraction value than case 3. Similar conclusions are obtain in the previous studies of Schmitt et al. [21] and Jarczyk and Pfitzner [25], with the LES visualizations showing similar variations between the two cases. These result also suggest the existence of a smaller potential core for the case 4, this characteristic in particular will be discussed later.

Figures 3 and 4 a) show the velocity field obtained in the present simulation. It is visible in both cases the appearence of entrainment close to the injector exit with ambient nitrogen being pulled into the jet stream. This phenomenon appears to be slightly more intense in test case 3 even this case slower injection velocity, this is probably due to the higher jet momentum caused by higher injection fluid density. It is also visible that more far from the injector the velocity vectors are bigger in case 3 than in case 4 that has higher injection velocity. The injection density appears to be determinant to the distance that a jet can reach.

In Figures 3 and 4 b) is shown the mixture fraction field for test cases 3 and 4. The images show a high concentration of injected fluid close to the injector exit and decreasing along the domain while getting far from the injector in both radial and axial direction. Comparison between the two cases show a faster decrease of the mixture fraction along the jet in case 4, this faster decrease however doesn't mean better mixture of the jet fluid with the chamber fluid. In fact there are bigger mixture fraction gradients in case 4, close to the injector the mixture fraction quickly decreases value but then, in the rest of the injection chamber, the ambience is dominated by mixture fraction values bellow 0.5. In case 3 even showing a slower decrease of mixture fraction and bigger penetration of injection fluid (apparently showing a slower mixture in beginning of jet) shows however better mixture having in most of domain mixture fraction values close to 0.5. These results of apparently better mixture in the case with smaller temperature and at which difference between injection density and chamber density is bigger can be considering in some way surprising.

Density field is shown in Figures 3 and 4 c) for test cases 3 and 4 respectively. Again the results show similar jet structure for both cases. Case 3 however shows a longer dense core than case 4. Having case 3 bigger density gradient between injected and chamber fluid and a lower injection velocity one could expect it to have a shorter dense core as well as a smaller jet penetration than case 4. However it happens the opposite, the explanation found by the authors of the present paper is that the fluid density due to its influence in fluid momentum rules the jet dynamics. The jet in case 3 even having slower injection velocity has in fact higher momentum and this causes it to have bigger penetration length. The higher jet momentum is also responsible for the more intense entrainment at the jet exit in case 3, the entrainment phenomenon is important for the fluid mixing, this explain the better mixing in case 3 when compared to case 4 observed in mixture fraction field. These results obtained by the present numerical approach are corroborated in the LES results of Schmitt et al. [21] where case 3 also shows to have a longer jet length and dense core than case 4.

The results obtained by the velocity and scalar fields also give us the proves that the jet behavior is mostly dominated by the convection terms while diffusion plays a minor role. In turn, convection is mostly dominated by the density. The calculation of density appear this way as a key factor in the modeling of this kind of flows.

The axial density distribution of cases 3 and 4 is shown in Figures 5 and 6 respectively for the present work modeling and also for the experimental and numerical results of other authors. Potential core length is one important characteristic of a jet, generally used by other authors to help quantifying it. Schmitt et al. [21] defines the potential core length as the axial distance at which the centerline density is 99% of the injected density, generally potential core length is expresses in multiples of injector diameters. In the present investigation was decided to use the same definition of potential core already used by Schmitt [21].

The results obtained for case 3 in the present investigation show a potential core of 12.3 injector diameters. It is longer when compared with the results of other authors, Schmitt et al. [21] for example shows a potential core length of 7.9 diameters and Jarczyk and Pfitzner[24] a length of around 9 diameters, it can however be observed that the obtained profile of the centerline density distribution follows the general trend found in the previous works. While until an axial distance of around 15 x/D the present results are not able to get a very good agreement with the experimental and even LES data, after this distance the presently numerical results are able to get in a exceptionally good proximity with the experimental data of Mayer [17], showing better agreement than both LES results. The same kind of centerline density distribution profile was obtained to case 4 in the present work. The potential core obtained of around 7.5 diameters is bigger than the one obtain by the two LES results which are 5.1 diameters in the work of Schmitt et al. [21] and around 6 jet diameters for Jarczyk and Pfitzner [25]. Analyzing experimental data of Mayer et al. [17] shows however little amount of evidence of the existence of a potential core for this test case.

During a big portion of the observed domain, since 9 jet diameters until around an axial distance of 20 x/D, the present results are positioned between the both LES works and very close to the experimental data. After this

distance, the obtained results are the ones that more close agreement share with the experimental data until the end of the observed domain, once again outperforming the LES approaches in the last part of domain. The general agreement in the axial density distribution with LES results and experimental data can be classified as quite good taking in consideration the limitations of the present numerical approach when compared with other simulation techniques, being even able to overcome the results of LES in the end of the exposed domain.

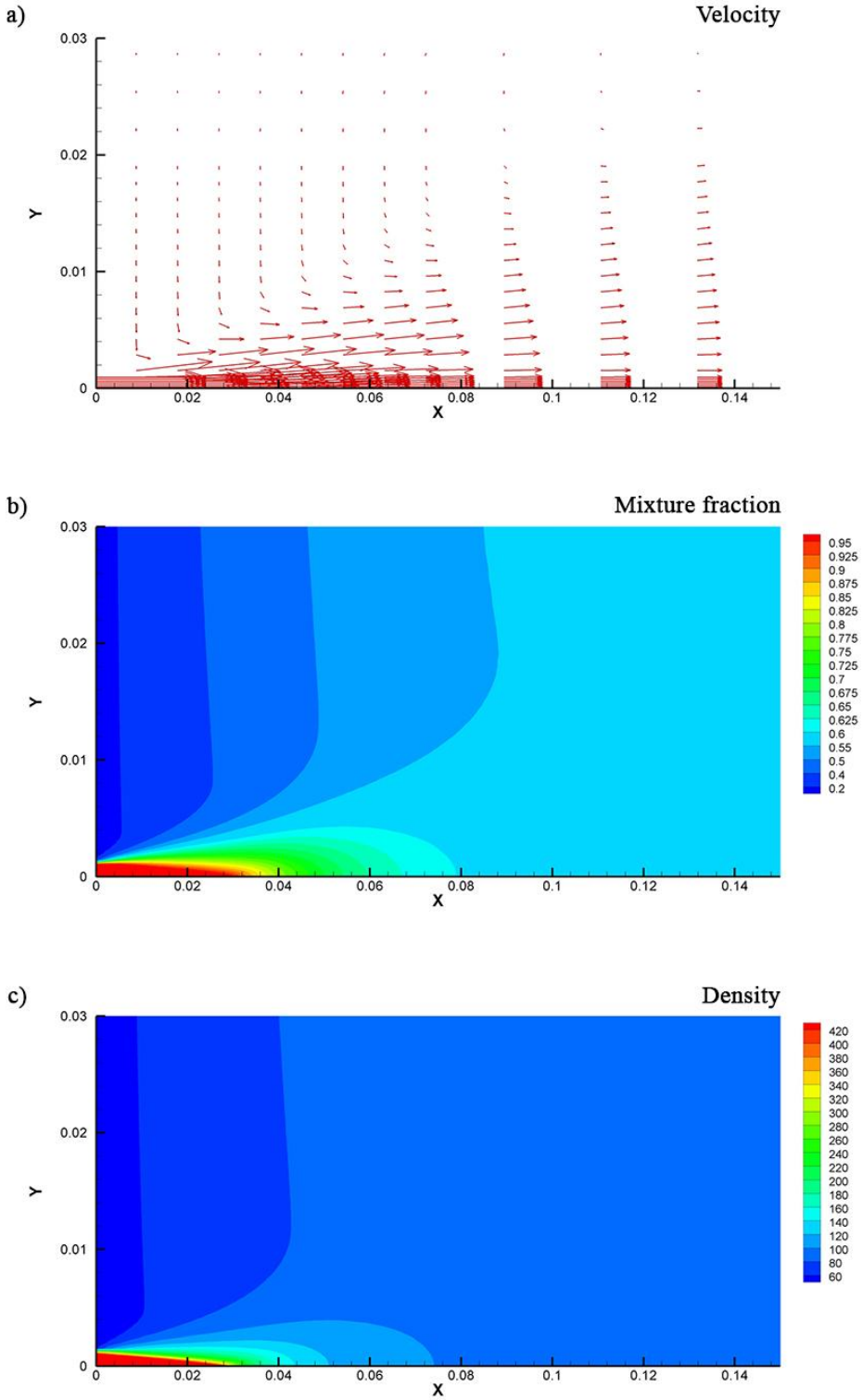

Fig. 3. Velocity and scalar fields of the jet for test case 3. a) Velocity Vectors; b) Mixture Fraction contours; c) Density contours.

The spreading angle of the jet is one of the most important parameters available to the use of a researcher when his objective is to characterize a jet. In order to determine the spreading of a jet becomes necessary to define the radial border of it. Several authors, including those cited in the present paper [21], [25], assume that the border of the jet is in the radial position where the density is half of the value in the centerline position at the same axial distance. This way is defined the Full Width of Half Maximum of Density (FWHM of Density)

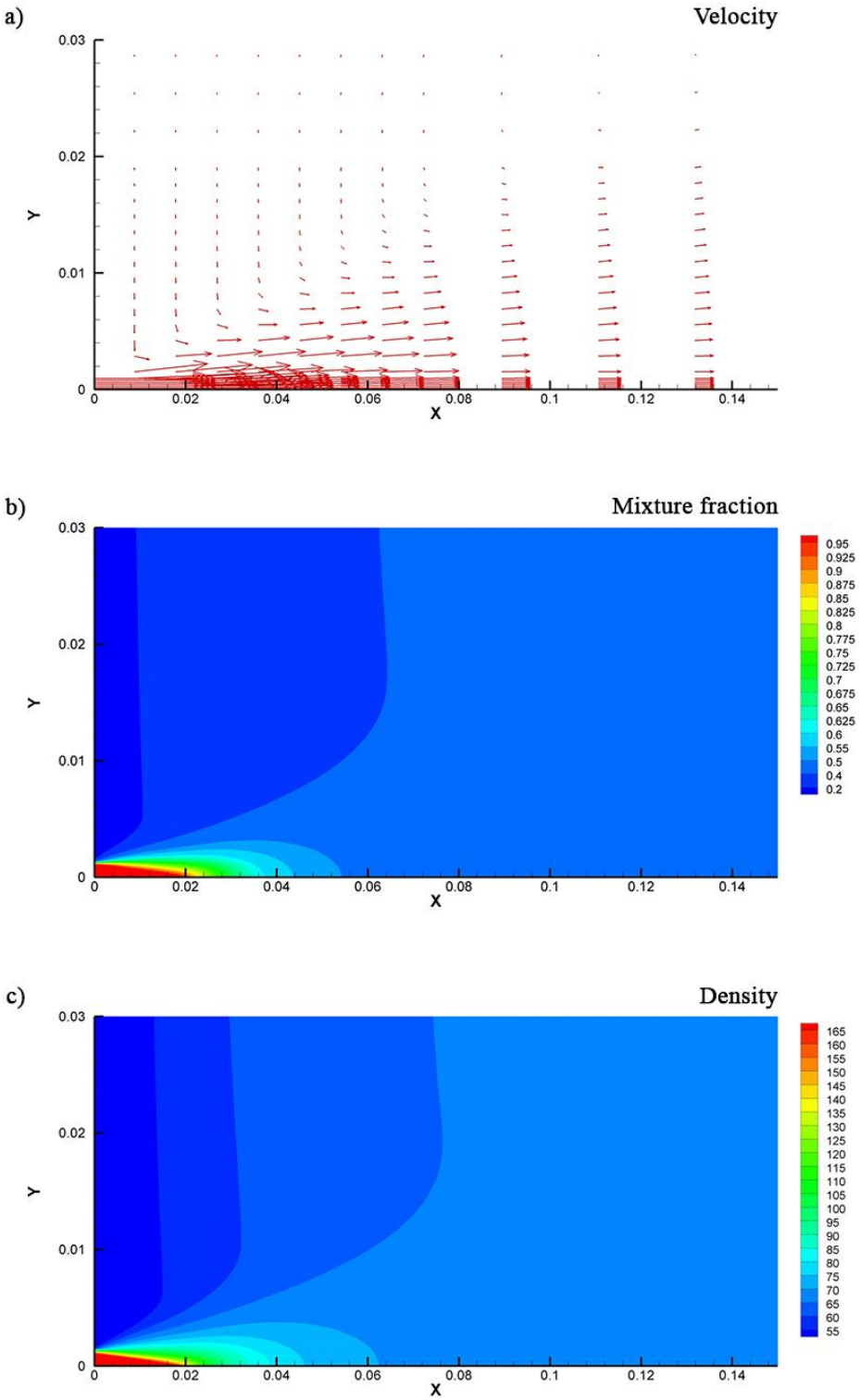

Fig. 4. Velocity and scalar fields of the jet for test case 4. a) Velocity Vectors; b) Mixture Fraction contours; c) Density contours.

and also the Half Maximum of Half Width of Density which has a value half of the FWHM and was used in work due to the fact that only half of the domain was simulated. In the work of Schmitt et al. [21] the tangent of the spreading angle of density was obtained by linear interpolation of the FWHM of Density between x/D = 15 and x/D = 25. In the present work was decided to use the same method but adapting it to the Half Width of Half Maximum of Density obtained in the present work. However care was always taken in order to never directly

compare directly FWHM with HWHM without the proper conversion between both.

Fig. 7 shows the HWHM of Density for test case 3 obtained in the present work and compared with the Raman measurements of Mayer et al. [17]. It can be observed that numerical results obtain in the present work follow a similar trend to the one obtained in the experimental data. The chart initially shows a decreasing of the half width that extends for the experimental data until 10 x/D and in present numerical data until approximately 12 x/D, while always smaller width in numerical data. After this point the half width of the jet starts increasing, showing that the jet is spreading, however the observed spreading is much bigger in the numerical data than in the Raman measurements. The tangent of spreading angle using the FWHM of Density is 0.196 for the experimental data and 1.441 in the present numerical approach, approximately 7 times

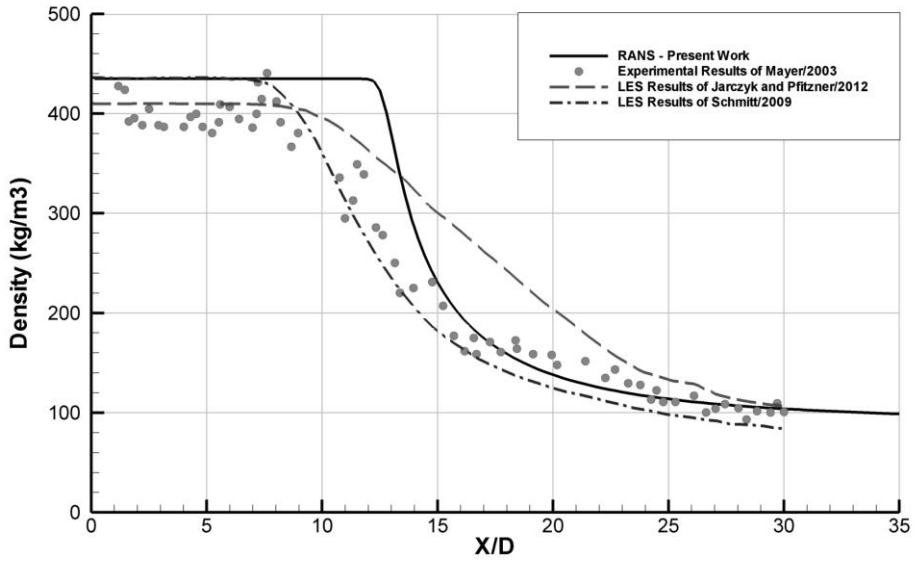

Fig. 5. Axial density distribution for Case 3 and comparisons with different authors results.

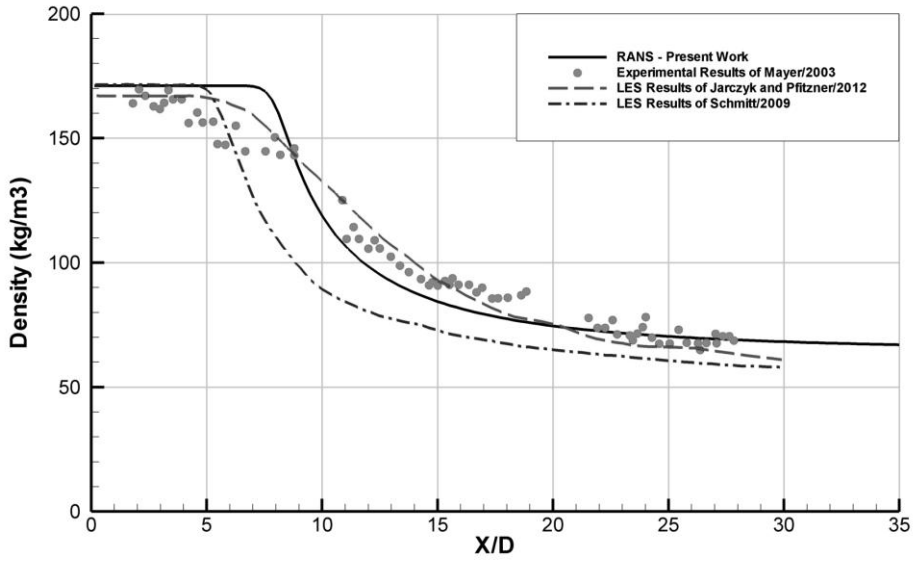

Fig. 6. Axial density distribution for Case 4 and comparisons with different authors results.

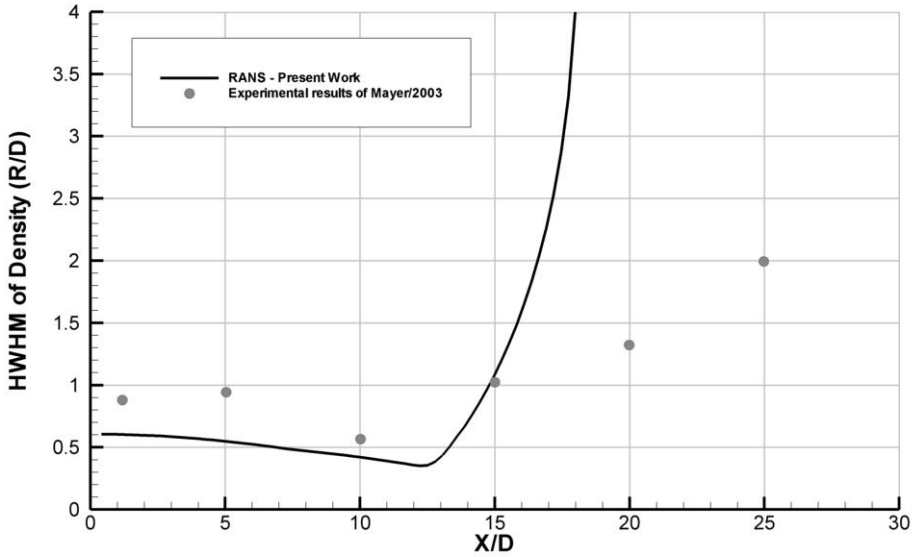

Fig. 7. Half Width of Half Maximum of Density for case 3 and comparison with experimental data of Mayer et al. [16].

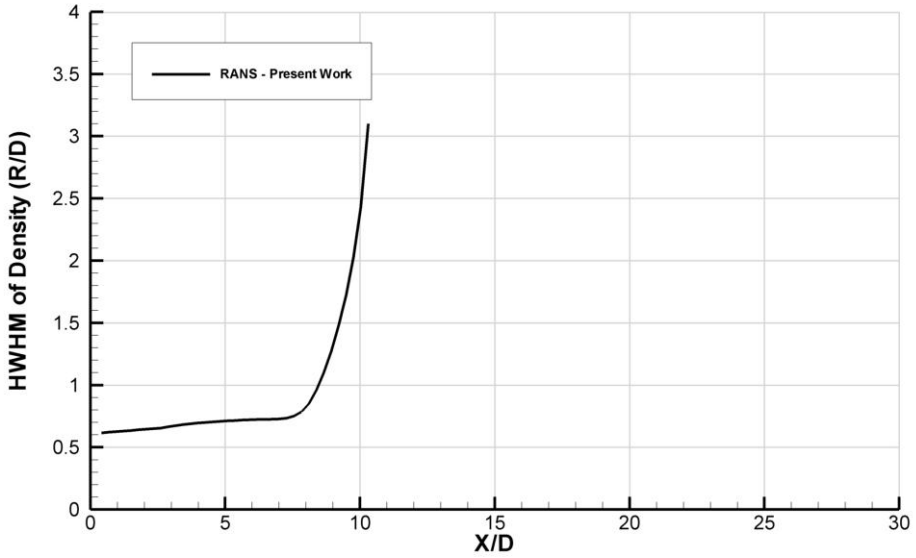

Fig. 8 - Half Width of Half Maximum of Density for case 4.

bigger. For the same case the LES simulation of Schmitt et al. [21] present a tangent of the spreading angle of 0.227 which slightly higher than experimental results but still much closer than the ones obtained in the present investigation.

In Fig. 8 is shown the HWHM of Density for case 4. For these case there were no available experimental data from the Raman measurements of Mayer et al. [17] and for this reason Fig. 8 only shows the results obtained on the present work. In the chart it is possible to observe in the beginning of the jet very slow increase of the of the jet width until an axial length of around 8 x/D, after this mark there's a sudden and very fast increase of jet width. Due to this sudden skyrocketing of the jet width obtain in present results, it is not possible to calculate tangent of the spreading angle by the use of the same methodology used in previous works since there weren't obtained values of the jet half width for axial length of 15 x/D and even less for 25 x/D.

Contrary to the results obtained for the axial density

distribution which have shown quite good agreement with experiments and LES results, the results of the Half Width of Half Maximum of Density reached in the present investigation are very far from other experimental and LES data. Results from Schmitt et al. [21] show that for case 4 the tangent of spreading angle is around 0.241, a little bit higher than for case 3. Further improvement in the present numerical approach are required in order to provide better agreement with experimental and LES data of jet spreading angle.

Figures 9 and 10 show the Half Width of Half Maximum of Mixture Fraction for cases 3 and 4 respectively. These results are obtained with the same method used for Density but in this case for Mixture Fraction. The charts represent this way the radial distance from the centerline at which the Mixture Fraction value is half of the value in the centerline, for each point in the axial direction. The tangent of the spreading angle based on the HWHM of Mixture Fraction could be calculated by the same method used for Density, however in these cases there are no results for a axial distance of 25 x/D and this way is not possible to perform the calculation using the same two points defined in [21]. The results of case 3 show a different profile from that obtained in the HWHM of Density having an initial zone with a positive tangent of spreading angle (contrary to experimental and present work data that initially shows a negative tangent) and then an increase of the tangent to almost vertical.

V. Conclusion

With the objective of studying, evaluating and developing numerical methods for better describing of injection process around and beyond critical condition, the present investigation has as task the evaluation of a numerical approach, originally designed to model gaseous jet flows with different densities, when used to model cryogenic jets at thermodynamic conditions near critical. As part of the task is also the goal of attempting to identify and later integrate the needed modifications to the numerical approach in order to make it more suitable to simulate the flows of interest.

With the task of evaluating the present numerical approach were modeled two test cases initially tested in a experimental work performed by Mayer et al. [17] and then numerically simulated by both Schmitt et al. [21] and Jarczyk and Pfitzner [25] using the technique of Large Eddy Simulation.

The numerical results obtained for the axial density distribution in the present investigation are in good agreement with experimental results of Mayer [17] and in some parts of the domain can even perform better than the LES investigations [21], [25]. However not so good agreement was found for the jet spreading angle results based on density, where the numerical approach while being able to reproduce the same shape of profile was very far from reproducing the magnitude of the jets spreading. These results lead to the conclusion that improvements must be included in the present numerical methods. There has been a trend between authors investigating jet at conditions near critical to use real gas

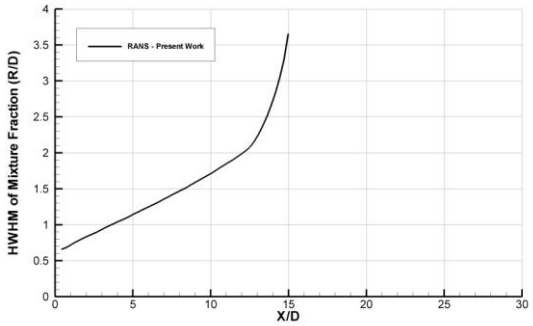

Fig. 9. Half Width of Half Maximum of Mixture Fraction for case 3.

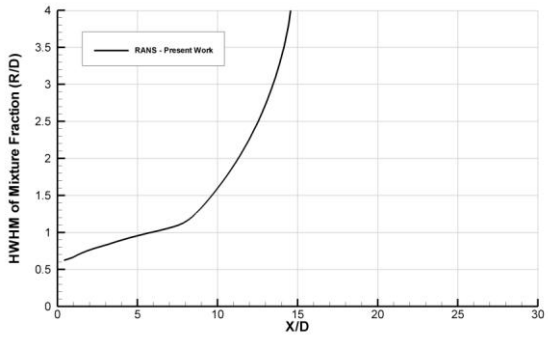

Fig. 10. Half Width of Half Maximum of Mixture Fraction for case 4.

equation of state to calculate de density [16], [21], [25], [26]. In the present numerical approach the mean density is calculated by a equation of state that is a linear function of the mixture fraction. As stated above this method of calculation of density in allowed for isothermal jets. However in the present test cases one is not in the presence of isothermal gases, so this method of calculating density can be one of the main causes of failing to predict the jet spreading angle.

Transcritical and supercritical jets are highly transient and very sensitive to small and local changes of temperature and pressure [27]. RANS methods unlike LES use only the average terms of velocity, pressure, temperature, etc, neglecting the small fluctuations that in transcritical and supercritical jet can have huge impact in the flow behavior. This reality could in fact also consist in one of the causes for incapacity of the present numerical approach to provide accurate predictions of the studied jet spreading angle. However Park [26], in his LES and RANS investigation, concluded that the suitable adoption of a equation of state is more decisive than the selection of turbulence model for the numerical performance. On the other hand Park also stated that when compared with LES results, the spreading rates of

RANS models are slightly higher.

Next work will be focused on the attempt of integrating a real gas equation of state into the present numerical formulation in order to provide the model with a different method for density calculation. With these changes the authors expect to solve the problems encountered in the present formulation and get better agreement with experimental data.

Acknowledgements

The author would like to thanks: Fundação para a Ciência e a Tecnologia (FCT), the Portuguese public agency for science and technology, for the financing of the present investigation by providing a PhD scholarship to the first author with the reference SFRH/BD/87822/2012. Also AeroG-LAETA associated laboratory, for providing integration in a research unit to the authors of the present communication. And finally to Universidade da Beira Interior - Covilhã, the host institution for the authors.

References

[1] S. E. Hosseini, M. A. Wahid, A. A. A. Abuelnuor, High Temperature Air Combustion: Sustainable Technology to Low Nox Formation, *International Review of Mechanical Engineering*, Vol. 6 No. 5, pp. 947-953, 2012.

[2] P. Seebald, and P. E. Sojka, Supercritical and Transcritical Injection, *Hand Book of Atomization and Sprays*, (edited by N. Ashgriz, Springer Science+Business Media, 2011, pp. 255-261).

[3] S. Martínez-Martínez, F. A. Sánchez-Cruz, J. M. Riesco-Ávila, A. Gallegos-Munoz, S. M. Aceves, Liquid Penetration Length in Direct Diesel Fuel Injection, *Applied Thermal Engineering*, Vol 28, Issues 14-15, pp. 1756-1762, 2008.

[4] B. Chehroudi, R. Cohn, D. Talley, *Spray/Gas Behaviour of Cryogenic Fluids under Sub- and Supercritical Conditions*, Eighth International Conference on Liquid Atomization & Sprays Systems, ICLASS-2000, Pasadena, California, USA, July 16-20, 2000.

[5] B. Chehroudi, R. Cohn, D. Talley, Cryogenic Shear Layers: Experiments and Phenomenological Modeling of the Initial Growth Rate under Subcritical and Supercritical Conditions, *International Journal of Heat and Fluid Flow*, Vol. 23, Issue 5, pp. 554-563, 2002.

[6] B. Chehroudi, D. Talley, E. Coy, Visual Characteristics and Initial Growth Rates of Round Cryogenic Jets at Subcritical and Supercritical Pressures, *Physics of Fluids*, Vol. 14, No. 2, pp. 850-861, 2002.

[7] W. O. H. Mayer, A. H. A. Schick, B. Vielle, C. Chauveau, I. Gökalp, D. G. Talley, R. D. Woodward, Atomization and Breakup of Cryogenic Propellants under High-Pressure Subcritical and Supercritical Conditions, *Journal of Propulsion and Power*, Vol.14, No.5, pp.835-842, 1998.

[8] Zong, N., Meng, H., Hsieh, S., Yang, V., "A numerical study of cryogenic fluid injection and mixing under supercritical conditions," *Physics of Fluids*, Vol. 16, No. 12, 2004, pp. 4248-4261.

[9] N. Zong, V. Yang, Cryogenic Fluid Jets and Mixing Layers in Transcritical and Supercritical Environments, *Combustion Science and Technology*, Vol. 178, No 1-3, pp. 193-227, 2006.

[10] J. P. H. Sanders, B. Sarh, I. Gokalp, Variable Density Effects in Axisymmetric Isothermal Turbulent Jets: a Comparison between a First- and a Second-order Turbulence Model, *Int. J. Heat Mass Transfer*, Vol. 40, No. 4, pp. 823-842, 1997.

[11] J. M. M. Barata, A. R. R. Silva, I. Golkalp, Numerical Study of Cryogenic Jets under Supercritical Conditions, *Journal of Propulsion and Power*, Vol. 19, No.1, pp. 142-147, 2003.

[12] E. Antunes, A. Silva, J. Barata, *Evaluation of a Numerical Variable Density Approach to Cryogenic Jets*, 50th AIAA Aerospace Sciences Meeting including the New Horizons Forum and Aerospace Exposition, Nashville, TN, 09-12 January 2012, AIAA 2012-1282.

[13] J. A. Newman, T. A. Brzustowski, Behavior of a Liquid Jet Near the Thermodynamic Critical Region, *AIAA Journal*, Vol. 9, No. 8, 1971, pp. 1595-1602.

[14] D. Papamoschou, A. Roshko, The Compressible Turbulent Shear Layer: an Experimental Study, *Journal of Fluid Mechanics*, Vol. 197, pp. 453-477, 1988.

[15] M. Oschwald, A. Schik, Supercritical nitrogen free jet investigation by spontaneous Raman scattering, *Experiments in Fluids*, Vol 27, Issue 6, pp. 497-506, 1999.

[16] M. Oschwald, M. M. Micci, Spreading Angle and Centerline Variation of Density of Supercritical Nitrogen Jets, *Atomization and Sprays*, Vol. 12, Issue 1-3, pp. 91-106, 2002.

[17] W. Mayer, J. Telaar, R. Branam, G. Schneider, J. Hussong, Raman Measurements of Cryogenic Injection at Supercritical Pressure, *Heat and Mass Transfer*, Vol. 39, Issue 8-9, pp. 709-719, 2003.

[18] M. Oschwald, J. J. Smith, R. Branam, J. Hussong, A. Schik, B. Chehroudi, D. Talley, Injection of Fluids into Supercritcal Environments, *Combustion Science and Technology*, Vol. 178, No. 1-3, pp. 49-100, 2006.

[19] C. Segal, S. A. Polikhov, Subcritical to Supercritical Mixing, *Physics of Fluids*, Vol. 20, Issue 5, pp.. 052101-1 - 052101-7, 2008.

[20] T. Schmitt, J. Rodriguez, I. A. Leyva, S. Candel, Experiments and numerical simulation of mixing under supercritical conditions, *Physics of Fluids*, Vol 24, Issue 5, 055104, 2012.

[21] T. Schmitt, L. Selle, B. Cuenot, T. Poinsot, Large-Eddy Simulation of transcritical flows, *Comptes Rendus Mécanique*, Vol. 337, Issue 6, pp. 528-538, 2009.

[22] T. Kim, Y. Kim, S. Kim, Numerical study of cryogenic liquid nitrogen jets at supercritical pressures, *Journal of Supercritical Fluid*, Vol. 56, Issue 2, pp. 152-163, 2011.

[23] L. Zhou, M. Xie, M. Jia, J. Shi, Large Eddy Simulation of Fuel Injection and Mixing Process in a Diesel Engine, *Acta Mechanica Sinica*, Vol. 27, Issue 4, pp. 519-530, 2011.

[24] J. Shinjo, A. Umemura, Surface instability and primary atomization characteristics of straight liquid jet sprays, *International Journal of Multiphase Flow*, Vol. 37, Issue 10, pp. 1294-1304, 2011.

[25] M. Jarczyk, M. Pfitzner, *Large Eddy Simulation of Supercritical Nitrogen Jets*, 50th AIAA Aerospace Sciences Meeting including the New Horizons Forum and Aerospace Exposition, Nashville, TN, 09-12 January 2012, AIAA 2012-1270.

[26] T. S. Park, LES and RANS simulations of cryogenic liquid nitrogen jets, *The Journal of Supercritical Fluids*, Vol. 72, pp. 232-247, 2012.

[27] J. Bellan, Supercritical (and Subcritical) Fluid Behavior and Modeling: Drops, Streams, Shear and Maxing Layers, Jets and Sprays, *Progress in Energy and Combustion Institute*, Vol. 26, Issues 4-6, pp. 329-366, 2000.

[28] G. Lacaze, J. C. Oefelein, A non-premixed combustion model based on flame structure analysis at supercritical pressures, *Combustion and Flame*, Vol. 159, Issue 6, pp. 2087–2103, 2012.

[29] *A. B. Bhasi*, *M. D. Bindu*, *P. S. Tide*, Jet Dynamics of Co-Axial Dual Compressible Jets for Different Exit Velocity Ratios, *International Review of Mechanical Engineering*, Vol. 8 No. 5, pp. 908-915, 2012.

Authors' information

[1]PhD student, Aerospace Sciences Department, University of Beira Interior.
[2]Assistant Professor, Aerospace Sciences Department, University of Beira Interior.
[3]Full Professor, Aerospace Sciences Department, University of Beira Interior.

Eduardo F. Antunes, Vila do Carvalho, Portugal, 23th April of 1988. M.Eng. in Aeronautical Engineering, University of Beira Interior, Covilhã, Portugal, 2011.
The first paragraph may contain a place and/or date of birth (list place, then date).
He presented two conference papers in AIAA conferences in 2012 and 2015 entitled respectively "Evaluation of a Numerical Variable Density Approach to Cryogenic Jets" and "RANS Modeling of Transcritical and Supercritical Nitrogen Jets". Current research interests are propulsion, fuel injection, jets and sprays, supercritical flows and computational fluid dynamics.
M.Eng. Antunes is a student member of American Institute of Aeronautics and Astronautics since 2011.

A.4 Paper Presented in the 12th International Conference on Energy for a Clean Environment

12th International Conference on Energy for a Clean Environment
July 5-9, 2015, Lisboa, Portugal

Modeling of Transcritical Jets by the use of a Real Fluid Equation of State

Eduardo Antunes*[a], André Silva[a] and Jorge Barata[a]

[a] *Universidade da Beira Interior, Covilhã 6200-001, Portugal*

Abstract

This work is dedicated to the study of cryogenic nitrogen jets under transcritical and supercritical chamber conditions, with the objective of simulating the process of fuel injection inside a combustion engine. A RANS numerical variable density approach, originally developed for the study of gaseous turbulent jets, was modified by the inclusion of a real fluid equation of state with the objective of providing accurate results for modeling of transcritical and supercritical jets, while requiring low computational resources. The original approach had already been tested for the modeling of flows around the critical point and provided interesting results, nevertheless the lack of real fluid thermodynamics exposed its limitations. The current study intended to overcome those limitations considering a new approach, yet difficulties still need to be dealt with for the temperature field calculation. The present results show improvement of the model for the calculation of the full width of half maximum of density and the predictions are in agreement with experimental data. The model presented in the current paper shows clear improvements in the calculation of the jet spreading angle.

Keywords: Critical Point, Cryogenic Jets, Equation of State, Fuel Injection, Supercritical Flows.

1. INTRODUCTION

Finitude of fossil fuels, climate changes and health hazards connected with gaseous emissions have been requiring society to find better alternative to the use of fossil fuels in transportation and energy production. However, until effective replacement is found, a more efficient use of fossil fuels must be reached, since humankind is still strongly dependent on them.

Increasing operating pressures and temperatures in combustion engines is a well known way of improving fuel efficiency and, consequently, reducing emissions to atmosphere. Thus, a trend have been followed by engine constructors to increase combustion chamber pressure and temperature.

However the increase of operating chamber pressure and temperature entails achieving of the thermodynamic critical point of fuels and oxidizers. Around and over the critical point there are relevant changes on the fluid behavior[1]–[5].

*Corresponding author email:

eduardofariasantunes@hotmail.com

Several researchers have studied fuel and oxidizer injection at transcritical and supercritical conditions both experimentally [1], [6]–[16] and numerically [15]–[28]. At supercritical conditions, when both pressure and temperature are above the critical point, the fluid shows a gas like behavior while retaining the density of a liquid [7], [9]–[12]. At conditions near and around the critical point the fluid behavior is not so well determined since a thermodynamic singularity appears. Properties like mass diffusivity, surface tension and latent heat reach zero, at the same time heat capacity at constant pressure, isentropic compressibility and thermal conductivity become zero [5]. The existence of this thermodynamic singularity causes the fluid to be extremely sensitive to small local changes of pressure and temperature, as well as the mixture characteristics in the case of multi components flows [7].

Four thermodynamic regimes can be identified around the critical point. These correspond to whether both pressure and temperature are subcritical, supercritical or if just one is above the critical point. The four regimes are shown in Figure 1. More research is proven to be necessary for the study of flows at conditions around the critical point, and so far a generally accepted numerical formulation for the modeling of transcritical jets

has yet to be found.

Previous investigations [17], [29], [30]studied applicability of the use of a variable density numerical approach, originally developed for turbulent jets, in modeling transcritical and supercritical jets. Interesting results were achieved, demonstrating the potential of this approach, however some aspects of this approach showed to be still not in total agreement with experimental data and better accuracy is desirable.

Experimental research has shown the strong dependence of the fluid behavior on the thermodynamic conditions to which the fluid is exposed. This way a correct approach must be able to correctly include real fluid thermodynamics in the modeling of transcritical and supercritical fluids. The use of a real fluid equation of state is a necessary approach for the treatment of existent thermodynamic characteristics since density is, at these conditions, strongly dependent on pressure and temperature [15], [16], [21]–[28], [31], [32]. For this approach several equations of state will be tested in order to identify the most suitable for the current test conditions. The selected equation of state is then implemented in the previous numerical approach for variable density jets used in [30], which was able to already achieve very interesting results for the case of study even not including any real fluid thermodynamics calculation procedure.

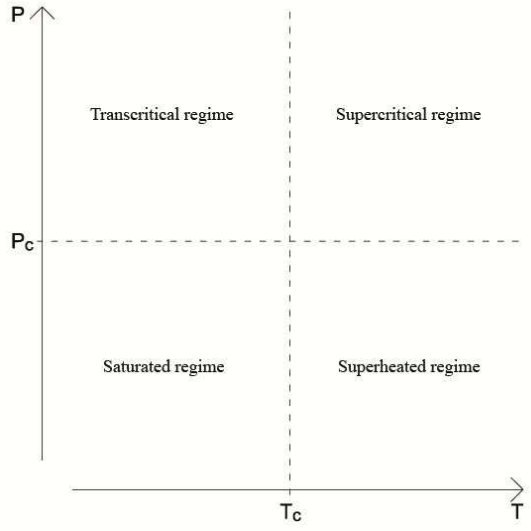

Figure 1 - The Four Thermodynamic Regimes around Critical point.

2. NOMENCLATURE

C_μ = coefficient in turbulence model
c_p = specific heat at constant pressure
ε = dissipation rate of turbulent energy
f = mixture fraction
F = mean mixture fraction
h = enthalpy
i = axial direction index
j = radial direction index
k = turbulent kinetic energy
k_{eff} = effective thermal conductivity
ϕ = generalized variable
ω = chamber-to-injection fluid density ratio (ρ_∞/ρ_0)
ω_f = acentric factor
P_c = critical pressure [MPa]
P_∞ = chamber ambient pressure [MPa]
P_r = reduced pressure (P_∞/P_c)
ρ = density [$kg.m^{-3}$]
ρ_0 = injected fluid density [$kg.m^{-3}$]
ρ_∞ = injection chamber's fluid density [$kg.m^{-3}$]
r = radial coordinate [m]
R/D = radial distancenormalizedby injector diameter
R_{diam} = injector radius [m]
R_e = Reynolds Number
S_ϕ = source term
t = time [s]
T = temperature [K]
T_c = critical temperature [K]
T_r = reduced pressure (T_∞/T_c)
u = axial velocity [$m.s^{-1}$]
U = mean axial velocity [$m.s^{-1}$]
U_{in} = injection axial velocity [$m.s^{-1}$]
v = radial velocity [$m.s^{-1}$]
v_t = turbulent kinematic viscosity
V = mean radial velocity [$m.s^{-1}$]
X = axial coordinate [m]
X/D = axial distance normalized by injector diameter

3. MATHEMATICAL MODEL

The mathematical model used in the present work is based on the one used by Barata et al. [17] and other previous works [29], [30] of the same authors. Modifications were included by the introduction of a real-fluid equation of state, this also demanded the inclusion of the calculation of

the temperature field which was not present in the original approach.

3.1 Governing Equations

The method to solve is based on the solution of the conservation equations for momentum and mass. Turbulence is modeled with the "k~ε" turbulence model. A similar method has been used for three-dimensional or axisymmetric flows and only the main features are summarized here.

In the conservation equations, mass weighted averaging is applied to avoid the appearance of many terms involving density fluctuations for which additional models are needed. A mass averaged quantity is defined as

$$\tilde{\phi} = \frac{\overline{\rho\phi}}{\bar{\rho}} \tag{1}$$

For the governing equations the standard parabolic truncation is employed. The mass averaged partial differential equations governing the steady, variable density axisymmetric flow may be written in cylindrical polar coordinates as

$$\frac{\partial \bar{\rho} UU}{\partial x} + \frac{1}{r}\frac{\partial r\bar{\rho} UV}{\partial r} = -\frac{\partial \bar{p}}{\partial x} - \frac{1}{r}\frac{\partial r\bar{\rho}\,\overline{\tilde{u'v'}}}{\partial r} \tag{2}$$

$$\frac{\partial \bar{\rho} UV}{\partial x} + \frac{1}{r}\frac{\partial r\bar{\rho} VV}{\partial r} = -\frac{\partial \bar{p}}{\partial x} - \frac{1}{r}\frac{\partial r\bar{\rho}\,\overline{\tilde{v'v'}}}{\partial r} + \bar{\rho}\frac{\overline{\tilde{w'w'}}}{r} \tag{3}$$

and the continuity equation as

$$\frac{\partial \bar{\rho} U}{\partial x} + \frac{1}{r}\frac{\partial r\bar{\rho} V}{\partial r} = 0 \tag{4}$$

To describe mixing of gases, the mixture fraction *F*, that represents the mass fraction of the nozzle fluid, is introduced. It obeys a convection-diffusion equation of the form

$$\frac{\partial \bar{\rho} UF}{\partial x} + \frac{1}{r}\frac{\partial r\bar{\rho} VF}{\partial r} = -\frac{1}{r}\frac{\partial r\bar{\rho}\,\overline{\tilde{v'f'}}}{\partial r} \tag{5}$$

In “k~ε” turbulence model, the Reynolds stresses are expressed in terms of the local strain rate:

(6)

with

$$\nu_t = C_\mu \frac{k^2}{\varepsilon} \tag{7}$$

The scalar flux in equation (5) is approximated with a gradient transport assumption

$$\overline{\tilde{u'_i f'}} = -\frac{\nu_t}{\sigma_f}\frac{\partial F}{\partial x_i} \tag{8}$$

From the foregoing we can deduced the parabolized set of equations in cylindrical coordinates where the generalized equation is

$$\frac{\partial}{\partial x}\left(\bar{\rho} U\tilde{\phi}\right) + \frac{1}{r}\frac{\partial}{\partial r}\left(r\bar{\rho} V\tilde{\phi}\right) = \frac{1}{r}\frac{\partial}{\partial r}\left(r\bar{\rho} D\frac{\partial \tilde{\phi}}{dr}\right) + S_\phi \tag{9}$$

where $\tilde{\phi}$ may stand for any of the velocities, turbulent kinetic energy, dissipation, or scalar property, and S_ϕ take on different values for each particular ϕ, described in detail by Sanders et al.[33].

In order to perform the integration of real fluid thermodynamics into the present approach, temperature is obtained through the equation of energy for steady flow shown here for one-dimensional case

$$\frac{\partial \bar{\rho} UT}{\partial x} = \frac{\partial}{\partial x}\left(\frac{k_{eff}}{c_p}.\frac{dT}{dx}\right) + S_h \tag{10}$$

In the present approach only convection and diffusion are taken in consideration for the temperature calculation. Thus no extra terms, that normally would fit in the source term (S_h), were calculated or included.

Several equations of state were evaluated by comparison with experimental values [34]. The equations of state were tested for pressures of 3, 4 and 5 MPa, Figure 2 shows the variation of density in order to temperature for a pressure of 4 MPa. Were tested a Peng-Robinson (PR) EoS proposed by Negro and Bianchi [23], the Soave-Redich-Kwong (SRK) proposed by Soave [35] and a PR and SRK EoS proposed by Loperena[36]. Finally the original Soave-Redlich-Kwong equation of state proposed by Soave in 1972 [35] was choosen for the present approach since is the one that for all tested pressures and temperatures shows better agreement with the experimental data. The equation of state is described below:

$$P = \frac{RT}{V_m - b} - \frac{a\alpha}{V_m(V_m + b)} \tag{11}$$

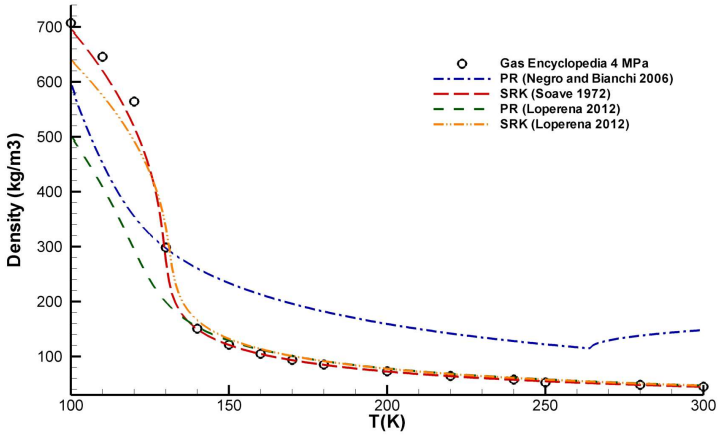

Figure 2.Comparison of Equations of State for 4MPa.

where

$$a = \frac{0.427R^2{T_c}^2}{P_c} \quad (12),$$

$$b = \frac{0.08664RT_c}{P_c} \quad (13)$$

and

$$\alpha = \left(1 + \left(0.48508 + 1.55171\omega_f - 0.15613{\omega_f}^2\right)\left(1 - {T_r}^{0.5}\right)\right)^2 \quad (14)$$

Where ω_f is the acentric factor.

3.2Numerical Method

The governing equations are solved using a parabolized marching algorithm which resembles the (elliptic) TEACH code[13]. The computations are performed by using the continuity equation to obtain the radial velocity (*V*). Using the radial momentum equation for *V* and solving a pressure correction equation for *V* in radial direction did not show any difference with the use of the continuity equation [13]. In this approach the numerical model was applied to variable density jets and for the present case it was used for the study of liquid cryogenic jets under supercritical pressures, and sub to supercritical temperatures.

3.3Flow configuration and Grid

In the present work were modeled the same flow configuration and test conditions used in the experimental work of Mayer [11] and later also simulated by Schmitt [21], Jarczyk and Pfitzner[24] and Antunes [30]. A cold jet of liquid nitrogen was injected through round injector of 2.2 mm diameter into a cylindrical chamber with a diameter of 122mm and length of 250mm, as shown in Figure 3. The test conditions are shown in Table 1 and named case 3 and 4 in order to follow the same nomenclature used before.

Table 1: Conditions of the test cases.

	Case 3	**Case 4**
Chamber Pressure [MPa]	3.97	3.97
Chamber Temperature [K]	298	298
Injection Temperature [K]	126.9	137
Injection Velocity [m/s]	4.9	5.4
ρ_0 [kg/m^3]	394	162
ρ_∞ [kg/m^3]	45.5	45.5
ω	0.1046	0.2661

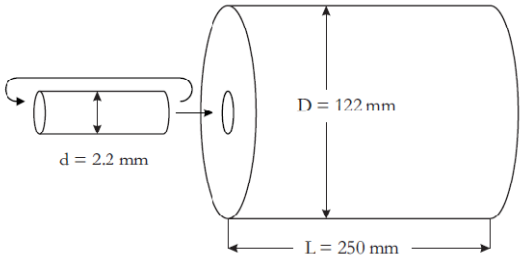

Figure 3. Chamber geometry[21].

The used grid was the same employed in the previous work [30] and represents half of the domain, since the symmetry until the external wall. Thus making the numerical domain 250 mm long and 61 mm width. The grid has 250 points in the axial direction and 100 points in the radial direction making a total of 25000 points.

In order to allow the setting of the desired numbers of points in one direction and at the same time keep the defined length and width of the domain was programmed a grid subroutine that allows to define the number of points and domain, while still being more refined close to the injector. In the axial direction the grid was defined by dividing 50% of the grid points between 30% of the domain length close to the injector, the other 50% of grid point are shared between 70% of the length domain more far from injector.

In radial direction a similar strategy was followed but in this case was first defined 20 grid points in the inlet region (1.1 mm) and the remaining 80 points were defined 40 (50%) to the first 30% of domain and the rest (40 points) for the last 70% of domain.

Since a new model was employed a grid dependency test was performed different grid sizes between 125x50 points and 250x100 proving that the grid has no effect in the results.

4. RESULTS AND DISCUSSION

In this section will be presented the results of Axial Density Distribution and Full Width of Half Maximum of Density for both test cases 3 and 4. From results of the FWHM of Density will be then obtained the jet spreading rate, which is one of the most relevant quantitative results in the evaluation of jets. The results obtained in the present modeling will be compared with previous results obtained by a different approach in which the density is obtained by linear relation from the Mixture Fraction using Amagat's law[17], [29], [30], [33]. Comparisons will also be made with the experimental work of Mayer [11], the main reference data of this work, and the large eddy simulations of Schmitt [21] and of Jarczyk and Pfitzner[24].

Figure 4 shows the axial density distribution for case 3 and compares the results obtained in the present investigation with the results obtained by the previous approach and also with experimental and LES results. Analizing the results we can first observe that the existence of an initial potential core is common to all the investigations. However the potential core obtained in the present work is much bigger, around 15 jet diameters (x/d), than what is obtained in experimental and large eddy

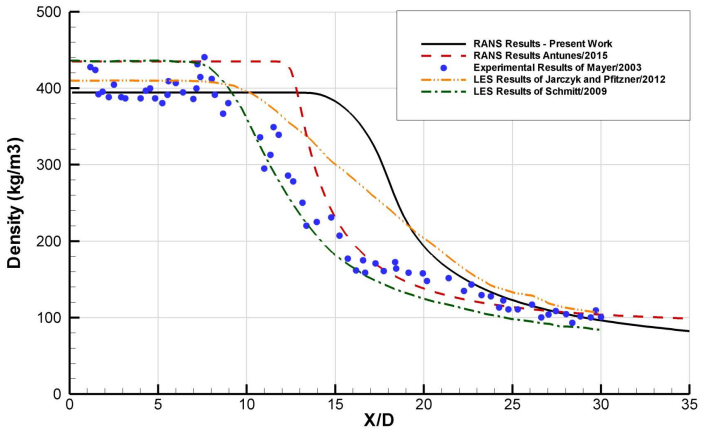

Figure 4. Axial Density Distribution for case 3.

simulation results, which is around 8 jet diameters for the results of Mayer. It is even longer than the one obtained by the previous approach [30] (12 x/d), which in its turn, was already longer than the other results. The initial value of density varies between investigations, this is due to the method of calculation of the density, since what is imposed in the two test cases is the injection temperature. After the potential core region the axial density of the present investigation starts decreasing quickly reaching the same values of experimental data at an axial distance around 22 x/d.

The axial density distribution for case 4 is shown in Figure 5. Similar conclusions to the ones taken for the previous case can be withdrawn from case 4. It is initially obtained a longer potential core than observed in other works, in fact experimental data suggest a very short or no potential core at all [11]. At an axial distance of around 15 jets diameters the current modeling start presenting approximately the same axial density of the experimental data of Mayer, being in fact the closest results to the experimental.

Comparing the obtained results with the previous approach, show us in case 3, reduction of the agreement with the experimental data. For the potential core only the LES approaches are able to show close agreement, further in the axial direction of the domain the approach used in [30] shows the closest agreement from all the models. For the case 4 again only the LES results are able to correctly predict the potential core length. Between 10 and 15 jet diameters, is the previous approach [30] that provides the closest results to experimental. After this axial distance, the current approach gives the closest agreement.

Figure 6 shows the Full Width of Half Maximum of Density for case 3 and compares it with the same results obtained by the previous approach [30] and the experimental data of Mayer [11]. The results obtained by the previous approach had shown a much bigger jet spreading rate than the experimental data. This was indeed the major reason of criticism to the previous model. Current results show on the other hand the opposite trend, the FWHM of density is always smaller than the experimental data. The evolution of the FWHM of Density follows the same trend of the experimental data with a slight decrease in the initial phase followed by a increase of the jet width. In the current approach the widening of the jet happens around 17 x/d instead of 10 x/d like in the experimental data. The results when compared with those obtained in previous approach are much closer to the experimental data, having also closer spreading rate.

For case 4 Mayer didn't provide any results for FWHM of Density, so Figure 7 only shows the results for the current investigation and for the previous approach. Like for case 3 the results of obtained in [30] for case 4 have a great increase of the FWHM of Density, denoting a fast expansion of the jet after the first zone of decreasing. Even not having experimental data to compare these results we could conclude this fast expansion has much bigger than what would be expected in reality for this kind of jet. Current results show a much smaller increase of the jet width, and this way is expected to be much closer to the real phenomenon.

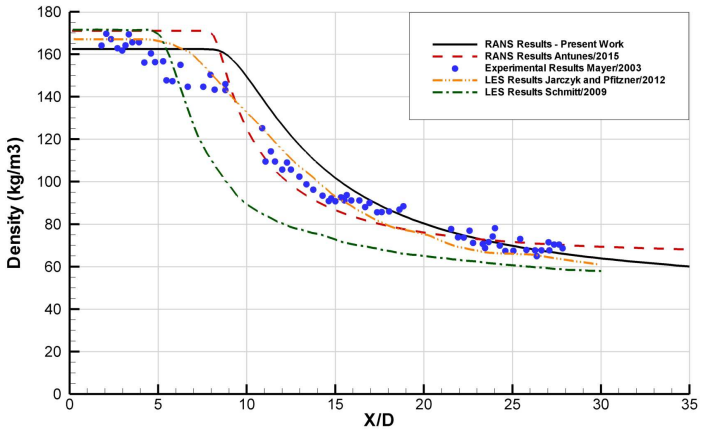

Figure 5. Axial Density Distribution for case 4.

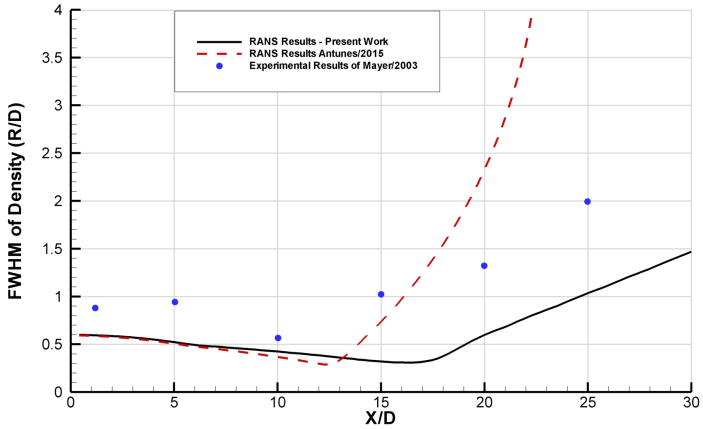

Figure 6. Full Width of Half Maximum of Density for case 3.

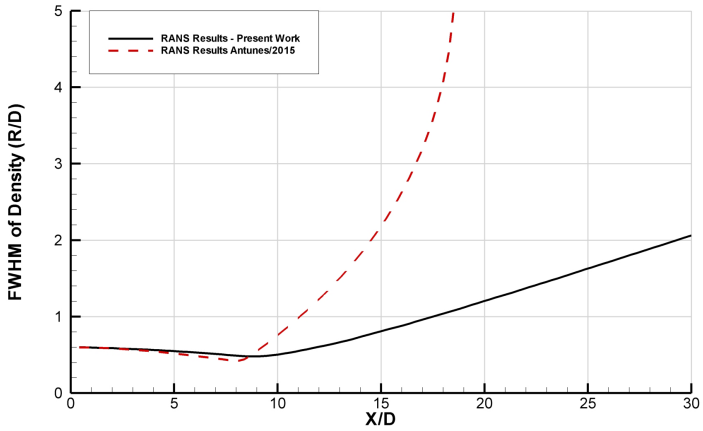

Figure 7. Full Width of Half Maximum of Density for case 4.

The jet spreading rate is calculated by the tangent of the Full Width of Half Maximum of Density between the axial distances of 15 x/d and 25 x/d, which is considered by other authors a more linear region. The results of the jet spreading rate are shown in Table 2 compared with the previous approach [30], the large eddy simulations of Schmitt et al. [21] and the experimental data of Mayer et al. [11]. For the case 4 of previous approach it was not possible to find valid results since the FWHM of Density was not available for point 25 x/d due to the too large expansion of jet. For both cases 3 and 4 the results are bellow the LES data. For the case 4 Mayer didn't provide results but for case 3 his result of spreading rate is above the obtained in the present work. The biggest difference of the current results are found by comparison with previous computational approach which had values of jet spreading angle around 10 times larger.

Table 2: Tangent of the jet spreading angle.

Case	Current Work	Antunes et al.[30]	Mayer et al. [11]	Schmitt et al. [21]
3	0.144	1.441	0.196	0.227
4	0.164	---	---	0.241

5. CONCLUSIONS

The current work had as objective the presentation of a new approach for the modeling of transcritical and supercritical nitrogen jets. In previous works was tested a RANS variable density approach, originally developed for the modeling of gaseous turbulent jets, to the study of cryogenic nitrogen jets at condition of pressure and temperature around the thermodynamic critical point [17], [29], [30]. The results shown good potential for modeling this kind of flows, surprisingly were even able to provide numerical results better agreeing with experiments for the axial density distribution than other more expensive computational approaches, for a relevant part of the domain [30]. However the lack of real fluid thermodynamics, which has been proved to be essential for modeling of transcritical and supercritical flows, exposed the limitations of the method.

The present work intends to document the first attempted of inclusion of real fluid thermodynamics to the approach used before. The authors hoped with this work to improve the performance of the previous model, and obtain this way an inexpensive method for modeling of jet flows at conditions around the thermodynamic critical point. The followed strategy passes by the inclusion of a real fluid equation of state on the previous model. This way density will be calculates in order to pressure and temperature instead of mixture fraction like before. While the equation of state was already selected and represents no important issues for the followed approach, the temperature calculation is still an issue that needs to be addressed better. The presented approach only takes in consideration the convection and diffusion in temperature calculation. However source terms must be taken in consideration. Future work will follow this direction.

Comparing the two approaches can be concluded that the new model obtains generally worse agreement for the axial density distribution. However for the FWHM of Density and jet spreading rate the obtained results are now much closer to the experimental and large eddy simulation data then before approach.

More work needs to be done in the energy equation in order to obtain more accurate calculation of the temperature field.

6. REFERENCES

[1]. J. A. Newman and T. A. Brzustowski, Behavior of a Liquid Jet near the Thermodynamic Critical Region, *AIAA J.*, vol. 9, no. August, pp. 1595–1602, 1971.

[2]. S. D. Givler and J. Abraham, Supercritical droplet vaporization and combustion studies, *Prog. Energy Combust. Sci.*, vol. 22, pp. 1–28, 1996.

[3]. K. Harstad and J. Bellan, Isolated fuid oxygen drop behavior in fluid hydrogen at rocket chamber pressures, *Int. J. Heat Mass Transf.*, vol. 41, pp. 3537–3550, 1998.

[4]. K. Harstad and J. Bellan, Interactions of fluid oxygen drops in fluid hydrogen at rocket chamber pressures, *Int. J. Heat Mass Transf.*, vol. 41, pp. 3551–3558, 1998.

[5]. J. Bellan, Supercritical (and subcritical) fluid behavior and modeling: drops, streams, shear and mixing layers, jets and sprays, *Prog. Energy Combust. Sci.*, vol. 26, pp. 329–366, 2000.

[6]. D. Papamoschou and A. Roshko, The compressible turbulent shear layer: an experimental study, *J. Fluid Mech.*, vol. 197, no. 1973, p. 453, 1988.

[7]. W. O. H. Mayer, A. H. A. Schik, B. Vielle, C. Chauveau, I. Gökalp, D. G. Talley, and R. D. Woodward, Atomization and Breakup of Cryogenic Propellants Under High-Pressure Subcritical and Supercritical Conditions, *J. Propuls. Power*, vol. 14, no. 5, pp. 835–842, 1998.

[8]. M. Oschwald and a. Schik, Supercritical nitrogen free jet investigated by spontaneous Raman scattering, *Exp. Fluids*, vol. 27, pp. 497–506, 1999.

[9]. B. Chehroudi, D. Talley, and E. Coy, Visual characteristics and initial growth rates of round cryogenic jets at subcritical and supercritical pressures, *Phys. Fluids*, vol. 14, no. 2, pp. 850–861, 2002.

[10]. B. Chehroudi, R. Cohn, and D. Talley, Cryogenic shear layers: Experiments and phenomenological modeling of the initial growth rate under subcritical and supercritical conditions, *Int. J. Heat Fluid Flow*, vol. 23, pp. 554–563, 2002.

[11]. W. Mayer, J. Telaar, R. Branam, G. Schneider, and J. Hussong, Raman measurements of cryogenic injection at supercritical pressure, *Heat Mass Transf. und Stoffuebertragung*, vol. 39, pp. 709–719, 2003.

[12]. M. Oschwald, J. J. Smith, R. Branam, J. Hussong, A. Schik, B. Chehroudi, and D. Talley, Injection of Fluids Into Supercritical Environments, *Combust. Sci. Technol.*, vol. 178, no. 908038079, pp. 49–100, 2006.

[13]. S. Martínez-Martínez, F. a. Sánchez-Cruz, J. M. Riesco-Ávila, a. Gallegos-Muñoz, and S. M. Aceves, Liquid penetration length in direct diesel fuel injection, *Appl. Therm. Eng.*, vol. 28, pp. 1756–1762, 2008.

[14]. C. Segal and S. a. Polikhov, Subcritical to supercritical mixing, *Phys. Fluids*, vol. 20, pp. 1–7, 2008.

[15]. A. M. Star, J. R. Edwards, K.-C. Lin, S. Cox-Stouffer, and T. a. Jackson, Numerical Simulation of Injection of Supercritical Ethylene into Nitrogen, *J. Propuls. Power*, vol. 22, no. 4, pp. 809–819, 2006.

[16]. T. Schmitt, J. Rodriguez, I. a. Leyva, and S. Candel, Experiments and numerical simulation of mixing under supercritical conditions, *Phys. Fluids*, vol. 24, 2012.

[17]. J. M. M. Barata and A. R. R. Silva, Numerical Study of Cryogenic Jets Under Supercritical Conditions, *Journal of Propulsion and Power*, vol. 19. pp. 142–147, 2003.

[18]. N. Zong, H. Meng, S. Y. Hsieh, and V. Yang, A numerical study of cryogenic fluid injection and mixing under supercritical conditions, *Phys. Fluids*, vol. 16, pp. 4248–4261, 2004.

[19]. N. Zong and V. Yang*, Cryogenic Fluid Jets and Mixing Layers in Transcritical and Supercritical Environments, *Combust. Sci. Technol.*, vol. 178, no. 908038079, pp. 193–227, 2006.

[20]. J. Sierra-Pallares, M. T. Parra-Santos, J. García-Serna, F. Castro, and M. J. Cocero, Numerical analysis of high-pressure fluid jets: Application to RTD prediction in supercritical reactors, *J. Supercrit. Fluids*, vol. 49, pp. 249–255, 2009.

[21]. T. Schmitt, L. Selle, B. Cuenot, and T. Poinsot, Large-Eddy Simulation of transcritical flows, *Comptes Rendus - Mec.*, vol. 337, no. 6–7, pp. 528–538, 2009.

[22]. T. Kim, Y. Kim, and S. K. Kim, Numerical study of cryogenic liquid nitrogen jets at supercritical pressures, *J. Supercrit. Fluids*, vol. 56, no. 2, pp. 152–163, 2011.

[23]. S. Negro and G. M. Bianchi, Superheated fuel injection modeling: An engineering approach, *Int. J. Therm. Sci.*, vol. 50, no. 8, pp. 1460–1471, 2011.

[24]. M. Jarczyk and M. Pfitzner, Large Eddy Simulation of Supercritical Nitrogen Jets, in *50th AIAA Aerospace Sciences Meeting Including the New Horizons Forum and Aerospace Exposition*, 9-12 January, 2012, AIAA 2012-1270.

[25]. S. K. Kim, H. S. Choi, and Y. Kim, Thermodynamic modeling based on a generalized cubic equation of state for kerosene/LOx rocket combustion, *Combust. Flame*, vol. 159, no. 3, pp. 1351–1365, 2012.

[26]. G. Lacaze and J. C. Oefelein, A non-premixed combustion model based on flame structure analysis at supercritical pressures, *Combust. Flame*, vol. 159, pp. 2087–2103, 2012.

[27]. T. S. Park, LES and RANS simulations of cryogenic liquid nitrogen jets, *J. Supercrit. Fluids*, vol. 72, pp. 232–247, 2012.

[28]. X. Petit, G. Ribert, G. Lartigue, and P. Domingo, Large-eddy simulation of supercritical fluid injection, *J. Supercrit. Fluids*, vol. 84, pp. 61–73, 2013.

[29]. E. L. S. F. Antunes, A. R. R. Silva, and J. M. M. Barata, Evaluation of Numerical Variable Density Approach to Cryogenic Jets, in *50th AIAA Aerospace Sciences Meeting Including the New Horizons Forum and Aerospace Exposition*, 9-12 January, 2012, AIAA 2012-1282.

[30]. E. Antunes, A. Silva, and J. Barata, RANS Modeling of Transcritical and Supercritical Nitrogen Jets, in *AIAA 53th AIAA Aerospace Sciences Meeting*, 5-9 January, 2015, AIAA 2015-0469.

[31]. N. Zong and V. Yang, An efficient preconditioning scheme for real-fluid mixtures using primitive pressure–temperature variables, *Int. J. Comut. Fluid Dyn.*, vol. 21, no. July 2013, pp. 217–230, 2007.

[32]. S. K. Kim and Y. Kim, Thermophysical properties of dimethyl ether at near- and supercritical pressures using generalized cubic EoS, *J. Supercrit. Fluids*, vol. 92, pp. 16–23, 2014.

[33]. J. P. H. Sanders, B. Sarh, and I. GÖkalp, Variable density effects in axisymmetric isothermal turbulent jets: a comparison between a first- and a second-order turbulence model, *Int. J. Heat Mass Transf.*, vol. 40, pp. 823–842, 1997.

[34]. L. Medard, *Gas Encyclopaedia*, Elsevier Science, Amsterdam, 1976.

[35]. G. Soave, Equilibrium constants from a modified Redlich-Kwong equation of state, *Chem. Eng. Sci.*, vol. 27, no. 6, pp. 1197–1203, 1972.

[36]. R. Monroy-Loperena, A note on the analytical solution of cubic equations of state in process simulation, *Ind. Eng. Chem. Res.*, vol. 51, pp. 6972–6976, 2012.

A.5 Abstract of the Comunication Presented in the Mechanical Engineering Conference - CEM 2016

Mechanical Engineering Conference - CEM 2016
Porto, Portugal, June 1-3, 2016

ON THE MODELLING OF TRANSCRITICAL NITROGEN JETS

Antunes, Eduardo[1]; Silva, André[2]; Barata, Jorge[3]

[1] Univ. Beira Interior, Aerospace Sciences Department, Portugal, eduardofariasantunes@hotmail.com
[2] University of Beira Interior, Department of Aerospace Science, Portugal, andre@ubi.pt
[3] University of Beira Interior, Department of Aerospace Science, Portugal, jbarata@ubi.pt

KEYWORDS: *Critical Point, Favre Averaged Navier-Stokes, Real Fluid Equation of State*

ABSTRACT: The importance of prevention of further climate changes and exhaustion of natural resources in our planet demand the reduction of emissions and fossil fuel consumption of combustion engines. In order to do so, operating pressure and temperature of such engines has been increasing, as it is a way of increasing combustion efficiency. The increase of pressure and temperature leads to reaching and surpassing the thermodynamic critical point of fuels and oxidizers. Several authors have been investigating fluid behaviour at conditions around and above critical and concluded that fluids suffer strong properties variations which decisively influence the processes of injection and combustion of fuels and oxidizers [1]. Thus, in order to correctly model flows at those conditions, one must accommodate the vigorous properties changes by the inclusion of real-fluid thermodynamics [2]. In the present work a Favre Averaged Navier-Stokes approach originally developed for the study of variable density gaseous jets was modified in order to include a real-fluid, Soave-Redlich-Kwong type, equation of state. This required also the development of a new procedure for temperature calculation based on the Favre Averaged Energy Equation. Strong variations of specific heat, thermal conductivity and viscosity at these conditions make the task of temperature calculation extremely changeling and difficulties are currently still being faced. The current approach distinguishes itself from other approaches that also make use of a real-fluid equation of state by the fact that uses the temperature to determine density instead of using the mixture fraction. Results exhibit the potential of the current approach when compared with the previous method that obtained the flow density through the calculation of mixture fraction [3].

REFERENCES

[1] Bellan J. Supercritical (and subcritical) fluid behavior and modeling: drops, streams, shear and mixing layers, jets and sprays. Prog. Energy Combust. Sci. 2000.Vol. 26. 329–366.

[2] Mayer W., Telaar J., Branam R., Schneider G., Hussong J. Raman measurements of cryogenic injection at supercritical pressure. Heat Mass Transf. 2003. Vol. 39. 709–719.

[3] Antunes E., Silva A., Barata J. RANS Modeling of Transcritical and Supercritical Nitrogen Jets. AIAA SciTech 2015, Orlando, Florida, 2015: pp. 1–14.

A.6 Abstract of the Comunication Presented in the Joint meeting of the Portuguese and Scandinavian-Nordic Sections of the Combustion Institute - 2016

http://meeting-ist.wixsite.com/cisections-pt-sn

MODELLING OF TRANSCRITICAL JETS BY THE USE OF A REAL FLUID EQUATION OF STATE WITH CONSTANT PROPERTIES

E.L.S.F. Antunes[1], A.R.R. Silva[1,2] and J.M.M. Barata[1]

[1]University of Beira Interior, Department of Aerospace Science, Portugal

Abstract

The prevention of further climate as well as the exhaustion of natural resources in our planet are two of the biggest challenges faced by humankind. To achieve this objectives emissions and fossil fuel consumption must be reduced. At the same time humankind puts great effort in the understanding of our universe, space flights are an important mean to achieve such knowledge and for those better performance and reliability of rocket engines are required.

Increasing the operating pressure and temperature of combustion engines such as diesel engines, gas turbines, rocket engines and others, is a known way of increasing efficiency and performance. Over the past years, this increase has become an important trend in the design of new power units.

This often leads to the fuel injection in internal combustion engines to happen at conditions around and exceeding the thermodynamic critical point. Several studies have demonstrated the change of behavior experienced by jets at transcritical and supercritical conditions [1].

Previous works attempted to evaluate the applicability of a numerical variable density approach, originally developed for the modeling of turbulent, isothermal, gaseous jets, to the study of cryogenic nitrogen jets under transcritical and supercritical conditions [2]–[4]. The obtained results proved the potential of such approach. However, this approach didn't take in consideration the real fluid thermodynamics or the heat transfer in the flow. To solve this limitations, the favre averaged energy equation was implemented into the formulation, allowing the determination of the temperature. The Soave-Redlich-Kwong and Peng-Robinson real fluid equations of state were also implemented into the approach. For the approach treated in the present communication, properties such as molecular viscosity, thermal conductivity, and specific heat at constant pressure were assumed as constants.

The approach was employed in the modeling the injection of cold nitrogen through a round injector, into a chamber filed with gaseous nitrogen at supercritical conditions. This configuration can be observed in Figure 1 and pretends to emulate the experimental study of Mayer et al. [5]. Two different test cases were treated, one corresponding to transcritical injection conditions and the other to supercritical injection. Both equations of state were tested and compared, also different values of fluid properties were tested in order to access their effect in the flow. The results for both cases were compared with the experimental data of Mayer [5] and the large eddy simulations of Schmitt et al. [6] and of Jarczyk and Pfitzner [7]. The results have shown that the Peng-Robinson equation of state produces generally higher values of density than the Soave-Redlich-Kwong. A very small influence of the fluid properties was noticed suggesting a bigger prevalence on the effects of turbulence in the flow. Moreover, the achieved results express an acceptable agreement with experimental data. Results of the Full Width of Half Maximum of Density, shown in Figure 2, allow the determination of the jet spreading rate and are in line with the experimental data.

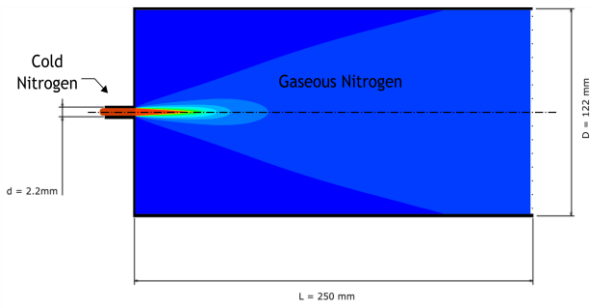

Figure 1: Flow Configuration.

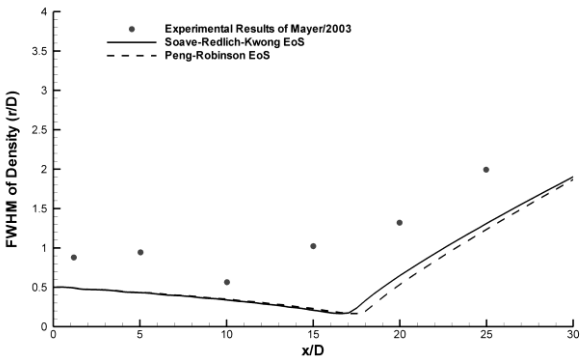

Figure 2: Full Width of Half Maximum of Density.

[2] Corresponding author: andre@ubi.pt

Acknowledgements

The author would like to thanks: Fundação para a Ciência e a Tecnologia (FCT), the Portuguese public agency for science and technology, for the financing of the present investigation by providing a Ph.D. scholarship to the first author with the reference SFRH/BD/87822/2012. Also, AeroG-LAETA associated laboratory, for providing integration in a research unit to the authors. And finally to Universidade da Beira Interior - Covilhã, the host institution for the authors.

References

[1]. J. Bellan, Supercritical (and subcritical) fluid behavior and modeling: drops, streams, shear and mixing layers, jets and sprays, *Prog. Energy Combust. Sci.*, vol. 26, pp. 329–366, 2000.

[2]. J. M. M. Barata and A. R. R. Silva, Numerical Study of Cryogenic Jets Under Supercritical Conditions, *Journal of Propulsion and Power*, vol. 19. pp. 142–147, 2003.

[3]. E. L. S. F. Antunes, A. R. R. Silva, and J. M. M. Barata, Evaluation of Numerical Variable Density Approach to Cryogenic Jets, in *50th AIAA Aerospace Sciences Meeting Including the New Horizons Forum and Aerospace Exposition*, 2012, no. January, pp. 1–14.

[4]. E. Antunes, A. Silva, and J. Barata, RANS Modeling of Transcritical and Supercritical Nitrogen Jets, in *53rd AIAA Aerospace Sciences Meeting*, 2015, no. January, pp. 1–14.

[5]. W. Mayer, J. Telaar, R. Branam, G. Schneider, and J. Hussong, Raman measurements of cryogenic injection at supercritical pressure, *Heat Mass Transf.*, vol. 39, pp. 709–719, 2003.

[6]. T. Schmitt, L. Selle, B. Cuenot, and T. Poinsot, Large-Eddy Simulation of transcritical flows, *Comptes Rendus - Mec.*, vol. 337, no. 6–7, pp. 528–538, 2009.

[7]. M. Jarczyk and M. Pfitzner, Large Eddy Simulation of Supercritical Nitrogen Jets, in *50th AIAA Aerospace Sciences Meeting Including the New Horizons Forum and Aerospace Exposition*, 2012, no. January, pp. 1–13.

A.7 Paper Accepted for Publication at Journal of Engineering and Applied Sciences

Variable Density Approach for Modeling of Transcritical and Supercritical Jets

Eduardo Antunes, André Silva, andJorge Barata
Aerospace Sciences Department, Universidade da Beira Interior, Covilhã, Portugal

Abstract – In order to study the high pressure and high temperature operating condition of a variety of internal combustion engines such as modern diesel engines, gas turbines, and liquid fuel rocket engines, a cryogenic nitrogen jet injected into supercritical chamber conditions was simulated numerically. The Favre Averaged Navier-Stokes equations were employed together with a k-ε turbulence model and using,instead of an ideal gas equation of state, the Amagat's law, in an approach originally conceived for gaseous turbulent jets with variable density. The present paper describes the assessment of the capabilities of the approach by comparison against experimental data as well as numerical simulation performed by other authors. The obtained results show an acceptable agreement with experiments for the axial density distribution,failing slightly in the prediction of the jet potential core. Good agreement is observed for radial density distribution as well as for the jet spreading rate.
Keywords:Critical Point, Cryogenic Jets, Fuel Injection, Rocket Engines, Supercritical Flows.

INTRODUCTION

The extremely important objective of prevention of further climate changes and exhaustion of natural resources in our planet demands the reduction of emissions and fossil fuel consumption of combustion engines. Also, in order to continue the progress in the understanding of our universe, better performance and reliability of rockets engines are required.

Increasing the operating pressure and temperature of combustion engines such as diesel engines, gas turbines, rocket engines and others, is a knownway of increasing efficiency and performance. Over the past years, this increase has become an important trend in the design of new power units.

The process of fuel injection plays one of the most important roles in the subject of combustion, Bakar (2007); Hariram and Mohan Kumar (2012); Zubanov et al. (2014). The wayfuel and oxidizer mix inside the combustion chamber of the several kinds of engines is key for the degree of combustion efficiency in power production, additionally, the maximum performance possible to extract from a power system is strongly dependent on fuel injection. Combustion instability problems in rocket engines that affect reliability and can recurrently lead to destructive failures in such systems are often linked to the process of fuel injection,Sutton, G. P. and Biblarz (2010).

Thus, in recent combustion engines, the investigation of fuel (and oxidizer) direct injection into combustion chambers at high values of temperature and pressure has appeared as an important issue. However, it happens that when operating pressure and temperature increase, the fuels and oxidizers used by the propulsion systems may experience the exceeding of their critical values. The issue is that, under conditions of pressure and temperature whichare around or exceedthe critical values, the behavior of the fluids is quite distinct than the one observed in conditions far from these,Bellan (2000).

Several authors have investigated jet in general and in particular the fluid behavior under and near supercritical conditions both by experimental and numerical approaches which resulted in the production of extensive bibliography,Antunes et al. (2012), (2015); Barata et al. (2003); Bellan (2000); Chehroudi et al. (2000); Chehroudi, Cohn, et al. (2002); Chehroudi, Talley, et al. (2002); H. Mayer et al. (1998); Jarczyk and Pfitzner (2012); Kim et al. (2011); Lacaze and Oefelein (2012); Martínez-Martínez et al. (2008); Mayer et al. (2003); Newman and Brzustowski (1971); Oschwald and Micci (2002); Oschwald and Schik (1999); Oschwald et al. (2006); Papamoschou and Roshko (1988); Park (2012); C. Rodrigues et al. (2012), (2015); Christian Rodrigues et al. (2013); Sanders et al. (1997); Schmitt et al. (2009), (2012); Seebald and Sojka (2011); Segal and Polikhov (2008); Shinjo and Umemura (2011); J. Sierra-Pallares et al. (2009); José Sierra-Pallares et al. (2012); Vieira et al. (2015); Zhou et al. (2011); Zong and Yang* (2006); Zong et al. (2004). As far as today, some conclusions have been reached and validated about the changes in the physical properties of fluids when they are around and above critical conditions. According to Bellan (2000), at the critical point mass diffusivity, surface tension, and latent heat vanish. On the other hand, the heat capacity at constant pressure, Cp, the isentropic compressibility, k_s and the thermal conductivity, λ, all become infinite. At supercritical conditions, which are characterized in the present work by assuming both pressure and temperature

Corresponding Author: Eduardo Antunes, Aerospace Sciences Department, Universidade da Beira Interior, Covilhã, Portugal.

above their respective critical points, a behavioral change is observed for the jet structure,which evolves from a liquid-gas injection to a gas-gas like injection,Chehroudi, Cohn, et al. (2002); Oschwald and Micci (2002); Oschwald et al. (2006); Segal and Polikhov (2008). However bigger questions appear about fluid behavior in conditions near critical for which it is still unknown if the fluid presents a behavior closer to a gas, a liquid or a mix of the two.Recent studies have pointed in the direction of identifying four different regions around the critical point. These regions are dependent on whether both pressure and temperature are supercritical, just one of them, or none. The thermodynamic region of the flow will strongly determine its behavior,Lacaze and Oefelein (2012).

Past works,Antunes et al. (2012); Barata et al. (2003) attempted to evaluate the applicability of a numerical variable density approach to cryogenic nitrogen jets injected into nitrogen gaseous environment for different chamber-to-injectant density ratio (ω). The results obtained were focused on the prediction of the jet spreading rate based on the half width of half maximum of density. Was attempted to establish a limit of applicability of the approach in terms of ω. And was shown agreement with the experimental work of Chehroudi et al. (2000)for chamber-to-injectant ratios between 0.025 and 0.1408.

The aim of the present work is to study, evaluate and develop numerical methods which are suitable to more accurately describe the injection process, in its various parameters, around and beyond critical condition. The present paper describes the injection of liquid nitrogen into gaseous nitrogen environment, consisting of a continuation and development of a previous work from the same authors Antunes et al. (2015) with theimposition of different boundary conditions as well as a different mesh. AFavre Averaged Navier-Stokes approach is adopted using a k-ε turbulence model initially developed for incompressible but variable density flows. Two different test cases were simulated using the same injector and chamber geometry shown in Fig. 1. A transcritical and a supercritical case were simulated, and their conditions are shown in Table 1. The transcritical case (supercritical pressure but subcritical temperature) corresponds to the case number 3 of Mayer et al. (2003) and the supercritical simulation to the case 4

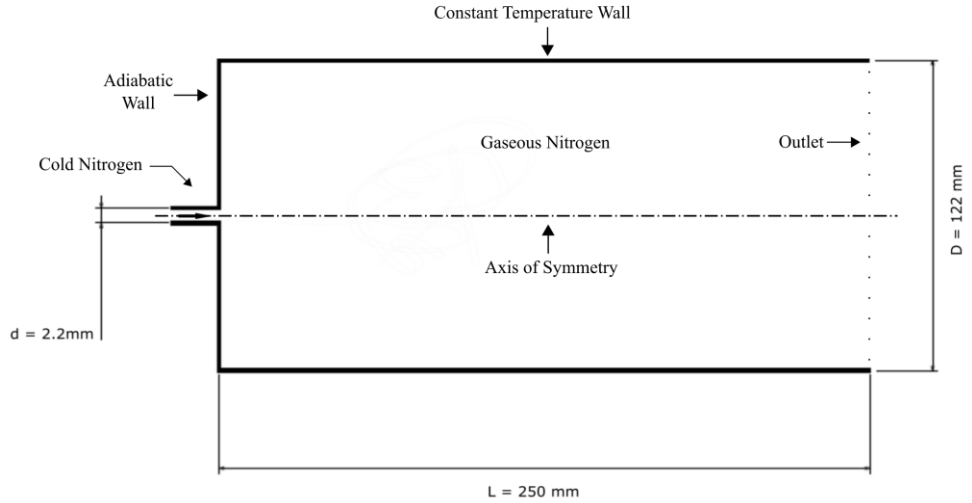

Fig. 1. Chamber geometry.

Table 1: Conditions of the test cases.

Condition	**Case 3 Transcritical**	**Case 4 Supercritical**
Chamber Temperature [K]	298	298
Chamber Pressure [MPa]	3.97	3.97
Injection Temperature [K]	126.9	137
Injection Velocity [m/s]	4.9	5.4
ρ_0 [kg/m^3]	435	171
ρ_∞ [kg/m^3]	45.5	45.5
ω	0.1046	0.2661

of the same author. The only difference between the transcritical case and the supercritical case is the injection temperature that is higher in the second case, however, this difference is enough to place them in two different thermodynamic regimes. The modeled cases were then compared with the experimental data of Mayer et al. (2003) and the Large Eddy Simulations of Schmitt et al. (2009) and of Jarczyk and Pfitzner (2012).

These two tests, in combination with the knowledge obtained in previous works, areexpected to give a better insight intothe injection phenomenon performed at conditions close to critical. Such an analysis is crucial to obtain more clues about whether the strategies adopted to model these flows are accurate enough.

NOMENCLATURE

C_μ	=	coefficient in turbulence model
D	=	injector diameter [m]
ε	=	dissipation rate of turbulent energy
f	=	mixture fraction
F	=	mean mixture fraction
i	=	axial direction index
j	=	radial direction index
k	=	turbulent kinetic energy
ϕ	=	generalized variable
ω	=	chamber-to-injection fluid density ratio (ρ_∞/ρ_0)
P_{cr}	=	critical pressure [MPa]
P_∞	=	chamber ambient pressure [MPa]
P_r	=	reduced pressure (P_∞/P_{cr})
ρ	=	density [kg.m^{-3}]
ρ_0	=	injected fluid density [kg.m^{-3}]
ρ_∞	=	injection chamber's fluid density [kg.m^{-3}]
r	=	radial coordinate [m]
R/D	=	radial distance normalized by injector diameter
R_{diam}	=	injector radius [m]
R_e	=	Reynolds Number
S_ϕ	=	source term
t	=	time [s]
T	=	temperature [K]
u	=	axial velocity [m.s^{-1}]
U	=	mean axial velocity [m.s^{-1}]
U_{in}	=	injection axial velocity [m.s^{-1}]
v	=	radial velocity [m.s^{-1}]
v_t	=	turbulent kinematic viscosity
V	=	mean radial velocity [m.s^{-1}]
X	=	axial coordinate [m]
x/D	=	axial distance normalized by injector diameter

MATERIALS AND METHODS

For the current investigation, the mathematical model and numerical approach followed the same line already used by Barata et al. (2003) and inprevious works,Antunes et al. (2012), (2015). This method is described in great detail by Sanders et al. (1997). In Sanders's publication is described a second order model, for which differential equations are used for the calculation of Reynolds stresses, and a first-order (k-ε) model. In the current work only the first order model was employed.

Governing Equations: The method originally developed to solve variable density jet flows is based on the solution of the conservation equations for momentum and mass. Turbulence is modeled with the "k~ε" turbulence model. A similar method has been used for three-dimensional or axisymmetric flowsAntunes et al. (2012); Barata et al. (2003); Sanders et al. (1997) and only the main features are summarized here.

In the conservation equations, mass weighted averaging is applied to avoid the appearance of many terms involving density fluctuations for which additional models are needed. A Favre averaged, or mass weighted averaged, quantity is defined as

$$\tilde{\phi} = \frac{\overline{\rho\phi}}{\overline{\rho}} \qquad (1)$$

For the governing equations, the standard parabolic truncation is employed. The mass averaged partial differential equations governing the steady, variable density axisymmetric flow may be written in cylindrical polar coordinates as

$$\frac{\partial \overline{\rho} UU}{\partial x} + \frac{1}{r}\frac{\partial r\overline{\rho} UV}{\partial r} = -\frac{\partial \overline{p}}{\partial x} - \frac{1}{r}\frac{\partial r\overline{\rho}\,\tilde{\overline{u'v'}}}{\partial r} \quad (2)$$

$$\frac{\partial \overline{\rho} UV}{\partial x} + \frac{1}{r}\frac{\partial r\overline{\rho} VV}{\partial r} = -\frac{\partial \overline{p}}{\partial x} - \frac{1}{r}\frac{\partial r\overline{\rho}\,\tilde{\overline{v'v'}}}{\partial r} + \overline{\rho}\frac{\tilde{\overline{w'w'}}}{r} \quad (3)$$

and the continuity equation as

$$\frac{\partial \overline{\rho} U}{\partial x} + \frac{1}{r}\frac{\partial r\overline{\rho} V}{\partial r} = 0 \qquad (4)$$

To describe themixing of gases, the mixture fraction F, that represents the mass fraction of the nozzle fluid, is introduced. It obeys a convection-diffusion equation of the form

$$\frac{\partial \overline{\rho} UF}{\partial x} + \frac{1}{r}\frac{\partial r\overline{\rho} VF}{\partial r} = -\frac{1}{r}\frac{\partial r\overline{\rho}\,\tilde{\overline{v'f'}}}{\partial r} \qquad (5)$$

In "k~ε" turbulence model, the Reynolds stresses are expressed in terms of the local strain rate:

$$-\bar{\rho}\widetilde{\overline{u'_i u'_j}} = \bar{\rho}(\nu_t+\nu)\left(\frac{\partial \tilde{u}_i}{\partial x_j}+\frac{\partial \tilde{u}_j}{\partial x_i}\right)-\frac{2}{3}\delta_{ij}\left(\bar{\rho}k+\bar{\rho}(\nu_t+\nu)\frac{\partial \tilde{u}_j}{\partial x_j}\right) \quad (6)$$

with

$$\nu_t = C_\mu \frac{k^2}{\varepsilon} \quad (7)$$

The scalar flux in equation (5) is approximated with a gradient transport assumption

$$\widetilde{\overline{u'_i f'}} = -\frac{\nu_t}{\sigma_f}\frac{\partial F}{\partial x_i} \quad (8)$$

From the foregoing, we can deduce the parabolized set of equations in cylindrical coordinates where the generalized equation is

$$\frac{\partial}{\partial x}\left(\bar{\rho}U\tilde{\phi}\right)+\frac{1}{r}\frac{\partial}{\partial r}\left(r\bar{\rho}\tilde{\phi}\right)=\frac{1}{r}\frac{\partial}{\partial r}\left(r\bar{\rho}D\frac{\partial \tilde{\phi}}{dr}\right)+S_\phi \quad (9)$$

where $\tilde{\phi}$ may stand for any of the velocities, turbulent kinetic energy, dissipation, or scalar property, and S_ϕ take on different values for each particular $\tilde{\phi}$, as described in detail by Sanders et al.Sanders et al. (1997).

To obtain the mean density an equation of state based on the Amagat's law is employed using the mean mixture fraction. With constant pressure, this leads to

$$\frac{1}{\bar{\rho}} = \frac{F}{\rho_o}+\frac{1-F}{\rho_\infty} \quad (10)$$

where density fluctuations have been neglected. This is allowed in isothermal jets because the instantaneous density, for which equation (10) is exact, is approximately a linear function of the instantaneous mixture fractionBarata et al. (2003).

Numerical Method: The governing equations are solved using a parabolizedmarching algorithm similar to the one reported in the (elliptic) TEACH code,Sanders et al. (1997). The computations are performed by using the continuity equation to obtain the radial velocity (*V*). In fact, it has been found (Sanders et al. (1997)) that using the radial momentum equation for *V* and solving a pressure correction equation for *V* in radial direction did not result inany difference when compared with the use of the continuity equation. In this approach, the numerical model was applied to variable density jets and for the present case it was used for the study of liquid cryogenic jets under sub-near critical pressures, and sub to supercritical temperatures.

In order to determine the tangent of the jet spreading angle, the Half Width of Half Maximum of the Density (HWHM of Density) is used.

Computational grid: The flow configuration can be observed in Fig. 1, with the cold nitrogen being injected through a round injector with 2.2 mm of diameter into a cylindrical chamber with a diameter of 122 mm and a length of 250 mm. The boundary conditions are well described in the same figure, with the imposition of a constant temperature wall in the north boundary, an adiabatic wall at the west boundary and the outlet condition exists in the east boundary. For this numerical approach, and since the flow is axisymmetric,it was only modeled half of the domain seen in Fig.1. and thus the south boundary is the symmetry axis. Therefore, the numerical domain becomes 250 mm long and 61 mm width. A grid was used with150 points in the axial direction and 65 points in the radial direction making a total of 9150 points.

In the construction of the grid, care was taken in order to assure that the defined computational domain was always kept independently of the size of the grid. Also, a higher refinement was introduced close to the injector, where higher variable gradients are expected and biggest interest exists for the current investigation. The grid follows a constant expansion in the axial direction, with the initial length size of the control volume being defined by the expansion rate and number of points imposed. For the radial direction, the initial distance between knots is kept contact during all the injector width and then follows a constant expansion until reaching the north boundary.

Because a new grid was used and no other previous works had used it before, a grid dependency test was performed. The axial density distributionwas used to test the grid dependency of the computations. Fig. 2compares the evolution of the density distribution along the symmetry axis for 3 different grid sizes.With a grid size of 106x46points, approximately half of the size in number of points, the results are already very close from those obtained from the used grid (150x65). And for the grid with approximately twice the size innumber of points (212x92) the difference is negligible. It can be concluded that for the used grid size the results donot depend on the grid size.

RESULTS

The numerical results obtained in the present work are presented in this section. To assess the accuracy of the simulations performed, the results are compared against the experimental data of Mayer et al. (2003) and large eddy simulations carried out by Schmitt et al. (2009)and Jarczyk and Pfitzner (2012). A discussion is also provided in order to reach the conclusions exposed in the next section.

Figures 3, 4 and 5 show the velocity, mixture fraction, and density fields respectively for transcritical and supercritical cases. Its allow us to obtain a general picture of the flow geometry. As said before, and highlighted in Table 1, the two test cases only differ from each other in the injection temperature (and consequently the injection density) and velocity, while the chamber conditions remain the same for both cases. Nevertheless,this difference in the injection temperature between the two cases is enough to position them in different thermodynamic regimes. In the transcritical case, the pressure in supercritical while the temperature is subcritical, while for the supercritical case both pressure and temperature are supercritical.

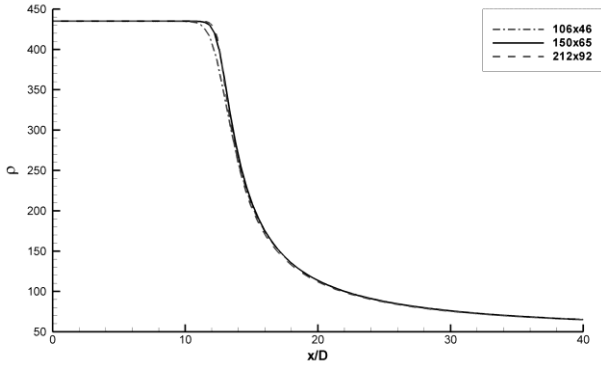

Fig. 2. Grid size dependency test based on the axial density distribution.

Comparison between both cases shows very similar jet structures.Nevertheless,the supercritical case presents a

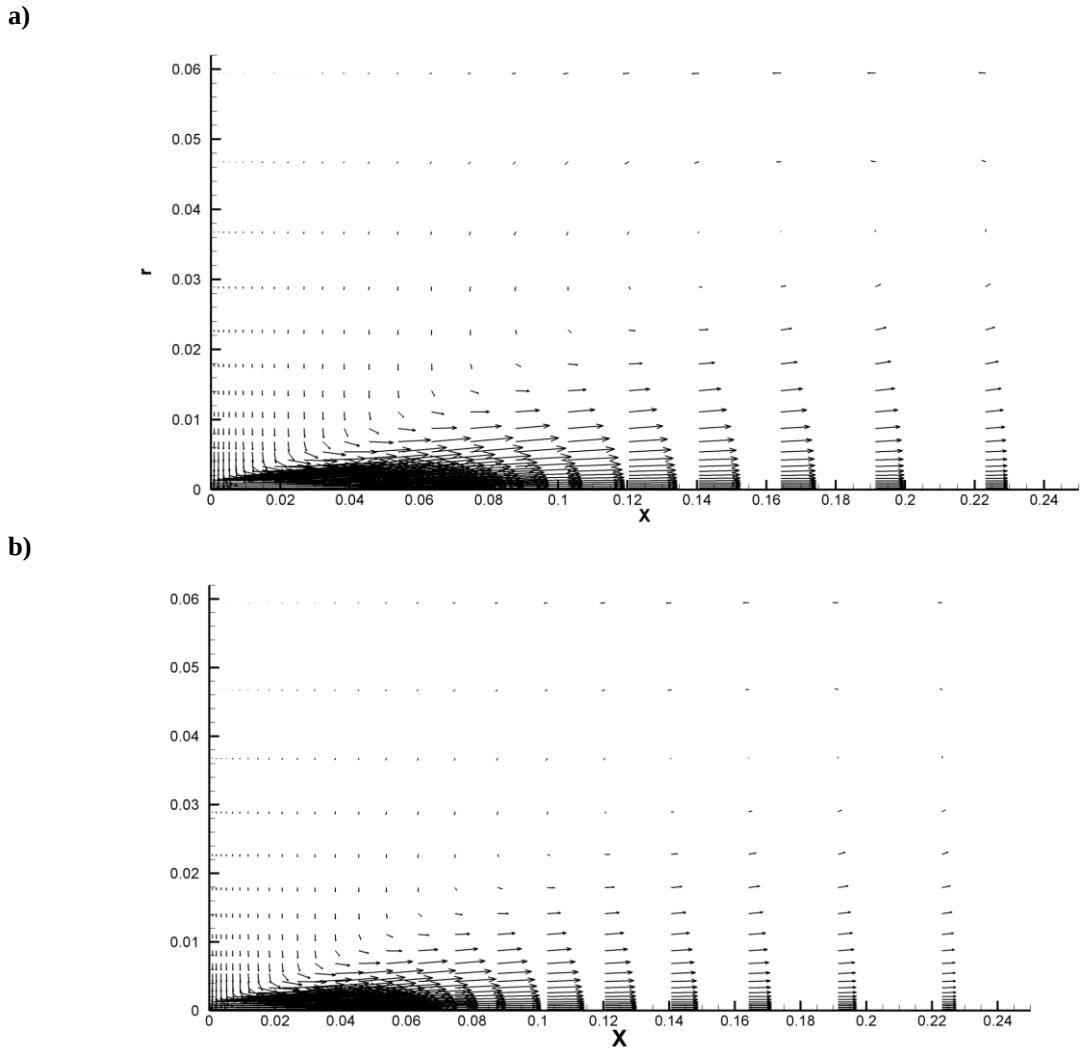

Fig. 3. Velocityfield of the jet for a) transcritical and b) supercritical conditions.

faster reduction of the density and mixture fraction value thanthe transcritical case. Similar conclusions are obtained in the previous studies of Schmitt et al. (2009) and Jarczyk and Pfitzner (2012), with the LES visualizations showing similar variations between the two cases. These results also suggest the existence of a smaller potential core for the supercritical conditions shown in case 4.This characteristic, in particular, will be discussed later.

Figure 3 show the velocity fields obtained in each of the simulations performed. It is visible in both cases the appearance of an entrainment close to the injector exit with ambient nitrogen being pulled into the jet stream. This phenomenon appears to be slightly more intense in transcritical regime even having a slower injection velocity. This is probably due to the higher jet momentum caused by higher injection fluid density. It is also visible that farther away from the injector, the velocity vectors are bigger in the transcritical case than in the supercriticaldue not only to the higher injection velocity but by the higher fluid density. The injection density appears to be determinant to the distance that a jet can reach.

In Figure4the mixture fraction fields are shown for test both tested cases. The images show a high concentration of injected fluid close to the injector exit which decreases as the distance to the injector in both radial and axial direction increases. Comparison between the two cases shows a faster decrease of the mixture fraction along the jet in supercritical conditions than in transcritical. However, it is important to note that this faster decrease doesnot mean anenhanced mixture of the jet fluid with the chamber fluid. In fact, there are higher mixture fraction gradients at supercritical conditions. Close to the injector the mixture fraction quickly decreases in value but then, in the rest of the injection chamber, the domain is dominated by mixture fraction values bellow 0.5. In the transcritical case, even though it evidences a slower decrease of mixture fraction and bigger penetration of injection fluid (apparently showing a slower mixture at the beginning of the jet),anincreased mixture is still visible asthe mixture fraction valuesclose to 0.5 are foundin most of thedomain. These results of theapparentlyincreased mixture in the case with smaller

a)

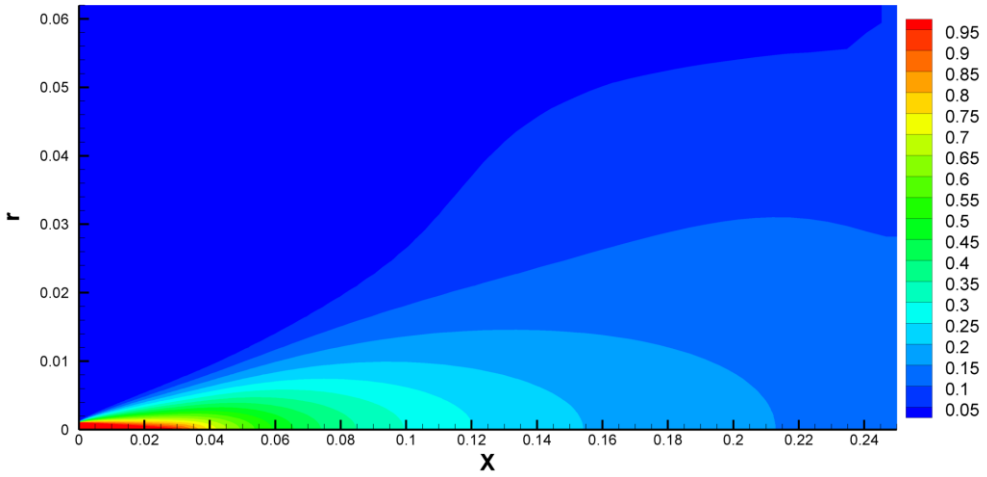

b)

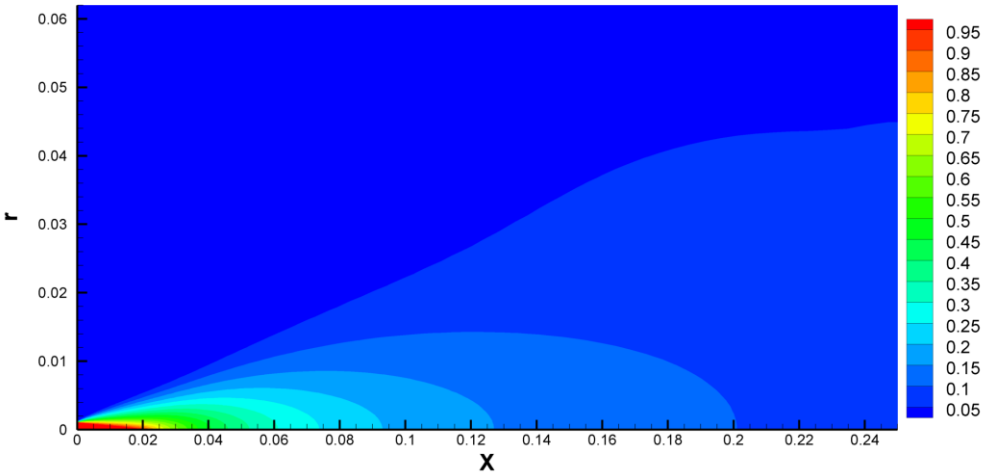

Fig. 4. Mixture fraction field of the jet for a) transcritical and b) supercritical conditions.

temperature and at which the difference between injection density and chamber density is higher can be considered in some way surprising.

The density fieldsare shown in Figure 5. Again the results show similar jet structure for both cases. The transcritical case, however, shows a longer dense core than the one observed at supercritical conditions. Having thetranscritical situation ahigher density gradient between injected and chamber fluid and a lower injection velocity, one could expect it to have a shorter dense core as well as a smaller jet penetration than supercritical casa. However,the opposite occurs.The explanation found by the authors of the present paper is that the fluid density, due to its influence in fluid momentum, rules the jet dynamics. Although the jet in transcritical conditionshas a slower injection velocity, ithas, in fact,a higher momentum which results in a bigger penetration length. The higher jet momentum is also responsible for the more intense entrainment at the jet exit in this case. The entrainment phenomenon is important for the fluid mixing. This explains the enhanced mixing attranscritical conditions when compared to supercritical. These results obtained by the present numerical approach are corroborated in the LES results of Schmitt et al. (2009)where case 3 also shows a longer jet length and a denser core than case 4.

The results obtained by the velocity and scalar fields also give us the evidence that the jet behavior is mostly dominated by the convection terms while diffusion plays a minor role. In turn, convection is mostly dominated by the density. The calculation of density appears this way as a key factor in the modeling of this kind of flows.

The axial density distributions of transcritical and supercritical casesare shown in Figures 6 and 7, respectively. The present numerical model is evaluated against experimental and numerical results of other authors. Potential core length is one important characteristic of a jet, generally used by other authors to help to quantify it.Schmitt et al. (2009) defines the potential core length as the axial distance at which the centerline density is 99% of the injected density. Generally, potential core length is expressed in multiples of injector diameters. In the present investigation, it was decided to use the same definition of potential core

a)

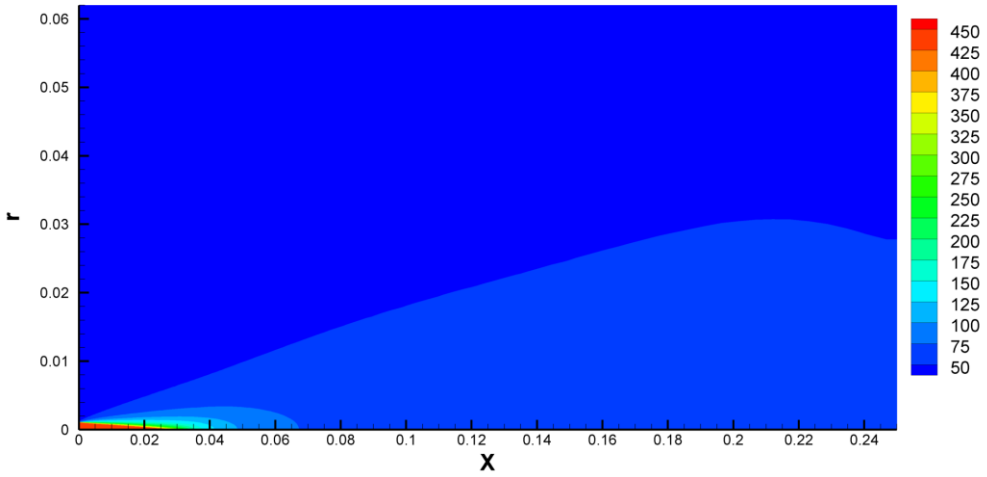

b)

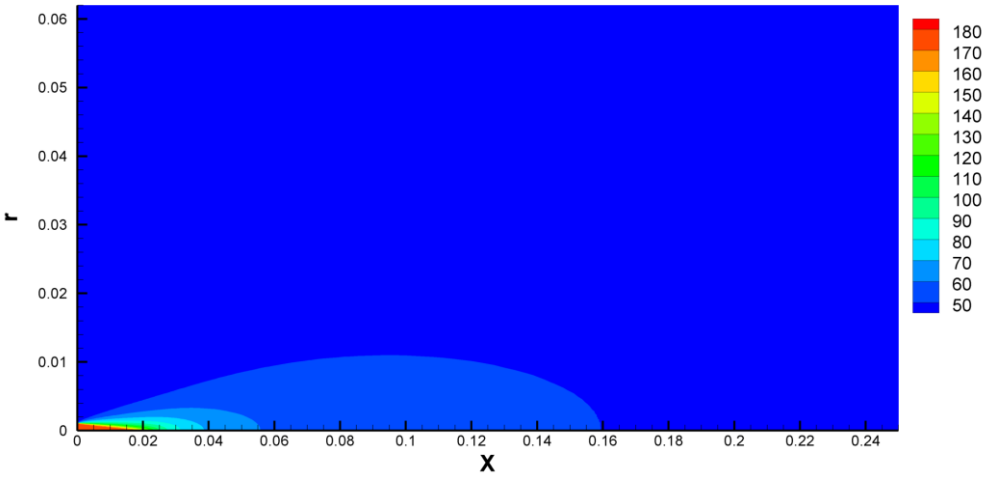

Fig. 5. Densityfield of the jet for a) transcritical and b) supercritical conditions.

already used by Schmitt et al. (2009).

The results obtained for thetranscritical case in the present investigation show a potential core of 11.8 injector diameters. It is longer when compared with the results of other authors.Schmitt et al. (2009) for example shows a potential core length of 7.9 diameters, whereas Jarczyk and Pfitzner (2012) identifies a length of around 9 diameters. The Large Eddy Simulation performed by Schmitt et al. (2009) shows the best agreement with the experimental data from all the numerical approaches. The Large Eddy Simulation of Jarczyk and Pfitzner (2012) overestimates the value of the density for a large range of the visible domain, from the potential core, and only getting closer to the experimental values at an axial distance of around 25 jet diameters. The current approach after clearly overestimating the potential core gets closer to the experimental data for a distance of 15 x/D, however, diverges from the experiments after 17 x/D. The results are nevertheless in line with the other investigations. The same kind of centerline density distribution profile was obtained for supercritical conditions in Figure 7. The potential core obtained of around 7.8 diameters is bigger than the one obtained with the two LES results which are 5.1 diameters in the work

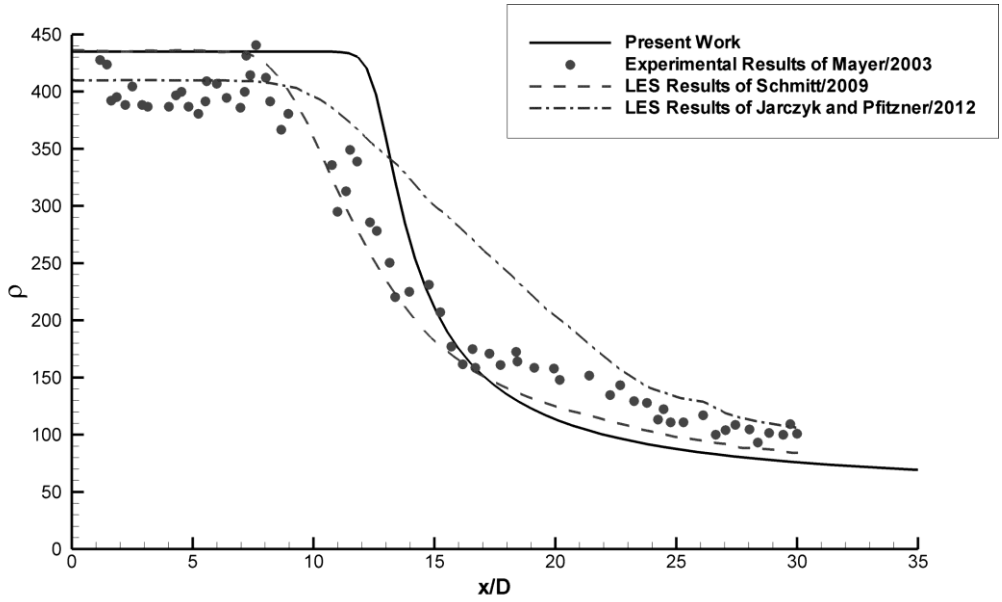

Fig. 6. Axial density distribution for transcritical case and comparisons with different authors' results.

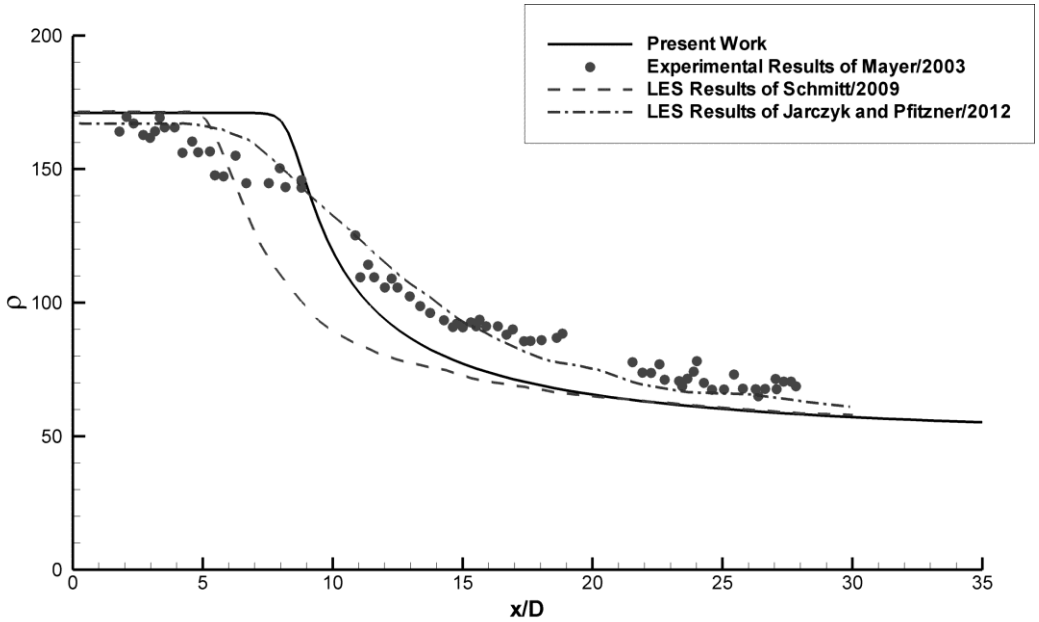

Fig. 7. Axial density distribution for supercritical case and comparisons with different authors' results.

of Schmitt et al. (2009) and around 6 jet diameters for Jarczyk and Pfitzner (2012). Analyzing experimental data of Mayer et al. (2003) there is little amount of evidence of the existence of a potential core for this test case.

For the supercritical test case, the numerical approach published by Jarczyk and Pfitzner (2012) provides the results with the closest agreement with the experimental data. The numerical results of Schmitt et al. Schmitt et al. (2009) under predict the density value at the centerline for all the visible domain with theexception of the points closest to the injector. The results of the present approach after the overestimation of the potential core under predict slightly the density value, gives, however, closer results to experimental data than Schmitt et al. (2009). Furtheraway from the injector the current results reach total agreement with the data from Schmitt.

Figures 8 and 9 show the radial density distribution of three different axial distances for transcritical and supercritical cases respectively. Figures a), b) and c) illustrate the axial distance of 1.2, 5 and 25 injector diameters, respectively. Figure 8 a) shows quite good agreement with experimental data of Mayer et al. (2003). For the same axial distance for supercritical conditions in Figure 9 a) the agreement is also good showing even an interception of experimental and numerical data during some range of the domain. For the axial distance of 5 x/D, in case 3, Figure 8 b), the experimental data show a decrease of density close to the centerline that is not observed in the current results.These results are naturally attributed to the longer potential core, obtained in the current approach, which havealready been visualized in Figure 6. Farther away from the centerline the numerical results find much closer agreement with the experiments. For the same case in Figure 8 c), at an axial distance of 25 x/D,the agreement obtained is not as good, since the numerical results are not able to replicate the flattened bell shape of the experimental data which shows an

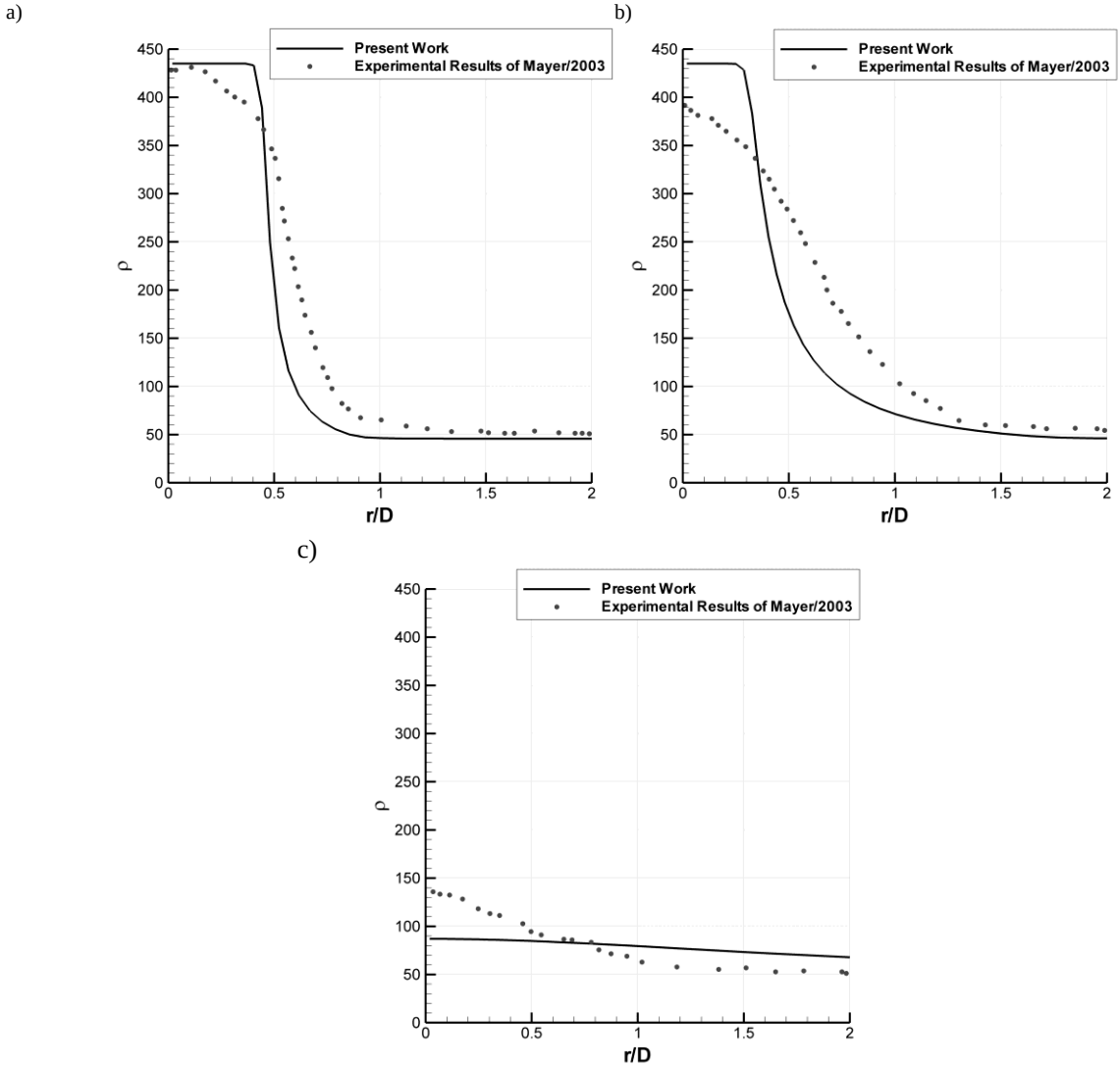

Fig. 8 - Radial Density Distribution for transcritical case. a) x/D = 1.2; b) x/D = 5; c) x/D = 25

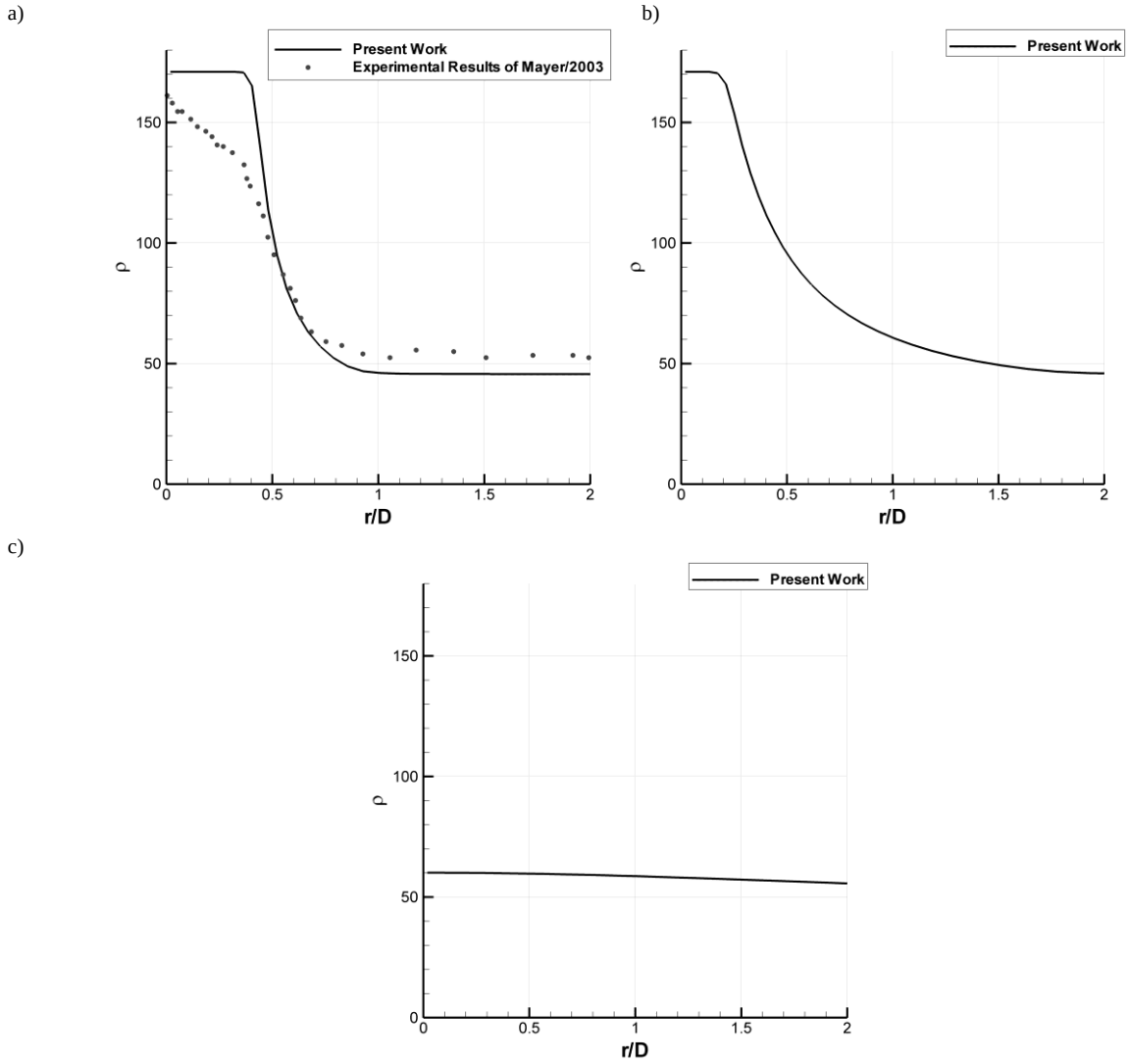

Fig. 9 - Radial Density Distribution for supercritical case. a) x/D = 1.2; b) x/D = 5; c) x/D = 25

almost constant value of density along the radial direction with only a slight decrease. For supercritical case,it can be observed that the results follow the same trend of case 3 and asimilar agreement is expected. The comparison between present results and experimental data shows a fair agreement between both, with some differences identified further downstream in the domain, showing some difficulty of the current approach to provide correct values of density in this zone.The spreading angle of the jet is one of the most important parameters available to the use of a researcher when his objective is to characterize a jet. In order to determine the spreading of a jet,it becomes necessary to define the radial border of it. Several authors, including those cited in the present paper,Jarczyk and Pfitzner (2012); Schmitt et al. (2009), assume that the border of the jet is in the radial position where the density is the average between the maximum value (located in the centerline position, at the same axial distance) and minimum value (the chamber density). This is how the Full Width of Half Maximum of Density (FWHM of Density) is defined. In the work of Schmitt et al. (2009)the tangent of the spreading angle of density was obtained by linear interpolation of the FWHM of Density between x/D = 15 and x/D = 25. In the present work,it was decided to use the exact same method.

Fig. 10 shows the FWHM of Density for test case attranscritical conditions obtained in the present work and is compared against the Raman measurements of Mayer et al. (2003). It can be observed that the numerical results obtained in the present work follow a similar trend as the one obtained in the experimental data. The chart initially shows a decrease of the half width that extends up to 10 x/D in the experimental data, whereas in the present numerical data it decreases until approximately 12 x/D, but always with a smaller width than in the experimental data. After this point, the half width of the jet starts increasing, showing that the jet is spreading. The observed numerical spreading rate is very much in line with the Raman measurements. The values

of the tangent of spreading angle using the FWHM of Density are expressed in Table 2 for the experimental data ofOschwald and Micci (2002) and ofMayer et al. (2003), the large eddy simulation of Schmitt et al. (2009), and the present work.At transcritical conditions ajet spreading rate tagent of around 0.2 is obtained by the two experimental works. The large eddy simulation of Schmitt et al. (2009) provides a slightly large value of spreading rate but still closer the value obtained by the present approach.

Figure 11 shows the FWHM of Density for thesupercritical case. For this case there were no available experimental data from the Raman measurements ofMayer et al. (2003) and for this reason Fig. 11 only shows the results obtained in the present work. In the chart, it is possible to observe at the beginning of the jet a very slow decrease of the jet width until an axial length of around 8 x/D. After this mark, there is an increase of the jet width following a tangent of the spreading angle of around 0.310. The results provided in Table 2 show that for this case the present approach provides a spreading rate in very close agreement with the experimental data of Oschwald and Micci (2002) clearly outperforming the results obtained by Schmitt et al. (2009) with their large eddy simulation which under predict the value of the tangent of the spreading rate.

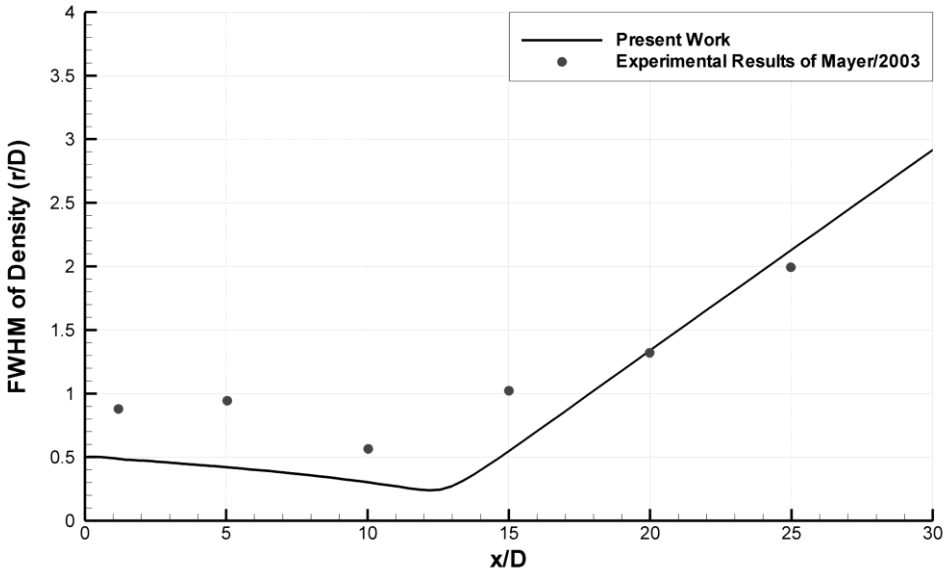

Fig. 10. Half Width of Half Maximum of Density for transcritical case and comparison with experimental data of Mayer et al.Mayer et al. (2003)

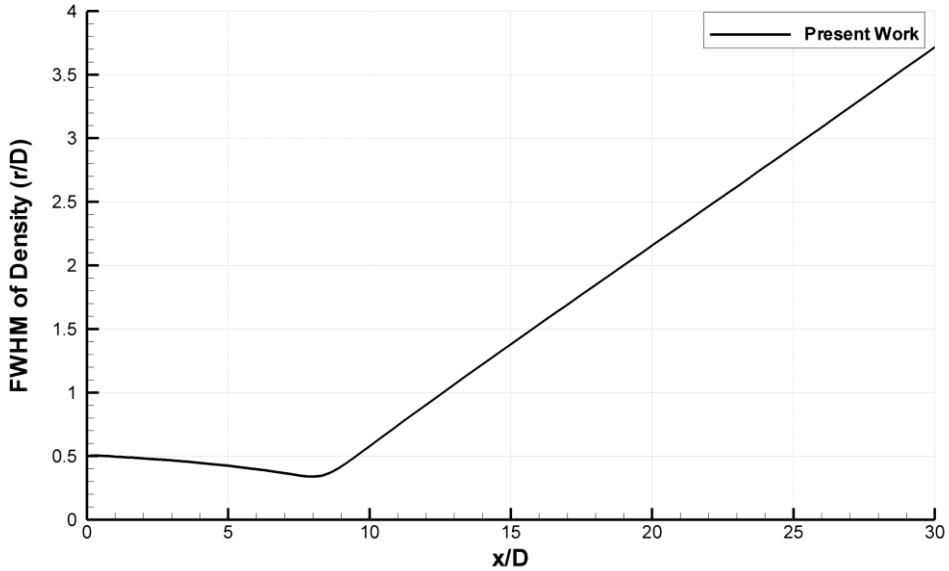

Fig. 11 - Half Width of Half Maximum of Density for supercritical case.

Table 2: Results of Jets Spreading Rate

	Oschwald and Micci (2002)	Mayer et al. (2003)	Schmitt et al. (2009)	Present Work
Transcritical Case	0.206	0.196	0.227	0.316
Supercritical Case	0.312	-	0.241	0.310

CONCLUSION

Aiming to study, evaluateand develop numerical methods for more accurately describingtheinjection process around and beyond critical conditions, a numerical approach – originally designed to model gaseous jet flows with different densities, and used in previous works to study the jet spreading angle for different density ratios – has been evaluated to model cryogenic jets at thermodynamic conditions near critical. As part of the task is also the goal of attempting to identify and later integrate the needed modifications to the numerical approach in order to make it more suitable to simulate the flows of interest.

To validate the present numerical approach,the results were compared against the experimental data reported byMayer et al. (2003)as well as two computational results performed under LES techniques - Schmitt et al.Schmitt et al. (2009) and Jarczyk and PfitznerJarczyk and Pfitzner (2012) - for two test cases.

For the axial density distribution, the numerical results obtained in the present investigation show acceptable agreement with experimental results of MayerMayer et al. (2003),with comparable results to those obtained by the LES investigationsJarczyk and Pfitzner (2012); Schmitt et al. (2009). However, difficulties still arise in the calculation of a correct length of the potential core. Fairly good agreement was found for the radial density distribution, with the results corroborating much of what was concluded in the axial density distribution. Close agreement with experimental data is achieved for the jet spreading rate. For the transcritical case theresults are very comparable with experimental, and not very far from the results provided by the large eddy simulation approach ofSchmitt et al. (2009), which is a much more computationally expensive approach. For the supercritical case the present approach provides the closest agreement with the experimental data of Oschwald and Micci (2002), the large eddy simulation of Schmitt et al. (2009) isn't able to reach a similar level of agreement at a much higher computational cost.

There has been a trend, between authors investigating jet at conditions near critical, to use a real gas equation of state to calculate the densityJarczyk and Pfitzner (2012); Oschwald and Micci (2002); Park (2012); Schmitt et al. (2009). In the present numerical approach, the mean density is calculated by an equation of state that is a linear function of the mixture fraction. As stated above this method of calculation of density is allowed in isothermal jets. However, in the present test cases, one is not in the presence of isothermal gases, so this method of calculating density can be one of the main causes of the discrepancies that still exist in density determination, for instance in the calculation of potential core length. The use of this simplified method of calculating density is justified in the present approach by the objective of evaluating the potential of this method before departing to different techniques more suitable of producing more accurate results.

Transcritical and supercritical jets are known to be highly transient and very sensitive to small and local changes of temperature and pressureBellan (2000). Reynolds or Favre averaged Navier-Stokes methods, unlike LES, only use the average terms of velocity, pressure, temperature, etc. These approaches lead to the neglecting of the small fluctuationsin transcritical and supercritical jets, which can have a huge impact on the flow behavior. This reality could in fact also be one of the causes for incapacity of the present numerical approach to provide accurate predictions of the studied jet spreading angle. HoweverPark (2012), in his LES and RANS investigation, concluded that the suitable adoption of an equation of state is more decisive than the selection of turbulence model for the numerical performance. According to Park, the potential core length is linked with the existing pseudo-boiling region. The pseudo-boiling region can be defined as the prolongation of the gas/liquid phase-change line and corresponds to a maximum of constant-pressure heat capacity at constant pressure Petit et al. (2013). Thus in order to ba able to provide a correct prediction of the jet potential core one must be able to correctly predict the fluid properties at thetransition between transcritical and supercritical conditions.

Future investigations will be focused on the integration of a real gas equation of state into the present numerical formulation providing to the model a different method for density calculation. With these changes, the authors expect to improve the agreement with experiments for the transcritical injection case while keeping the same level of agreement already achieved for the supercritical outperforming more expensive large eddy simulations.

ACKNOWLEDGEMENTS

The author would like to thanks: Fundação para a Ciência e a Tecnologia (FCT), the Portuguese public agency for science and technology, for the financing of the present investigation by providing a Ph.D. scholarship to the first author with the reference SFRH/BD/87822/2012. Also, AeroG-LAETA associated laboratory, for providing integration in a research unit to the authors. And finally to Universidade da Beira Interior - Covilhã, the host institution for the authors.

REFERENCES

Antunes, Eduardo, André Silva, and Jorge Barata. 2015. "RANS Modeling of Transcritical and Supercritical Nitrogen Jets." In *53rd AIAA Aerospace Sciences Meeting*, Kissimmee, Florida, 1–14.

Antunes, Eduardo, André R R Silva, and Jorge M M Barata. 2012. "Evaluation of Numerical Variable Density Approach to Cryogenic Jets." In *50th AIAA Aerospace Sciences Meeting Including the New Horizons Forum and Aerospace Exposition*, Nashville, Tennessee, 1–14.

Bakar, Rosli Abu. 2007. "Nozzle Holes Effect on Unburned Fuel in Injected and In-Cylinder Fuel of Four Stroke Direct Injection Diesel Engine." *Research Journal of Applied Sciences* 2(11): 1165–69.

Barata, J. M. M., A. R. R. Silva, and I. Gokalp. 2003. "Numerical Study of Cryogenic Jets Under Supercritical Conditions." *Journal of Propulsion and Power* 19: 142–47.

Bellan, J. 2000. "Supercritical (and Subcritical) Fluid Behavior and Modeling: Drops, Streams, Shear and Mixing Layers, Jets and Sprays." *Progress in Energy and Combustion Science* 26: 329–66.

Chehroudi, B., R. Cohn, and D. Talley. 2000. "Spray/Gas Behaviour of Cryogenic Fluids under Sub- and Supercritical Conditions." In *Eighth International Conference on Liquid Atomization & Sprays Systems, ICLASS-2000*, Pasadena, California, USA.

———. 2002. "Cryogenic Shear Layers: Experiments and Phenomenological Modeling of the Initial Growth Rate under Subcritical and Supercritical Conditions." *International Journal of Heat and Fluid Flow* 23: 554–63.

Chehroudi, B., D. Talley, and E. Coy. 2002. "Visual Characteristics and Initial Growth Rates of Round Cryogenic Jets at Subcritical and Supercritical Pressures." *Physics of Fluids* 14(2): 850–61.

H. Mayer, Wolfgang O. et al. 1998. "Atomization and Breakup of Cryogenic Propellants Under High-Pressure Subcritical and Supercritical Conditions." *Journal of Propulsion and Power* 14(5): 835–42.

Hariram, V., and G. Mohan Kumar. 2012. "The Effect of Injection Timing on Combustion, Performance and Emission Parameters with AOME Blends as a Fuel for Compression Ignition Engine." *Research Journal of Applied Sciences* 7(9): 510–19.

Jarczyk, M, and M Pfitzner. 2012. "Large Eddy Simulation of Supercritical Nitrogen Jets." In *50th AIAA Aerospace Sciences Meeting Including the New Horizons Forum and Aerospace Exposition*, , 1–13.

Kim, Taehoon, Yongmo Kim, and Seong Ku Kim. 2011. "Numerical Study of Cryogenic Liquid Nitrogen Jets at Supercritical Pressures." *Journal of Supercritical Fluids* 56(2): 152–63. http://dx.doi.org/10.1016/j.supflu.2010.12.008.

Lacaze, Guilhem, and Joseph C. Oefelein. 2012. "A Non-Premixed Combustion Model Based on Flame Structure Analysis at Supercritical Pressures." *Combustion and Flame* 159: 2087–2103. http://dx.doi.org/10.1016/j.combustflame.2012.02.003.

Martínez-Martínez, S. et al. 2008. "Liquid Penetration Length in Direct Diesel Fuel Injection." *Applied Thermal Engineering* 28: 1756–62.

Mayer, W. et al. 2003. "Raman Measurements of Cryogenic Injection at Supercritical Pressure." *Heat and Mass Transfer* 39: 709–19.

Newman, J.a., and T.a. Brzustowski. 1971. "Behavior of a Liquid Jet near the Thermodynamic Critical Region." *AIAA Journal* 9(August): 1595–1602.

Oschwald, M. et al. 2006. "Injection of Fluids Into Supercritical Environments." *Combustion Science and Technology* 178(908038079): 49–100.

Oschwald, M., and M.M. Micci. 2002. "Spreading Angle and Centerline Variation of Density of Supercritical Nitrogen Jets." *Atomization and Sprays* 12(1-3): 91–106.

Oschwald, M., and A. Schik. 1999. "Supercritical Nitrogen Free Jet Investigated by Spontaneous Raman Scattering." *Experiments in Fluids* 27: 497–506.

Papamoschou, Dimitri, and Anatol Roshko. 1988. "The Compressible Turbulent Shear Layer: An Experimental Study." *Journal of Fluid Mechanics* 197(1973): 453.

Park, Tae Seon. 2012. "LES and RANS Simulations of Cryogenic Liquid Nitrogen Jets." *Journal of Supercritical Fluids* 72: 232–47.

Petit, X., G. Ribert, G. Lartigue, and P. Domingo. 2013. "Large-Eddy Simulation of Supercritical Fluid Injection." *Journal of Supercritical Fluids* 84: 61–73. http://dx.doi.org/10.1016/j.supflu.2013.09.011.

Rodrigues, C., J. Barata, and A. Silva. 2012. "Liquid Film Dynamic on the Spray Impingement Modeling." *Atomization and Sprays* 22(9): 757–75. http://www.begellhouse.com/journals/6a7c7e10642258cc,64b3d5d415f8eb91,5fd0322a38047258.html.

———. 2015. "On the Modelling of Evaporating Sprays Impinging onto Solid Surfaces." *53rd AIAA Aerospace Sciences Meeting*: 1–10.

Rodrigues, Christian, Jorge Barata, and André Silva. 2013. "Spray Impingement Modelling: Evaluation of the Dissipative Energy Loss and Influence of an

Enhanced near-Wall Treatment." *Fuel Processing Technology* 107: 71–80. http://dx.doi.org/10.1016/j.fuproc.2012.08.002.

Sanders, J.P.H., B. Sarh, and I. GÖkalp. 1997. "Variable Density Effects in Axisymmetric Isothermal Turbulent Jets: A Comparison between a First- and a Second-Order Turbulence Model." *International Journal of Heat and Mass Transfer* 40: 823–42.

Schmitt, T., J. Rodriguez, I. a. Leyva, and S. Candel. 2012. "Experiments and Numerical Simulation of Mixing under Supercritical Conditions." *Physics of Fluids* 24.

Schmitt, T., L. Selle, B. Cuenot, and T. Poinsot. 2009. "Large-Eddy Simulation of Transcritical Flows." *Comptes Rendus - Mecanique* 337(6-7): 528–38. http://dx.doi.org/10.1016/j.crme.2009.06.022.

Seebald, P., and P.E. Sojka. 2011. "Supercritical and Transcritical Injection." In *Hand Book of Atomization and Sprays*, ed. N. Ashgriz. Springer Science+Business Media, 255–61.

Segal, C., and S. a. Polikhov. 2008. "Subcritical to Supercritical Mixing." *Physics of Fluids* 20: 1–7.

Shinjo, J., and a. Umemura. 2011. "Surface Instability and Primary Atomization Characteristics of Straight Liquid Jet Sprays." *International Journal of Multiphase Flow* 37(10): 1294–1304. http://dx.doi.org/10.1016/j.ijmultiphaseflow.2011.08.002.

Sierra-Pallares, J. et al. 2009. "Numerical Analysis of High-Pressure Fluid Jets: Application to RTD Prediction in Supercritical Reactors." *Journal of Supercritical Fluids* 49: 249–55.

Sierra-Pallares, José, Pablo Santiago-Casado, and Francisco Castro. 2012. "Numerical Modelling of Supercritical Submerged Water Jets in a Subcritical Co-Flow." *Journal of Supercritical Fluids* 65: 45–53. http://dx.doi.org/10.1016/j.supflu.2012.02.028.

Sutton, G. P., and O. Biblarz. 2010. *Rocket Propulsion Elements*. 8th ed. Hoboken, New Jersey: John Wiley & Sons, Inc.

Vieira, Diana F C, Jorge M M Barata, Fernando M S P Neves, and Andre R R Silva. 2015. "Numerical Simulation of Twin Impinging Jets in Tandem through a Crossflow." *Journal of Engineering and Applied Sciences* 10(6): 123–36.

Zhou, Lei, Mao-Zhao Xie, Ming Jia, and Jun-Rui Shi. 2011. "Large Eddy Simulation of Fuel Injection and Mixing Process in a Diesel Engine." *Acta Mechanica Sinica* 27: 519–30.

Zong, Nan, Hua Meng, Shih Yang Hsieh, and Vigor Yang. 2004. "A Numerical Study of Cryogenic Fluid Injection and Mixing under Supercritical Conditions." *Physics of Fluids* 16: 4248–61.

Zong, Nan, and Vigor Yang*. 2006. "Cryogenic Fluid Jets and Mixing Layers in Transcritical and Supercritical Environments." *Combustion Science and Technology* 178(908038079): 193–227.

Zubanov, Vasiliy, Vitaliy Egorychev, and Leonid Shabliy. 2014. "Hydrogen-Oxygen Rocket Engine Design Using CFD-Modeling." *Research Journal of Applied Sciences* 9(10): 660–63.

A.8 Paper Published in Combustion Engines

http://www.combustion-engines.eu/en/numbers/54/772

Article citation info:
ANTUNES, E., SILVA, A., BARATA, J. Modeling of transcritical and supercritical nitrogen jets. *Combustion Engines*. 2017, **169**(2), 125-132. DOI: 10.19206/CE-2017-222

Eduardo ANTUNES
Andre SILVA
Jorge BARATA

CE-2017-222

Modelling of transcritical and supercritical nitrogen jets

The present paper addresses the modelling of fuel injection at conditions of high pressure and temperature which occur in a variety of internal combustion engines such as liquid fuel rocket engines, gas turbines, and modern diesel engines. For this investigation a cryogenic nitrogen jet ranging from transcritical to supercritical conditions injected into a chamber at supercritical conditions was modelled. Previously a variable density approach, originally conceived for gaseous turbulent isothermal jets, employing the Favre averaged Navier-Stokes equations together with a "k-ε" turbulence model, and using Amagat's law for the determination of density was applied. This approach allows a good agreement with experiments mainly at supercritical injection conditions. However, some departure from experimental data was found at transcritical injection conditions. The present approach adds real fluid thermodynamics to the previous approach, and the effects of heat transfer. The results still show some disagreement at supercritical conditions mainly in the determination of the potential core length but significantly improve the prediction of the jet spreading angle at transcritical injection conditions.

Key words: *fuel injection, jets, critical point, supercritical flows, cryogenics*

1. Introduction

The increasing demand for higher efficiency and performance of power and propulsion systems lead to the practice of raising pressure and temperature inside the combustion chamber. Rocket engines combustion chambersare typically subjected to high values of pressure and temperature which commonly exceed the critical thermodynamic point of it working fluid. The widespread of turbocharging, high compression ratios and high pressure direct injection systems seen in diesel engines contributed to the increase of the operating pressures and temperatures inside the combustion chamber. Often, in these engines, fuel injection happens at pressures which exceed the critical value of the fuel. The development of more advanced materials used in gas turbines has led to higher compression ratios and allow for higher temperatures at the turbine inlet, in practice this translates in higher pressures and temperatures experienced by fuels when injected into the combustion chamber, conditions around and above the critical point are easier to be achieved. Finally, more recently, the policy of downsizing in small gasoline engines has led to the inclusion of much of the technologies already present in diesel engines, consequently causing an increase of operating pressures and temperatures as well.

The thermodynamic critical point of fuels and oxidizers is likely to be achieved in a large number of internal combustion engines. According to several authors this leads to fast variations of the fluid properties [1] which must be correctly understand and predicted in order to obtain the most efficient design of propulsion and power systems.

Recent studies have pointed in the direction of identifying four different regions around the critical point. When both pressure and temperature are below the critical point, the regime is called subcritical. When temperature is above critical point and the pressure bellow, the fluid behaves like an ideal gas. If only pressure is supercritical the regime can be called transcritical, regime which still raises a lot of questions to researchers since fluids appear to have mixed behaviour. Finally when both pressure and temperature are above the critical point the regime is called supercritical [2].

The present study is focused on the numerical investigation of injection under transcritical and supercritical conditions, a problematic that has been studied experimentally by several authors [3–14] as well as numerically [2, 9–11, 14–30]. As far as today, some conclusions have been reached and validated about the changes in the physical properties of fluids when they are around and above critical conditions. According to Bellan [1], at the critical point mass diffusivity, surface tension, and latent heat become zero. On the other hand, the heat capacity at constant pressure, Cp, the isentropic compressibility, k_s and the thermal conductivity, λ, all become infinite. At supercritical conditions a behavioural change is observed for the jet structure, which evolves from a liquid-gas injection to a gas-gas like injection [8, 10, 13, 31]. However bigger questions appear about fluid behaviour in conditions near critical for which it is still unknown if the fluid presents a behaviour closer to a gas, a liquid or a mix of the two. Also, the transcritical regime still constitutes an unknown in terms of fluid behaviour which deserves further studies.

To model transcritical and supercritical injection conditions a variable density approach, which employs the Favre Averaged Navier-Stokes equations and a $k-\varepsilon$ turbulence model was tested [32]. This approach originally developed for isothermal, incompressible, turbulent, gaseous jets. It was tested to model the injection of cold nitrogen at conditions ranging from transcritical to supercritical regime, into a chamber filled with gaseous nitrogen at supercritical conditions. Flow configuration can be observed in Fig. 1, while the test conditions are described in Table 1. The obtained results showed quite good accuracy of the simulations at supercritical injection conditions, when compared with experimental. However the agreement was worse for transcritical injection conditions. Reasons for this discrepancy with experimental data at transcritical injection conditions could be pointed to the fact that the used model didn't take in consideration the influence of heat transfer between the two fluids and also not including real fluid effect. In order

to address these drawbacks of the previous approach the Favre averaged energy equation was integrated in the existing formulation as well as real fluid equations of state. With these modifications the authors have the expectation to improve the model performance in the modelling of the jet at transcritical conditions as well as to introduce more understanding over the flow of study.

To do so, the same configuration used in previous investigation [32] was employed as well as the same test conditions. The results will be compared with experimental data [8, 9] as well as with other numerical approaches [19, 23].

2. Computational model

In the present work was used a mathematical model and numerical approach based on the model used by Barata et al. [15] and in previous works [29, 30, 32]. However, modifications were made, the Favre averaged energy conservation equation was introduced and the equation of state based of Amagat's law was replaced by real fluid equations of state.

2.1. Governing equations

The method to solve is based on the solution of the conservation equations for momentum and mass. Turbulence is modelled with the "k–ε" turbulence model. A similar method has been used for three-dimensional or axisymmetric flows and only the main features are summarized here.

Table 1. Conditions of the test cases

	Case 3	Case 4
Condition	Transcritical	Supercritical
Chamber Temperature [K]	298	298
Chamber Pressure [MPa]	3.97	3.97
Injection Temperature [K]	126.9	137
Injection Velocity [m/s]	4.9	5.4
ρ_0 [kg/m^3]	435	171
ρ_∞ [kg/m^3]	45.5	45.5
ω	0.1046	0.2661

In the conservation equations, mass weighted averaging is applied to avoid the appearance of many terms involving density fluctuations for which additional models are needed. A mass averaged quantity is defined as

$$\widetilde{\phi} = \frac{\overline{\rho\phi}}{\overline{\rho}} \tag{1}$$

For the governing equations the standard parabolic truncation is employed. The mass averaged continuity equation for the axisymmetric two-dimensional geometry can be written in cylindrical polar coordinates, and is given by

$$\frac{\partial \overline{\rho}.\widetilde{U}}{\partial x} + \frac{1}{r}\frac{\partial r\overline{\rho}.\widetilde{V}}{\partial r} = 0 \tag{2}$$

The momentum equations for axial and radial direction take the form

$$\frac{\partial \overline{\rho}.\widetilde{U}\widetilde{U}}{\partial x} + \frac{1}{r}\frac{\partial r\overline{\rho}.\widetilde{V}\widetilde{U}}{\partial r} = -\frac{\partial \overline{p}}{\partial x} - \frac{1}{r}\frac{\partial r\overline{\rho}.\widetilde{u''v''}}{\partial r} \tag{3}$$

and

$$\frac{\partial \overline{\rho}.\widetilde{U}\widetilde{V}}{\partial x} + \frac{1}{r}\frac{\partial r\overline{\rho}.\widetilde{V}\widetilde{V}}{\partial r} = -\frac{\partial \overline{p}}{\partial r} - \frac{1}{r}\frac{\partial r\overline{\rho}.\widetilde{v''v''}}{\partial r} + \frac{\overline{\rho}.\widetilde{w''w''}}{r} \tag{4}$$

The mixing of different fluids is described by introducing the scalar property of mixture fraction, F, this variable represents the mass fraction of the fluid at the injector. It obeys a convection-diffusion equation of the form

$$\frac{\partial \overline{\rho}.\widetilde{U}\widetilde{F}}{\partial x} + \frac{1}{r}\frac{\partial r\overline{\rho}.\widetilde{V}\widetilde{F}}{\partial r} = -\frac{1}{r}\frac{\partial r\overline{\rho}.\widetilde{v''f''}}{\partial r} \tag{5}$$

In "k–ε" turbulence model, the Reynolds stresses are expressed in terms of the local strain rate:

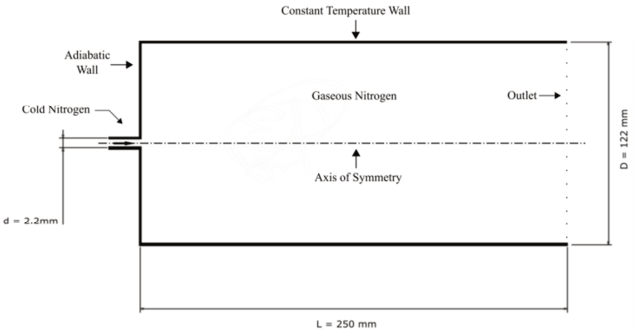

Fig. 1. Chamber geometry

$$-\overline{\rho}\widetilde{u_i''u_j''} = \overline{\rho}(\mu_t + \mu)\left(\frac{\partial \widetilde{u}_i}{\partial x_j} + \frac{\partial \widetilde{u}_j}{\partial x_i}\right) - \frac{2}{3}\delta_{ij}\left[\overline{\rho}\widetilde{k} + \overline{\rho}(\mu_t + \mu)\frac{\partial \widetilde{u_k}}{\partial x_k}\right] \tag{6}$$

with

$$\mu_t = C_\mu \frac{k^2}{\varepsilon} \tag{7}$$

The scalar flux in equation (5) is approximated with a gradient transport assumption

$$-\overline{\rho}\widetilde{u_i''f''} = -\frac{\mu_f}{\sigma_f}\frac{\partial \overline{F}}{\partial x_i} \tag{8}$$

From the foregoing we can deduced the parabolized set of equations in cylindrical coordinates where the generalized equation is

$$\frac{\partial}{\partial x}\left(\overline{\rho}.\widetilde{U}\widetilde{\phi}\right) + \frac{1}{r}\frac{\partial}{\partial r}\left(r\overline{\rho}.\widetilde{V}\widetilde{\phi}\right) = -\frac{1}{r}\frac{\partial}{\partial r}\left(r\overline{\rho}\Gamma\frac{\partial \widetilde{\phi}}{\partial r}\right) + S_\phi \tag{9}$$

where $\widetilde{\phi}$ may stand for any of the velocities, turbulent kinetic energy, dissipation, or scalar property, and S_ϕ take on different values for each particular $\widetilde{\phi}$ [33].

The previous works [29, 30, 32] didn't include in its formulation the conservation equation of energy. For the present investigation it had to be deduced and then integrated in the computational code. The Favre averaged energy equation for a steady flow in its vectorial form is represented by

$$\frac{\partial}{\partial x_j}\left(\overline{\rho}\widetilde{u}_j c_p \widetilde{T}\right) = -\frac{\partial}{\partial x_j}\left(c_p \frac{\mu}{Pr}\frac{\partial \widetilde{T}}{\partial x_j}\right) - \frac{\partial}{\partial x_j}\left[\underbrace{c_p\overline{\rho u_j'' T''}}_{(1)} + \frac{\overline{\rho}\widetilde{u}_j\widetilde{u}_k\widetilde{u}_k}{2} + \overline{\rho}\widetilde{u}_j\widetilde{k} + \underbrace{\widetilde{u_k}\overline{\rho u_j'' u_k''}}_{(2)} + \underbrace{\frac{\overline{\rho u_j'' u_k'' u_k''}}{2}}_{(3)} + \underbrace{c_p\frac{\mu}{Pr}\frac{\partial T''}{\partial x_j}}_{(4)} - \tilde{u}_i\tilde{\tau}_{ij} - \underbrace{\overline{u_i''\tau_{ij}}}_{(5)} + \underbrace{\widetilde{u}_i\overline{\tau_{ij}}''}_{(6)}\right] \quad (10)$$

The Favre averaged energy equation brings with it a large number of source terms, some of them can be solved directly, others, which are numbered, must be modelled.

Term (1), corresponding to turbulent transport of heat, can be modelled using a gradient approximation for the turbulent heat-flux:

$$c_p\overline{\rho u_j'' T''} \approx -c_p\frac{\mu_t}{Pr_t}\frac{\partial \widetilde{T}}{\partial x_j} \quad (11)$$

Term (2) is obtained from the turbulent-viscosity hypothesis expressed in equation (6)

$$\overline{\rho u_i'' u_j''} \approx \frac{2}{3}\rho\tilde{k}\delta_{ij} - \mu_t\left(\frac{\partial \widetilde{u}_i}{\partial x_j} + \frac{\partial \widetilde{u}_j}{\partial x_i} - \frac{2}{3}\frac{\partial \widetilde{u_k}}{\partial x_k}\delta_{ij}\right) \quad (12)$$

Terms (3) and (5), corresponding to turbulent transport and molecular diffusion of turbulent energy, can be neglected if the turbulent energy is small compared to the enthalpy, $k \ll \tilde{h}$. This is a reasonable approximation for most flows below the hyper-sonic regime. A better approximation might be a gradient expression of the form:

$$\frac{\overline{\rho u_j'' u_k'' u_k''}}{2} - \overline{u_i''\tau_{ij}} \approx -\left(\mu + \frac{\mu_t}{\sigma_k}\right)\frac{\partial k}{\partial x_k} \quad (13)$$

Term (4) is an artefact from the Favre averaging. It is related to heat conduction effects associated with temperature fluctuations. It can be neglected if $\left|\frac{\partial^2 \widetilde{T}}{\partial x_j^2}\right| \gg \left|\frac{\partial^2 \overline{T''}}{\partial x_j^2}\right|$, which is also true for virtually all flows.

And finally term (6) can also be neglected if $\left|\widetilde{\tau_{ij}}\right| \gg \left|\overline{\tau_{ij}}''\right|$, which is true to virtually all flows. The energy equation could also be put in the form of the general equation (9), it is not done here due to the fact of becoming a very long expression.

2.2. Real fluid equation of state

To obtain the mean density field an equation of state is employed. For many applications the ideal gas equation of state is the most common choice. However, as explained previously, the conditions of study of the present investigation escape the range of applicability of the concept of ideal gas. For this reason a real fluid equation of state seems to be a more convenient choice.

In the present investigation two different real fluid equations of state were analysed and employed in the numerical approach, the Soave-Redlich-Kwong and the Pend-Robinson equations of state.

The Soave-Redlich-Kwong equation can be expressed as

$$P = \frac{RT}{(V_m - b)} - \frac{a(T)}{V_m(V_m + b)} \quad (14)$$

where the coefficients a and b are described in detail in Soave [34].

The Peng-Robinson equation of state can be written as

$$P = \frac{RT}{(V_m - b)} - \frac{a(T)}{V_m(V_m + b) + b(V_m - b)} \quad (15)$$

once again the detailed formulation of coefficients a and b can be found in Peng and Robinson's work [35].

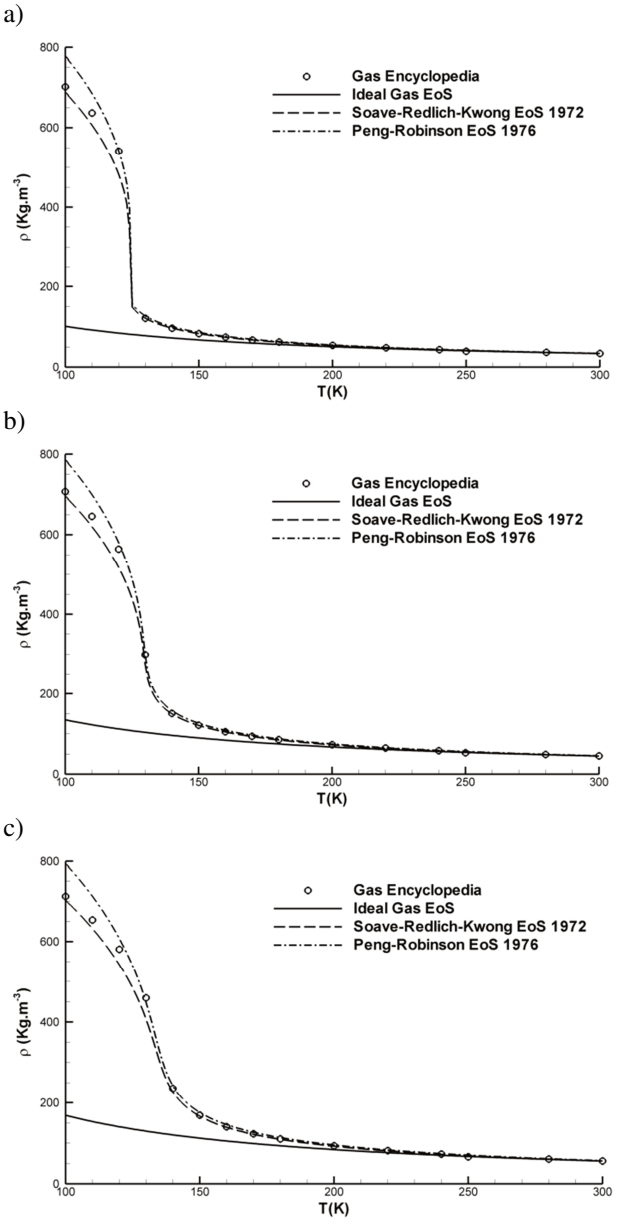

Fig. 2. Comparison of different equations of state at: a) 3 MPa; b) 4 MPa; c) 5 MPa

The performance of both equations of state was investigated in the present investigation. Fig. 2 shows the comparison, for three different pressures and under temperatures ranging from 100 K to 300 K, between the two real fluid equations of state and the data from gas encyclopaedia [36], having also as reference the performance of the ideal gas equation of state.

Results express very clearly the advantage that the two real fluid equations of state have over the ideal gas equation of state. What doesn't become so clear is which real fluid equation of state performs better. Thus, both equations of state were implemented into the computational approach in order to evaluate their performance in the modelling of the flow of interest.

In previous work [30, 32], fluid properties such as molecular viscosity, specific heat at constant pressure, and thermal conductivity had been assumed as constant. However, this was not the case for the present investigation. Experimental data from Gas Encyclopaedia [36] was used to generate linear functions which provide the value of such properties for different temperatures and pressures.

2.3. Numerical method

The governing equations are solved using a parabolized marching algorithm which resembles the (elliptic) TEACH code, and are described in detail in [33]. This approach was applied to variable density jets and then extended to the study of liquid cryogenic jets under sub-near critical pressures, and sub to supercritical temperatures in the present work.

2.4. Computational grid

An expansive grid in both directions was used, making it more refined when close to injector. In the axial direction a constant expansion rate is impose, as well as the domain length, due to this, the initial grid size is calculated by the grid construction routine. The determination of points in the radial direction is somewhat more complex. For the width of the injector, a fixed amount of points was set, which stablishes a constant distance between nodes. Outside of the injector radial size, the grid routine determines the expansion rate in order to fit the remaining points into the radial domain of the configuration. The grid has a size of 150 by 65 points, and for the injector 13 points are set in the radial direction. The rate of expansion in the axial direction is set as 2%.

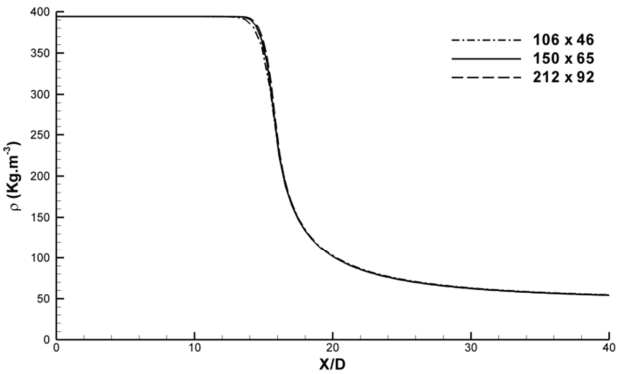

Fig. 3. Grid size dependency test based on the axial density distribution

In order to evaluate the influence of the grid on the converged solution grid dependency tests had to be performed. Figure 3 shows the grid dependency test, the used grid, of 150x65 points is compared with a more refined grid of 212x92 points and with a coarser grid of 106x46 points. The results used for comparison are the axial density variation in the centreline and its visible the independence of the solution from the grid size.

3. Results and discussion

Numerical results obtained in the present work are presented in this section and compared with the experimental data of Mayer et al. [9], the large eddy simulations of Schmitt et al. [19] and of Jarczyk and Pfitzner [23], and also with the results obtained using the unmodified approach [30, 32]. A discussion is also provided in order to reach the conclusions exposed in the next section.

Fig. 4 and 5 show the density field and streamlines for respectively the transcritical case and the supercritical case, in both figures image a) shows the results obtained while employing the Soave-Redlich-Kwong equation of state while image b) expresses the results achieved with the Peng-Robinson equation. Analysing Fig. 5 the most evident conclusion that can be taken is the appearance of a recirculation downstream of the injector, it is also evident the existence of entrainment of the chamber fluid into the injection fluid right after the injector. This jet structure is not affected by the choice of equation of state, both Fig.5 a) and b) show exactly the same jet structure. Comparing the results from both equations of state can be concluded that the Peng-Robinson equations produces higher values of density at the inlet, this is a result which could be anticipated by the results obtained in Fig. 2. It is also visible a longer potential core and deeper penetration of the jet into the chamber in the model with uses the PR equation. This can possibly be explained by the fact that the higher density at inlet causes a larger momentum, since velocity is the same, and this larger momentum takes longer to be dissipated. The supercritical case is represented in Fig. 6. A very similar jet structure is observed for this case when compared with transcritical injection conditions. There's also the appearance of entrainment close to the injector, and, further downstream, the existence of a recirculation. Comparing with Fig. 5 the potential core length and jet penetration is shorter for both equations of state. Like in the transcritical case also the Peng-Robinson equations of state produces higher values of density in the inlets which leads to a longer potential core.

Fig. 6 and 7 represent in better detail the evolution of density in the centreline of the jet. In Fig. 6 the axial density distribution for the transcritical case is shown for the current approach with both equations of state, these results are here compared with the experimental results from Mayer et al. [9] as well as with the results obtained with the previous approach, which obtained density from Amagat's law, and with two large eddy simulations of Schmitt et al. [19] and of Jarczyk and Pfitzner [23]. Both results of the different equations of state for the current approach show a much larger potential core than the one observed in the results of the other authors. With the Soave-Redlich-Kwong equation of state is obtained a potential core of 15.7 injector diameters, as for the Peng-Robinson equation a potential core of 16.4 injector diameters is obtained. For the same case Schmitt et al. reaches a potential core of 7.9 diameters while

Jarczyk and Pfitzner achieves a potential core with a length of around 9 diameters. These values of potential core length are also longer than the potential core of 11.8 obtained by the initial approach with Amagat's law. Further downstream the current approach keeps the difficulty in fitting the experimental data or the other LES investigations.

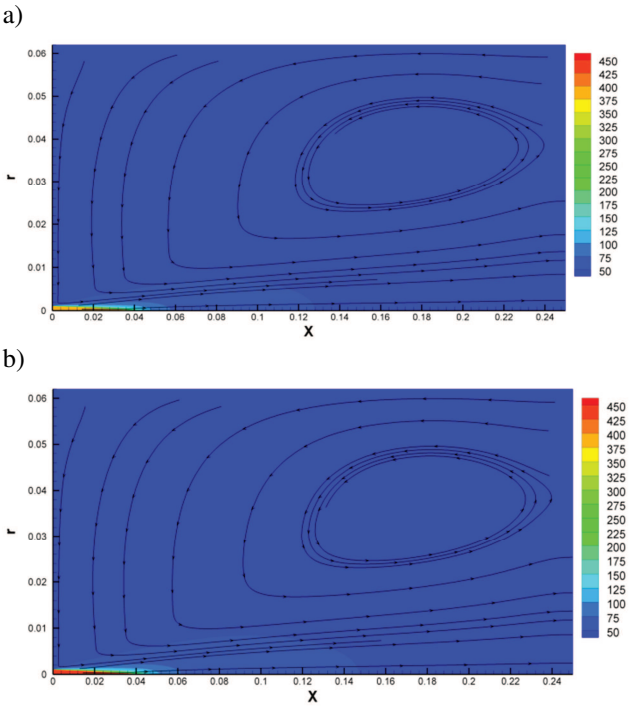

Fig. 4. Density field and streamlines for transcritical case, a) SRK EoS, b) PR EoS

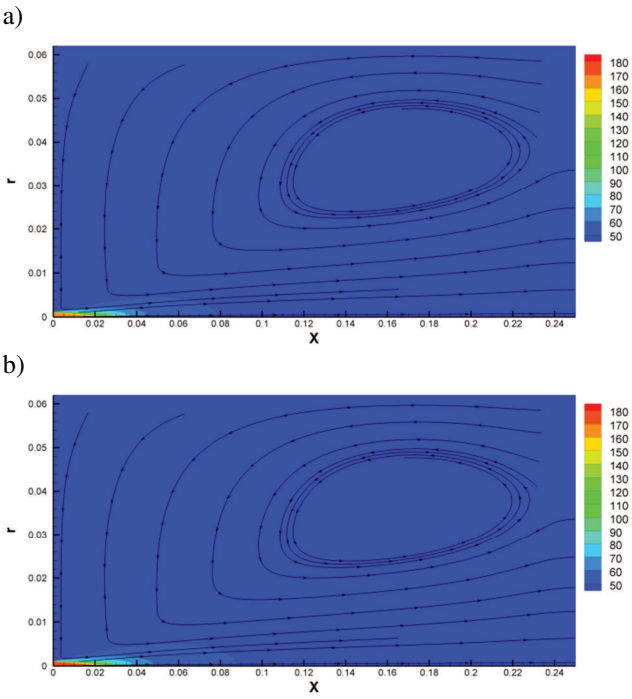

Fig. 5. Density field and streamlines for supercritical case, a) SRK EoS, b) PR EoS

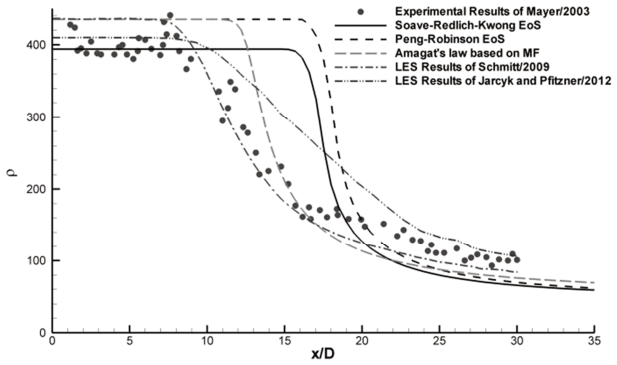

Fig. 6. Axial density distribution for transcritical case

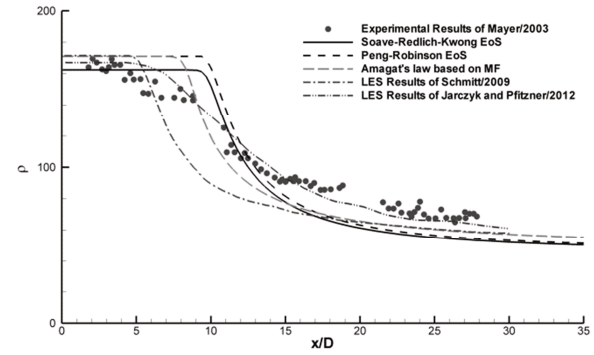

Fig. 7. Axial density distribution for supercritical case

The axial density distribution for the supercritical case is represented in Fig. 7. Again, the current approach employing the two different equations of state is compared with experimental and LES data as well as with the results obtained by the previous approach [30]. For the supercritical case a closer agreement with experimental data is obtained but the over prediction of the potential core length still exists. When using the Soave-Redlich-Kwong equation a potential core with a length of 9.4 injector diameters is observed, with the Peng-Robinson equation it increases to a length of 9.6 injector diameters. For the same test case the previous approach achieved a potential core length of 7.8 diameters, Schmitt et al. reached 5.1 while Jarczyk and Pfitzner predicted a potential core with a length of 6.0 injector diameters, it's important to refers that when analyzing the experimental results for this case the existence of a potential core is not evident. Downstream of the potential core is obtained a better agreement with experiments between 10 and 15 diameters but then there is a departure from the data provided by Mayer [9]. Still, for this condition, the LES from Schmitt et al. [19] is not able to provide superior agreement, while the previous approach provides a closer agreement. For this case is the large eddy simulation of Jarczyk and Pfitzner which provides the closest agreement.

The full width of half maximum of density is expressed for the transcritical and supercritical test cases respectively in Figures 8 and 9. In figure 8 are represented the values obtained by the previous and current approach as well as the experimental data provided by Mayer et al. [9]. Analyzing first the data from Mayer, it can be seen that initially the jet appears to have a radius of twice the radius of injector,

this is explained in the paper of Mayer [9] by the difficulty of the technique of Raman Scattering to provide accurate values of density when the values are high. There's then a decrease of the jet thickness until 10 x/D followed then by the expected expansion of the jet width. Similar evolution is observed by all the approaches presented in the present paper. However, when using the real fluid equations of state the potential core is longer thus delaying the expansion of the jet. In figure 12 only the results obtained by previous and current approach are exhibit since Mayer didn't provide results for this case. Nevertheless, the evolution of the full with of half maximum of density follows the same shape obtained for the transcritical case, with the previous approach showing wider expansion of jet.

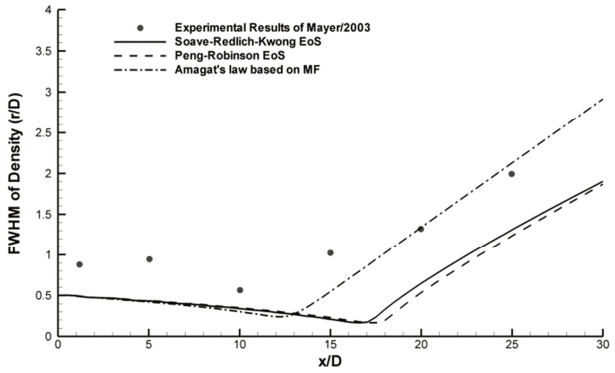

Fig. 8. Axial density distribution for transcritical case

From the results of the full width of half maximum of density, it can be obtained the tangent by linear interpolation which represents the jet expansion rate. The linear interpolation was performed by other authors between x/D = 15 and x/D = 25. In the present work these were generally the points chosen for the calculation, however as it is visible, for the current approach at transcritical conditions, the jet expansion starts only after x/D = 15, thus, for this situation the interpolation was performed between x/D = 20 and x/D = 30. These results are expressed in Table 2.

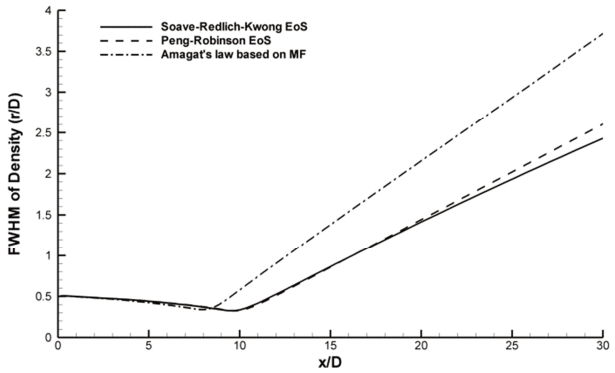

Fig. 9. Axial density distribution for supercritical case

For the transcritical case the experimental data of Mayer et al. [9] reached to a spreading rate of 0.196, a similar spreading rate was obtained by the experimental work of Oschwald and Micci [8]. The original approach used in the present investigation, for the same case predicted a spreading rate of 0.316 which is an over prediction of around 61% when compared with the data of Mayer. By the introduction of a real fluid equation of state a closer agreement for the spreading rate was reached, with values of 0.250 for the SRK equation and 0.266 with the PR equation of state, representing respectively a variation of 27.6% and 35.7% when compared with Mayer's work. The large eddy simulation of Schmitt et al. provides a spreading rate of 0.227 which is still closer to experimental data.

Table 2. Results of jet spreading rate

Case	First Approach Amagat's law	Current Approach		Mayer et al. 2003 [9]	Schmitt et al. 2009 [19]	Oschwald and Micci 2002 [8]
		SRK	PR			
Trans-critical	0.316	0.250	0.266	0.196	0.227	0.206
Super-critical	0.310	0.214	0.234	–	0.241	0.312

For the supercritical case Mayer et al. didn't provide results of the FWHM of Density thus not allowing the comparison of jet spreading angle. On the other hand Oschwald and Micci [8] as well as Schmitt et al. [19] did provide results allowing a comparison to be established. The results obtained from the first approach which makes use of Amagat's law replicate almost perfectly the jet spreading rate obtained by Oschwald and Micci [8]. Achieving a much better result that any of other predictions. The large eddy simulation of Schmitt et al. [19] provides an acceptable results as well, closely followed by the second approach when employing the Peng-Robinson equation of state and finally the furthest agreement comes from the second approach when employing the SRK equation of state.

4. Conclusions

With the objective of testing and developing new methodologies to model jets at conditions around the critical point, a methodology originally developed for the study of turbulent, variable density, isothermal jets was modified to include the effects of heat transfer and a real fluid equation of state. The effects of the variation of physical properties of fluid such as thermal conductivity, specific heat at costant pressure and molecular viscosity experienced with the variation of pressure and temperature were also included. To do so, in the present approach were introduced linear functions taken from the data provided by the Gas Encyclopaedia [36].

The original approach had already along this investigation proved his potential for the study of this kind of fluids, despite its simplicity and inexpensive computational requirements. It proved to provide good agreement with experimental data for supercritical injection conditions outperforming much more expensive large eddy simulations. However, it starts facing difficulties when dealing with flows in subcritical and transcritical conditions. By not accommodating the heat transfer and real fluid thermodynamics it fails to predict the correct behaviour of fluids in the transition to the two phase flow. The new approach intends overcome these lacks by the introduction of the Favre averaged energy equation and a real fluid equation of

state in the form of a Soave-Redlich-Kwong and a Peng-Robinson equations of state.

This new modified approach was able to improve the spreading angle results over the original approach under transcritical regime of injection, reaching a much closer agreement. The performance of the agreement at supercritical conditions unfortunately suffered a decrease.

Two different reasons could be pointed out to the decrease of accuracy at supercritical conditions. On one hand the data provided in Gas Encyclopaedia doesn't contain values of the properties in the critical point. The critical point represents a thermodynamic singularity, thus, the properties values at this point suffer a very pronounced variation which is not accessed by the present approach. On the other hand, the flow appears to be governed by the turbulent characteristics. The ratio between turbulent viscosity and turbulent thermal diffusivity is prone to suffer variations along the flow. Thus, the employment of a constant turbulent Prandtl number, Pr_t, may in fact not be the most efficient option. Future work will address these two points, expecting to obtain increased performance.

Acknowledgments

The present work has been performed under the scope of the activities of Aeronautics and Astronautics Research Center of the Associated Laboratory in Energy Transports and Aeronautics (AeroG-LAETA), UID/EMS/50022/2013.

The first authors would like to thanks to the Fundação para a Ciência e a Tecnologia (FCT), the Portuguese public agency for science and technology for the PhD scholarship SFRH/BD/87822/2012.

Nomenclature

a, b	real fluid equation of state coefficients
c_p	specific heat at constant pressure
C_μ	coefficient in turbulence model
D	injector diameter [m]
ε	dissipation rate of turbulent energy
f	mixture fraction
F	mean mixture fraction
i	axial direction index
j	radial direction index
k	turbulent kinetic energy
μ	molecular viscosity
μ_t	turbulent viscosity
ϕ	generalized variable
ω	chamber-to-injected fluid density ratio
P_{cr}	critical pressure [MPa]
P_∞	chamber ambient pressure [MPa]
P_r	reduced presure (P_∞/P_{cr})
Pr	Prandtl number
Pr_t	turbulent Prandtl number
ρ	density [kgm^{-3}]
ρ_0	injected fluid density [kgm^{-3}]
ρ_∞	injection chamber's fluid density [kgm^{-3}]
r	radial coordinate [m]
R	universal constant of gases
R/D	radial distance normalized by injector diameter
R_{diam}	injector radius [m]
R_e	Reynolds number
S_ϕ	source term
t	time [s]
T	temperature [K]
u	axial velocity [ms^{-1}]
U	mean axial velocity [ms^{-1}]
U_{in}	injection axial velocity [ms^{-1}]
v	radial velocity [ms^{-1}]
v_t	turbulent kinematic viscosity
V	mean radial velocity [ms^{-1}]
V_m	molar volume
X	axial coordinate [m]
x/D	axial distance normalized by injector diameter

Bibliography

[1] BELLAN, J. Supercritical (and subcritical) fluid behavior and modeling: drops, streams, shear and mixing layers, jets and sprays. *Prog. Energy Combust. Sci.* 2000, **26**, 329-366.

[2] LACAZE, G., OEFELEIN, J.C. A non-premixed combustion model based on flame structure analysis at supercritical pressures. *Combust. Flame*. 2012, 159, 2087-2103.

[3] NEWMAN, J.A., BRZUSTOWSKI T.A. Behavior of a liquid jet near the thermodynamic critical region. *AIAA J.* 1971, **9**, 1595-1602.

[4] MAYER, W.O.H. et al. Atomization and breakup of cryogenic propellants under high-pressure subcritical and supercritical conditions. *J. Propuls. Power.* 1998, **14**(5), 835-842.

[5] OSCHWALD, M., SCHIK, A. Supercritical nitrogen free jet investigated by spontaneous Raman scattering. *Exp. Fluids*. 1999, **27**, 497-506.

[6] CHEHROUDI, B., COHN, R., TALLEY, D. Gas behaviour of cryogenic fluids under sub- and supercritical conditions. Eighth International Conference on Liquid Atomization & Sprays Systems. *ICLASS-2000*, 2000.

[7] CHEHROUDI, B., COHN, R., TALLEY, D. Spray/gas behaviour of cryogenic fluids under sub- and supercritical conditions. Eighth International Conference on Liquid Atomization & Sprays Systems. *ICLASS-2000*, 2000.

[8] OSCHWALD, M., MICCI, M.M. Spreading angle and centerline variation of density of supercritical nitrogen jets. *Sprays*. 2002, **12**(1-3), 91-106.

[9] MAYER, W., TELAAR, J., BRANAM, R. et al. Raman measurements of cryogenic injection at supercritical pressure. *Heat Mass Transf.* 2003, **39**, 709-719.

[10] OSCHWALD, M. et al. Injection of fluids into supercritical environments. *Combust. Sci. Technol.* 2006, **178**, 908038079, 49-100.

[11] STAR A.M., EDWARDS J.R., LIN K.-C. et al. Numerical simulation of injection of supercritical ethylene into nitrogen. *J. Propuls. Power.* 2006, **22**(4), 809-819.

[12] MARTÍNEZ-MARTÍNEZ, S., SÁNCHEZ-CRUZ, F.A., RIESCO-ÁVILA, J.M. et al. Liquid penetration length in direct diesel fuel injection. *Appl. Therm. Eng*. 2008, 28, 1756-1762.

[13] SEGAL, C., POLIKHOV, S.A. Subcritical to supercritical mixing. *Phys. Fluids*. 2008, 20, 1-7.
[14] SCHMITT, T., RODRIGUEZ, J., LEYVA, I.A., CANDEL, S. Experiments and numerical simulation of mixing under supercritical conditions. *Phys. Fluids*. 2012, **24**.
[15] BARATA, J.M.M., SILVA, A.R.R., GOKALP, I. Numerical study of cryogenic jets under supercritical conditions. *Journal of Propulsion and Power*. 2003, **19**, 142-147.
[16] ZONG, N., MENG, H., HSIEH, S.Y., YANG, V. A numerical study of cryogenic fluid injection and mixing under supercritical conditions. *Phys. Fluids*. 2004, **16**, 4248-4261.
[17] ZONG, N., YANG, V. Cryogenic fluid jets and mixing layers in transcritical and supercritical environments. Combust. Sci. Technol. 2006, 178, 908038079, 193-227.
[18] AOUISSI, M., BOUNIF, A., BENSAYAH, K. Scalar turbulence model investigation with variable turbulent Prandtl number in heated jets and diffusion flames. Heat Mass Transf. und Stoffuebertragung. 2008, 44, 9, 1065–1077.
[19] SCHMITT, T., SELLE, L., CUENOT, B., POINSOT, T. Large-eddy simulation of transcritical flows. *Comptes Rendus - Mec*. 2009, **337**(6-7), 528-538.
[20] KIM, T., KIM, Y., KIM, S.K. Numerical study of cryogenic liquid nitrogen jets at supercritical pressures. *J. Supercrit. Fluids*. 2011, **56**(2), 152-163.
[21] ZHOU, L., XIE, M.-Z., JIA, M., SHI, J.-R. Large eddy simulation of fuel injection and mixing process in a diesel engine. *Acta Mech. Sin*. 2011, **27**, 519-530.
[22] NEGRO, S., BIANCHI, G.M. Superheated fuel injection modeling: An engineering approach. *Int. J. Therm. Sci*. 2011, 50(8), 1460-1471.
[23] JARCZYK, M., PFITZNER, M. Large eddy simulation of supercritical nitrogen jets. *50th AIAA Aerospace Sciences Meeting Including the New Horizons Forum and Aerospace Exposition*. 2012, **1**, 1-13.
[24] TERASHIMA, H., KOSHI, M. Approach for simulating gas-liquid-like flows under supercritical pressures using a high-order central differencing scheme. *J. Comput. Phys*. 2012, **231**(20), 6907-6923.
[25] TERASHIMA, H., KOSHI, M. Strategy for simulating supercritical cryogenic jets using high-order schemes. *Comput. Fluids*. 2013, **85**, 39-46.
[26] PARK, T.S. LES and RANS simulations of cryogenic liquid nitrogen jets. *J. Supercrit. Fluids*. 2012, 72, 232-247.
[27] Schuler, M.J., Rothenfluh, T., Von Rohr, P.R. Simulation of the thermal field of submerged supercritical water jets at near-critical pressures. *J. Supercrit. Fluids*. 2013, **75**, 128-137.
[28] PETIT, X., RIBERT, G., LARTIGUE, G., DOMINGO, P. Large-eddy simulation of supercritical fluid injection. *J. Supercrit. Fluids*. 2013, **84**, 61-73.
[29] ANTUNES, E., SILVA, A.R.R., BARATA, J.M.M. Evaluation of numerical variable density approach to cryogenic jets. *50th AIAA Aerospace Sciences Meeting Including the New Horizons Forum and Aerospace Exposition*. 2012, **1**, 1-14.
[30] ANTUNES, E., SILVA, A., BARATA, J. RANS modeling of transcritical and supercritical nitrogen jets. *53rd AIAA Aerospace Sciences Meeting*. 2015, **1**, 1-14.
[31] CHEHROUDI, B., COHN, R., TALLEY, D. Cryogenic shear layers: Experiments and phenomenological modeling of the initial growth rate under subcritical and supercritical conditions. *Int. J. Heat Fluid Flow*. 2002, **23**, 554-563.
[32] ANTUNES E., SILVA A., BARATA J. Variable density approach for modeling of transcritical and supercritical jets. *J. Eng. Appl. Sci.* 2017.
[33] SANDERS, J.P.H., SARH, B., GÖKALP, I. Variable density effects in axisymmetric isothermal turbulent jets: a comparison between a first- and a second-order turbulence model. *Int. J. Heat Mass Transf*. 1997, **40**, 823-842.
[34] SOAVE, G. Equilibrium constants from a modified Redlich-Kwong equation of state. *Chem. Eng. Sci*. 1972, **27**(6), 1197-1203.
[35] PENG, D.-Y., ROBINSON, D.B. A new two-constant equation. *Ind. Eng. Chem. Fundam*. 1976, **15**(1), 59-64.
[36] MEDARD L. Gas encyclopaedia, 1st ed. Amsterdam: *Elsevier Science*, 1976.

Eduardo Antunes, MEng. – Aeronautical Engineering at University of Beira Interior.

e-mail: *EduardoFariasAntunes@hotmail.com*

Prof. Jorge Barata, Habilitation – Aerospace Science Department at University of Beira Interior.

e-mail: *JBarata@ubi.pt*

André Silva, PhD. – Aerospace Science Department at University of Beira Interior.

e-mail: *Andre@ubi.pt*